7th EAWE PhD Seminar on Wind Energy in Europe

Seminar Proceedings

Delft University of Technology
27th and 28th October 2011
Delft, the Netherlands

7th EAWE PhD Seminar on Wind Energy in Europe

Seminar Proceedings

Delft University of Technology
27th and 28th October 2011
Delft, The Netherlands

7th EAWE PhD Seminar on Wind Energy in Europe

Delft University of Technology - 27th and 28th October 2011 - Delft, The Netherlands

Organized by Delft University Wind energy research institute
for European Academy of Wind Energy

Sponsored by:

Main Sponsor

SUZLON
POWERING A GREENER TOMORROW

Sponsor

SIEMENS

Organization board:
Chair:
Prof.dr.ir. Gijs van Kuik
Organizers:
Pieter Gebraad
Maxim Segeren
Giuseppe Tescione
Sylvia Willems

For info and contacts:
W: http://www.duwind.tudelft.nl/eaweseminar
E: duwind@tudelft.nl
T: +31 15 278 5170

For its offshore engineering Center of Competence in The Hague, the Netherlands, Siemens Wind Power A/S is looking for an experienced engineer for the position of

Team Manager – Offshore Support Structure Design

Would you help us to reach our goal to reduce the levelised cost of wind-generated electricity?

Join us and become the team manager of our offshore support structures design team. This team is part of the engineering department of Siemens Wind Power located in Brande, Denmark and is responsible for the design and optimization of present and future offshore support structures. In addition, the team is responsible for the dynamic analysis of the global response of the entire structural system including the wind turbine controller to external loading (e.g. wind and waves).

Main tasks & responsibilities

- Manage the entire design process for offshore wind turbine support structures, from conceptual design to final design and development of necessary calculation tools and design manuals
- Manage the team and successfully implement the strategy
- Hold design reviews and implement lessons learned
- Follow up on the project documentation and ensure that the work is in compliance with our procedures
- Control the certification process in cooperation with an external certification body
- Provide experience gathering and innovation in connection with new solutions
- Preserve and expand the constructive cooperation with Delft University of Technology and establish new co-operations with other (technical) universities / research institutes of good standing

You will be based in The Hague, the Netherlands. The work is performed in close dialogue with the Engineering Department and the Offshore Engineering Department both located in Brande, Denmark.

Required education, behavioural competencies and skills

- Academic education, preferably MSc Mechanical, Offshore, Civil or Aerospace Engineering and relevant experience with design of offshore supporting structures (preferably more than 5 years)
- Excellent communication and interpersonal skills
- Fluent in English
- Strong HSE and quality awareness
- Enthusiastic and pro-active
- Decisive
- Strong project planning and facilitating skills

We offer

A unique opportunity to work in an open and inspiring international environment and you will have an influence on the development of the design of foundations for offshore wind turbines. You will be part of a dynamic team with competent, ambitious and effective colleagues. We have an open and informal tone and create an environment where we profit by each other's competences. We are continuously working on increasing our effectiveness and finding the best, technical solutions.
You will enjoy good working conditions, flexible working hours and excellent educational opportunities and professional development.

Commencement: As soon as possible

Interested?

Please contact David Molenaar on tel. +31 70 333 3287 or by e-mail: david-pieter.molenaar@siemens.com. You can apply for this job online at www.siemens.nl/career. The application should include relevant documentation of education and / or relevant work experience as well as information of where you have seen the job advertisements.

Give your career wings

Siemens Wind Power

www.siemens.nl/career

SIEMENS

Dear wind energy PhD colleagues,

With great pleasure I welcome you to the 7th PhD seminar of the European Academy for Wind Energy organized by DUWIND, the wind energy research institute of TU-Delft.

This seminar is a success right from the 1st edition, and is unique: it is a seminar for and on behalf of PhD's. As in the previous editions, the presentations, posters, discussions and mutual contacts are not controlled by senior researchers but by the PhD community itself. You can present your ideas, questions, progress and (preliminary) results to PhD-colleagues, instead of a severe peer-reviewing audience. The previous seminars have shown that they contributed to convert all that you present and discuss here, to mature peer-reviewed publications. You can look for other PhD's working in the same field to discuss topics in detail or explore cooperation. More than once we have seen that these contacts have led to PhD's spending some months of their work at another institute or university. To facilitate this, the seminar gives enough room for personal contacts.

This is the place to thank the DUWIND team of PhD's that have organized this seminar: Pieter Gebraad, Giuseppe Tescione and Maxim Segeren. Together with DUWIND's secretary Sylvia Willems, you have done this very enthusiastically and professionally. Many thanks!

It is now up to you. I hope you will enjoy the seminar, and your stay in Delft.

On behalf of the board of the Academy,
Gijs van Kuik
Director of DUWIND

Contents

Session 1A

Rotor and Wakes Aerodynamics I

A study of the NACA 0012 blade using a parallel vortex method

Lene Eliassen[†], Michael Muskulus[*]
[†]Department of Mechanics and Structural Engineering and Material Science, University of Stavanger
Stavanger, Norway
[*] Department of Civil and Transport Engineering, Norwegian University of Science and Technology
Trondheim, Norway
E-mail: lene.eliassen@uis.no, michael.muskulus@ntnu.no

Keywords: Vortex panel method, Parallel computing, Wind turbine aerodynamics, Potential Flow

1 Introduction

The most commonly used tool for aeroelastic modeling of wind turbine blades is the beam element momentum (BEM) method. It is based upon two-dimensional airfoil characteristics, with corrections applied for some three-dimensional effects. Important phenomena such as dynamic wake and dynamic stall are implemented in BEM by way of semi-empirical equations. The usual implementation of the BEM method needs a few iterations to solve an implicit equation. The method is quite fast, which is one of the main reasons for its popularity [6].

For the aerodynamic loading of a wind turbine, it is not only important to model the incoming wind correctly. For accurate results also the wake behind the turbine needs to be considered. The induced velocity due to the wake affects the inflow velocity and the angle of attack distribution over the rotor disk [9]. Although this is taken care of in BEM by semi-empirical induction factors, a proper treatment of the wake is needed to ensure that the aerodynamic loads are correctly represented, especially in dynamic (transient) wind fields or under yawed conditions.

In this paper a vortex method is applied to calculate aeroelastic loads. This class of methods is seldom used for aerodynamic computations of wind turbines due to its relatively high computational cost compared with the BEM method. Its advantage is that the wake is included in the calculations in a straightforward manner, allowing for more accurate results, in a wider range of situations. However, the basic vortex method we have used, is based upon the assumption of a potential flow (inviscid, irrotational and incompressible). In reality the flow around the wind turbine is viscous, compressible and rotational, and phenomena such as the boundary layer, stall and tower shadow can not be modelled with the basic method we have used. Extensions of the vortex method exist that address these issues [1, 10], but these are not considered here.

Up to now, vortex methods have mostly been used to investigate two dimensional flow fields and simple steady state three dimensional cases, whereas full scale analyses of wind turbines are rare due to their computational cost. The most computationally demanding operation for the vortex method is solving for the velocity field [4]. This calculation can be done in parallel, which allows for shortening the time of computation.

The purpose of the present study was to reduce the computational time of the vortex code. In order to reduce the computational cost we did a parallel implementation of our panel vortex code on a general purpose graphics unit (GPU).

2 Method

2.1 Vortex Method

The vortex method assumes the flow around the airfoil and the wake to be inviscid, irrotational and incompressible. A velocity potential, Φ, that describes such a flow is assumed to exist. The continuity equation for this flow is the Laplace equation [4]:

$$\nabla^2\Phi = 0 \tag{1}$$

The basic strategy of vortex methods is to build up a solution to Eq. (1) by superposition of simple basic solutions. We have chosen the singular source, with strength σ, and doublet elements, with strength μ, as building blocks to represent the potential flow in our panel method. These building blocks are often referred to as singular elements. The solution can then be written as [4]:

$$\Phi(x,y,z) = -\frac{1}{4\pi}\int_{\text{body + wake}}\left[\mu\mathbf{n}\cdot\nabla\left(\frac{1}{r}\right) - \sigma\left(\frac{1}{r}\right)\right]\mathrm{d}S \tag{2}$$

where $\mathbf{n}$ is the outward normal vector on the airfoil surface, S is the boundary surface and r is the distance from the evaluated point to the singular elements. The surface of the airfoil is divided into linear segments and the potential can be integrated numerically as a finite sum. The wake is modelled by discrete particles representing singular vorticity elements. An example airfoil is shown in Figure 1.

Two boundary conditions are established in order to solve for the source and doublet distributions in Eq. (2). The first

Figure 1: An example airfoil and wake modeled with linear panel segments of constant strength. Qualification points at which the potential is evaluated are also shown.

is the boundary condition on the solid surface of the wing, which states that there should be no flow across it. We have used the Dirichlet boundary condition to fulfill this condition [4]:

$$\frac{\partial \Phi}{\partial n} = \mathbf{n} \cdot \mathbf{Q}_\infty, \tag{3}$$

where $\mathbf{n}$ is the vector normal to the airfoil surface and the wake, and $\mathbf{Q}_\infty$ is the free stream velocity vector. This condition is required to be fulfilled at each so-called qualification point, see Fig. 1.

The second boundary condition is related to the wake, and is based on the Helmholtz law that implies that the total circulation is constant and does not change in time. In our approach we have used the classical two dimensional Kutta condition to model this [4]:

$$\gamma_{\text{T.E.}} = 0, \tag{4}$$

where $\gamma_{\text{T.E.}}$ is the vorticity at the trailing edge.

Using Eq. (2) and the two boundary conditions (Eq. 3 and Eq. 4), leads to a linear system of equations by which one can establish the strengths of the doublets and sources. Here we have chosen to require the linear panel elements to have constant strengths, leading to a first-order panel method. Several higher-order methods are available, but we chose this simple approach due to its robustness and speed.

The strength of the singular elements defines the fluid flow, and pressure loads can be established. The sources add thickness to the surface, and are therefore not included in the wake, which is modelled only by doublet elements. The wake is modeled as a free developing wake, and is moving parallel to the fluid flow. The position of the wake points is updated at every time-step to ensure a continuous development of the wake.

The vortex method implemented here is a two-dimensional panel code, but can relatively easily be extended into a full three-dimensional code. A detailed description of the method is given by Katz and Plotkin [4].

2.2 Implementation

The method has been implemented both in MATLAB (The Mathworks, Inc.), for rapid prototyping, and in C++. The C++ version includes two different codepaths, one for using the central processor unit (CPU) exclusively, and one for using both the CPU and the GPU for asynchronous parallel computations.

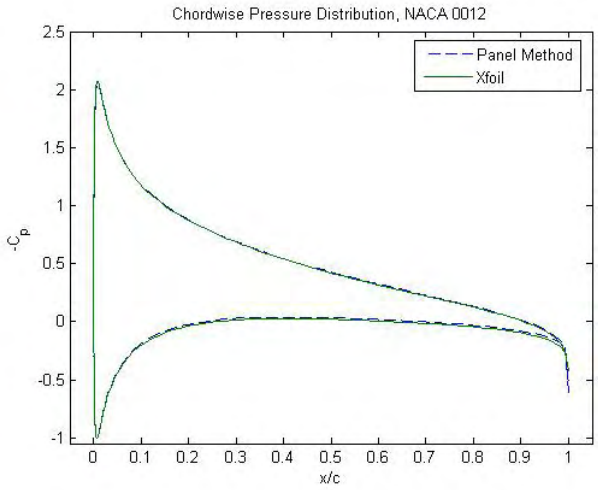

Figure 2: The pressure distribution of the NACA 0012 airfoil at an angle of attack of 5^o; computed with both the panel method and the Xfoil code[13]

The GPU was originally developed for graphical applications, but has evolved into a programmable processor with computing power exceeding that of the common multicore CPUs [8]. It is easily programmed in a subset of C/C++ [5]. In this project a single workstation with an Intel Xeon quad-core CPU (running at 2.39 GHz) and a NVIDIA Tesla C2050 GPU (448 processor elements running at 1.15 Hz) has been used.

The GPU was programmed with the latest CUDA Toolkit (Version 4.0, NVIDIA Corporation), using the Thrust library (Version 1.4.0) [3]. This library allows the user to rapidly write codes that can run both with or without a GPU, and thus removes the need for using different source code in most places. The linear system was solved with the ATLAS BLAS/LAPACK library on the CPU [12], and with the MAGMA library (Version 1.0) for the GPU [11]. The velocity of the wake particles was calculated by brute-force, considering all mutual interactions. This is not feasible for larger simulations, but was used here for simplicity and to study whether pursuing further improvements is promising.

3 Application

The NACA 0012 airfoil is used for the validation of the code. The surface of the airfoil is divided into 160 panel elements. There was some numerical problems near the trailing edge due to the blunt trailing edge of the airfoil. Two additional panel elements were added to correct for this.

3.1 Pressure Distribution

A stationary case was used for the first test. A wake panel was placed far behind the trailing edge, and the wake was assumed to have constant strength. This situation is very similar to the method employed by the well-known airfoil

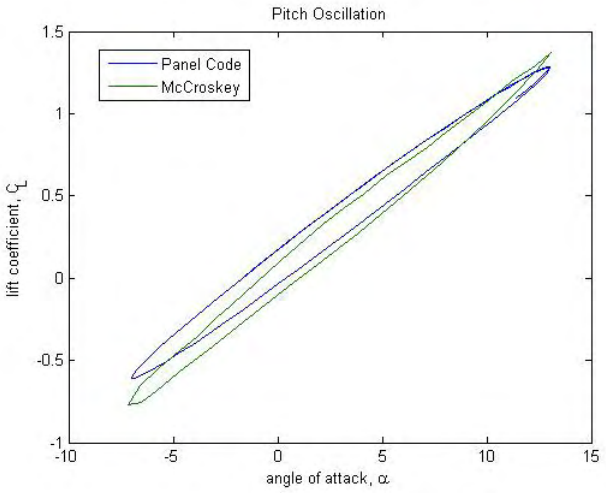

Figure 3: Lift coefficient loops for the pitch oscillation of a NACA 0012 airfoil. Experimental data from McCroskey [7] and results from the panel vortex method are compared.

design software Xfoil [13]. The pressure distribution on the airfoil at an angle of attack of 5 degrees is shown in Figure 2.

This calculation does not require much time, but is used to verify that the code is correct. The latter is implied by the close match of the two pressure distributions.

3.2 Oscillating airfoil

In this example the airfoil is experiencing periodic pitch oscillations. The wing is given a reduced frequency of $k = \frac{\omega c}{2Q_\infty} = 0.1$. The free-stream velocity is set to $U_\infty = 102\mathrm{m/s}$. These values were chosen to fit experimental data from McCroskey et al. [7]. The variation of angle of attack was prescribed as a sinusoidal motion, $\alpha(t) = 3^o + 10^o \sin \omega t$. This is a relatively large pitching motion, and there might be flow separation occurring, which the current vortex method might not resolve well.

The experimental results [7] were extrapolated from a printed graph and the curves in Figure 3 may suffer from erroneous readings of the original graph.

During the simulations it was found that the results are sensitive to the location of the first wake panel. Here it is placed at a distance of $0.2 \cdot U \cdot \delta t$, based on recommendations given by Katz and Plotkin [4].

4 Results

The method was validated and agrees well with earlier results, both in the steady case and for the pitch oscillation. However, the panel method used here does not account for flow separation. The effect of flow separation is shown as a slightly lower lift coefficient for larger angles of attack during the pitch-down motion in Figure 3. However, this effect can not be seen from the graph.

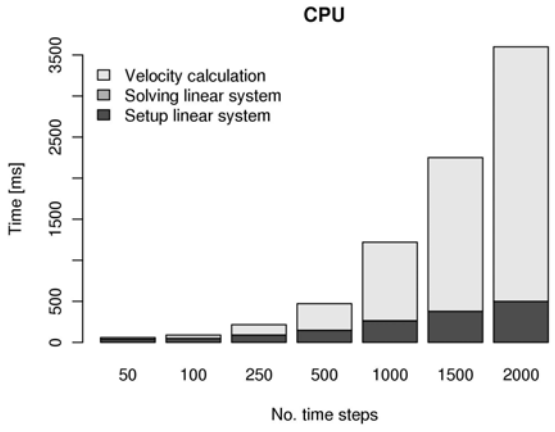

Figure 4: Computational times on the CPU for each time step

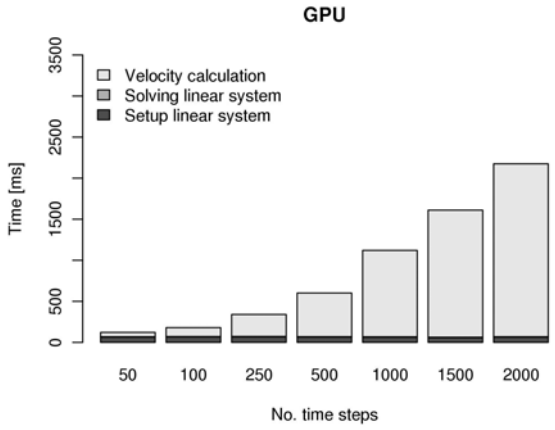

Figure 5: Computational times on the CPU + GPU for each time step

The computational times are shown in Figure 4 for the CPU implementation, and in Figure 5 for the mixed CPU+GPU configuration.

For the CPU, both setting up the linear system and calculating the velocities of all particles needs time that increases quadratically with the number of time steps. For the GPU, setting up the linear system requires almost constant time, which hints at that the GPU is not utilized fully. However, solving the linear system does not contribute significantly to the total running time.

Calculating the velocities is the major bottleneck for both configurations. For the GPU+CPU configuration, the trend is a slower increase in running time compared to the CPU.

In general, computing on the GPU requires a larger overhead cost, and data transfers between GPU and CPU are slow. Therefore the GPU code is expected to run slightly slower than the CPU version for small numbers of time steps.

At about 1500 time steps, the computations on the

GPU+CPU start being faster relative to the CPU configuration. It is faster by a factor of two at 2000 time steps.

5 Conclusions and discussion

We have implemented and validated a simple vortex panel method. Using a GPU resulted in a reduction of the runtimes for larger numbers of particles. This trend is expected to continue. Due to the overhead in data transfer and device control, the true power of the GPU will only be realized for large numbers of particles. A large portion of computational time will be spent idling, when used for smaller numbers.

As promising as these results are, the simple brute-force method used is still too slow to be used for most practical purposes. However, there exist a large number of algorithms for approximating the long-range interactions between particles in an efficient way [2], and we plan to implement such an improved scheme in the near future.

We believe that the computational time of the vortex method can be significantly reduced by using parallel implementation schemes, and that a three-dimensional wind turbine aeroelastic code based upon the vortex method is realistic in the near future. There are other challenges to be addressed as well, such as how to include viscosity and compressibility effects into the simulations.

References

[1] G.-H. Cottet and P.D. Koumoutsakos. Vortex methods. Cambridge University Press, 2008.

[2] M. Griebel, S. Knapek and G. Zumbusch. Numerical simulation in molecular dynamics. Springer, 2007.

[3] J. Hoberock and N. Bell. Thrust: a parallal template library, 2010. Available at http://www.meganewton.com/. Accessed 30 August 2011.

[4] J. Katz and A. Plotkin. Low-speed aerodynamics. Cambridge University Press, 2001.

[5] D.B. Kirk and W.W. Hwu. Programming massively parallel processors. Morgan Kaufmann, 2010.

[6] J.F. Manwell, J.G. McGowan and A.L. Rogers. Wind energy explained. John Wiley & Sons, 2009.

[7] W.J. McCroskey. A critical Assesment of Wind Tunnel Results for the NACA 0012 Airfoil. National Aeronautics and Space Administration. Technical Memorandum 100019 Ames Reasearch Center, 1987.

[8] E. Lindholm, J. Nickolls, S. Oberman, J. Montryn. NVIDIA Tesla: A unified graphics and computing architecture. IEEE Computer Society, IEEE Micro, 28:39-55, 2008.

[9] J. G. Leishman, G. L. Martin. Challenges in Modelling the Unsteady Aerodynamics of wind Turbines. 21st ASME Wind Energy Symposium and the 40th AIAA Aerospace Sciences Meeting. AIAA 2002–0037.

[10] T. Sarpkaya. Vortex element methods for flow simulation. Adv. Appl. Mech., 31:113—247, 1994.

[11] S. Tomov, R. Nath, P. Du and J. Dongarra. MAGMA user's guide, version 0.2, 2009. Available from http://icl.cs.utk.edu/magma. Accessed 30 August 2011.

[12] R.C. Whaley, A. Petitet and J. Dongarra. Automated empirical optimizations of software and the ATLAS project. Parall. Comput., 27:3–35, 2001.

[13] Xfoil, Subsonic Airfoil Development System. Available at http://web.mit.edu/drela/Public/web/xfoil/. Accessed 30 August 2011.

Centrifugal Pitch Systems for Small Wind Turbines

Dipl.-Ing. Eckhard Gauterin[1], M.Sc. Niels Harborth
[1]stipendiary of Reiner Lemoine Stiftung
Reiner Lemoine Institut
Ostendstraße 25, 12459 Berlin/ Germany
E-mail: eckhard.gauterin@rl-institut.de, niels.harborth@rl-institut.de

Keywords: Small wind turbines (SWT); pitch system; cost reduction; mechanical solution; mechanical, mathematical and simulation model.

1 Introduction

From the historical point of view mechanical pitch mechanisms are one fundamental concept of modern pitch systems. In the 17th century wind mills reduced the power input e.g. with the help of jalousie blades [1] and even in the 1980th mechanical pitch systems were used in modern wind turbines like the Dutch LAGERWEY LW18 with 80 kW rated power [2].

Within this paper the mechanical, mathematical and simulation model of a mechanical pitch system for small wind turbines (SWT) is presented. With the help of these models simulations for dimensioning the mechanical parameters of mechanical pitch systems can be obtained. Beside these simple models can be used for further education purposes.

This topic also serves the authors to consolidate their knowledge in control engineering and lay the foundation for PhD projects in extreme load reduction with the help of passive pitch systems.

It is also part of a current research project at the Reiner Lemoine Institute (RLI), which was established in Berlin/ Germany in 2010 by Prof. Jochen Twele to support the renewable energy transition with applied research activities.

2 Relevance of mechanical pitch systems

SWT are more often working in parallel mains, demonstrated by market development in countries with special SWT feed in tariffs like Great Britain and Denmark within the last years [3], but they are also suitable for isolated operation, especially in lower power range characterised by weak grid stability.

Unfortunately investment costs from € 2000,- to € 5000,- per kW nominal power are still high [4]. Therefore cost reducing design is essential, in some cases to be realised with simple mechanical solutions, e.g. for over speed protection.

In isolated operation far away from transmission nets and maybe in structurally weak regions maintenance friendly and fail safe design is very important, therefore simple mechanical solutions are preferable for these conditions. But not all mechanical pitch systems guarantee an acceptable over speed protection, as explained in chapter 4 using the example of the already mentioned SWT research project. Within this project the aero dynamical blade layout linked to the design of the mechanical pitch system is analysed.

3 Current SWT research project at RLI

3.1 Objectives of the project

The client, a Baltic wind turbine manufacturer wants to launch the pilot series of a 5kW SWT until end of 2011 with the agenda of € 1000,- per kW rated power sales price.

On one hand this agenda should be achieved with an innovative, permanent excited ring generator, on the other hand with simple mechanical and only few components. Consequently a passive downwind concept and mechanical pitch system is chosen.

3.2 SWT specification

The SWT is equipped with a rotor of 6m which defines a swept area specific rated power of 177 W/m^2, so the SWT is applicable for weak wind conditions.

The direct driven, speed variable ring generator is regulated by a full load converter and characterised by its 400mm huge diameter that effects in a lightweight design.

The SWT design is carried out for wind class II acc. IEC 61400-2 (2006) [5], so the turbine can also be installed at shoreline sites.

4 INTRODUCTION TO THE ANALYSED MECHANICAL PITCH SYSTEMS

4.1 Types of mechanical pitch systems

Beside two wind fane, eclipse and tilting rotor mechanism [1], that turn vertically or horizontally after maximum rotor thrust is reached, two centrifugal forced mechanisms have been discussed within this project. Both mechanisms guarantee over speed protection also at low and medium wind speeds respectively rotor thrust, as the rotor accelerates at sudden grid loss so that the pitch mechanism is activated. This feature is very important for isolation operation, as grid stability is not guaranteed. As isolation operation is one of the clients focused markets, centrifugal pitch mechanism have been selected to be analysed more closely for the SWT project.

These systems also fulfil the requirements acc. IEC 61400-2 (2006) [5] regarding maximum rotor speed in case of grid/ energy supply failure, so the concept also stands out from several competitors' concepts which are just equipped with generator short cut brake option.

4.2 Functionality of both systems

From **Figure 1** and **Figure 2** the basic principles of both centrifugal forced mechanisms can be derived.

Both systems, characterised by different ways of guidance, are spring-loaded and return to the initial position rather pitch angle with decreasing rotor speed.

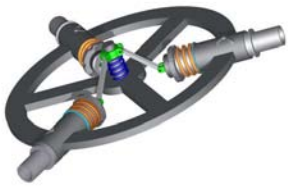

Figure 1: Swivel-Pitch-System **Figure 2:** Pivot-Pitch-System

The so called ***Swivel Pitch System*** is characterised by eccentrically mounted and edgewise swivelling rotor blades. This swivelling motion increases with rising rotation speed and is linked by guiding rods with the blade pitching motion (see **Figure 1**).

The system is particularly suitable with downwind SWT, because of a stepless blade dipping in the lee side of the tower. Therefore vibrations caused by unsteady tower circulation are reduced.

Equipped with a mechanical synchronisation all blades hold almost the same centre of gravity in each operation point, so there is nearly no mass imbalance. However there is a strong nonlinear relation between swivelling and pitching motion which causes a more challenging system layout.

Referring to this issue the so called ***Pivot Pitch System*** is much easier to design as rotation speed and pitch angel are linearly related. As the concentrically aligned and guided blades just move radially, the system is more fragile to mass imbalance. At rotation speeds in the range of 200 to 250 min^{-1} mass imbalances cause significant high differences in the centrifugal forces. Therefore a strong synchronisation mechanism is essential for this system. - Additionally an optimal cut in pitch angle can be implemented with an additional decreasing notch design and another spring-load. With this option a more cost effective blade design by continuous casting can be achieved.

Both systems do not need additional masses to derive a pitching motion, as they are just forced by rotation speed.

Due to less complexity and less parts needed the ***Pivot Pitch System*** was finally selected for this project. Within future research activities at RLI also the ***Swivel Pitch System*** will be analysed by simulation and experiments.

5 MECHANICAL AND MATHEMATICAL MODEL OF THE *PIVOT PITCH SYSTEM*

5.1 Basic assumptions of the mechanical model

To understand the influence of the mechanical parameters on the dynamic behaviour of the system just a rigid model of the rotor is derived in the first step. So this model reduces the loads to forces and torques at the rotor and disregards the blade, drive train and tower deformations as well as grid feedback influences.

As the SWT is characterised by a direct driven concept and the generator, integrating the drive train main bearings, is placed straight to the rotor, the influence of the drive train dynamic seems to be negligible compared to the blade and tower dynamic, which will be included in the second step mechanical model later on.

5.2 The mechanical and mathematical model

The mechanical model reduces the rotor to a plane transformation of a rigid blade (see **Figure 3**).

This blade model is loaded by the accelerating aero dynamical torque $\boldsymbol{M_A}$, the rotor decelerating generator torque $\boldsymbol{M_G}$ and the mass moment of inertia $\boldsymbol{J_{B,xx}}$, all part of the torque balance (1) with orientation acc. Germanischer Lloyd Guideline [6].

$$\boldsymbol{J_{B,xx}} \cdot \ddot{} = \boldsymbol{M_A} - \boldsymbol{M_G} \qquad (1)$$

Furthermore a rotation speed depending centrifugal force F_C applies which outwards orientation, a spring force F_S to relocate the blade at decreasing rotation speed and a damping force F_D to prevent an up swinging dynamic behaviour in opposite direction to the centrifugal force.

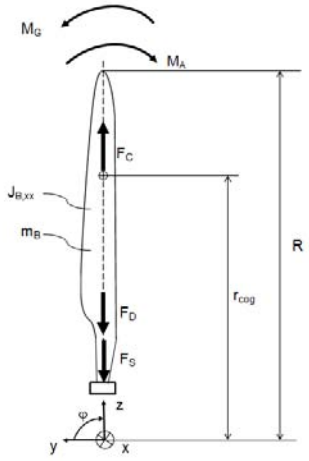

Figure 3: Mechanical blade model

Together with the mass inertia these forces form the force balance (2) in z direction.

$$m_{B,xx} \cdot \ddot{z} = F_c - F_S - F_D \tag{2}$$

The centrifugal force F_C is calculated acc. equation (3) with the parameters rotor blade mass m_B, angular velocity (below named ***rotation speed*** to put it simply) and the distance $r_{B,CoG}$ from blade centre of gravity to drive train axis.

$$F_c = m_B \cdot r_{B,CoG} \cdot \quad ^2 \qquad \& \qquad \equiv \tag{3}$$

The spring is loaded with the pretension $F_{S,0}$, which acts against the centrifugal force F_c and calculated acc. equation (4) to avoid radial translations below rated rotation speed $_r$.

$$F_{S,0} = -F_c \tag{4}$$
$$= -m_B \cdot r_{B,CoG} \cdot \quad ^2_r$$

The pitching motion is forced by a pin mounted to the blade and guided by an ascending notch in the pitch bearing, which is mounted to the hub body. As the blade translation is depending on the rotation speed and starts not until the rated rotation speed is exceeded (because of the spring pretension) a continuously increasing reduction of the power input is achieved with the increasing pitch angle for increasing rotation speeds.

As explained in chapter 4 and derivable from equations (2), (3) and (4) the power input reduction depends on the rotation speed. Therefore even at low and medium wind speeds the power input reduction is guaranteed.

The damping force F_D is defined just with the translation velocity $\dot{z}$ and the damping rate d.

With the kinematic ratio i_z of blade translation z and pitching motion acc. equation (5) …

$$z = i_z \cdot \tag{5}$$

… and equations (3) and (4) integrated in equation (2) the force balance results to equation (6):

$$\ddot{} = \frac{1}{m_{B,xx} \cdot i_z} \cdot (m_B \cdot r_{B,Cog} \cdot \quad ^2 - F_{S,0} - \ldots \tag{6}$$
$$\ldots - k_S \cdot i_z \cdot \quad - d \cdot i_z \cdot \dot{})$$

The rotor accelerating aero dynamical torque M_A is calculated acc. stream tube theory (see e.g. [1]) and equation (7) with the air density , the wind speed in front of the rotor plane v, the blade radius R and the torque coefficient c_M, which is depending on the tip speed ratio and the active pitch angle .

$$M_A = \frac{1}{2} \cdot \quad \cdot v^2 \cdot \quad \cdot R^2 \cdot R \cdot c_M (\ , \ ) \tag{7}$$

To determine the torque coefficient c_M the characteristic torque diagram has to be calculated. Within this project the RLI tool ABAUKAS is used for this job and in **Figure 4** the diagram is given.

For the generator torque M_G the operation range has to be considered. As the pitch behaviour is analysed, the generator torque at full load operation range (at wind speeds v exceeding rated wind speed) is calculated. For a centrifugal forced pitch system the generator torque is, in opposition to electrically or hydraulically operated pitch systems, not constant. Though the generator power is kept constant at rated power $P_{G,r}$, the rotation speed has to change with the changing wind speeds between rated and maximum rotation speed $_r$ and $_{max}$ to obtain a pitching motion. Therefore the generator torque M_G has to be calculated acc. equation (8).

$$P_{G,r} = M_G(v) \cdot \quad (v) \Leftrightarrow M_G(v) = \frac{P_{G,r}}{(v)} \tag{8}$$

After integrating equations (7) and (8) in the torque balance (1) the final torque balance is given with equation (9):

$$J_{B,xx} \cdot \ddot{} = \frac{1}{J_{B,xx}} \cdot \left(\frac{1}{2} \cdot \quad \cdot v^2 \cdot R^3 \cdot c_M \left(\quad , \quad \right) - \frac{P_{G,r}}{(v)} \right) \tag{9}$$

Force and torque balance (6) and (9) describe the system motion with the help of two nonlinear differential equations coupled by the kinematic ratio of translation and pitching motion.

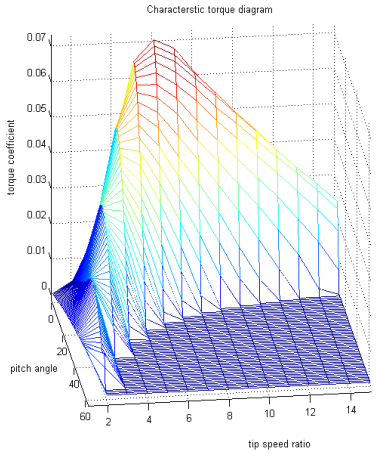

Figure 4: Characteristic torque diagram

6 Simulation Model

6.1 Structure pattern

Each term of the coupled nonlinear differential equations (6) and (9) can be transferred in a block of a structure pattern as shown in **Figure 5** (with the time integration added). The upper part of the pattern results out of the force balance (6), the lower part out of the torque balance (9) and the coupling is carried out by transferring the rotation speed.

6.2 Transfer to a simulation model

Once the structure pattern is achieved it can be transferred in a block diagram and the coupled nonlinear differential equations (6) and (9) can be solved in time domain e.g. with the software Matlab Simulink.

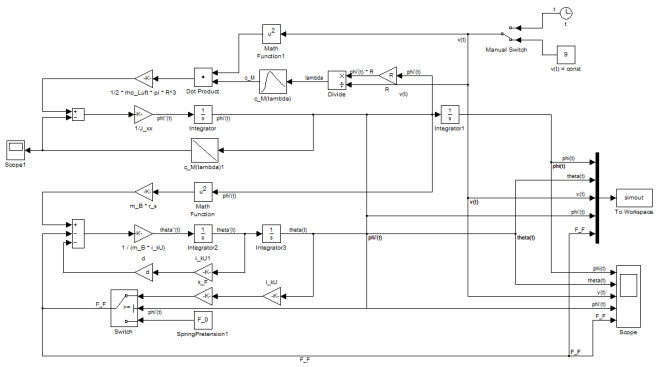

Figure 5: Structure pattern (in Matlab Simulink)

With the current simulation model just constant wind speeds act as input parameters, but also deterministic wind speeds acc. [5] like extreme operation gust will be used to analyse the behaviour.

From the simulation the rotation speed and pitch angle are gained. By varying the control parameters ***spring rate*** k_S, ***damping rate d*** and ***kinematic ratio*** i_z the dynamic behaviour of the pitch system can be influenced and optimised.

7 Conclusions

The relevance and functionality of two centrifugal forced mechanical pitch systems are presented. For one system the mechanical, mathematical and simulation model is derived.

The simple mechanical principal is profitable for commercial applications and its clear and simple models makes is useful for further education purposes e.g. to illustrate the relation between aerodynamics, drive train dynamics and control engineering.

8 Forecast

After simulations also experimental analysis with the help of an 1:1 prototype of the pitch system will be carried out at RLI laboratories within the next month to validate the numerical results. Probably at the next PhD seminar the technical and economical achievements can be presented.

References

[1] Gasch, R.; Twele, J.: Windkraftanlagen; Wiesbaden; Vieweg+Teubner Verlag; 6. Auflage; 2010

[2] Hau, E.: Windkraftanlagen; Berlin; Springer Verlag; 4. Auflage; 2008

[3] Frey, M.: Kleinwindenergie: Vor dem Sprung in den Massenmarkt; forum. new power; 2/2011: 32-34

[4] Bundsverband Windenergie: Wirtschaftlichkeit & Vergütung von Kleinwindenergieanlagen; Berlin; BWE; 12/2010: 4-5.

[5] Standard IEC 61400-2:2006: Wind turbines - Part 2: Design requirements for small wind turbines

[6] Germanischer Lloyd: Guideline for the Certification of Wind Turbines; Hamburg; GL-Group; Edition 2010

Validating OpenFOAM with the MEXICO Dataset

I. Herraez, B. Stoevesandt, J. Peinke
TWIST Turbulence, Wind Energy and Stochastics, University of Oldenburg
Ammerlaender Heerstr. 136, 26131, Oldenburg, Germany
E-mail: {iherraez, bstoevesandt, peinke}@uni-oldenburg.de

Keywords: aerodynamics, wind turbine, CFD, wind tunnel

1 Introduction

Improving the aerodynamics of wind turbines is of great importance for achieving a higher energy yield, reducing their load level, and ultimately optimizing their cost-effectiveness. The use of CFD can facilitate enormously this task. Reliable simulation models are needed for that. Thoroughly validations with high-quality measurements are therefore also indispensable. Within this work the MEXICO-turbine is simulated with the open source CFD software OpenFOAM. The results are then compared and validated with measurements. The scope is on one hand to asses the suitability of this software for wind energy applications and on the other hand to analyze in detail the flow characteristics of the turbine.

2 The MEXICO and MexNEXT Projects

The MEXICO project stands for Model Experiments in Controlled Conditions [1]. The measurement campaign took place in December 2006 and involved the extensive measuring of load and flow data from a 3 bladed wind turbine placed in the LLF (Large Low-Speed Facility) wind tunnel of DNW. This closed circuit wind tunnel is located in the Netherlands, and has an open section of 9.5x9.5 m2. The wind turbine has a rotor diameter of 4.5 m. The blades are twisted and their design is based on 3 different aerodynamic profiles (DU91-W2-250 in the root region, RISO-A1-21 in the middle region and NACA 64-418 in the tip region). The measurements were carried out under different flow conditions, including 2 different rotational speeds (324 rpm and 424 rpm), several wind speeds (ranging from 10 to 30 m/s), several pitch angles (from -5.3 deg to 1.7 deg) and several yaw-inflow angles (from 0 deg to 45 deg). The measurements include PIV flow data from upwind and downwind of the rotor, pressure distributions along 5 different blade sections (obtained from Kulite pressure transducers), blade root loads (measured with strain gauges) and tower bottom loads (measured with a weight balance). The IEA Task 29 MexNEXT started in June 2008 and finished in June 2011. The project had the scope of analyzing in detail the available measurement data from the MEXICO experiment and using them for validating different numerical models. The gained knowledge should allow to predict with a greater accuracy the wind turbine aerodynamics. 20 research institutes from 11 different countries participated in this project [2] [3] [4] [5].

3 Used Software

The use of open source software is very attractive for research purposes. On one hand, the license costs of commercial software can be avoided. On the other hand, open source software allows the user to analyze and customize the code. For these reasons, this work has been done with the finite-volume open source CFD package OpenFOAM [6]. OpenFOAM consists of over 80 solvers for performing different kinds of fluid dynamics simulations and over 170 utilities for performing pre- and postprocessing tasks. The mesh has been done with the tool snappyHexMesh, which is also included in the OpenFOAM package. The simulations are carried out with the steady-state solver MRFSimpleFoam. The post-processing has been performed with Paraview and Octave.

4 Simulation Model

The mesh is an unstructured grid consisting of 32 million cells (hexaedra and split hexaedra). The areas where the greatest gradients are expected have been accordingly refined. A good boundary layer resolution is guaranteed with y+ smaller than 2 in the region of the blades. Only the blades and the nacelle have been modeled. Therefore, any tower and wind tunnel effects are in principle neglected. These assumptions are however believed to be acceptable since the mentioned effects are expected to play a minor role in the MEXICO experiment [5]. The domain is cylindrical and its length is 15 times the rotor diameter, while its diameter is 8 times the rotor diameter. Dirichlet boundary conditions are set for the wind speed in the inlet (u=10, 15 or 24 m/s) and for the pressure in the outlet (set to atmospheric pressure). The wind turbine has non-slip boundary conditions. The wind speed in the outlet and the pressure in the inlet are set to Neumann conditions (in this case zero gradient). MRFSimpleFoam, the selected OpenFOAM solver, is a RANS solver able of dealing with multiple systems of reference (inertial and non-inertial for stationary and rotating parts respectively). The Coriolis and centripetal forces are added

to the momentum equations in the parts subjected to rotation. In this way, it is possible to simulate a rotating system without a moving mesh, so the simulation process is simplified and accelerated. The turbulence model k-omega SST is used for the computations. The simulations are run in parallel in a computer-cluster of the University of Oldenburg. Using 540 processors it takes about 4 hours to calculate 12000 time steps. Successive simulations are run starting with a very low rotational speed and increasing it slowly until the aimed speed of 424 rpm is reached. This helps to make the simulations more stable. Three different runs corresponding to three different wind speeds are performed: 10, 15 and 24 m/s. The rotational speed is kept constant at 424 rpm, the pitch angle is always -2.3 deg and no yawed inflow is considered.

5 Results

The analysis of the results is based on the pressure distributions along the blade sections and on the PIV flow measurements.

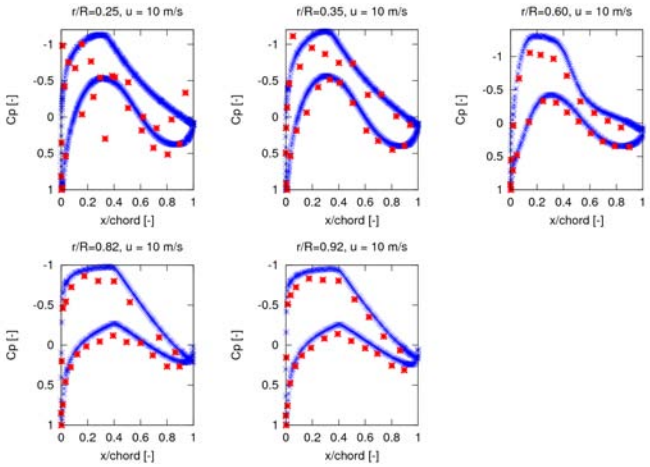

Figure 1: Pressure distribution along the blade for u=10m/s

Fig. 1 presents the pressure distribution along 5 sections of the blades for 10 m/s wind speed. The red dots represent the measurements and the blue ones indicate the simulation results. The same is shown in *Fig.* 2 and *Fig.* 3 for the wind speeds 15 and 24 m/s respectively. As it can be seen, a good agreement between measurements and simulations exists in general on the outer blade sections. However, the measurements and the simulations mismatch completely in the inner blade sections when the wind speed is low (10 and 15 m/s). In those cases, the measurements follow a very strange pattern, which is believed to be unrealistic. It is therefore suspected that during those measurements the pressure transducers had some kind of instability which caused the striking results [3]. Thus the mentioned distributions are not considered for the

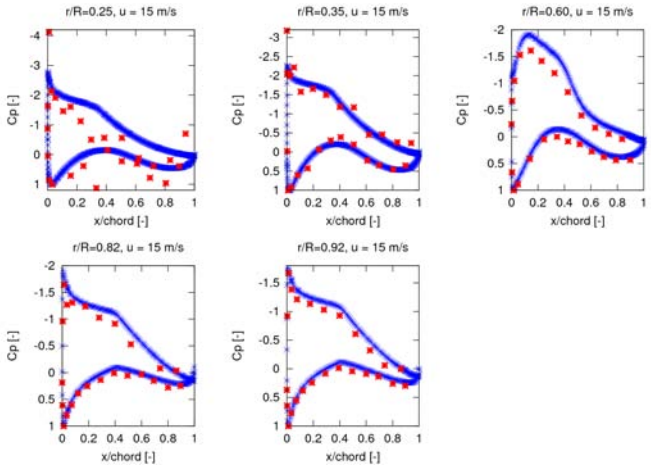

Figure 2: Pressure distribution along the blade for u=15m/s

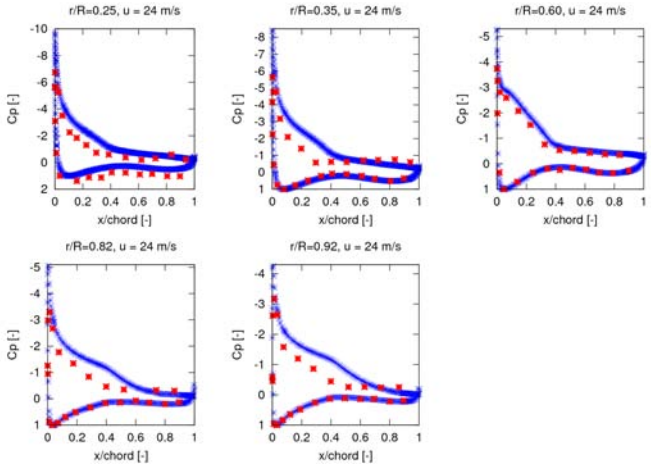

Figure 3: Pressure distribution along the blade for u=24/s

validation. In general it can be stated that the simulations were able to predict satisfyingly the pressure distributions along the blade. The use of a finer mesh in the blade region, and specially modeling a thicker boundary layer (which in the model consists of only 3 layers of very fine cells) could be helpful for improving a bit the simulations. In the MEXICO-experiment the transition between laminar and turbulent flow was triggered on the blades with a zig-zag tape placed in the spannwise direction at 5 percent chord. Since the simulations are run fully turbulent, this could be also one reason for the light disagreement between experiments and simulations. Tunnel or tower effects could play a certain role.

Interestingly, for a wind speed of 24 m/s there is also a noticeable mismatch between measurements and simulations on the suction side of the outer blade regions. Since the rotational speed is kept constant and the wind speed is increased, the angle of attack also rises. This could lead to a greater generation of vortexes in the

blade tip region. In order to predict better this phenomena a finer mesh in the blade tip area and a thicker boundary layer is most probably required. This might be the reason for the disagreement.

The wake of the wind turbine is analyzed with PIV measurements. *Fig.* 4 and *Fig.* 5 show two axial traverses of the wind speed corresponding respectively to a radial position r/R = 0.6 and r/R=0.82. In both pictures the axial velocity is normalized with the inlet velocity (y-axis). The axial position (x-axis) is normalized with the rotor diameter.

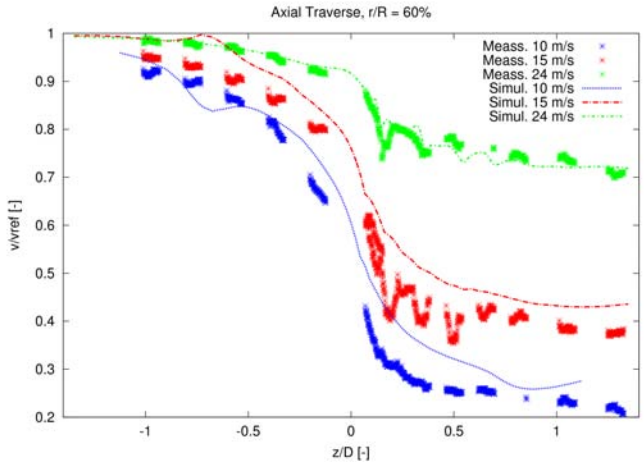

Figure 4: Axial traverse of axial wind speed at r/R=0.6

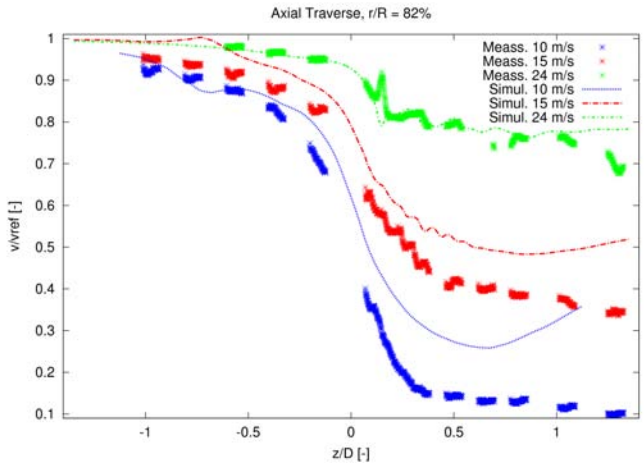

Figure 5: Axial traverse of axial wind speed at r/R=0.82

As it can be seen, upwind of the wind turbine (negative axial position) the simulations can predict better the flow than downwind of it. The traverse at 0.6 r/R radial position presents in general a better agreement with the simulations than the traverse at 0.8 r/R. The wind speed in the near wake area is overestimated by the simulations when the inlet wind speed is 10 m/s or 15m/s. This is very disconcerting, since the simulated pressure distributions for those wind speeds fit satisfyingly the measurements at the radial positions of interest. At 24 m/s the simulations match much better the PIV measurements in spite of having a greater disagreement in the pressure distributions. No satisfying explanation exists so far for this. One more interesting characteristic of the PIV measurements is the ripples that can be seen in *Fig.* 4 and *Fig.* 5 for 15 and 24 m/s. As explained above for the pressure distributions, at high wind speeds the angle of attack is also bigger. This implies a greater tendency of the flow to detach and create vortexes, which are responsible for increased fluctuations of the wind speed. To have these vortexes in the blade tip region was already expected. It is encouraging to see that the simulations also present such ripples for both wind speeds (*Fig.* 5). The striking thing is to have these ripples also at the radial position 0.6 r/R (*Fig.* 4).

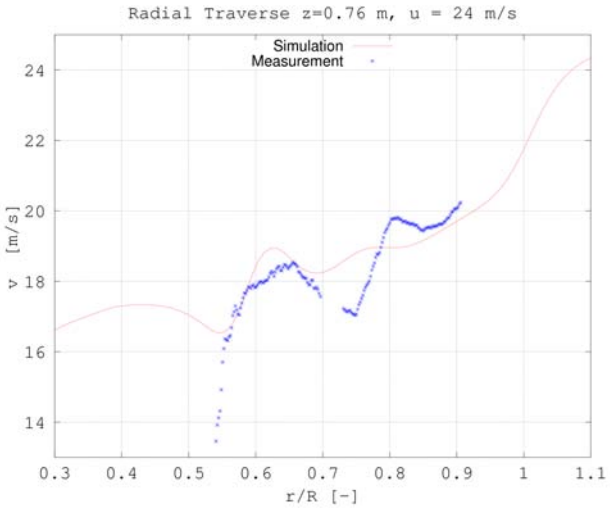

Figure 6: Radial traverse of the axial wind speed at the axial position 0.76 m behind the rotor for the wind speed 24 m/s

There seems to be also some kind of unexpected flow separation at that region. The simulations are able to predict it for 24 m/s but not for 15 m/s. In order to analyze this issue in more detail, a radial traverse of the axial wind speed is analyzed. The traverse is 0.85 m behind the rotor and the inlet wind speed is 24 m/s. (*Fig.* 6). As it can be seen, at around the radial position 0.6 r/R, the wind speed drops suddenly. Unfortunately, no wind speed measurements are available at the inner region of the rotor. However, according to the simulations the wind speed starts to recover again at around 0.53 r/R.

This critical region where the wind speed is reduced drastically coincides with the transition between the RISO-A1-21 and the NACA 64-418 profiles. This seems to be the reason for the discussed flow separation. Using the lambda-2 criterion for vortex core identification, a

vortex in the region of interest (radial position 0.6 r/R) can be clearly seen, as it is shown in *Fig.* 7. This confirms the existence of the predicted vortex at the transition area between the above mentioned profiles.

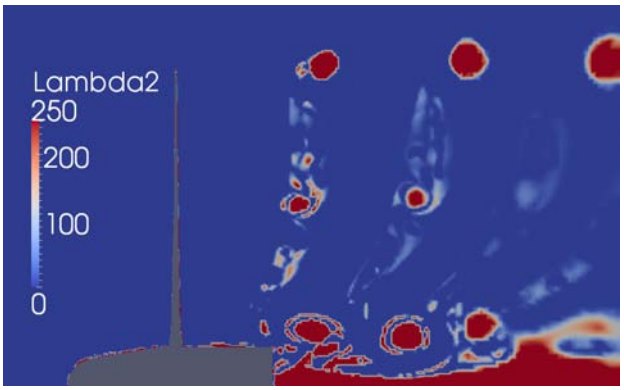

Figure 7: Identification of vortexes behind the rotor by means of the Lambda2 criterion

6 Conclusions

Within the present work the open source CFD code OpenFOAM has been validated against the MEXICO measurement data-set. Pressure distributions and near wake flow data have been used for the validation. In both cases a reasonable agreement between measurements and simulations exists. Furthermore the presence of a vortex at the radial position 0.6 r/R was satisfyingly detected in the simulations (for an inlet wind speed of 24 m/s). A finer mesh will be used in future simulations for a better analysis of the flow conditions over the rotor and on the near-wake area. Special attention will be paid to flow separation phenomena and 3D effects.

References

[1] J. G. Schepers and H. Snel, (2007): Model Experiments in Controlled Conditions, Final report, CN-E-07-042, Energy Research Center of the Netherlands, ECN

[2] J.G. Schepers, K. Boorsma, C. Kim, T. Cho (2011): Results from Mexnext: Analysis of detailed aerodynamic measurements on a 4.5 m diameter rotor placed in the large German Dutch Wind Tunnel DNW, EWEA Annual Event

[3] A.Bechmann, N.N. Sorensen and F. Zahle (2011): CFD simulations of the MEXICO rotor, Wind Energy Journal, Vol 14, Issue 5, pages 677689

[4] T. Lutz (2011). Near Wake studies of the Mexico Rotor , EWEA Annual Event

[5] P.-E. Rethore, N.N. Sorensen, F. Zahle and H. A. Madsen. (2011): CFD Model of the MEXICO wind tunnel, EWEA Annual Event Energy Research Center of the Netherlands, ECN

[6] http://www.openfoam.com

Session 1B

Wind Turbine Structural Design and Materials I

Evaluation of Dual Axis Resonant Fatigue Testing of Large Wind Turbine Blades
Peter Greaves, Dr. Robert Dominy, Dr. Hui Long

Fatigue of welded structures, investigation of new welding procedures
Peter Schaumann, Mareike Mickley (speaker)

Assessing Nonlinear Effects on Structural Dynamics of Wind Turbine Blades – Effect of Buckling on Composite Damping
Dimitris I. Chortis, Dimitris A. Saravanos

Evaluation of Dual Axis Resonant Fatigue Testing of Large Wind Turbine Blades

Peter Greaves, Dr. Robert Dominy, Dr. Hui Long
Energy Group, Durham University
South Road, Durham, UK
E-mail: {p.r.greaves,r.g.dominy,hui.long}@dur.ac.uk

Keywords: rotor blades, fatigue, full scale testing, resonant testing

1 INTRODUCTION

The blades are perhaps the most critical components of a wind turbine. A catastrophic failure of one blade can lead to the whole turbine being destroyed and widespread damage to the turbine's surroundings. For this reason, full scale tests are performed on all new designs of turbine blade as part of the certification process to ensure that they are fit to survive the loading that they will encounter in service. The most cost effective way of performing fatigue testing is resonant testing, which involves exciting the blade at its natural frequency using a moving mass attached to the blade. The test loads are designed to cause the same amount of damage as the service life after around 5 million cycles, and the tests are usually performed in the flapwise and edgewise directions separately. However, performing the tests separately means that interactions between the two loadings that occur in service are not represented in the fatigue test. Dual axis forced displacement fatigue testing (in which the loads are applied by hydraulic cylinders attached to fixed structures) has been performed for many years [1], but this test method results in a linear bending moment distribution which is also not representative of what occurs in service. When using resonant testing it is possible to optimize the bending moment distribution along the length of the blade by adding static masses.

Narec (the National renewable energy centre for the UK) has funded this research to better understand a novel method of dual axis resonant fatigue testing that they have developed.

2 METHOD

In order to ascertain whether dual axis resonant testing represents an improvement over single axis resonant testing, it is first necessary to understand the damage that is done to the blade in service. It is then possible to compare how well single axis and dual axis resonant tests compare to the damage caused by the service life. Figure 1 shows the process that was used.

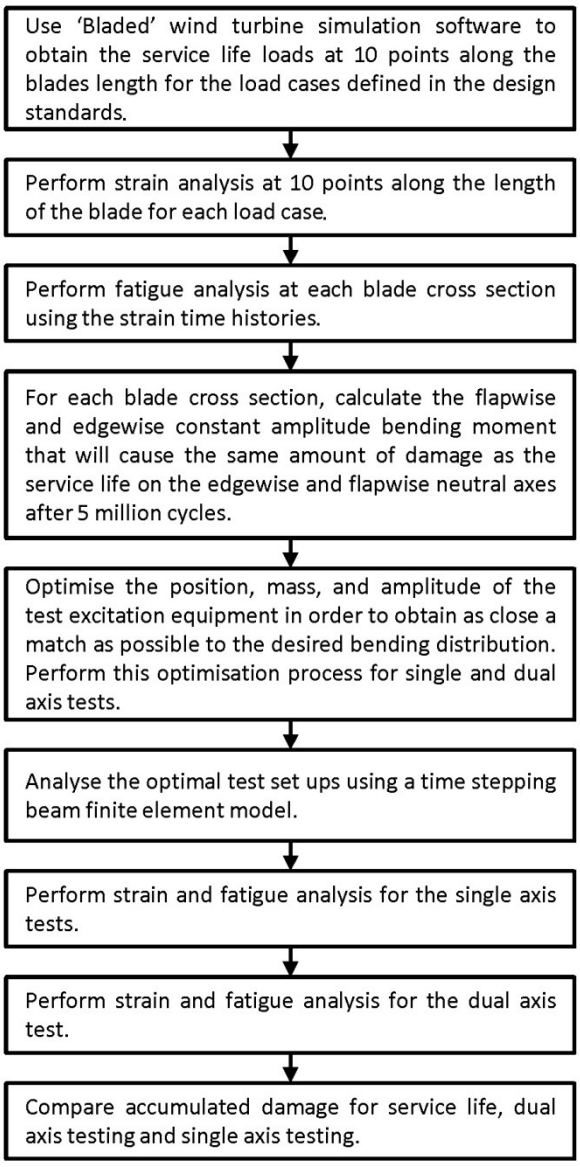

Figure 1: Analysis flowchart

2.1 Design loads

The design standards specify the load cases for which fatigue analysis must be performed [2]. These load cases were analysed using the wind turbine simulation software 'Bladed' developed by Garrad Hassan. The turbine for which the analysis was performed was a 2MW offshore turbine that is supplied with Bladed as a demonstration model. The blade is 38.75m long and has sectional properties (mass/unit length, flapwise bending stiffness, edgewise bending stiffness etc.) defined at 10 points along its length. Using this software, time histories of the flapwise and edgewise bending moments at each blade cross section for each of the load cases specified in the design standards were generated.

2.2 Strain analysis

The aerofoil used on the 2MW turbine model was an LS1. Coordinate data was obtained for this aerofoil [3] and used, along with the data for the chord, thickness and location of the centre of mass (which was assumed to be coincident with the elastic centre) given in the GH Bladed model to generate a series of 36 equally spaced points around each of the 10 blade sections as shown in Figure 2.

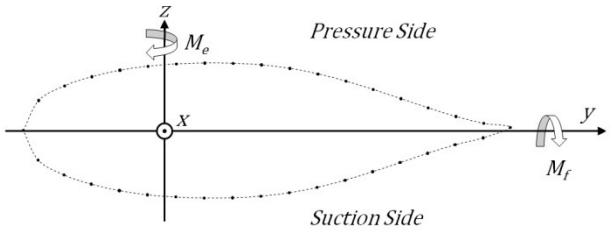

Figure 2: Strain calculation

By looking at strain instead of stress it was possible to perform the analysis without knowledge of the blades layup. Only the longitudinal strain was of interest as there is very little fatigue data available for shear and combined stresses. A sensitivity analysis showed that the inclusion of strains due to the axial loads had little effect and as it was a source of uncertainty (because the axial stiffness is not known) it was decided that it should be neglected.

A strain time history at a point can then be easily generated from the flap and edge bending moment time histories using equation (1). The parameters are defined in Figure 2.

$$\varepsilon_x = \frac{M_F z}{EI_F} + \frac{M_E y}{EI_E} \quad (1)$$

2.3 Fatigue analysis

The fatigue analysis method used to look at damage on the blade is widely used in the wind industry. First, the strain time history is rainflow counted. The algorithm used was that developed by Downing and Socie [4]. This allows variable amplitude load time history to be analysed as a series of constant amplitude cycles, defined by their range, mean and frequency of occurrence (as each cycle occurs only once in a one hour simulation the frequency of occurrence was calculated from the wind speed distribution).

Miner's rule states that the damage done by a series of constant amplitude cycles is equal to the number of times the cycle occurs divided the number of cycles that it would take to fail the material [5]. The damage sum is the sum of the damage for all of the cycles that occur.

$$D = \sum \frac{n}{N} \quad (2)$$

The number of cycles to failure was calculated using a Goodman diagram for a blade material for which much data is available (material DD16 from the DOE/MSU database [6]). This material is predominantly composed of +/-45° layers and as such is representative of materials used for the shells of blades. With N known the damage caused by each cycle can then be calculated. The damage sum for each of the 36 points around the blade was recorded for all 41 load cases.

2.4 Test design

Once the damage caused by the service life was known, flapwise and edgewise test loads which caused the same amount of damage as the service life on the edgewise and flapwise neutral axes were calculated. 5 million flapwise cycles were assumed, with the number of edgewise cycles calculated from the ratio of the edgewise and flapwise natural frequencies. By calculating the test loads for each of the 10 blade cross sections it was possible to develop a target bending moment distribution for the flapwise and edgewise directions.

If a dual axis test is to evaluate the blade better than single axis tests then it will be necessary to obtain the correct bending moment distribution along the blade length in both the flap and edge directions simultaneously. The test loads can only be exactly right at one point along the blade length; the rest of the blade will be under or over tested by varying degrees depending on the bending moment distribution. Furthermore, any static masses and excitation equipment used to tune the mode shape in the flap direction will also affect the edge direction. In order to optimise the test set up so that the loads are as close as possible to the desired value along the whole length of the blade, an optimisation routine was conceived. This consisted of a 1-D beam finite element model of the blade

programmed in MATLAB coupled to a genetic algorithm, also programmed in MATLAB.

The damped steady state response of the blade to harmonic loading can be predicted using modal superposition. The method used was based on that defined in Rao [7]. 1-D beam elements were used to minimise computation time, and also because no data other than bending stiffness and mass distribution is available for the blade. The mass of the excitation equipment is calculated as the sum of the static mass (the mounting equipment and static parts of the excitation equipment) and the dynamic mass (the excitation mass and the moving parts of the excitation equipment). The Eigenvalues and Eigenvectors can easily be found in MATLAB once the stiffness and mass matrices are known, and this information can be used to find the steady state response using modal superposition.

The amplitude of the excitation force is found using equation (3)

$$F = MA(2\pi f)^2 \tag{3}$$

where M is the dynamic mass, A is the amplitude of its motion and f is the excitation frequency of the system, found from the system Eigenvalues. The compact resonant mass (CRM) excitation system as used at Narec operates at the resonant frequency of the blade, and the response is adjusted by changing the amplitude of the motion of the mass, so this assumption is correct. The air resistance is more complex; it lags the force from the excitation equipment by approximately 180° and is almost sinusoidal so it can be represented in the force vector as a harmonic force.

However, because the peak velocity of a point on the blade is calculated from its amplitude (which in turn is calculated using the force vector) there is a case of a circular reference.

The drag force is calculated at each node with equation (4)

$$F = \frac{1}{2}\rho A C_d v^2 \tag{4}$$

where ρ is the density of air, A is the area around the node, C_d is the drag coefficient and v is the velocity of the node, calculated from the amplitude of motion and the frequency of the oscillations. Clearly, a larger drag force will result in smaller oscillations, which will in turn result in a smaller drag force, meaning larger oscillations and so on. In order to find the steady state response, the drag force was calculated using the scaled mode shape of the first natural frequency. The response was then calculated using this drag force, and the difference between the scaled mode shape and the achieved response was calculated. A scaling factor that gives a difference between the scaled mode shape and the calculated response of 0 was then obtained using a bisection search. It was found that in order to get good agreement between data for full scale blade tests obtained from Narec and the model very high drag coefficients were required. A flat plate in steady flow might have a drag coefficient of 2; in order to get agreement with the physical data a drag coefficient of 4.5 is necessary. Computational fluid dynamics work performed at Narec has shown that drag forces experienced by the blade due to the more complex flow result in an effective drag coefficient of this order.

The code can be used to calculate the difference between the desired bending moment distribution in the flap and edge directions and that which is achieved with a given test setup; this value can be used as a fitness criteria for a genetic algorithm. The algorithm used was developed in MATLAB using the method defined in [8].

The finite element code also checks if the inertial forces that the excitation equipment experiences exceed the capabilities of the equipment, and returns a very low fitness score if this is the case.

Once a test set up has been found it is analysed more thoroughly using a transient 3-D beam finite element model of the blade. This allows the effects of coupling between the flapwise and edgewise modes due to the twist of the blade, and nonlinear effects such as air resistance to be properly accounted for.

3 Results and Discussion

The results of the test optimisation process are shown in Figure 3.

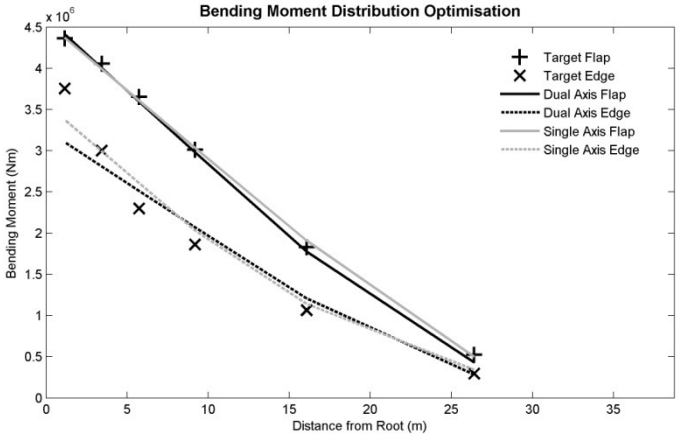

Figure 3: Bending moment optimisation results

It is harder to match the edgewise distribution to the target because the edgewise fatigue comes mainly from the self weight of the blade, meaning that its bending moment distribution would be most closely matched by a blade with no equipment mounted on it. This is impossible in practice.

It is obvious from Figure 3 that the bending moment distribution obtained if only one axis is being optimised is better than that for dual axis, but the results show that the effect is not too pronounced.

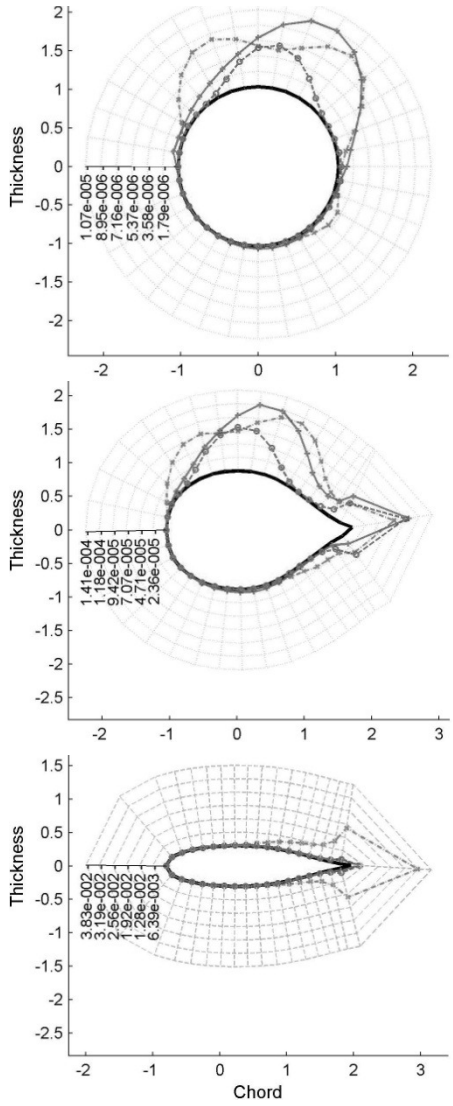

Figure 4: Damage sums at root, transition and tip sections

Figure 4 compares the Miner damage sums due to the service life, a dual axis test and single axis tests. It is clear that near the root where the blade is thicker dual axis testing is far more representative of the service life than single axis tests. However, closer to the tip the fact that the dual axis test loads cannot be optimised as well as the single axis loads becomes apparent as dual axis testing is overtesting the blade. The dual axis test that the optimisation routine generated would take 60% as long as the single axis tests so it is a significantly quicker method.

4 CONCLUSIONS

It has been shown that the interactions between the edgewise and flapwise bending moments in service result in the blade being damaged in areas that are not properly tested by single axis fatigue testing. If the load levels are correct in both axes at a given point on the blade then dual axis testing represents a considerable improvement over single axis testing. However, because any attempt to optimise the flapwise bending moment distribution effects the edgewise bending moment distribution it is harder to set up a dual axis test that matches the target loads along the length of the blade. Using the optimisation method described in this paper allows the load distribution to be tuned in both axes, although the distribution obtained if only one axis is optimised is still better. It was also found that whether the test was dual or single axis, pitching the blade so that the mean loads were tensile on the pressure side towards the trailing edge was beneficial.

Dual axis is also a much quicker test method; on the blade that this analysis has been performed on it takes around 60% of the time that single axis tests would take.

The results show that dual axis can definitely give manufacturers more confidence that a blade will survive its service life, and therefore can contribute to a reduction in the weight of blades.

REFERENCES

[1] Hughes, S., W. Musial, and T. Stensland, Implementation of Two Axis Servo-Hydraulic System for Full-Scale Testing of Wind Turbine Blades, in Windpower '99. 1999, NREL: Burlington, Vermont.

[2] BSI, BS EN 61400 Wind Turbines, in BS EN 61400-1: Design Requirements. 2005.

[3] http://www.ae.illinois.edu/m-selig/

[4] Downing, S.D. and D.F. Socie, Simple rainflow counting algorithms. International Journal of Fatigue, 1982. **4**(1): p. 31-40.

[5] Miner, M.A., Cumulative damage in fatigue. Journal of Applied Mechanics, 1945. **12**(3): p. A159-A164.

[6] http://www.coe.montana.edu/composites/

[7] Rao, S.S., Mechanical Vibrations. 4th ed. 2004, Upper Saddle River: Pearson Education.

[8] Mitchell, M., An Introduction to Genetic Algorithms. 1998, Boston, Massachusetts: MIT Press. 10.

Fatigue of welded structures, investigation of new welding procedures

Peter Schaumann, Mareike Mickley (speaker)
ForWind - Center for Wind Energy Research
Institute for Steel Construction, Leibniz University Hannover
Appelstr. 9A, 30167 Hannover, Germany
E-mail: mickley@stahl.uni-hannover.de

Keywords: Support structures of wind energy converters, new welding technology, fatigue of welded joints, numerical simulation

1 Introduction

Increasing dimensions of wind energy converters and their support structures lead to a significant increase of dimensions and masses of steel components in recent years. Powerful installations, equipment and devices for moving, cutting, forming and welding are needed for an efficient and timely manufacturing. Joining components with high plate thicknesses up to 100 mm leads to a bottleneck in the manufacturing process chain.

Regarding the design for steel structures under varying loads, fatigue cracking may be one reason for failure. The locally concentrated heat input during welding causes changes in material, geometry and stress distribution. Welded joints therefore belong to fatigue critical details of support structures. Connections, which are carried out with newly developed procedures, therefore must fulfill the normative regulations in terms of ultimate and fatigue strength. This paper addresses the development of welding technique in connection with numerical simulation.

2 High-Performance Welding procedures

In particular, submerged arc welding (SAW) is very well suited for joining components with large cross sections as well as for producing long welds and therefore is widely used in heavy structural and shipbuilding industries. As an alternative, beam welding with laser, plasma or electron beams show the so called deep-weld effect, which is essential for joining thick plates within fewer welding passes and with higher welding velocities.

Compared to arc welding procedures components with the same plate thicknesses can be welded with fewer passes which results in

- high welding velocities,
- lower energy input per length,
- minor distortions, and
- small heat-affected zones.

But there are some disadvantages as well. Because of the small diameter of the beam, these techniques are very prone to developing weld gaps. That is why the welding preparation has to be precise for high-quality welds. In addition, the low energy input and high welding velocities result in a fast cool down and this in turn causes a hardness increase which mainly influences the mechanical qualities of the weld.

A notable characteristic of beam welding techniques for joining thick plates is the deep-weld effect. This effect stands for a concentration of welding energy on a small area, resulting in a high heat flow density. Above a heat flow density q of about 10^4 J/mm², a capillary tube, also called keyhole, is formed over the thickness of the component as shown in Figure 1.

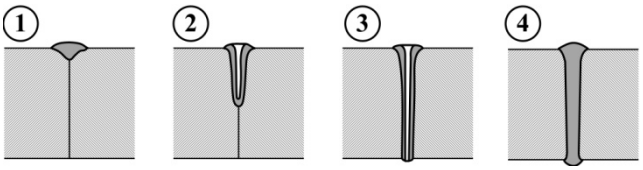

(1) kinetic energy resulting in the collision between beam and component is converted into heat
→ material melts and partly evaporates
(2) high vapour pressure in the melt
→ material is displaced to the sides, causing a deeper penetration of the beam
(3) persistent capillary tube (key hole), surrounded by melted material
(4) finished solidification
→ welded seam, drilled hole or cutting line

Figure 1: Generation of the deep-weld effect [1]

The use of a beam energy source in combination with a second electric arc energy source has attracted remarkable attention since the early nineties of the last century. Widely used in practical application is laser welding technology in combination with conventional gas metal arc welding like MAG or MIG. Hybrid welding techniques try to combine the advantages of both, beam and arc welding techniques, to yield better gap bridging ability, add hot (molten)

material to the process, and provide for higher efficiency and slower cooling rates. Both techniques operate in one molten pool. For practical application, plate thicknesses up to 15 mm (pipelines) are possible but usually do not exceed 8-10 mm. In research and development up to 25 mm are tried. However, within this thickness range, the connection is affine to developing hot cracks in the centre of the solidifying molten pool; hence, the process is subject of ongoing current research [2][3][4].

As part of the research project OPTIWELD funded by the German Federal Ministry for the Environment, Nature Conservation and Nuclear Safety, for the first time a combination of plasma beam and submerged arc welding processes is being investigated with the goals of making reliable and fast welding possible.

At the beginning of the project, a prototype with a combination of plasma key hole and single wire submerged arc welding was installed at project partner Kjellberg Finsterwalde Schweißtechnik, see also Figure 2. The fundamental idea for this new welding procedure is based on the patent EP 1570 939 A1 ‘Unterpulverschweißen’ [5].

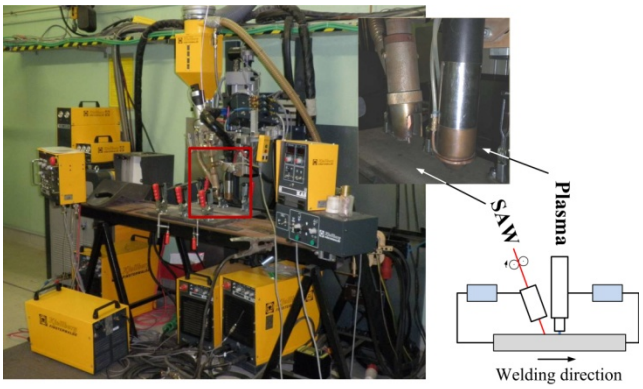

Figure 2: Prototype of Plasma and SAW

First of all, tests were carried out for gathering more information about the interaction between plasma key hole and submerged arc welding and for finding the best arrangement of both techniques. The best results provide configuration with the plasma key hole welding first followed by submerged arc welding. At the moment square butt welds of plates with thicknesses of 10 up to 15 mm with 1 mm gap can be welded reliably. To reach higher plate thicknesses, modifications of the welding torch and power source of the plasma key hole process are necessary.

Figure 3 shows a summary of the intended improvement by reducing the needed weld preparation and weld passes for a plate thickness of 30 mm. If this welding sequence can be reached by the new procedure,the welding time will be reduced significantly to only a sixth of the originally needed time.

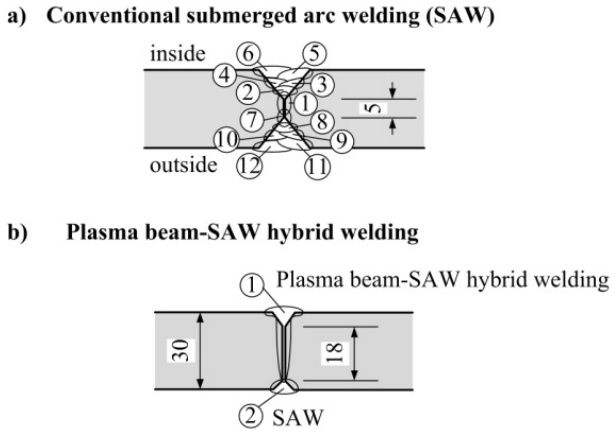

Figure 3: Comparison of weld form, welding sequence and number of passes

3 Initial Situation - Submerged Arc Welding

First step to verify the new developed hybrid welding procedure is to define a reference as a base for comparison. For the manufacturing of wind turbine towers this is submerged arc welding. This procedure is tailor made for long welds with large seam cross sections. Protected from the atmosphere by the flux, the processes in the weld pool are stable and high variations in welding current, voltage and speed are possible. The variety of applications can be increased by the usage of multi-wire techniques.

For the commonly used wire diameters of 3 to 5 mm the current lies in a range of 300 and 1200 A and the voltage lies between 25 and 40 V. When using multi-wire techniques, melting deposition rates from about 15 kg/h and welding speeds of 30 till 120 cm/min can be reached. For example, 20 mm thick plates with a DY weld preparation can be welded with an averaged welding speed of 60 cm/min, a current of 450 to 600 A and voltage of 27 to 32 V within 6 runs [6, 7, 8].

Finally, following requirements for newly developed welding procedures can be summarized

- Minimizing the number of weld layers and reduction of the weld seam cross-section and production time,
- High quality providing for a high fatigue resistance (hardness, ductility, geometry),
- Lower energy input per length for decreasing welding distortions,
- Because of the reachable cutting tolerances good gap bridging ability is necessary,
- Easy integration into production processes of large components.

In cooperation with the German tower manufacturer SIAG Tube & Tower GmbH, submerged arc welding tests under real manufacturing conditions on plates with 20, 30 and 40 mm thicknesses were arranged. Welding parameters like current, voltage and welding velocity were documented. In addition, temperatures and strains at varying distances from the weld seam were captured punctually during the welding process. Figure 4 shows the test setup and the arrangement of measurement equipment. In Figure 5 welding preparation and the welding sequence for the tests with 20 mm plate thicknesses are presented.

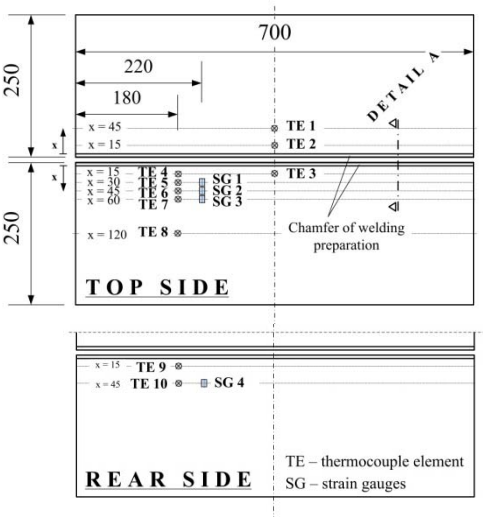

Figure 4: Test setup with measurement equipment

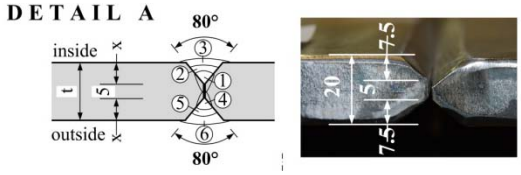

Figure 5: Weld preparation of Detail A and welding sequence, t = 20 mm

Today numerical simulations are a powerful tool and integral part of the everyday engineers' work to optimize the design of structures. This development is also true for production processes like metal forming and casting technologies. Also the simulation of welding gains more and more importance with increasing processing power of computers. This is a complex and comprehensive field of investigation and research. According to Radaj [9] simulation of welding can be divided into three parts: process, microstructural and structural simulation. The results of these sub-simulations depend on each other and interact to solve the global problem. Initial point of the simulation is the process simulation to get the temperature field as input for the microstructural and structural simulation.

Moreover these simulations offer a closer look on welding residual stresses and distortions over the whole component. Especially, welding residual stresses are important for the fatigue resistance of the connection and can be input parameter for the fatigue assessment by local approaches, for example for the notch strain approach. The calculated welding distortions can be used to optimize welding sequences and heating. In the end, costs for straightening operations can be reduced.

A numerical model of the welded samples has been implemented. To reduce computing time for this nonlinear, transient analysis and for symmetry reasons, the problem was reduced to a half model. This will only be possible, if the arrangement of weld layers is symmetrical as well. This is true for the plates with 20 mm thickness. Material properties, convection and radiation as well are defined temperature dependent. Furthermore the welding process is replaced by the commonly used double ellipsoid heat source according to Goldak [10]. This model offers a wide range of modification to validate the simulation results with the measured temperatures. The 3rd, 5th and 6th passes were tandem wire passes. Therefore two equivalent heat sources were arranged, one for each weld wire and welding process. The input parameters for the heat source model are based on the weld parameters and weld pool dimensions. As first assumptions of the dimensions of the weld end crater were used. Each welding pass is simulated. The continuous closing of the gap is considered by the element death and birth functionality.

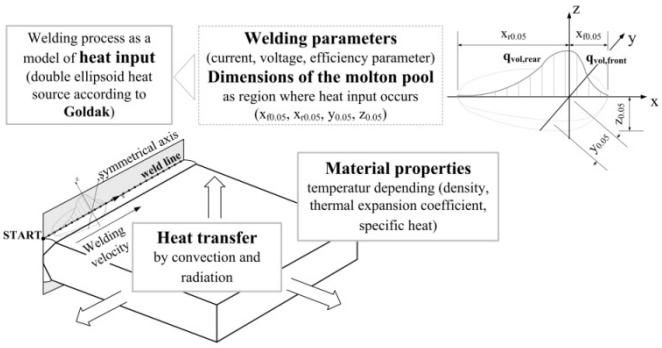

Figure 6: Assumptions for FE-Model in the ANSYS® program system

In Figure 7 the temperatures of the welding test and the numerical results at distances of 15, 30 and 45 mm from the weld are shown. The numerical results show high similarity to the measured temperatures after some modifications of the weld pool dimensions and can be used for the microstructural and structural simulation.

As a first conclusion it can be said that the computing time of 3D welding simulations are very time-consuming and the modification needs a lot of experience to get satisfying results. The structural analyses take much longer than the temperature field simulations. For practical application and

for large structures, alternative solutions have to be considered. For first investigations one possibility could be to regard a cross-sectional 2D model.

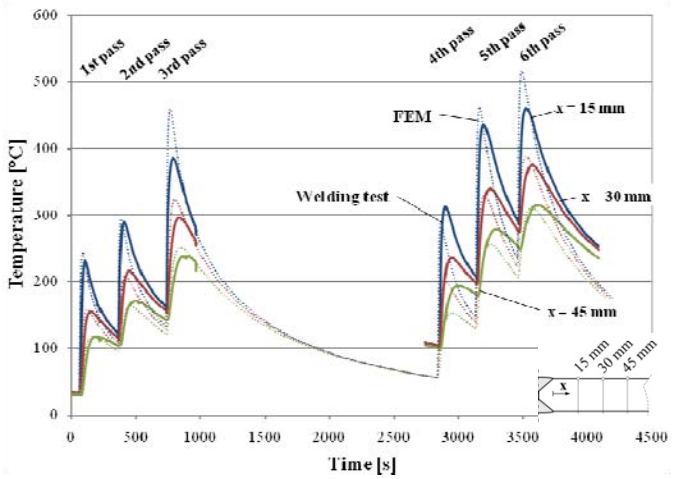

Figure 7 Temperatures at different distances to the weld in comparison to the simulated temperatures

4 Conclusions

The increasing demand of large components in the steel working industry, especially the offshore industry, shows the need for high performance and faster welding techniques. This is also true for the herein described tower manufacturing where plate thicknesses increase with increasing wind turbine height and power output. At first, the requirements for newly developed welding procedures have been emphasized on by using the example of wind tower production. Until now the performance of the newly installed hybrid welding is reliable for plate thicknesses up to 15 mm. For further improvements, modifications of the welding power source and the welding torch of the plasma key hole welding are necessary. Besides, more investigations are planned to avoid welding defects like cracks or welding pores reliably.

Furthermore welding tests at the tower manufacturer define the base for comparison. Out of these components (500 x 700 mm) welding samples (500 x 70 mm) were made for further ultimate and fatigue limit testing.

Parallel to this, a numerical finite element model has been developed. By the means of the measured temperatures during the welding tests, the simulation can be validated. The next step is to use the results of the temperature field as input for the calculation of structure mechanics to get a closer look on residual stresses, which are important for the fatigue resistance, and distortions, which are important for the modification of production processes.

Acknowledgement

The authors would like to thank the German Federal Ministry for the Environment, Nature Conservation and Nuclear Safety for the financial support to carry out the investigations within the research project “OPTIWELD - Ökologische und ökonomische Hochleistungsfügetechniken für Stahlrohrtürme von Windenergieanlagen”.

References

[1] A. H. Fritz, G. Schulze. Fertigungstechnik. 7. Auflage. Springer-Verlag Berlin Heidelberg, 2006.

[2] C. Bagger, F.O. Olsen. Review of laser hybrid welding. Journal of Laser Applications, Volume 17, Number 1, February 2005.

[3] J. Defalco. Practical Application for Hybrid Laser Welding. Welding Journal: 47-51, October 2007.

[4] C. Fuhrmann. Laser-Lichtbogen-Hybridschweißen bis zu Blechdicken von 25 mm. Dissertation. Shaker Verlag, 2007.

[5] D. Hinneberg, B. Eisenstein, A. Panoch. European patent application EP 1 570 939 A1 – Unterpulver-Schweißverfahren. Applicant: Howaldtswerke-Deutsche Werft, 2005.

[6] U. Dilthey. Schweißtechnische Fertigungsverfahren 1 – Schweiß- und Schneidtechnologien. 3. Auflage. Springer-Verlag Berlin Heidelberg, 2006.

[7] DVS Merkblatt 0915. Unterpulver-Mehrdrahtschweißen. 2000.

[8] G. Hochreiter. Unterpulverschweißen in der Praxis. expert-Verlag. Renningen-Mahlsheim, 1995.

[9] D. Radaj. Schweißprozesssimulation – Grundlagen und Anwendung. Fachbuchreihe Schweißtechnik 141. Verlag für Schweißen und verwandte Verfahren DVS-Verlag GmbH. Düsseldorf, 1999.

[10] J. A. Goldak, M. Akhlaghi. Computational Welding Mechanics. Springer Science+Business Media Inc., 2005.

Assessing Nonlinear Effects on Structural Dynamics of Wind Turbine Blades – Effect of Buckling on Composite Damping

Dimitris I. Chortis, Dimitris A. Saravanos
Structural Analysis & Active Materials Group, University of Patras
University Campus - Patras, Rio, Greece
E-mail: {dchortis,saravanos}@mech.upatras.gr

Keywords: Nonlinear Damping, Buckling, Composites

1 ABSTRACT

A theoretical and computational framework is presented for analyzing the small-amplitude free vibrational response of composite laminated strips subject to large in-plane forces. Nonlinear Green-Lagrange strains are incorporated in the governing equations assuming a Kelvin viscoelastic solid. A novel beam finite element is developed capable of yielding new nonlinear stiffness and damping matrices of the structure. The beam finite element is capable of predicting the damped free-vibration response and the modal characteristics of an in-plane deflected composite strip. Numerical results quantify the geometric nonlinear effect of compressive in-plane loads and the variation of modal damping and natural frequencies of composite strips during buckling and postbuckling response. Experimental measurements of a cross-ply Glass/Epoxy beam subject to buckling were conducted and correlated with the finite element predictions.

2 INTRODUCTION

Composite materials and laminates are extensively used in applications involving large initial stresses and extreme buckling loading cases such as new pressurized composite fuselage structures and long wind-turbine rotor blades exceeding 60m. Understanding and predicting the effect of complex nonlinear stiffness and damping structural behavior of composite laminates subject to compressive loads are important steps for improving the vibrational and aeroelastic response of many composite structures.

There are various analytical models and experimental works in the area of damping mechanics of composite materials and laminates [1-4]. Saravanos et al. developed a finite element for the prediction of the damped response of tubular laminated composite beams [5]. Lesieutre and Kosmatka [6-8] presented analytical solutions based on classical laminate theory, including effects of membrane loads on the damping of prestressed beams. Kosmatka [9] studied the vibration response of a geometrically-imperfect post-buckled Carbon/Epoxy beam and examined the effect of compressive load on the natural frequency and modal damping during beam transition from the pre- to post-buckling region. Recently, Chortis et al. [10] reported a damping mechanics beam finite element model for the prediction of nonlinear damping of laminated composite strips under large in-plane tension loads, assuming a Kelvin viscoelastic solid model.

The main objective of the present paper is the characterization of stiffness and damping parameters, both analytically and experimentally, of laminated strips under in-plane compressive loads. The kinematic assumptions include Green-Lagrange nonlinear strains and the first order shear deformation theory (FSDT), assuming a Kelvin viscoelastic solid. A new damped beam finite element is developed, capable of providing the effective and the tangential (linearized) matrices of the structure and predicting the natural frequencies and modal damping values of the composite structure subject to small-amplitude free-vibration. Numerical results evaluate the contribution of first and second order nonlinear terms on the modal characteristics of composite plate-strips under in-plane compressive loads. To that direction, experiments are conducted on a Glass/Epoxy $[0_2/90_2]_s$ cross-ply composite beam and excellent correlations with the predicted results both for the natural frequencies and the modal loss factors are presented.

3 DAMPING MECHANICS FRAMEWORK

The impact of nonlinear effects are predicted through a multi-scale model, first in the beam section level, with proper calculation of stiffness and damping terms, and finally into the structural stiffness and damping matrices of the system. A plate-beam or strip with arbitrary lamination is considered (Fig. 1a). The beam is assumed to be neither curved nor pre-twisted.

3.1 Section Kinematics

We assume first order shear section deformation, which admits extension along x-axis, bending in z direction and

shear in x and z directions, with kinematic assumptions of the following form [5]:

$$u(x,z,t) = u^0(x,t) + z\beta_x(x,t)$$
$$w(x,z,t) = w^0(x,t) \quad (1)$$

where: u , w are the displacement components of the section and β_x is the bending rotation angle; superscript 0 indicates mid-section and the comma in the subscripts indicates differentiation.

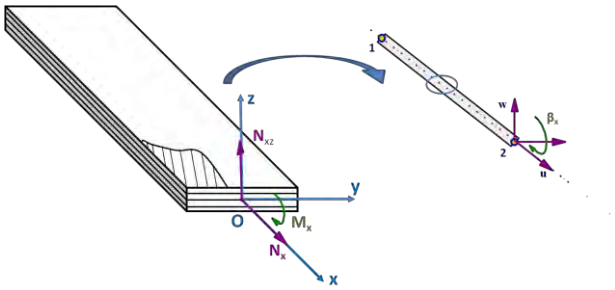

Figure 1: Laminated composite strip-beam element: (a) cross-section module; (b) finite element and nodal degrees of freedom.

In order to capture the effect of initial in-plane loads, we consider a nonlinear Green-Lagrange normal strain component. The shear strain acting on the cross-section is assumed to remain linear.

$$\varepsilon_x = u_{,x} + \frac{1}{2}w_{,x}^2 \quad , \quad \varepsilon_{xz} = u_{,z} + w_{,x} \quad (2)$$

where, $\boldsymbol{\varepsilon}$ are the engineering strains. Combining Eqs. (1) and (2), the detailed normal and shear strains of the section are expressed as follows:

$$\varepsilon_x(x,z) = \varepsilon_x^0(x) + \frac{1}{2}w_{,x}^{0^2}(x) + zk_x(x)$$
$$\varepsilon_{xz}(x,z) = w_{,x}^0 + \beta_x \quad (3)$$

3.2 Equations of Motion

The equations of motion of the beam are described by the following variational form:

$$\int_0^L dx \int_A \delta H dz + \int_0^L dx \int_A \delta T dz + \oint_\Gamma \delta \bar{\mathbf{u}}^T \bar{\boldsymbol{\tau}} d\Gamma = 0 \quad (4)$$

where: H and T are the strain and kinetic energy; $\bar{\boldsymbol{\tau}}$ are surface tractions on the free surface Γ; A is the cross-sectional area covered by material and L is the length of the beam.

The strain energy variation of the section δH_{sec} is represented by the integral over the cross-sectional area as follows:

$$\delta H_{\text{sec}} = b\int_h \delta \boldsymbol{\varepsilon}_c^T \boldsymbol{\sigma}_c dz \quad (5)$$

where $\boldsymbol{\varepsilon}_c$ and $\boldsymbol{\sigma}_c$ are the off-axis strains and stresses of a rotated composite ply, respectively; c indicates off-axis ply and b is the width of the section.

A strain based Kelvin viscoelastic constitutive model was considered, next. Thus, the ply stresses are related to the strain in the form:

$$\boldsymbol{\sigma}_c = [\mathbf{Q}_{cs}]\boldsymbol{\varepsilon}_c + [\mathbf{Q}_{cd}]\dot{\boldsymbol{\varepsilon}}_c \quad (6)$$

where, $\mathbf{Q}_{cs}$ and $\mathbf{Q}_{cd}$ are off-axis stiffness and damping matrices of the composite ply. This is a simple viscoelastic model in the time domain, which predicted modal damping reasonably well.

Substituting Eq. (6) into Eq. (5), the final expression for the strain energy variation over the cross-sectional area is:

$$\delta H_{\text{sec}} = b\int_h \left(\delta \boldsymbol{\varepsilon}_c^T \left([\mathbf{Q}_{cs}]\boldsymbol{\varepsilon}_c + [\mathbf{Q}_{cd}]\dot{\boldsymbol{\varepsilon}}_c\right)\right) dz = \delta H_s + \delta H_{ds} \quad (7)$$

where, δH_s and δH_{ds} are the expressions for the strain and dissipated energy variation of the beam cross-section, respectively.

3.3 Section Stiffness and Damping Terms

Replacing the normal and shear strain expressions provided by Eqs. (3), in Eq. (5), integrating over the laminate thickness and assuming negligible transverse normal and shear laminate stresses N_y , N_{xy} , N_{yz} and transverse and shear moments M_y , M_{xy} along the coordinate axes O_{xyz} , the stored and the dissipated strain energy in the section take the following general form:

$$\delta H_s = \delta H_{s_0} + \delta H_{s_1} + \delta H_{s_2}$$
$$\delta H_{ds} = \delta H_{ds_0} + \delta H_{ds_1} + \delta H_{ds_2} \quad (8)$$

where the subscripts s , ds indicate the cross-section strain and dissipated energy terms, respectively, containing linear, nonlinear first and second order components.

4 DAMPED BEAM FINITE ELEMENT

A three-dimensional shear beam finite element was developed for the nonlinear quasi-static damped dynamic analysis of composite beams encompassing the aforementioned nonlinear mechanics (Fig. 1b). The element has 3 DOFs at each node (indicated with superscript i), and approximates the generalized displacements by c^0 continuous shape functions $N^i(x)$,

$$\left\langle u^o(x), w^o(x), \beta_x^i(x) \right\rangle = \sum_{i=1}^{n} N^i(x) \left\langle u^{oi}, w^{oi}, \beta_x^i \right\rangle \qquad (9)$$

where, n is the number of element nodes.

By applying the previous kinematic assumptions into the equations of motion, the equilibrium **u(t)** is provided by the following equation,

$$\mathbf{\Psi(u,t)} = [\mathbf{M}]\ddot{\mathbf{u}} + [\mathbf{C}]\dot{\mathbf{u}} + [\mathbf{K}]\mathbf{u} - \mathbf{F(t)} \qquad (10)$$

4.1 Small amplitude vibration

For vibrating beams subject to a large static in-plane stress, we specialize their motion to the case of a perturbation vibration around a nonlinear static equilibrium point $\mathbf{u}_s$, such that $\mathbf{u(t)} = \mathbf{u}_s + \bar{\mathbf{u}}(\mathbf{t})$, where overbar indicates perturbation quantities. In this case, the equilibrium takes the form,

$$\mathbf{\Psi(u,t)} = [\mathbf{M}]\ddot{\bar{\mathbf{u}}} + [\mathbf{C}]\dot{\bar{\mathbf{u}}} + \left([\mathbf{K}]\mathbf{u}_s - \mathbf{F}_s\right) + \frac{\partial\left([\mathbf{K}]\mathbf{u}\right)}{\partial \mathbf{u}}\bar{\mathbf{u}} - \bar{\mathbf{F}}(\mathbf{t}) \qquad (11)$$

We observe that since $\mathbf{u}_s$ is a point of static equilibrium, the imbalance force vector between the internal forces and externally applied mechanical loads is $\mathbf{\Psi}_s = \left([\mathbf{K}]\mathbf{u}_s - \mathbf{F}_s\right) = \mathbf{0}$ and the term $\left[\bar{\mathbf{K}}\right] = \partial\left([\mathbf{K}]\mathbf{u}\right)/\partial\mathbf{u}$ is the tangential or linearized stiffness of the structure at the point of static equilibrium. Hence, Eq. (11) takes the final form which describes the small vibration of the beam.

$$\mathbf{\Psi(u,t)} = [\mathbf{M}]\ddot{\bar{\mathbf{u}}}(\mathbf{t}) + [\mathbf{C}]\dot{\bar{\mathbf{u}}}(\mathbf{t}) + [\bar{\mathbf{K}}]\bar{\mathbf{u}}(\mathbf{t}) - \bar{\mathbf{F}}(\mathbf{t}) = \mathbf{0} \qquad (12)$$

4.2 Modal damping

Eq. (12) may be solved either directly to yield the complex eigenvalues of the system or by using an energy approach for the calculation of structural damping. In the present paper we use the second method, where the numerical solution of the undamped system provides the undamped modal frequencies and the relative mode shapes of the beam structure. The modal loss factor is calculated as the following ratio of the respective dissipated to the maximum stored modal energy in the structure:

$$\eta_m = \frac{\omega_m}{2\pi} \frac{\bar{\mathbf{U}}_\mathbf{m}^\mathbf{T}\left[\mathbf{C(u)}\right]\bar{\mathbf{U}}_\mathbf{m}}{\bar{\mathbf{U}}_\mathbf{m}^\mathbf{T}\left[\bar{\mathbf{K}}\mathbf{(u)}\right]\bar{\mathbf{U}}_\mathbf{m}} \qquad (13)$$

Where ω_m and $\bar{\mathbf{U}}_\mathbf{m}$ are the undamped modal frequency and displacement vector, respectively.

4 NUMERICAL RESULTS

The developed beam finite element was evaluated both numerically and experimentally through a series of validation cases for a composite $[0_2/90_2]_s$ Glass/Epoxy cross-ply specimen [10]. The finite element code was formulated using the displacement control method and the Newton-Raphson iterative technique. Regarding the experimental procedure (Fig. 2), the beam was attached on a hydraulic uniaxial testing machine MEYES 100KN with both ends being clamped by hydraulic wedge grips; one remaining immovable while an in-plane displacement was applied to the other end at a rate of 0.01mm/min and during the load application, vibration analysis tests were performed for various in-plane buckling loads.

Figure 2: Experimental Setup

The dynamic tests were performed using two different excitation methods; in the first, an impact hammer was used to excite the first bending mode of the beam and the response was measured via a PZT-5 piezoceramic plate, adhered on the beam surface near the clamped edge, (Fig. 2), whereas in the second method, the response was measured via a miniature accelerometer attached at the midspan of the beam.

In Fig. 3 the variation of the first bending frequency for various increasing compressive displacement values is shown. Because of a geometric imperfection observed in the tested beam, a transverse force F_z was considered at the midspan of the beam. For the case of $F_z = 1.0\text{N}$ the finite element code follows the experimental response for various values of applied in-plane displacement. Especially the use of the PZT-5 piezoceramic plate as sensor seems to outperform in comparison with the accelerometer.

The capabilities of the beam element are better illustrated in Fig. 4, where the first modal loss factor of the composite beam for an increasing in-plane displacement is presented.

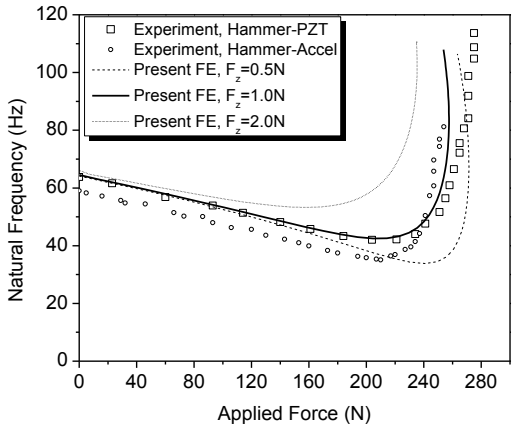

Figure 3: Predicted and measured first bending natural frequency under compressive load.

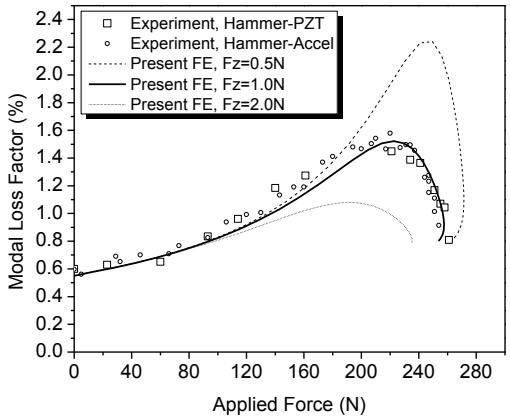

Figure 4: Predicted and measured first bending modal loss factor under compressive load.

In the prebuckling region the beam gradually loses its stiffness and consequently the modal damping follows an increasing path. At the critical buckling load the damping reaches its maximum value and thereafter it follows a decreasing path as the beam repossess its stiffness in the postbuckling region. The predicted results are in excellent agreement with the experimental measurements using either a PZT-5 piezoceramic sensor or an accelerometer.

5 Conclusions

A theoretical framework was presented to predict the dynamic response of composite beams subject to in-plane buckling loading. The following major conclusions can be summarized from the obtained numerical results:

1. There is a strong influence of stress stiffening effects on the natural frequencies and modal damping values of composite beams subject to in-plane compressive loading.
2. The excellent correlation between predicted and experimental results gives credence to the developed finite element. The beam transition from the pre- to the post-buckling response could be detected by monitoring the modal characteristics values.

References

[1] Z. Hashin. Complex moduli of viscoelastic composites-I. General theory and application to particulate composites. International Journal of Solids and Structures, 6:539-552, 1970.

[2] R.D. Adams and D.G.C. Bacon. Measurement of the flexural damping capacity and dynamic Young's modulus of metals and reinforced plastics. Journal of Physics D: Applied Physics, 6(1):27-41, 1973.

[3] R.F. Gibson and R. Plunkett. Dynamic mechanical behavior of fiber-reinforced composites: measurements and analysis. Journal of Composite Materials, 10:325-341, 1976.

[4] D.A. Saravanos and C.C. Chamis. Unified micromechanics of damping for unidirectional and off-axis fiber composites. Journal of Composites Technology & Research, 12(1):31-40, 1990.

[5] D.A. Saravanos, D. Varelis, T.S. Plagianakos and N. Chrysochoidis. A shear beam finite element for the damping analysis of tubular laminated composite beams. Journal of Sound and Vibration, 291:802-823, 2006.

[6] J.B. Kosmatka. Damping behaviour of initially-stressed beams. Proceedings of the 49th AIAA/ASME/ASCE/AHS/ASC structures, structural dynamics, and materials conference, Schaumburg:1-11, 2008.

[7] G.A. Lesieutre. How membrane loads influence the modal damping of flexural structures. AIAA Journal, 47:1642-1646, 2009.

[8] G.A. Lesieutre. Finite elements for dynamic modeling of uniaxial rods with frequency-dependent material properties. International Journal of Solids and Structures, 29(12):1567-1579, 1992.

[9] J.B. Kosmatka, Damping variations in post-buckled structures having geometric imperfections. Proceedings of the 51st AIAA/ASME/ASCE/AHS/ASC structures, structural dynamics, and materials conference, Orlando:1-7, 2010.

[10] D.I. Chortis, N.A. Chrysochoidis, D.S. Varelis and D.A. Saravanos. A damping mechanics model and a beam finite element for the free-vibration of laminated composite strips under in-plane loading. Journal of Sound and Vibration, 330(23):5660-5677, 2011.

Session 2A

Rotor and Wakes Aerodynamics II

Quasi-simultaneous interaction method for solving boundary layer flows in primary and characteristic variables
H.A.Bijleveld, A.E.P.Veldman

Aerodynamic Design of Airfoils for 10-20 MW Vertical Axis Wind Turbines
Ben Geurts

A Low Order Numerical Model of the Inherent Wake Inside an Infinitely Long Row of Wind Turbines
Søren Andersen, Jens Nørkær Sørensen, and Robert Mikkelsen

Quasi-simultaneous interaction method for solving boundary layer flows in primary and characteristic variables

H.A.Bijleveld, A.E.P.Veldman
JBI Institute for Mathematics and Computer Science , Rijksuniversiteit Groningen
P.O.Box 407, 9700 AK Groningen, the Netherlands
E-mail: bijleveld@ecn.nl

Keywords: boundary layer, viscous-inviscid interaction

1 INTRODUCTION

The growth in size of wind turbines and their blades requires more accurate prediction methods for the determination of aerodynamic loads. Current methods for predicting aerodynamic loads on wind turbine blades use engineering models and a steady approach of the flow field like e.g. BEM (Blade-Element Momentum) methods and XFOIL [1, 2]. On the other hand, carrying out a full Navier-Stokes simulation of the flow field (e.g. RANS) can give higher accuracy of the prediction, but it consumes too much computational time to be a practical design tool.

The goal of ROTORFLOW of ECN, is to create a wind turbine rotor aerodynamics simulation code that requires little user expertise and computational effort, but can compute in detail the unsteady aerodynamic characteristics of rotor airfoils. The simulation of separated flows will be feasible. It will be a combination of a panel method flow solver for the unsteady, incompressible, inviscid external flow and an integral boundary layer solver for the unsteady, viscous flow near the blade surface using a finite volume approach [3]. The flow field is split into an inviscid and a viscous region, see Figure 1. The strong interaction between these two flow regions in separated flows will be accounted for by a quasi-simultaneous viscous-inviscid interaction method [4]. The interaction method ensures the exchange between the integral boundary layer variables of the viscous flow and the inviscid flow variables. This method has extensively been applied in aircraft applications (e.g. [5]), but is hardly used in the design of wind turbine blades.

This paper will focus on the quasi-simultaneous interaction method.

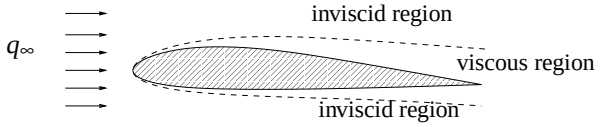

Figure 1: Domain decomposition into a viscous and inviscid region. Interaction takes place at the dashed line. q_∞ represents the inflow field.

The viscous region of Figure 1 is modeled as a boundary layer through the use of integral boundary layer equations. The primary variables of interest are the velocity vetor at the edge of the boundary layer ($\vec{u}_e$), the displacement thickness (δ^*), momentum thickness (θ) and the shape factor (H).

The numerical approach for the simulations of the boundary layer will be based on a finite volume approach. Therefore, a set of equations in partial differential form is required either in primary or characteristic variables. The interaction law equation from the quasi-simultaneous interaction method is substituted in the integral boundary layer equations obtaining a set of partial differential equations.

This paper focusses on the application of the strong quasi-simultaneous interaction method. We will show that the simulations performed with primary and characteristic variables in the sets of equations yield the same results.

2 VISCOUS-INVISCID INTERACTION METHODS

The philosophy of viscous-inviscid interaction methods is that it exchanges the velocity vector and the boundary layer displacement thickness - modeled via a transpiration velocity - between the inviscid and viscous region until a matching solution between the two regions is obtained.

The phenomenon of interaction can be described as:

$$P = \begin{cases} \vec{u}_e & = E[\delta^*] \\ \vec{u}_e & = B[\delta^*] \end{cases}, \tag{1}$$

with E and B the set of external flow and integral boundary layer equations respectively.

In Figure 2 the relations between u_e and δ^* for the viscous (E) and inviscid (B) flow are drawn schematically where for convenience the inviscid flow relation is supposed to be linear. The aim of any viscous-inviscid interaction method is to ensure a connection between the solution of the flow domains. This is achieved if E has a slope that is steep enough to have an intersection with the curve of B.

Several types of interaction methods have been developed.

The most straightforward method is the direct method. In this method, the viscous and inviscid regions are calculated

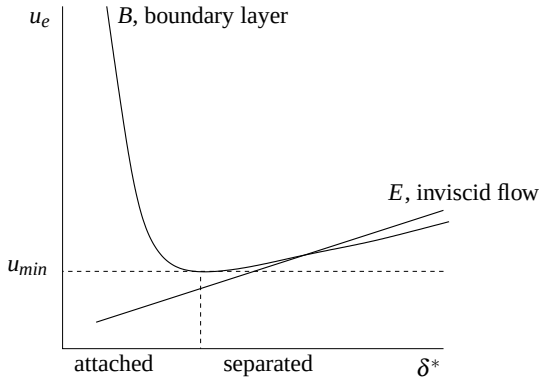

Figure 2: Schematic representation of the relation between u_e and δ^* for B and E.

subsequently:

$$P_{direct} = \begin{cases} \vec{u}_e^{(n)} & = E[\delta^{*(n-1)}] \\ \delta^{*(n)} & = B^{-1}[\vec{u}_e^{(n)}] \end{cases}, \tag{2}$$

where n is the iteration number. This method works well for attached flows where the effect of the boundary layer on the external flow is small. However, at the point of separation a singularity occurs and B^{-1} cannot be determined. This is the well-known Goldstein singularity. This can also be learned from Figure 2 as for not every u_e a corresponding δ^* can be found in the boundary layer model. Figure 2 shows that the minimum of the B-curve is at the point of separation.

Solving the boundary layer equations with a known displacement thickness instead of a known velocity is an inverse method:

$$P_{inverse} = \begin{cases} \delta^{*(n)} & = E^{-1}[\vec{u}_e^{(n-1)}] \\ \vec{u}_e^{(n)} & = B[\delta^{*(n)}] \end{cases}. \tag{3}$$

Catherall and Mangler first proposed this method and this method is able to calculate separated flows. The convergence of the interaction scheme is slow, however.

The direct and inverse method assume a hierarchy between the flow regimes and are so-called weak interaction methods. Avoiding this hierarchy can be achieved by solving the viscous and inviscid flow simultaneously:

$$P_{simultaneous} = \begin{cases} \vec{u}_e^{(n)} - E[\delta^{*(n)}] & = 0 \\ \vec{u}_e^{(n)} - B[\delta^{*(n)}] & = 0 \end{cases}. \tag{4}$$

This is a robust method and calculates separated flow well. The XFOIL code of Drela is based on this idea [1]. However, a drawback of this method is that the equations for both flows are modeled in one system of equations, reducing the flexibility in flow modeling and increasing software complexity.

Veldman [6] combined the advantages of the direct and simultaneous method in the quasi-simultaneous interaction scheme, see Figure 3. This method solves the viscous flow region together with an *approximation* (indicated with I) of the external flow and subsequently solves the inviscid flow:

$$P_{quasi-simultaneous} = \begin{cases} \vec{u}_e^{(n)} & = E[\delta^{*(n-1)}] \\ \vec{u}_e^{(n)} - I[\delta^{*(n)}] & = B[\delta^{*(n)}] - I[\delta^{*(n-1)}] \end{cases} \tag{5}$$

where I is the approximation of the external flow which is called *interaction-law*. The interaction-law is formulated such that it has no influence on the converged solution: when $\delta^{*(n)} = \delta^{*(n-1)}$, I cancels from equation (5). In Figure 3 the interaction-law is sketched together with the inviscid and boundary layer relations. The interaction-law is formulated such that it always has an intersection with B even in cases where E might not intersect.

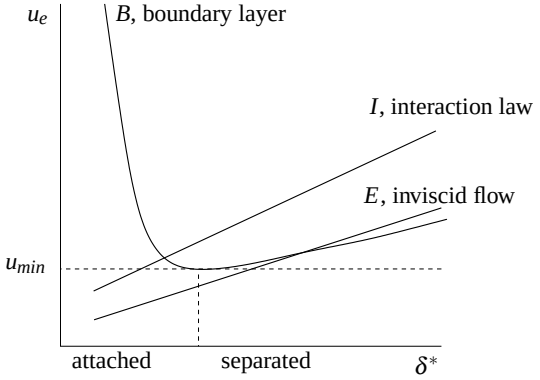

Figure 3: Schematic representation of the relation between u_e and δ^* for B, E and I.

In the past, several interaction-laws have been applied. The interaction-law applied in this work is based on the 3D quasi-simultaneous interaction-law formulation of Bijleveld and Veldman [4].

3 INTERACTION-LAW

In the quasi-simultaneous interaction method, the interaction-law I is applied. The interaction-law is a simplification of the external flow in such a way that only the essentials of the inviscid flow are taken into account. The resulting strong interaction method closely resembles a direct method, with the advantage that separated flow can be calculated. For the formulation of the interaction-law equation, only the local influence of the external flow on the boundary layer is taken into account. This results in a very simple algebraic expression for the interaction-law:

$$I : \vec{u}_e = \vec{f}(\delta^*, E), \tag{6}$$

The right-hand side contains information of δ^* and the external flow. For three-dimensional applications the interaction-law equation (6) is, [4]:

$$\begin{cases} I_{3D,u_e} : u_e - c_x q_e \delta_x = \mathrm{RHS}_x \\ I_{3D,v_e} : v_e - c_y q_e \delta_y = \mathrm{RHS}_y \end{cases} \tag{7}$$

The transpiration velocities, $(q_e\delta_x)$ and $(q_e\delta_y)$, appear in the formulation of the inviscid flow. The coefficients c_x and c_y are defined as:

$$c_x = -\frac{\Delta y}{\pi \Delta x^2} \ln \left| \frac{(\sqrt{\Delta x^2 + \Delta y^2} + \Delta x)^2}{(\sqrt{\Delta x^2 + \Delta y^2} - \Delta x)^2} \right| \tag{8}$$

$$c_y = -\frac{\Delta x}{\pi \Delta y^2} \ln \left| \frac{(\sqrt{\Delta x^2 + \Delta y^2} + \Delta y)^2}{(\sqrt{\Delta x^2 + \Delta y^2} - \Delta y)^2} \right|. \tag{9}$$

with Δx, Δy the local mesh width.

4 Implementation of interaction-law

In this section we will formulate the three-dimensional boundary layer model that is used in the simulations. At the end of the section we show how the set of equations in characteristic variables is obtained.

In the 3D turbulent boundary layer model three integral boundary-layer equations are employed together with suitable closure relations. The two integral momentum equations are in an orthogonal Cartesian coordinate system:

$$\frac{\partial}{\partial x}(\theta_{xx} q_e^2) + \frac{\partial}{\partial y}(\theta_{xy} q_e^2) = -q_e \delta_x^* \frac{\partial u_e}{\partial x} - q_e \delta_y^* \frac{\partial u_e}{\partial y} + \tau_{w_x} \tag{10}$$

$$\frac{\partial}{\partial x}(\theta_{yx} q_e^2) + \frac{\partial}{\partial y}(\theta_{yy} q_e^2) = -q_e \delta_x^* \frac{\partial v_e}{\partial x} - q_e \delta_y^* \frac{\partial v_e}{\partial y} + \tau_{w_y}. \tag{11}$$

The entrainment equation reads:

$$\frac{\partial}{\partial x}(u_e \delta - q_e \delta_x^*) + \frac{\partial}{\partial y}(v_e \delta - q_e \delta_y^*) = q_e C_E, \tag{12}$$

with δ the boundary-layer thickness, δ^* the boundary layer displacement thickness, θ_{xx}, θ_{xy}, θ_{yx} and θ_{yy} the x- and y-momentum thicknesses, τ the skin-friction and C_E the entrainment coefficient.

The closure model used is from Mager [7] and Houwink [8].

4.1 Substitution of interaction-law equation

The interaction-law equation is substituted in the boundary layer equations. This is done by first expanding the derivatives of the boundary layer equations and then substitute for the terms with derivatives of the velocity the derivative of the interaction-law equation. In this way the set of equations remains a set of first order partial differential equations. This is needed in order to rewrite them in characteristic variables. An advantage is that the number of equations to be solved is reduced from 5 to 3 for 3D applications.

The resulting set of equations can now be written as:

$$[P]\frac{\partial \phi}{\partial x} + [Q]\frac{\partial \phi}{\partial y} = \{R\} \tag{13}$$

with $\{\phi\} = \{\theta, H, \tan\beta\}$, the vector of unknowns and $[P]$, $[Q]$ matrices with the expanded terms.

4.2 Characteristic variables

A system in characteristic variables is a decoupled system of ordinary differential equations. These equations can be solved separately in their corresponding characteristic direction which are obtained via the eigenvectors of the system. The eigenvalues need to be determined and from that a transformation matrix S is constructed containing the eigenvectors. The transformation that we apply is:

$$S\psi = \phi, \quad S\frac{\partial \psi}{\partial x} = \frac{\partial \phi}{\partial x}; \quad \left(\frac{\partial S}{\partial x} = 0\right). \tag{14}$$

with ψ the vector of characteristic variables. By multiplying the system with $[P]^{-1}$, applying the transformation of equation (14) and subsequently multiplying with $[S]^{-1}$ we can write equation (13) as:

$$\begin{aligned} &[P]\frac{\partial \phi}{\partial t} + [Q]\frac{\partial \phi}{\partial x} = \{R\} \quad \Rightarrow \\ &\frac{\partial \psi}{\partial t} + [\Lambda]\frac{\partial \psi}{\partial x} = [S]^{-1}[P]^{-1}\{R\}, [\Lambda] = [S]^{-1}[P]^{-1}[Q][S] \end{aligned} \tag{15}$$

and $[\Lambda]$ a diagonal matrix containing the eigenvalues. The equations are decoupled. As the systems with primary and characteristic variables are analytically equal, simulations with both sets should yield equal results.

Characteristic directions give an indication of the directions of information in the boundary layer flow. For two-dimensional boundary layer flow these are always upstream in the interaction method [2]. For three-dimensional flows over dented plates this is not the case due to the 3D geometry.

5 Results

Simulations with the system of equations in primary and characteristic variables have been performed. The geometries used are a flat and a dented plate, see Figure 4.

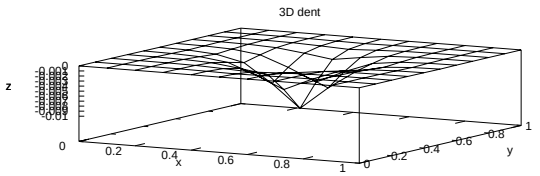

Figure 4: Geometry of dented plate with dent depth 1% of plate length.

The simulations have been performed on an equidistant grid with $\Delta x = 1/120$, $\Delta y = 1/20$ and $Re = 11.5 \cdot 10^6$.

In Figure 5 and 6 the converged results of the boundary layer displacement thickness in streamwise direction and the skin-friction for a boundary layer flow over a flat plate are shown at $y = 0.5$. Figures 7 and 8 show the same variables for the simulation over the dented plate.

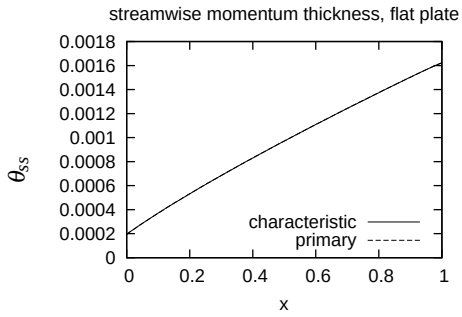

Figure 5: Momentum thickness θ_{ss} at $y = 0.5$ on a flat plate.

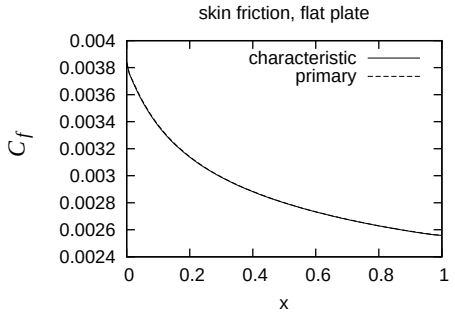

Figure 6: Skin friction at $y = 0.5$ on a flat plate.

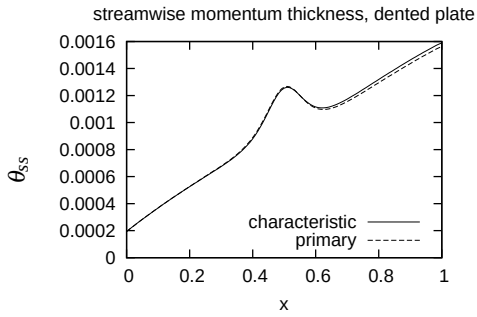

Figure 7: Momentum thickness θ_{ss} at $y = 0.5$ on a dented plate with dent depth 1 % of plate length.

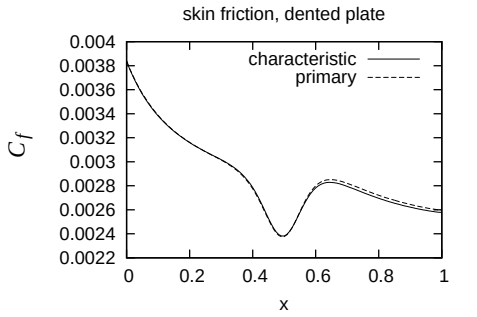

Figure 8: Skin-friction at $y = 0.5$ on a dented plate with dent depth 1 % of plate length.

For both flat and dented plates, the results of simulations with both sets of equations yield the same converged results. For a flat plate the results are identical. For dented plates small differences are observed which diminish for simulations on finer grids. The differences are probably due to the different numerical approaches.

6 Conclusion

The quasi-simultaneous interaction method has been applied to three-dimensional boundary layer flows over a flat and dented plate. It can be concluded that the use of primary and characteristic variables converge to the same result for all cases investigated. This proves that the quasi-simultaneous interaction method is suitable for application on finite volume discretizations.

References

[1] M. Drela. XFOIL: An Analysis and Design System for Low Reynolds Number Airfoils. Low Reynolds Numbers Aerodynamics, 1989.

[2] H.A. Bijleveld and A.E.P Veldman. Prediction of Unsteady Flow over Airfoils using a Quasi-Simultaneous Interaction Method, EWEA 2011, Brussels, Belgium, March 14-17, 2011.

[3] H. Özdemir. Development of a discontinuous Galerkin method for the unsteady integral boundary layer equations. 8th Euromech Fluid Mechanics Conference, Bad Reichenhall, Germany, September 13-16, 2010.

[4] H.A. Bijleveld and A.E.P Veldman. RotorFlow: a Quasi-simultaneous interaction for the prediction of aerodynamic flow over wind turbine blades. The Science of Making Torque from Wind - Heraklion, Crete, 2010.

[5] A.J. van der Wees and J. van Muijden. A Robust Quasi-Simultaneous Interaction Method for a Full Potential Flow with a Boundary Layer with Application to Wing/body Configurations. Proceedings of the 5th symposium on numerical and physical aspects of aerodynamic flows, 1992.

[6] A.E.P. Veldman. New, quasi-simultaneous method to calculate interacting boundary layers. AIAA Journal 19:79-85, 1981.

[7] A. Mager. Generalization of Boundary-Layer Momentum-Integral Equations to Three-Dimensional Flows Including those of Rotating System. NACA R-1067, 1952.

[8] R. Houwink and A.E.P Veldman. Steady and Unsteady Flow Computations for Transonic Airfoils. AIAA 84-1618, 1984.

[9] B.A. Nishida. Fully Simultaneous Coupling of the Full Potential Equation and the Integral Boundary Layer Equations in Three Dimensions. PhD thesis Massachusetts Institute of Technology, USA, 1996.

Aerodynamic Design of Airfoils for 10-20 MW Vertical Axis Wind Turbines

Ben Geurts
DUWIND, Faculty of Aerospace Engineering, Delft University of Technology
Kluyverweg 1, 2629HS Delft, The Netherlands
E-mail: B.M.Geurts@tudelft.nl

Keywords: aerodynamics, VAWT, airfoil design

1 Introduction

This research aims to design high-Reynolds airfoils, for large Vertical Axis Wind Turbines (VAWTs). Back in the eighties, Sandia National Laboratories did research on large VAWTs. The airfoils used were mostly symmetric NACA 4-digit (NACA00XX) and SNLA2150 airfoils, or very closely related [1],[2]. With the coming of new simulation techniques, the design of airfoils for VAWTs has been under investigation more recently [3],[4]. However, this is limited to small-scale VAWTs operating in low Reynolds numbers. This paper attempts to explain the procedure used to come up with airfoil designs which are optimal for use in future large-scale VAWT applications.

2 Airfoil Optimization

In order to identify which geometrical airfoil properties have an effect on the VAWT performance, a generic airfoil optimizer is used. The optimizer creates random airfoils by means of a number of shape functions. After evaluation of the cost function, the optimizer creates a new generation of airfoils cross-breeded from the best performing airfoils in the previous generation. It is unpractical to run a full VAWT simulation for every airfoil, so it is useful to determine possible airfoil performance characteristics representing their suitability in VAWT applications. A number of potential cost function parameters are given in table 1.

The most important parameter given in table 1 is the steepness of the lift slope $\frac{dC_L}{d\alpha}$. As explained in [5], the power of a VAWT is generated through vorticity shedding. Consequently, the shed vorticity is the main contribution to the induction in the wake. An airfoil with a steeper $C_L - \alpha$ curve will generate more shed vorticity when subjected to the same range of angles of attack, and thus it will produce more power. On the other hand, the stronger shed vorticity will cause a stronger induction, and thus lower the local flow velocity at the rotor, reducing the local angles of attack. In order to take this effect into account, the experienced range of angles of attack should be included within the optimization loop. This is done using the output data from a set of 2D inviscid vortex simulations.

Table 1: Optimization parameters affecting VAWT power

Parameter	Cost function relevance
Thickness	Thick airfoils are easier to manufacture
C_D	Low drag
C_m	Negative aerodynamic moment counteracts the torque
$\frac{dC_L}{d\alpha}$	Steeper lift slope results in more shed vorticity for the same chord

3 2D VAWT simulation approach

In order to have an expression for the performance of a 2D VAWT, a combination is made of an inviscid free-wake vortex model and viscous 2D airfoil data. As mentioned before, the wake of a VAWT is created by the shedding of vorticity from the blade. This happens as a consequence of the changing circulation around the airfoil in the course of a rotation. When two different airfoils are considered with the same lift slope, they will create the same amount of shed vorticity when they are exposed to the same angles of attack in the course of a rotation. With the same shed vorticity, the wake can be assumed to also be the same, which justifies the assumption that the experienced angles of attack are also the same. Neglecting viscous effects inside the wake, we can now calculate the VAWT performance with viscous airfoil data. The restriction here is that for the assessment of a new airfoil the angles of attack are used of an inviscid simulation of which the (inviscid) lift slope matches the (viscous) lift slope of the assessed airfoil.

3.1 Inviscid Simulations

The inviscid lift slope of NACA00XX airfoils has a very linear behavior with respect to airfoil thickness, as can be seen in figure 1. Figure 1 shows the amount of increase of the lift coefficient C_L matching an increase of one degree of the angle of attack α in the linear part of the $C_L - \alpha$ curve for symmetric NACA 4-digit airfoils with thicknesses from 3% up to 35%.

Within the optimization, it is now a simple effort to determine the viscous lift slope of an airfoil, and from there choose a simulation featuring a NACA00XX airfoil which has a matching inviscid $\frac{dC_L}{d\alpha}$. It is possible to simply interpolate the angles of attack at specific azimuth angles from

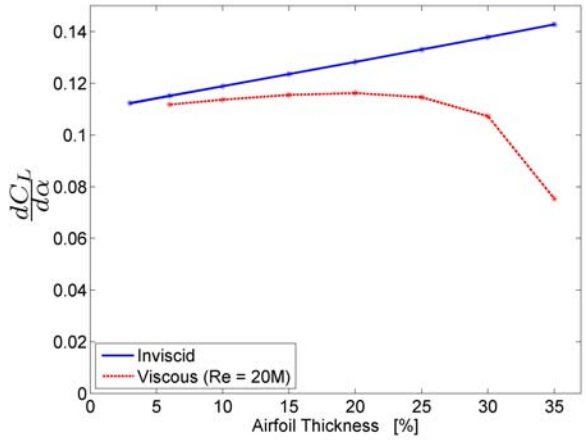

Figure 1: Lift slope $\frac{dC_L}{d\alpha}$ for airfoils of changing thickness (from NACA0003 till NACA0035) obtained with XFoil

the different NACA00XX simulations when the $\frac{dC_L}{d\alpha}$ is not an exact match.

Consider for example the case where we want to investigate the performance of a NACA0020 airfoil. Assuming the airfoil is operating around a Reynolds Number of 20 milion, the viscous $\frac{dC_L}{d\alpha}$ can be found from the red (dotted) line in figure 1, i.e. $\frac{dC_L}{d\alpha} = 0.116$. When checking this value on the blue (inviscid) line, we find that the viscous NACA0020 would have the same wake structure as an inviscid NACA0007 airfoil. Using the ranges of angles of attack obtained from interpolation between the NACA0006 and NACA0010 simulations in combination with viscous NACA0020 airfoil data, we can calculate the performance of the VAWT with NACA0020 airfoil sections. Similarly, we can apply the same procedure for any imaginable airfoil shape, as long as we can calculate the viscous polars for it.

3.2 Viscous performance calculation

Using the (interpolated) range of angles of attack, it is a straightforward task to use viscous airfoil data in order to obtain the blade loading at every instance of the rotation. Integrating the tangential force components multiplied with the rotational velocity gives the power produced by the VAWT.

3.3 Optimization challenges

With the viscous-inviscid combination, it is possible to include the power (or a representing factor thereof) within the cycle of an airfoil optimization without having to include a full-scale simulation of the VAWT operation. It is a more elaborate approach than simply optimizing for the lift slope, but this way the increasing induction associated with an increase of the $\frac{dC_L}{d\alpha}$ is taken into account.

Including the Pitching Moment

Running the optimizer using the power of the VAWT means that the aerodynamic moment on the blades is also included. A negative pitching moment coefficient as it occurs in most applications has a negative effect on the rotor torque. This drives the optimizer to designs featuring reflex camber near the trailing edge, in order to create a positive pitching moment coefficient. One of these shapes is shown in blue in figure 2. They are not only difficult to manufacture, the occurrence of strong aerodynamic pitching moments is generally also not advised from structural point of view.

Excluding the Pitching Moment

When leaving out the contribution to power from the aerodynamic pitching moment, the optimizer works towards airfoils with high negative pitching moments, manifested by very thin and strongly cambered trailing edge sections. At the same time the thickness remains reasonably large, and is located close to the leading edge. An example of the thin trailing edge airfoils is shown in red figure 2.

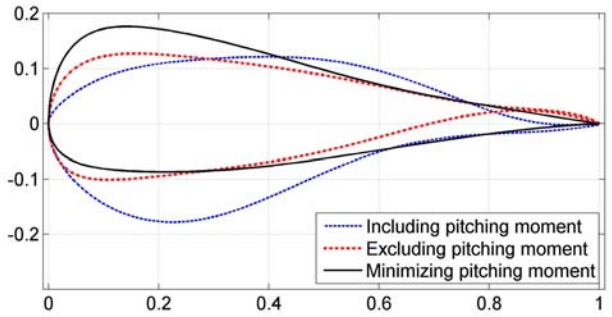

Figure 2: Resulting airfoils from the optimizer (including and excluding the pitching moment from the power calculation and minimizing the pitching moment in the optimization

Minimizing the Pitching Moment

The presence of an aerodynamic pitching moment, either positive or negative, is generally undesired from structural point of view. Also in order to overcome the low manufacturability of the newly created airfoils, it is chosen to optimize for a (absolute) pitching moment as low as possible. This results in airfoils which still have a high thickness close to the leading edge, combined with a very small amount of negative (reflex) camber near the trailing edge to overcome the positive moment coefficient contribution of the overall positive camber. The resulting airfoil is shown in black in figure 2.

4 Conclusions

The use of a viscous-inviscid combination to determine the performance of large scale VAWTs is suitable to be incorporated in a generic airfoil optimization procedure. Studying the outcome of the optimizations with different cost functions provides insight in the airfoil features that influence the performance of the VAWT.

A large thickness, especially close to the nose, has a beneficial effect on the VAWT performance, also adding to the manufacturability of large scale blades.

A positive pitching moment coefficient can provide an increase of the rotor torque. This positive moment can be achieved by adding reflex camber near the trailing edge.

This aim can result in airfoil shapes which are difficult to manufacture, and have strong aerodynamic pitching moment loadings, possibly unwanted from structural point of view.
In order to avoid strong aerodynamic pitching moments, the use of reflex camber should be limited to counteracting the negative pitching moment associated with a positive main camber.

REFERENCES

[1] P.C. Klimas. Tailored Airfoils for Vertical Axis Wind Turbines. Sandia Report, SAND84-1062, 1984.

[2] Flowind Corp. Final Project Report: High Energy Rotor Development, test and evaluation. Sandia Report SAND96-2205, 1996.

[3] M. Islam, D. S-K. Ting and A. Fartaj. Design of a Special-purpose Airofoil for Smaller-Capacity Straight-Bladed VAWT. Wind Engineering Volume 31, no.6, 401-424, 2007.

[4] Y. Sun, L. Zhang. Airfoil Optimization of Vertical-axis Turbines Based on CFD Method. Second Intern. Conf. on Computer Modeling and Simulation, 2010.

[5] C. Simão Ferreira. The near wake of the VAWT, 2D and 3D views of the VAWT Aerodynamics. PhD dissertation, TUDelft, 2009

A Low Order Numerical Model of the Inherent Wake Inside an Infinitely Long Row of Wind Turbines.

Søren Andersen, Jens Nørkær Sørensen, and Robert Mikkelsen
Department of Mechanical Engineering, Fluid Section, Building 403,
Technical University of Denmark, DK-2800 Lyngby Denmark
E-mail: {sjan, jns, rm}@mek.dtu.dk

Keywords: Wind Farms, Wake Model, CFD, POD

INTRODUCTION

In large wind farms, both onshore and offshore, the clustered wind turbines will operate in the wake of the upstream turbines irrespective of the wind direction. A wind turbine operating in the wake of one or more wind turbines yields less power and at the same time increased fatique loadings are exerted on the turbine from the induced turbulence. As wind farms get bigger, there is an increased demand for detailed knowledge and understanding of the interaction of the combined wake effects from multiple wind turbines inside wind farms. Several analytical wake models exist e.g. Jensen [6] and Frandsen [3]. Genereally, these models does not include the dynamic wake interaction.

The wake interaction in wind farms have also been studied using CFD and Large Eddy Simulation (LES) combined with Actuator Disc and Line methods. The Navier-Stokes based actuator disc method was introduced by Sørensen and Myken [9] to simulate axisymmetric flows around wind turbines. An extension to full 3-dimensional flows was later introduced as the Actuator Line technique (ACL) developed by Sørensen and Shen [10]. The actuator disc and line methods were implemented in the CFD modelling code, EllipSys3D, by Mikkelsen [8]. Previously, in their PhD work, Troldborg [12] and Ivanell [5] used the actuator line technique to simulate single and multiple wind turbines clustered in wind farms. These simulations have given valuable insigts into the wake dynamics, but demand long run times unfit for running numerous cases e.g. to optimize farm layout.

The tradeoff between including the complex dynamics of the resolved flow and computational speed is therefore still a pending issue when applying wake models for wind farm optimization. The present work seeks to construct a model which achieves both goals.

METHODS

Numerical simulations are performed using EllipSys3D, a finite-volume, multi-block general purpose Navier-Stokes solver, see Michelsen [7] and Sørensen[11]. A LES turbulence model using a Smagorinsky mixed scales model is used for turbulence closure. ACL introduces body forces in the flow domain along the turbine blades. These body forces are derived from Flex5 and 2D airfoil data corrected for 3D effects. Flex5 is an aeroelastic code for calculating loads on wind turbines, see e.g. Øye [13]. The introduction of local body forces along the blades enables the ACL method to resolve both the tip and root vortices without having to resolve the flow inside the boundary layers over the blades, which would demand a full DNS. The wind turbine is modelled as the three bladed NM80 turbine, also known as the Tjæreborg turbine with a blade length of $40m$. A controller is implemented for the turbine which is a combination of a generator power controller for small wind speeds($< 12m/s$) and a PI-pitch angle controller for higher wind speeds, as described by Hansen et al. [4].

The wake interaction is examined in an idealized case of an infinitely long row of turbines with uniform inflow of $10m/s$ and no atmospheric boundary layer and no ambient turbulence, thereby enabling the study of the inherent turbulence generated by the wind turbines alone. The domain consists of a 54 block structure in a Cartesian grid with a total of approximately $6 \cdot 10^6$ grid points. Each rotor blade is resolved by 19 grid points. The domain is $20R \times 20R \times 10R$ in X, Y, Z respectively.

The domain is sufficiently large($A_{domain} > O(100A_{turbine})$) to have far field boundary conditions on the transverse and vertical boundaries. Cyclic boundaries are applied in the flow direction, i.e. between the inflow and outflow, thereby reducing the domain to a single turbine. The cyclic boundary conditions essentially constitute a model of a wind turbine located in the middle of an infinitely long row of wind turbines. Hence, the distance between the individual wind turbines equals the domain length, $10R$. The turbine(s) introduce turbulence into the flow for each turnaround, untill the turbulence statistics have converged, thereby making it possible to study the inherent turbulence of the turbines. The turbulence is assumed to have converged once the turbulent flow has approached a stationary random process. Once the turbulent properties have converged, 2000 vertical slices of the three velocity components are extracted immediately upstream the wind turbine for an area covering a circle with $2.5R$ with a grid resolution of 93×93. These slices depict the incoming flow as experienced by the next turbine. The

2000 slices are equivalent of one full turnaround, i.e. the free stream velocity flows through the domain once.

The low order model is constructed from a double Fourier transform and a Proper Orthogonal Decomposition of the velocity components in these slices. The double Fourier transform is applied to span the temporal and azimuthal variations in Fourier space assuming periodicity in both directions. The POD is then applied to the complex Fourier coefficients, as outlined by Citriniti and George [2]. POD is a statistical method yielding an optimal linear subspace, optimal in terms of the variance of the energy content. POD is a proven method for examining large coherent structures from stationary random processes, see Berkooz et al. [1]. It is important to note that these individual structures or POD modes might not be physical structures in the sense that they are visible to an observer, but merely a result of the mathematical operations lumping the energy content into an optimal set of modes.

So to recap, the idea behind the low order model is to decompose the temporal and azimuthal dependancies through Fourier modes and the radial dependancies in the POD modes. It is then possible to reconstruct the flow field capturing the most important spatial and temporal flow structures by using an optional number of Fourier and POD modes. The low order model consists of a triple-sum, given as:

$$u(r,\theta,t) \approx (\hat{u}(r,m,f) = \sum_{f=0}^{F-1}\left(\sum_{m=0}^{M-1}\left(\sum_{k=0}^{K-1}\hat{a}_k(m,f)\phi_i^k(r,m,f)\right)e^{i2\pi m\theta}\right)e^{i2\pi\frac{ft}{T}}\right) \quad (1)$$

where F, M, and N are the number of temporal Fourier, azimuthal Fourier and POD modes respectively. $\hat{a_k}$ are the POD coefficients and ϕ are the POD eigenfunctions. The model incorporates all three velocity components, but only the streamwise velocity is shown in the following analysis.

Results

A snapshot in time reveals a complex flow pattern, see Figure 1, which shows the streamwise velocity $10R$ downstream. The inplane velocity is indicated with vectors and the rotor position is outlined. Larger flow structures are clearly seen, but the counterclockwise rotation initiated by the rotor is no longer dominant in the complex flow field.

Figure 2 shows the turbulent kinetic energy content at hub height as function of the number of time step, and applying a filter reveals how the flow approaches a stationary random process. The vertical lines indicate where the slices are extracted.

$10R$ downstream is in the intermediate region between near and far wake. The turbulent kinetic energy spectrum clearly

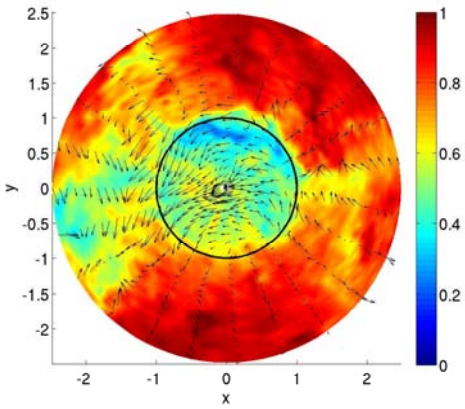

Figure 1: Instantaneous snapshot of the flow $10R$ downstream the rotor. Contours show streamwise velocity and vectors show lateral and vertical velocity components.

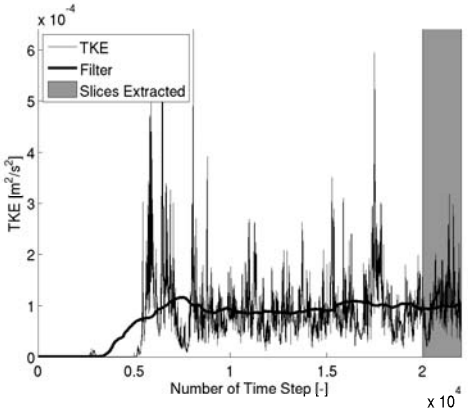

Figure 2: TKE and filtered TKE with extracted period.

reveals the 3P and the higher harmonics from the blade passings, see Figure 3. The turbulent kinectic energy spectrum is averaged over both radial and azimuthal directions, but reveals the same behaviour at each point in space.

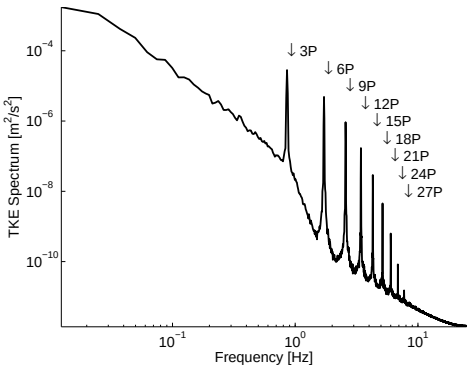

Figure 3: Turbulent Kinetic Energy spectrum averaged azimuthally and radially.

Figure 4 shows the cummulated and normalized value of the first 100 POD modes of the total 2000. It shows how 99.11% of the variance is included for $k = 50$.

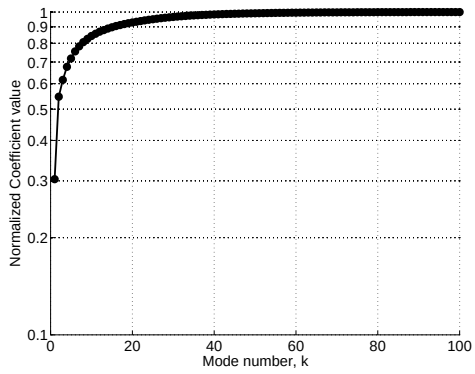

Figure 4: Normalized and cummulated POD coefficients for the first 100 modes.

Figure 5 shows the absolute value of the Fourier coefficients and the reconstructed Fourier coefficients using only the first 1,5 and 20 modes. The figure shows coefficients for U components. Clearly, the main features of the temporal and azimuthal coefficients are reconstructed well, using only a limited number of POD modes. Furthermore, it is evident that there are a limited number of important modes in the temporal Fourier coefficients, while a larger range needs to be included for the azimuthal modes.

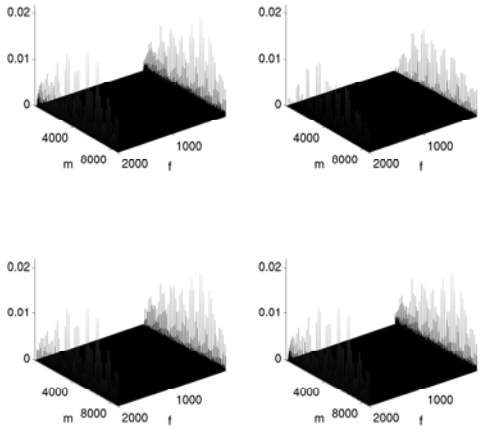

Figure 5: a): Absolute Fourier coefficients for U-velocity as function of azimuthal (m) and frequency (f) modes. b)-d): Reconstructed Fourier Coefficients with 1, 5 and 20 POD modes, respectively.

Figure 6 shows the reconstructed flow field at the same time as Figure 1. The three first figures (6(a)-6(c)) have been reconstructed using the largest 20 Fourier modes in time, all the azimuthal Fourier modes and the first 1,5, and 20 POD modes, respectively. The POD modes reconstruct 30%, 77%, and 97% of the variance of the temporal and azimuthal Fourier coefficients, as seen in Figure 4. Figure 6(d) shows the fully reconstructed flow with 200 POD modes and all 93 modes in both temporal and azimuthal directions. All four clearly resembles the general flow field from the CFD result, Figure 1, and an increasing amount of dynamic complexity as the number of modes increase.

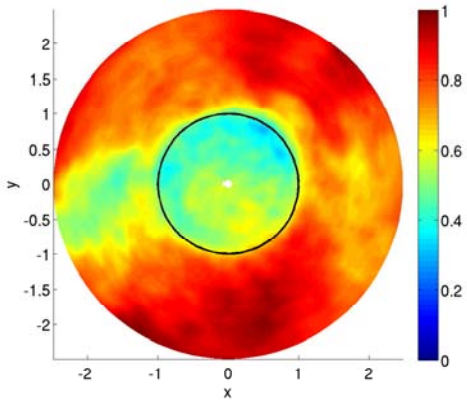

(a) K = 1, M = 93, F = 20.

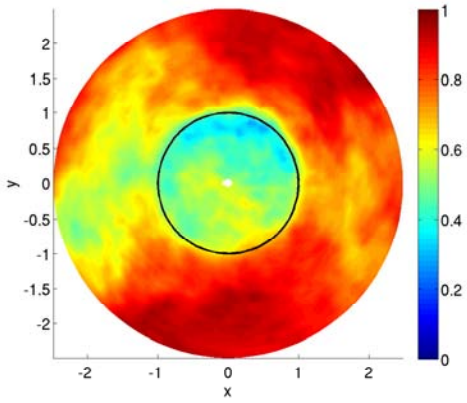

(b) K = 5, M = 93, F = 20.

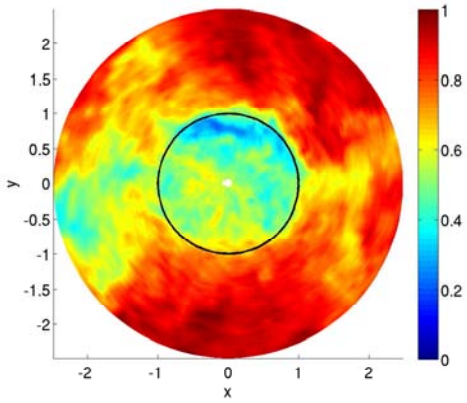

(c) K = 20, M = 93, F = 20.

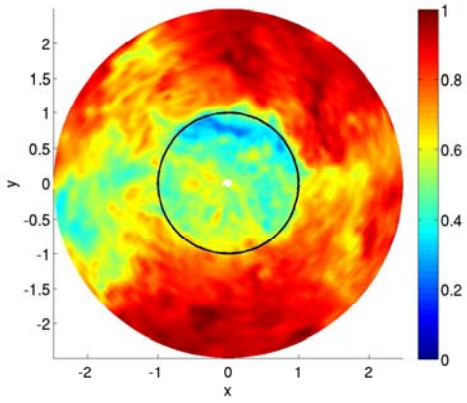

(d) K = 200, M = 93, F = 93.

Figure 6: Reconstructed flow field for various number of modes included.

CONCLUSION

CFD computations have been ussed to simulate the wake interactions deep inside a large wind farm. The flow develops in complexity until the flow reaches a stationary random process. Despite the highly turbulent flow deep inside the wind farm, the blade passing and higher harmonics of the blade passings are still very clear in the incoming flow of the next wind turbine.

The CFD results have been used to construct a low order model of the incoming flow, which can reconstruct the main features of the incoming flow. The decomposition reveals a large dependancy on azimuthal Fourier modes, and less on the radial and temporal modes. However, the flow field is clearly reconstructed using only a limited number of modes. The reconstructed flow field can subsequently be used for optimization purposes where there is a demand for fast computation of the dynamic behaviour of the incoming flow to be used in conjuction with an aeroelastic code, such as Flex5.

REFERENCES

[1] Berkooz, G., Holmes, P., and Lumley, J. L. The Proper Orthogonal Decomposition in the Analysis of Turbulent Flows. Annu. Rev. Fluid Mech. 1993, 25:539-75.

[2] Citriniti, J.H., and George, W.K. Reconstruction of the Global Velocity Field in the Axisymmetric Mixing Layer Utilizing the Proper Orthogonal Decomposition. J. Fluid Mech. 2000, vol. 418, pp. 137-166.

[3] Frandsen, S. and Barthelmie, R. and Pryor, S. and Rathmann, O., and Larsen, S. and Højstrup, J. and Thøgersen, M. Analytical modelling of wind speed deficit in large offshore wind farms. Wind Energy, vol. 9, 2006.

[4] Hansen, M.H., Hansen, A., Larsen, T.J., Øye, S., Sørensen, P., and Fuglsang, P. Control Design for a Pitch-Regulated, Variable Speed Wind Turbine. Risø-R-1500, , RisøNational Laboratory, Roskilde, Denmark, 2005.

[5] Ivanell, S. S. A. Numerical computations of wind turbine wakes. PHD KTH, Mechanics, 2009.

[6] Jensen, N. O. A Note on Wind Generator Interaction. Risø-M-2411, 1983.

[7] Michelsen, J. A. Basis3D-a platform for development of multiblock PDE solvers. Report AFM 92-05, Dept. of Fluid Mechanics, DTU, 1992

[8] Mikkelsen, R. Actuator Disc Methods Applied to Wind Turbines. MEK-FM-PHD, DTU, 2003.

[9] Sørensen, J. N. and Myken, A. Unsteady actuator disc model for horizontal axis wind turbines. J. Wind Eng. Ind. Aerodyn., vol. 39, 1992.

[10] Sørensen, J. N. and Shen, W. Z. Numerical modelling of Wind Turbine Wakes. Journal of Fluids Engineering, vol. 124, 2002.

[11] Sørensen, N. N. General Purpose Flow Solver Applied to Flow over Hills. PhD, Risø-R-827(EN), RisøNational Laboratory, Roskilde, Denmark, 1995.

[12] Troldborg, N. Actuator Line Modeling of Wind Turbine Wakes. MEK-FM-PHD, DTU, 2008.

[13] Øye, S. Flex4 simulation of wind turbine dynamics. Proceedings of 28th IEA Meeting of Experts Concertning State of the Art of Aeroelastic Codes for Wind Turbine Calculations. Available through International Energy Agency.

Session 2B

Wind Turbine Structural Design and Materials II

Adaptive Trailing Edge Flaps for Active Load Reduction

Leonardo Bergami
Wind Energy Division, Ris DTU - National Laboratory for Sustainable Energy,
VEA-118, Frederiksborgvej 399, 4000 Roskilde, Denmark
E-mail: leob@risoe.dtu.dk

Keywords: smart rotors, ATEF, active load control

1 Introduction

The size of modern utility-scaled horizontal-axis wind turbines shows a continuously increasing trend. As the rotor size increases, the loads affecting the wind turbine scale up, not only as an effect of the increased mass of the structure, but also as a consequence of larger variations in the flow field spanned by the wind turbine blades; such variations originate, for instance, from atmospheric turbulence, wind shear, tower shadow, and wakes from other turbines.

Future generations of wind turbines would benefit from, and maybe necessitate, a control system able to alleviate the loads on the structure, for instance, by, for instance, actively controlling the aerodynamic forces along the blades so to compensate for variations in the flow field.

The concept is known as *smart rotor*: the active control system collects information on the current wind turbine state through different *sensors*, the informations are then processed by a *control algorithm*, and sent to *actuators* modifying the aerodynamic forces along the blade.

Several institutions in Europe and US are investigating smart rotor potentialities [1, 2], and different control strategies and actuator devices have been proposed. Some solutions point at using already existing actuators, as the pitch system, and integrate it with sensors and control algorithms so to control each blade pitch individually [3]. Other studies propose to use actuators that modify the aerodynamic forces locally along the blade span, as, for instance, micro-tabs[4], rotating flaps, or adaptive trailing edge flaps [5, 6].

The current work focuses on an adaptive trailing edge flap (ATEF) active control system, where the flap actuator deflects the aft part of the airfoil section by applying a smooth and continuous deformation shape to the airfoil camber line. Compared to a classic rotating flap, the continuous deformation shape results in better lift over drag performances, and lower noise emissions.

The paper briefly presents the aerodynamic model for lift, drag and moment on an airfoil undergoing arbitrary motion and flap deflection. In the following section, indications on the design process and requirements to the active flap control system are retrieved from a preliminary load analysis on the NREL 5-MW wind turbine in its baseline configuration [7]. Future work will then aim at designing an active flap control solution for the studied wind turbine, and assess the benefits of the active control system on the overall loading conditions.

2 Model and Method

The presence of active flap devices poses new challenges in the modeling of the aerodynamic forces that generates along the wind turbine blades. CFD tools like Reynolds Averaged Navier Stokes (RANS) solvers provide accurate solutions, but the computation requirements are still too demanding for the tool to be efficiently integrated in an aeroelastic simulation tool.

Most simulation tools used to compute the aeroelastic response of a wind turbine in the time domain are based on implementations of the Blade Element Method (BEM) [8]. Under the BEM assumption of independent annular elements on the rotor plane, the rotor aerodynamic is determined from the lift and drag forces along the blades; the aerodynamic forces are then computed independently for each 2D airfoil section in which the blade has been discretized into.

This work presents an aerodynamic model to compute lift, drag, and moment coefficients for an airfoil section equipped with an Adaptive Trailing Edge Flap. The model reproduces both steady and dynamic characteristics of the forces on the airfoil undergoing arbitrary (within the limits of plane wake assumption) motion and flap deflection. The dynamic effects reproduced by the model can be split into three categories.

Added mass effects, or *non-circulatory* contributions, describe the forces that arise simply as a reaction of the fluid accelerated by the airfoil (or the flap) motion. The term has no memory effects, and only depends on the instantaneous motion of the airfoil or flap.

Effects from *wake dynamics*, or *potential flow* effects, describe the memory effects of the vorticity shed into the wake, following a change of the airfoil aerodynamic loading, as, for instance, due to a variation in angle of attack or flap deflection.

Dynamic stall effects represent the dynamics of the forces on an airfoil undergoing flow separation (stall).

2.1 Potential flow part

In this part of the model, the aerodynamic forces are computed assuming the airfoil always operates in fully attached flow conditions; viscous effects on the aerodynamic forces are thus neglected (potential flow assumption).

The deficiency, or time lag, on the lift force, caused by the vorticity shed into the wake, is modeled through an equivalent effective downwash speed, as in the model from Hansen et al. [9].

Gaunaa [10] shows that, under the assumptions of potential flow and thin-airfoil theory, the effective downwash speed for an airfoil undergoing arbitrary motion and camber line deformation can be evaluated as a superposition of indicial step responses. The indicial response function is expressed in an exponential form, similar to Jones's function for the flat plate response, thus allowing for an efficient time step integration algorithm.

The effective downwash speed is then split into an equivalent effective angle of attack α_{eff} and flap deflection β_{eff} contributions; the effective angle of attack and flap deflection are used in the look-up of the input steady data, returning thus aerodynamic forces that account for the wake memory effects.

2.2 Dynamic stall part

The flow separation part of the model follows the Beddoes-Leishmann dynamic stall formulation given in Hansen et al. [9]. The circulatory lift is expressed as a weighted sum of a fully attached and a fully separated contribution:

$$C_L^{\text{Circ.Dyn}} = C_L^{\text{att}} f^{dyn} + C_L^{\text{fs}}(1 - f^{dyn}). \tag{1}$$

The dynamics of the flow separation along the airfoil are described through the separation function f^{dyn}, which assigns the weight between the fully attached and the fully separated component. The value of the function depends on the potential flow lift, and on a steady separation function f^{st}.

The steady values of the separation function f^{st}, fully attached C_L^{att}, and fully separated C_L^{fs} lift coefficients are retrieved from the steady input data C_L^{st}. All the quantities are now function of both angle of attack and flap deflection, and their computation is not as straightforward as in the rigid airfoil case. The computations are performed in an external 'preprocessing unit', which allows the user to check, and, eventually, correct the steady data that will be used as input in the aerodynamic model.

In the preprocessing unit, the steady state input lift C_L^{st} is split into a fully attached and a fully separated contribution, assuming that the fully attached part has a linear dependency on both angle of attack α and flap deflection β:

$$C_L^{lin} = \frac{\partial C_L}{\partial \alpha}(\alpha^{st} - \alpha_0) + \frac{\partial C_L}{\partial \beta}\beta^{st}. \tag{2}$$

The steady separation function is then computed from the expression for the flat-plate lift in Kirchoff flow, as:

$$f(\alpha,\beta)^{\text{st}} = \left(2\sqrt{\frac{C_L^{st}}{C_L^{lin}}} - 1\right)^2. \tag{3}$$

The separation function should be real and bounded $0 \leq f^{\text{st}} \leq 1$, thus singularities arise whenever $C_L^{st}/C_L^{lin} < 0$ or $C_L^{st}/C_L^{lin} > 1$. The singularities are avoided by simply rounding the function to the closest boundary value; further 'manual adjustments' will need to be applied by the user to avoid discontinuities in the lift coefficient and separation function input data.

Once the separation function f^{st} is determined, three flow regions are identified.

Fully attached region, where the separation function is $f^{st} = 1$. Here, C_L^{att} is taken equal to C_L^{st}, rather than C_L^{lin}, so to maintain the steady lift coefficient equal to the input one:

$$f^{st} = 1 \quad \rightarrow \quad \begin{cases} C_L^{att} = C_L^{st} \\ C_L^{fs} = C_L^{st}/2 \end{cases}; \tag{4}$$

Fully separated region, where the separation function is $f^{st} = 0$:

$$f^{st} = 0 \quad \rightarrow \quad \begin{cases} C_L^{fs} = C_L^{st} \\ C_L^{att} = C_L^{lin} \end{cases}; \tag{5}$$

Transition region:

$$0 < f^{st} < 1 \quad \rightarrow \quad \begin{cases} C_L^{att} = C_L^{lin} \\ C_L^{fs} = \frac{C_L^{st} - C_L^{lin} f^{st}}{1 - f^{st}} \end{cases}. \tag{6}$$

The model has been validated by comparison with RANS solutions for an airfoil undergoing harmonic pitching motion and flap deflection, and it has been implemented in the multi-body aeroelastic simulation tool HAWC2 [11].

2.3 Method

The aeroelastic simulation tool HAWC2 is used to evaluate the aeroelastic response of the NREL 5-MW baseline wind turbine [7] in the time domain. A wide set of simulation conditions is outlined following the design load cases (DLC) prescribed by the IEC standard [12]; simulations include both stochastic, and deterministic wind fields inputs, normal operation and extreme events. The resulting simulated loads are summarized in terms of ultimate loads, and equivalent fatigue loads.

The equivalent fatigue loads are computed from the simulated time series by applying a Rain Flow Counting algorithm, and Palmgren-Miner rule for linear fatigue damage. The equivalent fatigue loads account for the amount of time the wind turbine is expected to spend in each simulated condition. A relative fatigue contribution k is evaluated as the ratio between the fatigue damage accumulated in a specific operation condition, and the total life-time fatigue damage.

3 Preliminary Load Analysis

A preliminary analysis is carried out on the NREL 5-MW baseline wind turbine. The analysis of the wind turbine in its baseline configuration allows to identify the DLC that are critical in terms of fatigue or ultimate loads. Active load alleviation in these specific cases would directly benefit the whole wind turbine structure. The critical cases provide thus a convenient set of simulation conditions for designing, testing, and assessing the performances of the active load control system.

Fatigue loads have been monitored at the blade root, in flapwise (M_x), edgewise (M_y), and torsion (M_z), at the tower base flange in fore-aft (M_{FA}) and side-to-side (M_{SS}) directions, and for the main shaft torsion (M_{DT}).

Relative contributions to the total life-time fatigue damage are grouped according to the operation condition that has generated the fatigue damage, figure 1. Operations in normal power production (DLC 1.1) are responsible for most of the fatigue loads on the structure, mainly because of the time the turbine is expected to spend in these conditions. Therefore, an active load alleviation system operating during normal power production can yield to a sensible reduction of the overall fatigue damage.

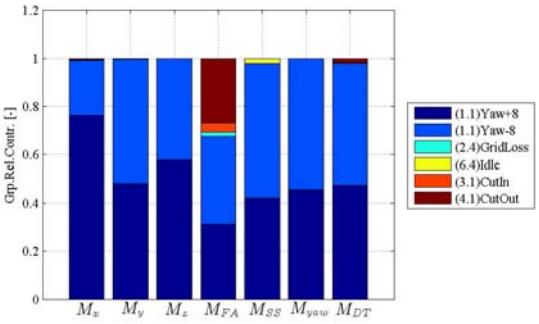

Figure 1: Fatigue damage relative contributions grouped by operation condition.

The same load-measuring locations are used to monitor ultimate loads; the maximum loads reported in each operation condition are plotted in figure 2. The highest simulated loads occur for operations under an extreme coherent gust (DLC 2.3), extreme turbulence (DLC 1.3), or extreme coherent gust with direction change (DLC 1.4). These cases should be thus considered during the design process of the active load control system, since a reduction of these maximum loads might yield a beneficial reduction of the overall structural requirements.

To obtain an overview on which frequency range the active control should focus on, an attempt is made to determine which frequencies returns the highest fatigue load contributions. A frequency spectrum is retrieved from the simulated loads, and Benasciutti and Tovo's [13] method is applied to

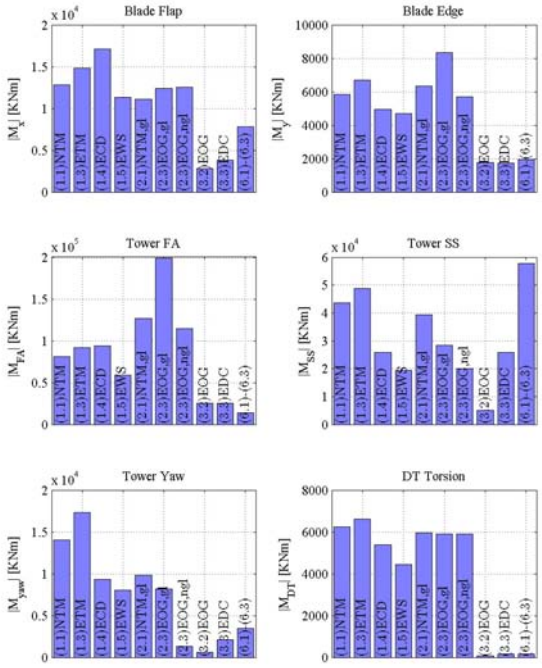

Figure 2: Ultimate load analysis. Maximum loads reported in each simulation condition.

obtain an equivalent fatigue damage rate from the load spectrum. The relative contribution from each frequency range is determined by setting to zero its spectral energy content and comparing the resulting fatigue damage rate with the original-full spectrum fatigue damage.

The result is presented as a 'fatigue-spectrogram' plot, figure 3, where the relative contributions to fatigue damage depend on both frequency and wind speed; red colors indicate higher fatigue contributions. The relative contributions from different wind speeds account for the time each wind speed bin is expected to occur.

For the blade flapwise root moment, figure 3, the largest fatigue contributions originate at high wind speeds, and from frequencies close to 1P (and its harmonics). Furthermore, both for blade and tower loads (not shown here), frequencies above 5 Hz yield only a modest contribution to the overall fatigue damage.

To conclude, the preliminary load analysis allows to identify a set of load cases which are critical in terms of either fatigue or ultimate loads. This reduced set of cases provides a convenient test field for the future design of the active control system, as load alleviation in these design cases would yield a direct benefit on the overall loading conditions.

Fatigue analysis in the frequency domain have highlighted that the highest contributions to the fatigue damage originates from loads with frequencies below 5 Hz, giving thus

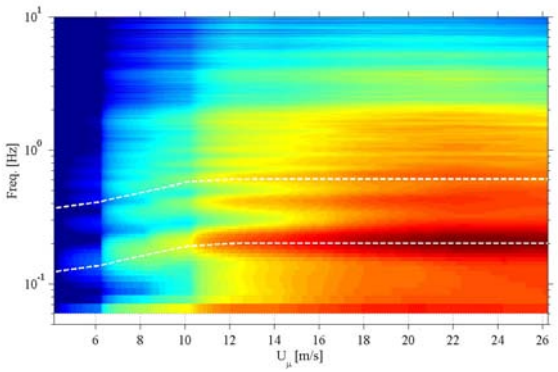

Figure 3: Fatigue analysis in the frequency domain. Blade flapwise root moment, relative contribution to the total fatigue damage from different frequencies and wind speeds.

a clear indication on the frequency range the active control system should focus on.

4 Future work: Active load control

An active load control system will be designed for the NREL 5-MW reference wind turbine, using Adaptive Trailing Edge Flaps actuators, and structural loads sensors. First, the placement of the ATEF sections along the blade span needs to be optimized, accounting for factors as the flap effect on the measured loads, time delay, and structural constraints.

Once the flap positions have been fixed, the ATEF control algorithm is designed; the requirements outlined in the previous analysis, as well as the critical set of load cases will help in the design process. The control algorithm will most likely be a Model Predictive Control, and system identification techniques will be investigated in order to obtain the linear model required by the MPC controller.

The flap actuators and the active load control algorithm will be included in the aero-servo-elastic model of the NREL 5-MW wind turbine, and simulation will be performed with the HAWC2 code. As in the preliminary analysis, simulation conditions will be based on the design load cases prescribed in the IEC standard [12], and the loads will be evaluated in terms of equivalent fatigue loads and ultimate loads.

A comparison of the fatigue and ultimate loads resulting from simulations with and without active flap control will directly measure the impact of the ATEF system on the overall turbine loading conditions; as well as that, the comparison will bring new elements to be considered in the (ineluctably iterative...) design process. Finally, the comparison between flap and baseline configurations will allow to quantify the potential of the ATEF system for active load alleviation on MW-sized wind turbines.

References

[1] T. K. Barlas and G. van Kuik. State of the art and prospectives of smart rotor control for wind turbines. *Journal of Physics: Conference Series*, 75(1):012080 (20 pp.), 2007. Journal Article.

[2] Matthew A. Lackner and Gijs van Kuik. A comparison of smart rotor control approaches using trailing edge flaps and individual pitch control. *Wind Energy*, 13(2-3):117–134, March 2010.

[3] T. J. Larsen, H. A. Madsen, and K. Thomsen. Active load reduction using individual pitch, based on local blade flow measurements. *Wind Energy*, 8(1):67–80, 2005. Journal Article.

[4] Scott J. Johnson, Jonathon P. Baker, C. P. van Dam, and Dale Berg. An overview of active load control techniques for wind turbines with an emphasis on microtabs. *Wind Energy*, 13(2-3):239–253, March 2010.

[5] Peter Bjoern Andersen, Lars Henriksen, Mac Gaunaa, Christian Bak, and Thomas Buhl. Deformable trailing edge flaps for modern megawatt wind turbine controllers using strain gauge sensors. *Wind Energy*, 13(2-3):193–206, March 2010.

[6] A. W Hulskamp, J. W van Wingerden, T. Barlas, H. Champliaud, G. A. M van Kuik, H. E. N Bersee, and M. Verhaegen. Design of a scaled wind turbine with a smart rotor for dynamic load control experiments. *Wind Energy*, 14(3):339–354, April 2011.

[7] J. Jonkman, S. Butterfield, W. Musial, and G. Scott. Definition of a 5-MW reference wind turbine for offshore system development. Technical Report NREL/TP-500-38060, National Renewable Energy Laboratory (NREL), February 2009.

[8] Martin Hansen. *Aerodynamics of wind turbines : rotors, loads and structure*. James & James, London, 2000.

[9] Morten Hartvig Hansen, Mac Gaunaa, and Helge Aagaard Madsen. A Beddoes-Leishman type dynamic stall model in state-space and indicial formulations. Technical Report R-1354(EN), Risoe National Laboratory, Roskilde (DK), 2004.

[10] M. Gaunaa. Unsteady two-dimensional potential-flow model for thin variable geometry airfoils. *Wind Energy*, 13(2-3):167–192, 2010.

[11] Torben Juul Larsen. How 2 HAWC2 the user's manual. Technical Report R-1597(EN), Risoe National Laboratory. Technical University of Denmark, 2009.

[12] International Electrotechnical Commission. IEC 61400-1: Wind turbines part 1: Design requirements. Technical report, International Electrotechnical Commission, 2005.

[13] D. Benasciutti and R. Tovo. Comparison of spectral methods for fatigue analysis of broad-band gaussian random processes. *Probabilistic Engineering Mechanics*, 21(4):287–299, October 2006.

Internal resonances and modal interactions of nonlinear free and forced vibrations of 3D rotating beams

Stoykov S., Ribeiro P.
DEMec/IDMEC, Faculdade de Engenharia, Universidade do Porto
R. Dr. Roberto Frias, s/n, 4200-465 Porto, Portugal
E-mail: {stanislav.stoykov, pmleal}@fe.up.pt

Keywords: nonlinear vibration; steady-state response; stability of periodic solutions; bifurcation diagrams.

1 INTRODUCTION

The dynamic analysis of rotating beams has been investigated by many researchers because of its importance of various engineering structures such as helicopter blades, wind turbines, robot arms, etc. Structural problems in wind turbines have obtained increasing attention due to the trend towards larger, lighter and more flexible structures. As the length of the turbine blade increases and its weight decreases, large vibration amplitudes become more frequent. These vibrations violate the small displacements assumption and give rise to a nonlinearity known as geometrical nonlinearity. Unlike in linear systems, in geometrically nonlinear systems the frequency of vibration and its mode shape change with the amplitude of vibration. Therefore, the natural frequency may become commensurable with other frequency of the system and internal resonance may appear.

Many studies exist on investigation of the bending linear natural frequencies of rotating beams. Hodges and Rutkowski [1] analysed free vibrations of rotating beams by a variable finite element method. Bazoune and Khulief [2] investigated the free linear vibrations of rotating uniform and tapered beams. The effects of rotational speed, hub radius, setting angle, taper parameters on the natural frequencies were investigated for flapwise and lagwise vibrations. Lin and Hsiao [3] derived the differential equations of rotating beam showing the effect of Coriolis force on the natural frequencies. Considering the research of nonlinear models, Pesheck at al. [4] derived a reduced model for rotating beams using the nonlinear normal modes. The derived method is able to catch internal resonances between two transverse and transverse and axial modes. Turhan and Bulut [5] investigated the lagwise vibrations of rotating beams including geometric nonlinearities. The authors revealed that the rotating speed may change the behaviour from hardening to softening. Younesian and Esmailzadeh [6] analysed nonlinear flapwise vibrations of rotating beams with variable speed. The effect of acceleration and deceleration rates on the vibration amplitude was investigated. In what concerns 3D beam models, Bazoune at al. [7] investigated spinning tapered beams considering bending, axial and torsional displacements. Ozgumus and Kaya [8] developed a bending-torsional model for double tapered beams considering only flapwise bending displacements.

In the current work, the nonlinear vibrations of 3D beam which rotate in one plane are investigated by a *p*-version finite element method. The nonlinearity is taken into account considering nonlinear strain-displacement relations and more nonlinear terms appear from the inertia forces due to the rotation of the beam. The model is based on Timoshenko's theory for bending and Saint-Venant's for torsion. Employing the harmonic balance method, the differential equation of motion is converted into a nonlinear algebraic form and then solved by a continuation method. The variation of the amplitude of vibration with the frequency of vibration is determined and presented in the form of backbone curves. Coupling between modes is investigated, internal resonances are found and the ensuing multimodal oscillations are described. Some of the couplings discovered lead from planar oscillations to oscillations in the three dimensional space.

2 MATHEMATICAL MODEL

Beams with rectangular cross section, uniform thickness and elastic, homogeneous and isotropic materials are considered. The beam may vibrate in any direction and it rotates with a constant speed in a fixed plane. Two coordinate systems are considered: one is fixed and the other rotates; the latter presents the rotational motion of the beam and will be called "transport coordinate system". The centers of both coordinate systems coincide. Let the speed of rotation be Ω, the fixed coordinate system is denoted by $S_0(X,Y,Z)$and the transport coordinate system by $S_1(x,y,z)$ Figure 1.

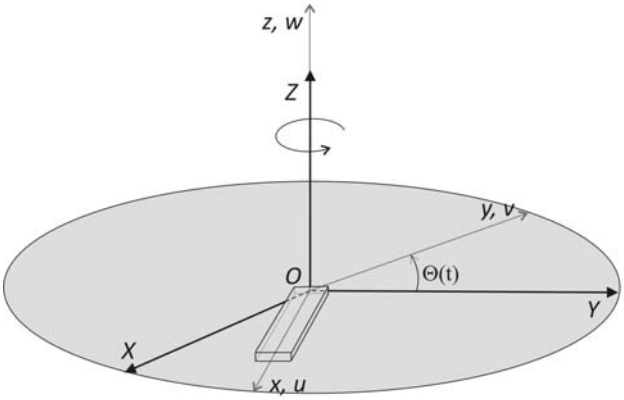

Figure 1: Axes and displacements of the rotating beam model.

The deformation of the beam is expressed in the transport coordinate system by displacement components u, v and w respectively for longitudinal, transverse along y and transverse along z. These displacements are functions of time and space coordinates and are based on Timoshenko's theory for flexure and Saint-Venant's theory for torsion:

$$\begin{aligned} u(x,y,z,t) &= u_0(x,t) - y\,\varphi_z(x,t) + z\,\varphi_y(x,t) \\ &\quad + \psi(y,z)\,\frac{\partial \theta_x}{\partial x}(x,t) \\ v(x,y,z,t) &= v_0(x,t) + y\cos\big(\theta_x(x,t)\big) - y \\ &\quad - z\sin\big(\theta_x(x,t)\big) \\ w(x,y,z,t) &= w_0(x,t) + y\sin\big(\theta_x(x,t)\big) \\ &\quad + z\cos\big(\theta_x(x,t)\big) - z \end{aligned} \tag{1}$$

where v_0 and w_0 are the transverse displacements on the middle line of the beam in the y and z directions respectively, u_0 is the longitudinal displacement on the middle line, θ_x is the rotation of the cross section about the longitudinal axis x, φ_y and φ_z denote rotations of the cross section about the y and z axes, respectively and $\psi(y,z)$ is the warping function.

The relative displacements of the beam are expressed in the transport coordinate system, but the effect of the rotation of this system will be included in the equation of motion via the inertia forces. Let $P(x, y, z)$ be an arbitrary point of the beam expressed in the transport coordinate system before deformation. The absolute acceleration of point P is the acceleration of this point with respect to the fixed coordinate system. It is given by the following expression [9]:

$$\begin{aligned} \vec{a}_{P_{S0}} = \vec{a}_{P_{S1}} + \vec{\alpha}_{10} \times \overrightarrow{OP} + \vec{\omega}_{10} \times \left(\vec{\omega}_{10} \times \overrightarrow{OP}\right) + \\ + 2\vec{\omega}_{10} \times \vec{v}_{P_{S1}}, \end{aligned} \tag{2}$$

where $\vec{a}_{P_{S0}}$ is the absolute acceleration of point P, i.e. the acceleration of P with respect to S_0, $\vec{a}_{P_{S1}}$ is the relative acceleration of P, i.e. the acceleration of P with respect to S_1, $\vec{v}_{P_{S1}}$ is the relative velocity of P, $\vec{\omega}_{10}$ is the angular velocity of the transport coordinate system, $\vec{\alpha}_{10}$ is the angular acceleration of the transport coordinate system and $\overrightarrow{OP}$ is the position vector of P with respect to the centre of S_1. Furthermore,

$\vec{a}_{P_{S1}}$ presents the relative acceleration;

$\vec{\alpha}_{10} \times \overrightarrow{OP} + \vec{\omega}_{10} \times \left(\vec{\omega}_{10} \times \overrightarrow{OP}\right)$ presents the transport acceleration;

$2\vec{\omega}_{10} \times \vec{v}_{P_{S1}}$ presents the acceleration of Coriolis.

The virtual work of the internal forces remains the same as for non-rotating beam, it is given in [10] and here just the main concepts are shown. The axial and shear strains are derived from Green's strain tensor, but the longitudinal terms of second order are neglected. Hence, the direct and the transverse shear strains are:

$$\begin{aligned} \varepsilon_x &= \frac{\partial u}{\partial x} + \frac{1}{2}\left(\frac{\partial v}{\partial x}\right)^2 + \frac{1}{2}\left(\frac{\partial w}{\partial x}\right)^2 \\ \gamma_{zx} &= \frac{\partial w}{\partial x} + \frac{\partial u}{\partial z} + \frac{\partial v}{\partial z}\frac{\partial v}{\partial x} + \frac{\partial w}{\partial z}\frac{\partial w}{\partial x} \\ \gamma_{xy} &= \frac{\partial u}{\partial y} + \frac{\partial v}{\partial x} + \frac{\partial v}{\partial x}\frac{\partial v}{\partial y} + \frac{\partial w}{\partial x}\frac{\partial w}{\partial y} \end{aligned} \tag{3}$$

The stresses are related with the strains by Hooke's law and a shear correction factor is applied only to the bending terms as explained in [10].

The strains, the stresses and the absolute acceleration are expressed by the displacement components u, v and w which are expressed by the displacements on the middle line defined in (1). These displacements of the beam centroidal axis are expressed by shape functions and generalised displacements, following the p-version finite element formulation. Applying the principle of virtual work, the following equation of motion in time domain is obtained:

$$\begin{aligned} \mathbf{M}\,\ddot{\mathbf{q}} + \mathbf{CR}(\mathbf{q},\Omega)\,\dot{\mathbf{q}} + \mathbf{K}(\mathbf{q})\,\mathbf{q} + \mathbf{T}(\Omega)\,\mathbf{q} \\ = \mathbf{F} - \mathbf{R}(\Omega) \end{aligned} \tag{4}$$

where $\mathbf{M}$ is the mass matrix which is defined from the inertia forces related to the relative acceleration; $\mathbf{CR}(\mathbf{q},\Omega)$ is matrix which is defined from the inertia forces connected with the acceleration of Coriolis, it depends on the vector of generalized displacements and on the speed of rotation; $\mathbf{K}$ is the stiffness matrix, it is defined from the internal forces; $\mathbf{T}(\mathbf{q},\Omega)$ and $\mathbf{R}$ are a matrix and a vector, which are due to the transport acceleration; $\mathbf{F}$ is the vector of external forces, $\mathbf{q}$ is the vector of generalized displacements, which depends on time.

Periodic solutions will be investigated and the harmonic balance method applied. The equations of motion in space present both quadratic and cubic nonlinear terms and have terms related with velocity due to the acceleration of Coriolis. Thus, a series with constant term and even and odd harmonics with cosine and sine are selected. In this way an algebraic system of equations is obtained, with new unknowns, which are the coefficients of the harmonics and do not depend anymore on time. The time dependent generalised coordinates are replaced by their Fourier expansion, inserted in the equation of motion and the HBM is employed. The resulting equation of motion in the frequency domain is of the form:

$$\left(-\omega^2\,\mathbf{M}^{\mathbf{HBM}} + \omega\,\mathbf{CR}^{\mathbf{HBM}}(\mathbf{Q},\Omega) + \mathbf{K}^{\mathbf{HBM}}(\mathbf{Q}) + \right. \\ \left. + \mathbf{T}^{\mathbf{HBM}}(\Omega)\right)\mathbf{Q} = \mathbf{F}^{\mathbf{HBM}} - \mathbf{R}^{\mathbf{HBM}}(\Omega), \tag{5}$$

where $\mathbf{Q}$ is the vector with coefficients of the harmonics. The frequency domain equation of motion (5) is solved by the arc-length continuation method used. The method is composed of two main loops: in the external loop a predictor to the solution is defined and in the internal loop this predictor is corrected by Newton method.

3 RESULTS

At that point, an internal resonance of free vibrations of non-rotating beams is presented. It is shown than due to a bifurcation the plane bending vibration can evolve to vibration in space and then to vibration in the other plane. The beam is clamped-clamped with dimensions 0.02 × 0.0175 × 0.58 m. Figure 2 presents bifurcation diagrams of both transverse displacements (in *z* and *y* directions) and torsion. Computations were started at the first linear bending mode of vibration in the transverse direction *z*, from where a so called main branch develops. This main branch has several bifurcation points, but here only the bifurcation point found at $\omega/\omega_{l1} \approx 1.05$ is presented. From this bifurcation point starts a secondary branch related with bending of the beam in the both transverse directions and also with torsion. This secondary branch goes to a bifurcation point on another main branch, which has only bending in *y*, i.e. not in the plane in which the analysis was started. Torsion is only different from zero on the secondary branch, because of the bending-torsion coupling when both transverse displacements are excited. The second main branch to which the secondary branch leads is related with the vibration of the second bending mode of the beam in the other transverse direction and with the third harmonic. Actually, the first linear frequency of bending in *w* is ω_{wl1}=1676.44 rad/s and the second linear frequency of bending in *v* is ω_{vl2}= 5230.56 rad/s which explains the existence of the bifurcation point related with the third harmonic: $\omega_{vl2}/3 \approx 1.05\ \omega_{wl1}$.

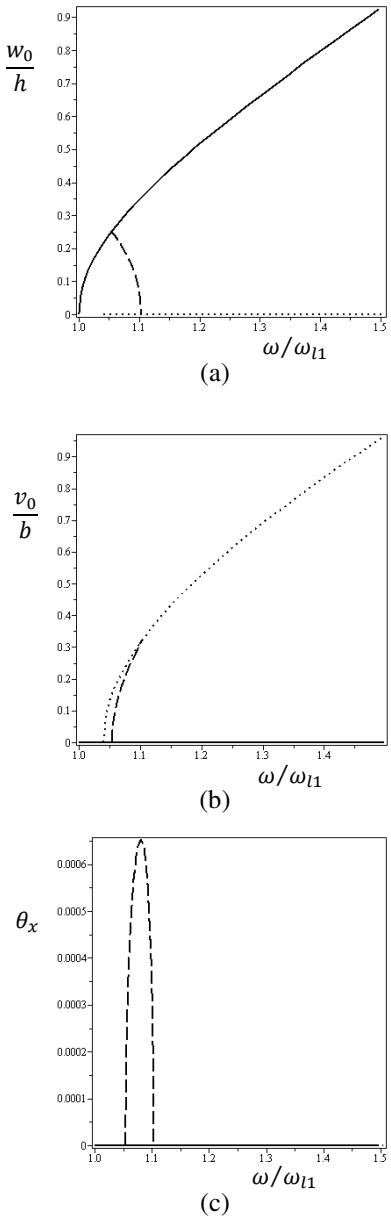

Figure 2: Bifurcation diagrams of first mode of bending; —— first main branch, · · · secondary branch, - - - second main branch. *h* – thickness of the beam, *b* – width, ω_{l1} – first linear natural frequency in bending in *z;* (a) Total amplitude measured in *z* direction, (b) Total amplitude measured in *y* direction, (c) Total torsion (the first main and the second main branches coincide).

4 CONCLUSIONS

The evolution of the natural mode shapes and natural frequencies of vibration, in a plane and in space, of rotating beams is analysed. The model employed, took into account geometrical nonlinearity in the stiffness and the inertia forces due to the rotation were included in the inertia terms. It was demonstrated that, due to the internal

resonance between modes in different transverse planes, secondary branches exist and they relate the nonlinear mode of vibration in one plane to the vibration mode in space or another plane.

REFERENCES

[1] Hodges D., Rutkowski M., Free-Vibration Analysis of Rotating Beams by a Variable-Order Finite-Element Method, AIAA Journal, Vol. 19, No. 11, November 1981.

[2] Bazoune A., Khulief Y., Further Results for Modal Characteristics of Rotating Tappered Timoshenko Beams, Journal of Sound and Vibration (1999) 219 (1), 157 – 174.

[3] Lin S., Hsiao K., Vibration Analysis of a Rotating Timoshenko Beam, Journal of Sound and Vibration (2001) 240 (2), 303 – 322.

[4] Pesheck E., Pierre C., Shaw S., Modal Reduction of a Nonlinear Rotating Beam Through Nonlinear Normal Modes, Journal of Vibration and Acoustics 124 (2002), 229-236.

[5] Turhan Ö., Bulut G., On Nonlinear Vibrations of a Rotating Beam, Journal of Sound and Vibration 322 (2009) 314-335.

[6] Younesian D., Esmailzadeh E., Non-linear Vibration of Variable Speed Rotating Viscoelastic Beams, Nonlinear Dyn (2010) 60 193-205.

[7] Bazoune A., Khulief Y. A., Stephen N. G., Mohiuddin M. A., Dynamic response of spinning tapered Timoshenko beams using modal reduction, Finite Elements in Analysis and Design 37 (2001) 199-219.

[8] Ozgumus O. O., Kaya M. O., Energy expressions and free vibration analysis of a rotating double tapered Timoshenko beam featuring bending-torsion coupling, International Journal of Engineering Science 45 (2007) 562-586.

[9] Shabana A. A., Dynamics of Multibody Systems, Cambridge University Press 2005.

[10] Stoykov S., Ribeiro P., Nonlinear forced vibrations and static deformations of 3D beams with rectangular cross section: The influence of warping, shear deformation and longitudinal displacements, International Journal of Mechanical Sciences 52 (2010) 1505-1521.

An Integrated Design Tool for Large Wind Turbine Blades

Lars Frøyd, Ole G. Dahlhaug
Vannkraftlaboratoriet, NTNU
Alfred Getz' Vei 4, 7030 Trondheim, Norway
E-mail: {lars.froyd,ole.g.dahlhaug}@ntnu.no

Keywords: Integrated design, wind turbine blades, aero-dynamic design, structural design.

ABSTRACT

This paper describes a new tool for integrated design of blades for horizontal axis wind turbines (HAWTs). The purpose of this design tool is to generate aeroelastic models of wind turbine blades based on a limited set of input parameters. This makes the design tool suited, for instance, for parametric studies of different wind turbine configurations at a conceptual stage. The output of the design tool is aerodynamic and structural properties of the blade that can be exported to e.g. time-domain aeroelastic simulation tools like FAST, HAWC2 and GH Bladed, as illustrated in Figure 1. The aerodynamic and structural design methods were explained in [1], and a practical design task was performed in [2]. The design tool is implemented in MATLAB.

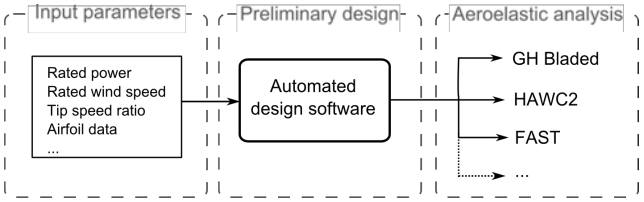

Figure 1: Visualisation of design software purpose

INTRODUCTION

The first generations of offshore wind turbines are designed more or less similar to onshore turbines, although the different environmental loads and less severe design constraints related to visual appearance and noise offshore may allow different turbine configurations like down-wind turbines, two-bladed turbines and higher tip velocities. The cost break-down offshore may also favour different turbine configuration, as the rotor cost is a relatively much smaller part of the total cost of the complete turbine: Small weight savings in the tower top (rotor or nacelle) may allow significant weight/cost reductions in the substructure. This may for instance suggest the use of lighter blades, which can be achieved by utilising more carbon fibre in the blades or a higher specific power (kW/m^2) rating.

Conceptual investigation of wind turbines are often carried out on wind turbine models using aero-elastic simulations, but creating suitable simulation models is work intensive. Even rescaling an existing turbine model is challenging due to dynamics and interactions. For parametric studies, a large number of models have to be created, and the tool is developed to reduce this effort. The design method is limited to pitch controlled HAWTs with three-bladed rotors, but still covers the most relevant design space for offshore wind turbines.

OVERVIEW OF DESIGN SOFTWARE

The design process follows a linear approach, starting with the aerodynamic design and continuing afterwards with the structural design as illustrated in Figure 2.

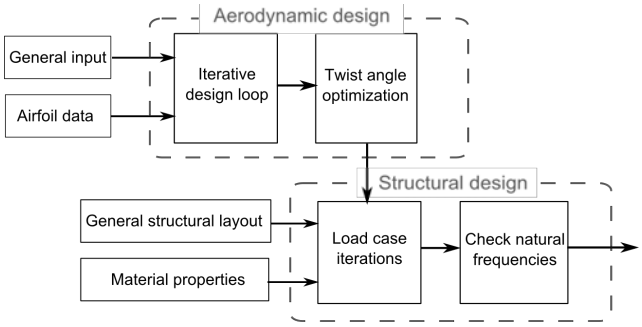

Figure 2: Design software flow diagram

This means that there currently is no feedback loop where the aerodynamic design can be modified based on the results of the structural design. Instead it is up to the user to carry out aeroelastic analyses of the final design, evaluate the results and manually correct the input if design improvements can be achieved. While this approach makes the design software very efficient, it does also mean that the software described here is not an optimisation tool, nor does it claim to produce optimal blade designs. However, with sensible input it is possible to quickly create realistic blade designs.

INPUT DATA

The aerodynamic design is based on input of rated turbine power, design wind speed (at rated power) and design tip speed ratio. Furthermore, an airfoil family of different

thickness to chord ratios must be specified, with corresponding lift and drag coefficients for each airfoil. A continuous thickness distribution is specified by a fifth order Bezier curve and the discrete airfoils are mapped to this curve as shown in Figure 3. Between each discrete airfoil, the lift and drag data are interpolated according to the actual thickness.

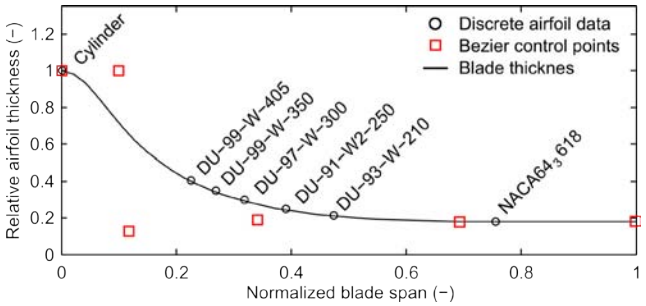

Figure 3: Thickness to chord distribution input

The ideal design method will give a chord length that is unrealistically large close to the root. To avoid this, the chord length is manipulated so that it follows close to the optimal chord at the outer parts of the blade, but is kept within reasonable dimensions closer to the root. This is done through four parameters (shown in red in Figure 4) and is explained further in [1].

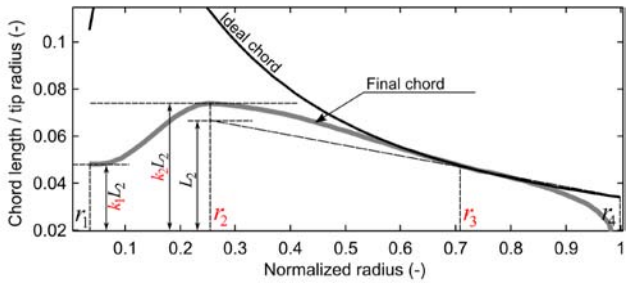

Figure 4: Chord length distribution parameters

This means that for a given airfoil family, a basic blade design can be characterized by only 12 design variables, of which five is related only to the thickness distribution and four is related only to the chord length. By keeping one or more of these constant it is possible to reduce the independent variables further, which can be useful for optimization purposes. If needed, more advanced features like blade pre-curve and flatback root designs can be controlled by Bezier control points similar to the ones in the thickness specification.

For the structural design, the shape of each airfoil must be known (XY-coordinates) and an initial layout of the blade materials must be specified along with corresponding material properties like density, Young's modulus and shear modulus. An illustration of a blade internal view is shown in Figure 7.

AERODYNAMIC DESIGN METHOD

The aerodynamic shape of the rotor blades is found using an iterative blade element momentum method, based on the inputs listed earlier. A flow chart of the aerodynamic design process is shown in Figure 5. The complete description is too long for this paper, but a short introduction is presented below. A thorough explanation is available in [1].

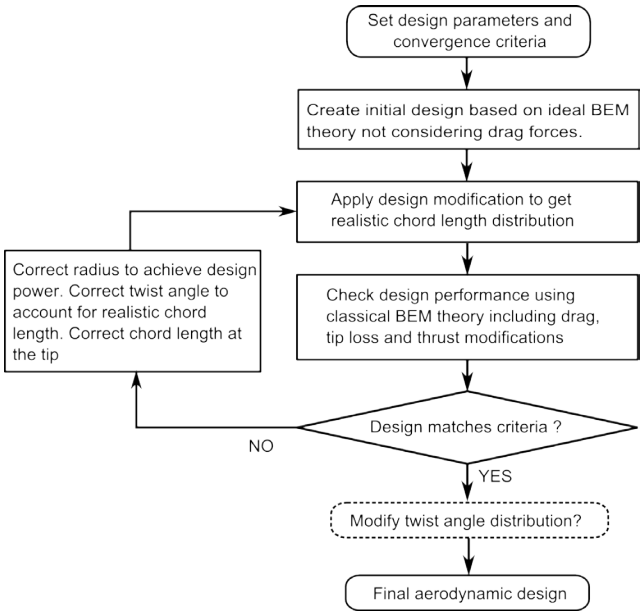

Figure 5: Aerodynamic design flow chart. Modified from [1]

By neglecting the drag it is possible to determine an ideal chord length and twist angle distribution. This chord length is then modified to give realistic blade geometry. This modification will also influence the distribution of aerodynamic induction in the axial direction and the aerodynamic forces. To keep the induction close to the ideal value of 1/3 the twist angle is modified on the main parts of the blade. This gives an even distribution of aerodynamic forces, and typically increases the power coefficient somewhat, but it does not guarantee that the final twist distribution is optimal, and it may also not be very smooth.

To overcome this, a twist angle modification can be applied after the main design iteration has converged: A fourth order Bezier curve is fitted to the original twist distribution by a weighted least-squares approach. By fixing the endpoints and enforcing zero twist gradient at the root, the task is reduced to a two-variable problem, and the optimal twist distribution can be found by varying the remaining Bezier control points around the values for the fitted curve and investigating the low wind speed performance.

This approach smoothens and optimises the twist angle with the rest of the design fixed, but it does no longer ensure that the aerodynamic forces are evenly distributed throughout the blade. A combination of even axial induction and smooth twist distribution is only possible with careful selection of airfoils with matching lift and drag coefficients.

The tapered tip design is found by simple aerodynamic considerations and is not manipulated with coefficients like the root design. This approach has not been verified, but comparison with the NREL 5 *MW* blade design (Figure 8) shows that the tip shape matches quite well.

STRUCTURAL DESIGN METHOD

The structural design is constrained by the aerodynamic design, as all the structural features must be fitted inside of the aerodynamic shell. There is no feedback from the structural design to the aerodynamic design as mentioned earlier, giving a structural design approach as illustrated in Figure 6.

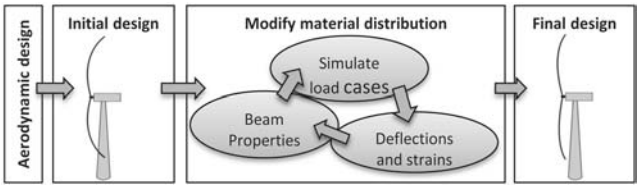

Figure 6: Illustration of the structural design approach

The structure is typically built up like a classical blade with dual shear webs and sandwich leading- and trailing edge skins as illustrated in Figure 7. The structure is divided into four units, the leading edge skin, the trailing edge skins, the shear webs and the spar caps. Each of these parts is built up of layers of different composite materials.

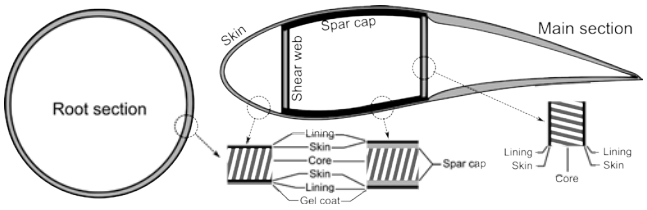

Figure 7: Internal view of blade. Example structural layout

The thickness of each layer must be specified initially, but are then modified in an iterative design loop until the final design is achieved. In the design loop, the beam properties are estimated using classical laminate theory, utilising the simple geometric shape of each part. With the beam properties known, a simple steady-state aeroelastic simulation is performed for a number of relevant load cases, and the deflections and strains are found. If the deflections or strains are unacceptable, material is added at strategic locations and the beam properties are recalculated. This is continued until all load cases are passed with due safety margins.

In the current implementation, the structural design is based on four failure criteria:

1. Flapwise blade deflections distance to the tower.
2. Maximum levels for material stresses and strains.
3. 1p damage-equivalent fatigue loads in edgewise direction (where “p” denotes the rotor frequency).
4. Blade structural frequencies within the 1p or 3p range or matching the first tower frequency.

The above list may seem incomplete, as there could be other dominating effects, for instance structural and aeroelastic instabilities like buckling and flutter, but more advanced analyses are required for reliable prediction of these effects. The risk of flutter can be reduced by using shell material with a high content of $^{+}$/- 45° fibres. Recent analyses indicate that typical 10 *MW* blades designed with the design software are not prone to flutter [3].

It would also be beneficial to include fatigue loads in the flapwise direction and in the edgewise direction other than from the deterministic 1p loads, but this would require more expensive time domain simulations or frequency domain analyses. Theoretically, in the low strain designs of carbon fibre or hybrid glass/carbon blades it is expected that the blades are more critical in ultimate loading than in fatigue loading due to smaller deflections and good fatigue performance of carbon fibre. This is, however, less obvious for real blades as ply drops will cause local stress concentrations [4] and because it has been difficult to achieve good compression strength of carbon fibre in actual composite laminates due to misalignment and waviness introduced in the manufacturing process [5], [6].

VERIFICATION

Due to the lack of detailed design data and specifications of commercial wind turbines in the public domain, it was decided to use the NREL 5 *MW* wind turbine as a case for comparison, although the specifications [7] of this turbine are also far from complete. The comparison showed good agreement except close to the root where the design method underestimated the material use [1]. To improve this, the root build-up that is necessary to make space for the root fastenings and bolts is now also taken into account. An updated comparison is shown in Figure 8 - Figure 10. The new design corresponds well with the NREL blades, especially when considering that neither material choices or material properties, nor the design basis is known for this turbine model.

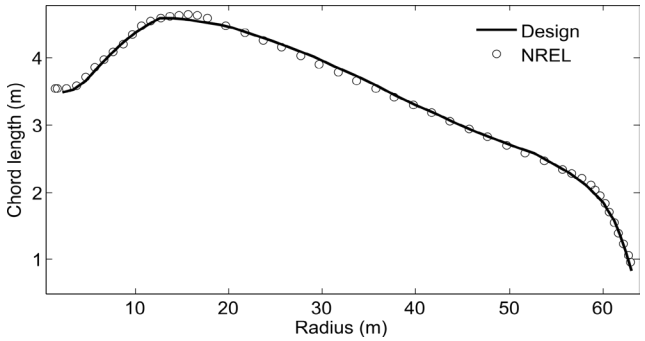

Figure 8: Chord length comparison

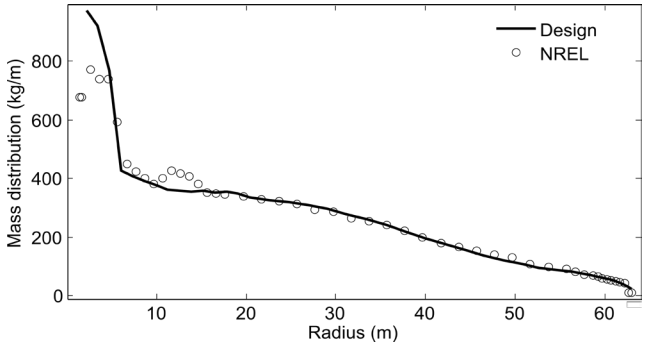

Figure 9: Comparison of mass distribution

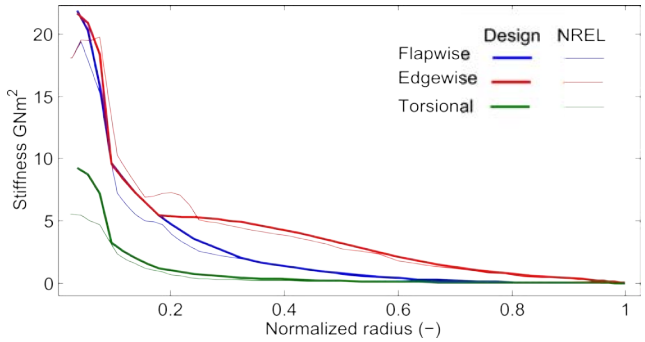

Figure 10: Comparison of stiffness distributions

The outboard blade properties correspond very well although there are some small deviations. The differences in edgewise stiffness relates to the small differences between the actual chord and the chord from the design method. The deviations in the flapwise and torsional stiffness are dependent, and may relate to differences in the thickness distribution of the two models, seen in Figure 11.

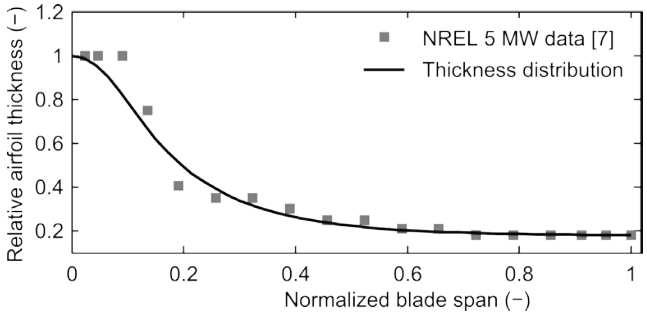

Figure 11: Comparison of thickness data input and NREL data

CONCLUSION AND FURTHER WORK

A simplified design method has been developed and implemented in a design tool. The purpose is to simplify the aerodynamic and structural design of rotor blades for large wind turbines. Despite the simplifications in the analyses and the limited number of design load cases, the results are reasonable and considered useful in a preliminary design phase, although further verification is advisable. The aerodynamic design routines give efficient and reasonably looking blade designs with sensible input. The structural design of the main parts of the blade compares well with existing wind turbine models when the available blade geometry data is used as input to the design model. Further verification will be carried out through aeroelastic simulations of various load cases to determine the fatigue loads, and by comparison of ultimate loads and extreme deflections calculated by the design tool with the results of the aeroelastic simulations.

ACKNWLEDGEMENTS

Thanks to NOWITECH and Statkraft Ocean Energy Research Program for funding this research.

REFERENCES

[1] L. Frøyd and O. G. Dahlhaug, “A Conceptual Design Method for Parametric Study of Blades for Offshore Wind Turbines,” in *Proc. of the ASME 2011 30th Int. Conf. on Ocean, Offshore and Arctic Engineering*, Rotterdam, 2011.

[2] L. Frøyd and O. G. Dahlhaug, “Rotor Design for a 10 MW Offshore Wind Turbine,” in *Proc. of ISOPE 2011 21st International Offshore (Ocean) and Polar Engineering Conference*, Maui, Hawaii, 2011.

[3] S. R. Vatne, “Aeroelastic Instability and Flutter for a 10 MW Wind Turbine,” Master’s thesis, NTNU, Trondheim, Norway, 2011.

[4] D. A. Griffin, “Blade System Design Studies Volume 1:Composite Technologies for Large Wind Turbine Blades,” Sandia National Laboratories, SAND2002-1879, 2002.

[5] K. Mason, “Carbon/glass hybrids used in composite wind turbine rotor blade design,” *Composites World*, 2004. [Online]. Available: http://www.compositesworld.com/articles/carbonglass-hybrids-used-in-composite-wind-turbine-rotor-blade-design. [Accessed: 27-May-2011].

[6] G. Gardiner, “Carbon Fiber in the Wind : Composites World.” [Online]. Available: http://www.compositesworld.com/articles/carbon-fiber-in-the-wind. [Accessed: 27-May-2011].

[7] J. M. Jonkman, S. Buttefield, W. Musial, and G. Scott, “Definition of a 5-MW Reference Wind Turbine for Offshore System Development,” National Renewable Energy Laboratory, 2009.

Session 3A

Wind Modelling, Forecasting and Resource Assessment I & Rotor and Wakes Aerodynamics III

Atmospheric boundary layer velocity profiles generated by an active grid

N. Reinke, E. Renken, P. Knebel, J. Peinke and M. Hölling
ForWind, Center for Wind Energy Research,
University of Oldenburg
26111 Oldenburg, Germany
E-mail: nico.reinke@uni-oldenburg.de

Keywords: Active grid, atmospheric boundary layer, and turbulence

1 Introduction

The atmospheric boundary layer (ABL) is a highly turbulent wind field for which the wind speed increases with height. This vertical profile of the mean wind speed depends on the local topography as well as on the local thermal conditions and is often described by a logarithmic function in a height between approximately 1cm and 100 meters [1]. This region is called Prandtl layer[11]. Besides this profile the wind conditions are described by the turbulence intensity T. T is defined as the ratio between the standard deviation of the velocity time series σ_u and the mean velocity $\bar{u}$,

$$T = \frac{\sigma_u}{\bar{u}}. \tag{1}$$

Wind fluctuations are characterized additionally by the velocity increments, $u'(\tau) = u(t+\tau) - u(t)$, which show an intermittent behavior on very small (seconds) to very large scales τ (days) [2]. The probability density functions (PDF) of those increments with intermittency show so called heavy tails. This means that, extreme events, like very heavy gusts, appear much more frequently than expected by standard models, which assume a Gaussian distribution for the PDFs of the velocity increments [3]. This rough environment is the workplace for wind energy converters (WEC). For experiments e.g. on wind turbine models in a wind tunnel, it is crucial to be able to reproduce the characteristics of these ABLs. The classical way for the generation of vertical velocity profiles is the use of passive roughness elements, which are brought into the wind tunnel. The length of those conditioning sections is of the order of 10 meters. Another way to generate such wind fields is the use of an active grid [4, 5, 7]. The active grid gives the opportunity to modify a laminar flow to a controllable turbulent and asymmetric velocity field with repeatable conditions. Compared to the upper manner, the active grid influences the flow over the whole cross section and the flow reaches its final conditions about 1 meter behind the grid. Hence the active grid is a proper manner for small wind tunnels like the tunnel in Oldenburg. The first step in our research with the active grid was to create mean velocity gradients (close to logarithmic functions) in the test section like known from the ABLs and furthermore to use special dynamical excitations to reproduce desired intermittent statistics of velocity increments [10]. Our work was inspired by the investigations by Cekli and van de Water [9] who showed that velocity profiles may be generated by different horizontal blockage ratios with his active grid. This paper will give an overview of the work on velocity profiles and will also show a new quality of reproducibility of turbulent structures. Being able to reproduce turbulent structures allows us to perform new experiments regarding the impact of turbulence on the performance of wind turbine models and different anemometers exposed to the same turbulence.

2 Velocity profiles

The normal velocity profile behind the nozzle of a wind tunnel is uniform and has a low turbulence intensity T (T<1%), close to the laminar case. With the active grid behind the nozzle the velocity field is more turbulent, but the mean velocity field is still uniform as long as the flaps of the axes cause the same mean blockage to the incoming velocity field.

The active grid at ForWind consists of seven horizontal and nine vertical axes with 7.4 x 7.4 cm^2 square flaps mounted to the axes as shown in figure 1. Each of these axes is connected to a step motor and can be controlled individually. All axes can be moved at a maximum angular velocity of 900 degrees per second and with an angular precision of 0.07 degree. The measurements were performed with a hot wire (1mm wire length) on a traverse. The traverse moves the hot wire through the measurement volume with a spatial errors of $\pm$1mm. Typically we measured time series of 4,000,000 data points with a sampling frequency of 20kHz for every spatial position.

To get a nonuniform flow field like in the ABL we adjusted a mean solidity gradient over the height behind the nozzle with the active grid in such a way that we get a logarithmic velocity profile like known from the Prandtl layer in the ABL. This changing blockage ratio is possible by adjusting the axes motion. All the seven horizontal axes were oscillating in a sinusoidal way define by

$$y_i(t) = A_i \, sin(\omega_i t + \phi_i) + O_i, \tag{2}$$

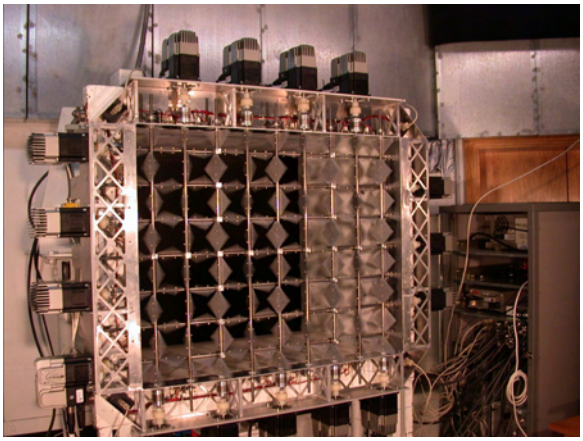

Figure 1: The active grid mounted in front of the nozzle in the wind tunnel of the University of Oldenburg. The Grid comprised seven horizontal and nine vertical axes, each of them is controlled per step motor individually

where A_i is the amplitude of the oscillation, ω_i is the angular frequency, t is the time, ϕ_i is the phase and O_i is the offset of the i-th axis. The solidity for each axis can be adjusted by the amplitude A_i and the offset O_i. One resulting velocity profile vs. height of the test section in a semi logarithmical plot where just the offset O_i was changed with height is shown in figure 2. This measurement also shows that a strong velocity gradient of

$$\frac{\Delta u}{\Delta x} = \frac{u_{max} - u_{min}}{x_{u_{max}} - x_{u_{min}}} \approx \frac{1\ m/s}{0.5\ m} = 2\ s^{-1} \qquad (3)$$

can be achieved.

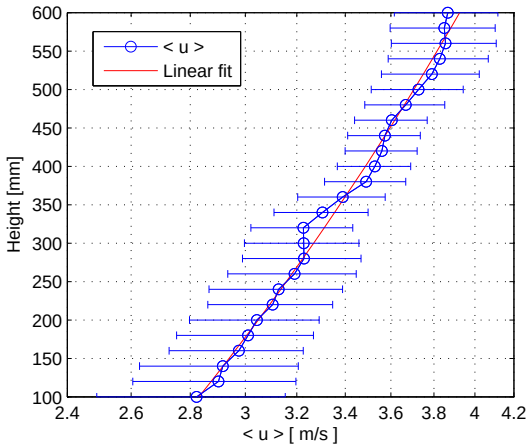

Figure 2: Mean velocity profile vs. the test section's height in a semi logarithmical plot. The error bars have a length of 0.5 times the standard deviations σ_u. The fitting curve in red illustrates the logarithmical shape.

The standard deviation σ_u indicates that the velocity field is very turbulent across the whole profile. The measurement is trimmed in height due to shear layer effects of the open test section at the measuring position of about 1.2 meter behind the active grid. The deviations in the velocity profile from an ideal log profile are coming from the influence of the horizontal axes. Other measurements closer to the grid show these deviations more pronounced. One possibility to minimize this effect seems the production of strong turbulence with the vertical axes since measured velocity profiles with no oscillating vertical axes deviated more from the logarithmic shape.

3 Reproducibility

The reproducibility of experimental conditions in the test section of the wind tunnel is crucial for the comparability of measurements. In the standard case of a laminar flow and very low turbulence intensity T (T<1%) respectively, it is straight forward to define reproducibility. For the turbulent case this becomes more difficult to define what reproducibility should mean.

In this article we take the mean velocity $\bar{u}$ and turbulence intensity T as criteria for reproducibility. As mentioned above we measured via hot-wires velocity time series downstream from the active grid to the inlet of the test section. For one data set (or measurement series) 11 spatial points were chosen in one horizontal line downstream recorded in a distance of 24cm up to 124cm behind the grid. The line of points was located in the core of the test section. During the measurement all axes of the active grid were rotating in a sinusoidal way with a frequency of 1 Hz and an amplitude of 90 degrees. Thereby all flaps start with their movement parallel to the incoming flow (offset=0°).

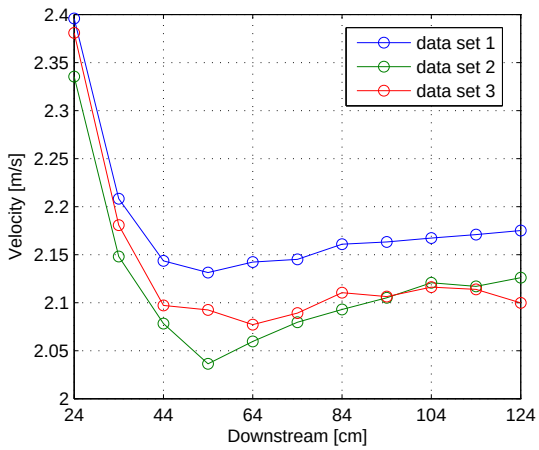

Figure 3: Evolution of mean velocity $\bar{u}$ with increasing distance to the active grid

Figure 3 shows the evolution of the mean velocity $\bar{u}$ with increasing distance to the active grid of three measurement series . It shows that $\bar{u}$ decreases in the first 20cm (between 24cm and 44cm) about 9% and stabilizes afterwards to a almost constant value. This decreasing behavior seems to be a problem of the measurement technique. The velocity measurements with a hot wire in very high turbulent flows (T>0.2, see figure 5) is problematically. In this case it is well known that the absolute values of velocity will be over

estimated. The analysis regarding the reproducibility is not affected by this since the hot wire reacts the same way even under such bad conditions. To quantify the reproducibility we estimate the percentage differences D,

$$D = \frac{X - Y}{(X + Y)/2} * 100, \tag{4}$$

between the mean velocity measurements, see figure 4. In equation 4 here X and Y denote two different mean velocity measurements series. The curves of figure 4 show fluctuations between -1.5% and 4.5%.

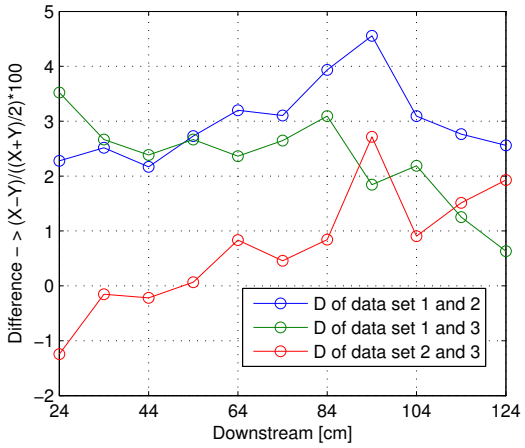

Figure 4: Percentage difference D between the mean velocity distributions from figure 3

A second parameter of interest is the turbulence intensity T of the flow, see equation 1. Figure 5 presents the T values downstream obtained from the same measurement series as before. The agreement is over a wide range very good. An analysis downstream like in figure 4 with equation 4 reveals that the percentage difference is in a range of ±4%. This deviation fits well to the deviation range of the mean velocity, which makes sense according to equation 1.

Coming back to the problem of a proper verification of the reproducibility of turbulent flows, it is obvious that the analysis of a mean value and the turbulence intensity is not sufficient. There are many further aspects one may consider. In the following we will investigate the probability density function (PDF) of the velocity increments $u'(\tau)$, as general two point quantities. Note, knowing the PDF of $u'(\tau)$, also all high order moments of $u'(\tau)$ are given. The time step τ is a further important parameter for the whole analysis, but in this article we just investigate the smallest measured time step given by the sampling frequency, as for this time step the PDF should be most intermittent. Our measurements show that the results are also valid for a wide range of different τ. As we are interested in the reproducibility of the intermittency we use velocity increments, x, normalized by the standard deviation of u'

$$x = \frac{u'}{\sigma_{u'}}. \tag{5}$$

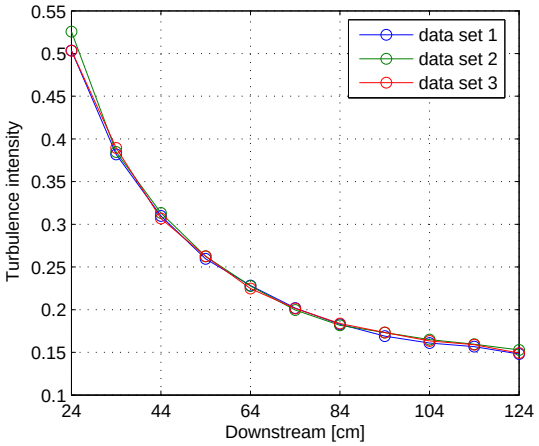

Figure 5: Turbulence intensity behind the active grid achieved from the three velocity data sets

This normalization allows to compare different time series with each other. Next we parametrize the form of the PDFs by the Castaing paramter λ^2. In figure 6 three PDFs are shown namely PDF of a time series, an estimation of the PDF with the Castaing model and a Gaussian normal distribution with a standard deviation of σ=1. The measured PDF is a heavy tailed distribution, compared to the red Gaussian normal distribution occur much more extreme events.

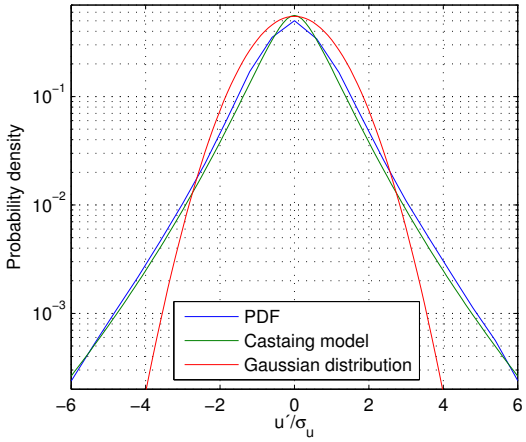

Figure 6: The blue curve is the probability density function (PDF) measured 24cm behind the active grid, $\tau = 1/30000s$. The green curve comes form the Castaing model based on the form parameter λ^2. The red curve is a gaussian normal distribution, with a standard deviation of one

The form factor λ^2 was directly calculated from the measured time series using

$$\lambda^2 = \frac{1}{4}\, log\left(\frac{\langle (u' - \bar{u'})^4 \rangle}{3\ \sigma_{u'}^4}\right), \tag{6}$$

where the symbols $\langle\ \rangle$ as well as the bar denote the mean value of the inner argument. If λ^2 is zero the PDF is equal to

a Gaussian distribution. The further λ^2 increases the more the time series have an intermittent behavior. As λ^2 describes the form of the PDF we use this parameter for our last aspect of reproducibility. In figure 7 the behavior of λ^2 downstream is illustrated for our three measurement series. Straight behind the active grid λ^2 is maximal and decreases till about 70cm downstream. After this decreasing part a more or less saturated part begins, what may be addressed as developed turbulence. The three curves show the same development downstream. An analysis downstream like in figure 4 with an corresponding estimation like equation 4 shows that the reproducibility of intermittency is in a range of $\pm 12\%$.

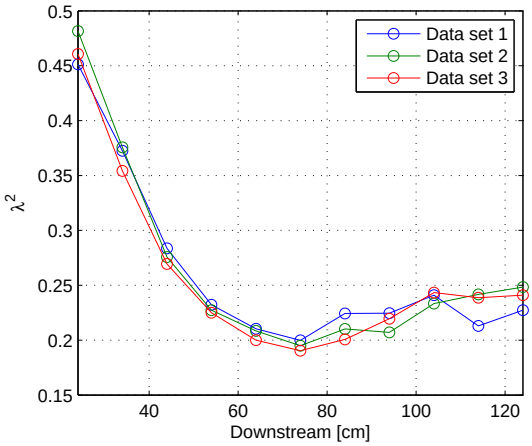

Figure 7: λ^2 calculated from the three measured data sets at different positions behind the active grid

4 Conclusions

In the first part possibilities to modify a uniform flow with the active grid to a flow with a velocity gradient of 2 s^{-1} is presented. Furthermore the velocity profiles could reach a logarithmical shape in the sense of a Prandtl layer, which is the background of many investigations for ABLs, specially for wind energy converters. The second part gives an insight in as far experimental conditions are repeatable with the active grid. Three measurement series were recorded for this reason and compared. It is shown, that the mean velocity and the turbulence intensity downstream of the active grid are quantities which are to a high degree repeatable (error of $\pm 4\%$). The investigations of the form parameter λ^2 reveal, that the differences between the data sets were in a range of $\pm 12\%$. However, λ^2 has the same development downstream and is in this sense repeatable. In the next experiments we will try to smooth the log velocity profile and find the limits in modification of the velocity gradient. Furthermore we will validate our results with a laser doppler anemometer. In the present investigation we excited the grid in a sinusoidal way where for the following experiments we will investigate the influence of a stochastic excitation. Another step will be to combine both aspects the velocity profile and the repeatability.

References

[1] D. Etling: Theoretische Meteorologie. Springer-Verlag, Berlin, 2008.

[2] R. I. Harris: The Macrometeorological Spectrum - A Preliminary Study Journal of Wind Engineering and Industrial Aerodynamics, 2008, 96, 2294-2307

[3] F. Böttcher, Ch.Renner, H.-P. Waldl, and J. Peinke: On the Statistics of Wind Gusts. Boundary-Layer Meteorology, 108, 163-73 (2003)

[4] H. Makita; Realization of a large-scale turbulence field in a small wind tunnel, Fluid Dyn. Res. **8**, 53-64 (1991).

[5] L. Mydlarski and Z. Warhaft; On the onset of high-Reynolds-number grid-generated wind tunnel turbulence, J.Fluid Mech. **320**, 331-368 (1996).

[6] R.E.G. Poorte; On the motion of bubbles in active grid generated turbulent flows, (PhD thesis, University of Twente, 1998).

[7] H.S. Kang, S. Chester, and C. Meneveau; Decaying turbulence in an active-grid-generated flow and comparisons with large-eddy simulation, J. Fluid Mech. **480**, 129-160 (2003).

[8] J.V. Larssen; Large Scale Homogenous Turbulence and Interactions with a Flat-Plate Cascade (PhD thesis, Virginia Polytechnic Institute and State University Blacksburg, 2005).

[9] H. E. Cekli, and W. van de Water: Tailoring turbulence with an active grid. Exp. in Fluids, Volume 49, 409416 (2010)

[10] P. Knebel, A. Kittel, and J. Peinke: Atmospheric Wind Field Conditions Generated by Active Grids. Exp. in Fluids, 2011, pp. 1-11, 10.1007/500348-011-1056-8

[11] H. Oertel: Prandtl - Führer durch die Strömungslehre. Vieweg + Teuber, 2008, 12.,ISBN-13: 9783834804303

[12] L. Breiman: Probability. Addison - Wesley, Boston, 1968

[13] B. Castaing, Y. Gagne, E. J. Hopfinger: Velocity probability density functions of high reynolds number turbulence. Physica D 1990; 46: 177200, doi:http://dx.doi.org/10.1016/0167-2789(90)90035-N

Study of Turbulence Structure with Atmospheric Stratification

Abhijit Chougule
Risø DTU
4000 Roskilde, Denmark
E-mail: absch@risoe.dtu.dk

Keywords: spectral tensor, atmospheric stratification, eddy lifetime

1 INTRODUCTION

The study of atmospheric turbulence has gained much attention towards wind energy sector because of subsequent estimation of its loading effects upon wind turbines. Wind in the atmosphere is fluctuating and hence is turbulent in nature, which generates the dynamic loads on structures like wind turbines. The fluctuations over mean wind along with mean wind itself are expected to be varying depending upon the whether atmosphere is neutral, stable, highly stable or unstable etc. Therefore it is important to generate stability dependent spectral tensor model which gives spatial structure of turbulence with atmospheric stability.

This PhD project is basically about study and development of spatial structure of turbulence with atmospheric stratification, by augmenting the spectral tensor model of Mann [3] to include buoyancy effects, i.e. stratifications. The approach with stable atmospheric stratification is discussed in this paper (§3). Also the available spectral tensor model is compared with LES data from NCAR with different stability cases, in simple form by means of anisotropy tensor (§2.1).

2 TURBULENCE STRUCTURE UNDER NEUTRAL STRATIFICATION

Risø has produced a model for the three-dimensional spectrum of turbulence in the neutral surface layer [3], which is widely used in wind energy industry to simulate inflow turbulence for load calculations. The spectral velocity tensor is defined as,

$$\Phi_{ij}(\boldsymbol{k}) = \frac{1}{(2\pi)^3}\int R_{ij}(\boldsymbol{r})\exp(-\mathrm{i}\boldsymbol{k}\cdot\boldsymbol{r})\mathrm{d}\boldsymbol{r}, \qquad (1)$$

where $R_{ij}(\boldsymbol{r}) = \langle u_i(\boldsymbol{x})u_j(\boldsymbol{x}+\boldsymbol{r})\rangle$, is the covariance tensor, $\mathbf{u}(\boldsymbol{x})$ is fluctuation over mean wind $\mathbf{U}(\boldsymbol{x})$ and $\langle\ \rangle$ denotes ensemble averaging.

The spectral velocity tensor model incorporates rapid distortion theory (RDT) [5], with an assumption of uniform mean shear to estimate the structure of turbulence over flat terrain and gently varying orography in neutral flow. The RDT equation for neutral stratification is given as,

$$\frac{D}{Dt}dZ_i(\boldsymbol{k},t) = \left(2\frac{k_i k_1}{k^2} - \delta_{i1}\right)\left(\frac{dU}{dz}\right)dZ_3(\boldsymbol{k},t), \qquad (2)$$

where, $dZ_i(\boldsymbol{k},t)(i=1,2,3)$ are Fourier velocity components given in terms of a generalized stochastic Fourier-Stieltjes integral: $u_i = \int e^{i\boldsymbol{k}\cdot\boldsymbol{x}}dZ_i(\mathbf{k},t)$ and $k^2 = |\boldsymbol{k}|^2$. The wave number vector evolves with time as, $\frac{dk_j}{dt} = -k_i\frac{dU_i}{dx_j}$, which gives $\boldsymbol{k} = \{k_1, k_2, k_{30} - \alpha_s t\}$, where $\alpha_s = \frac{dU}{dz}$ and the initial wave vector, $\boldsymbol{k}_0 = \{k_1, k_2, k_{30}\}$. The spectral velocity tensor as given in (1) is modeled from the relation,

$$\frac{\langle dZ_i^*(\boldsymbol{k}(t),t)dZ_j(\boldsymbol{k}(t),t)\rangle}{dk_1dk_2dk_3} = \Phi_{ij}(\boldsymbol{k}(t),t) \qquad (3)$$

The equation (2) can be solved analytically and equations for $\Phi_{ij}(\boldsymbol{k})$ are obtained in analytic form as in Mann spectral tensor model. The initial conditions are isotropic turbulence with spectral tensor and von Kármán energy spectrum respectively as,

$$\begin{aligned}\Phi_{ij}(\boldsymbol{k}_0,0) &= \frac{\langle dZ_i^*(\boldsymbol{k}_0,0)dZ_j(\boldsymbol{k}_0,0)\rangle}{dk_1dk_2dk_3} \\ &= \frac{E(k)}{4\pi k^4}(\delta_{ij}k^2 - k_ik_j), \qquad (4)\\ E(k) &= \alpha\varepsilon^{\frac{2}{3}}L^{\frac{5}{3}}\frac{(Lk)^4}{(1+(Lk)^2)^{\frac{17}{6}}}. \qquad (5)\end{aligned}$$

The available Mann spectral velocity tensor model contain only three adjustable parameters: a lengthscale L,describing the size of the largest energy-containing eddies, a non-dimensional number Γ used in the parametrization of eddy lifetime [3], and the third parameter is a measure of the energy dissipation $\alpha\varepsilon^{2/3}$, where $\alpha = 1.7$ and ε is the rate of viscous dissipation of specific turbulent kinetic energy. The three parameters are determined from one point measurements.

Due to symmetries in the model, there are only four (co-)variances viz., $\sigma_u^2, \sigma_v^2, \sigma_w^2$ and $\langle uw\rangle$ which are non-zero, and are calculated numerically from $\Phi_{ij}(\boldsymbol{k}(t),t)$ by $\langle u_iu_j\rangle = \int\Phi_{ij}(\boldsymbol{k}(t),t)\mathrm{d}\boldsymbol{k}$. The (co-)variances become function of L,Γ, and $\alpha\varepsilon^{2/3}$.

2.1 Analysis of anisotropy stress tensor from Mann model with LES data

The Mann model is compared with LES data from NCAR, in simple way by analyzing anisotropy tensor b_{ij}, in the Lum-

ley triangle ([5]). The anisotropy tensor is defined as,

$$b_{ij} = \frac{R_{ij}}{2k} - \frac{1}{3}\delta_{ij}, \tag{6}$$

where, $k = \frac{1}{2}R_{ii}$, is turbulent kinetic energy, $R_{ij} = \langle u_i u_j \rangle$, is Reynolds stress tensor. From equation (6), anisotropy tensor has zero trace i.e. $b_{ii} = 0$. Since R_{ij} is symmetric second order tensor and hence b_{ij}; the three principal invariants are;

$$\mathrm{I}_b = b_{ii}(=0) \tag{7}$$

$$\mathrm{II}_b = \frac{1}{2}b_{ij}b_{ji} \tag{8}$$

$$\mathrm{III}_b = \det(\mathbf{b}), \tag{9}$$

It is also convenient to define two variables, η and ξ as,

$$6\eta^2 = -2\mathrm{II}_b = b_{ij}b_{ji} \tag{10}$$

$$6\xi^3 = 3\mathrm{III}_b = b_{ij}b_{jk}b_{ki} \tag{11}$$

The matrix **b** can also be transformed into principal axes where offdiagonal terms become zero with eigen values λ_1, λ_2 and λ_3. Also, $b_{ii} = \lambda_1 + \lambda_2 + \lambda_3 = 0$ or $\lambda_3 = -(\lambda_1 + \lambda_2)$ and from (8)-(9), (10)-(11) we get,

$$\eta^2 = \frac{1}{3}(\lambda_1^2 + \lambda_1\lambda_2 + \lambda_2^2) \tag{12}$$

$$\xi^3 = -\frac{1}{2}\lambda_1\lambda_2(\lambda_1 + \lambda_2) \tag{13}$$

In summary, given the Reynolds stress tensor, η and ξ are calculated from either (10)-(11) or (12)-(13). For Mann model, b_{ij} is calculated numerically as discussed above. In its normalized form, b_{ij} becomes only function of the Γ parameter, and the state of the anisotropy tensor can be represented in a $\xi - \eta$ plane with varying Γ between 0 to 4.

Also anisotropy tensor is calculated from high temporal and spatial resolution LES of the atmospheric boundary layer over flat, homogeneous terrain for varying stability from NCAR, kindly provided by Ned Patton. The calculations are done for three different stability cases; moderately stable ($z_i/L_{MO} = 2$), unstable ($z_i/L_{MO} = -10$) and neutral ($z_i/L_{MO} = 0$), where z_i is boundary layer depth and L_{MO} is Obukhov length. The LES dataset consists of instantaneous volume $3D$ fields, between heights $50m$ to $150m$. The variance and covariance are calculated for each stability case for each snapshot and at each z level in horizontal slice and then averaged over all snapshots. The results are plotted as shown in figure 2. At any time and point in turbulent flow, the state of Reynolds stress tensor can be presented as point in ξ-η plane. There are some special states of Reynolds stress tensor that corresponds to particular points and curves in this plane called Lumley triangle as discussed in [5] and shown in figure 1.

The LES neutral data falls closer to the curve which corresponds to values of Γ between 3-4. The deficiency of the Mann spectral tensor model can be observed when

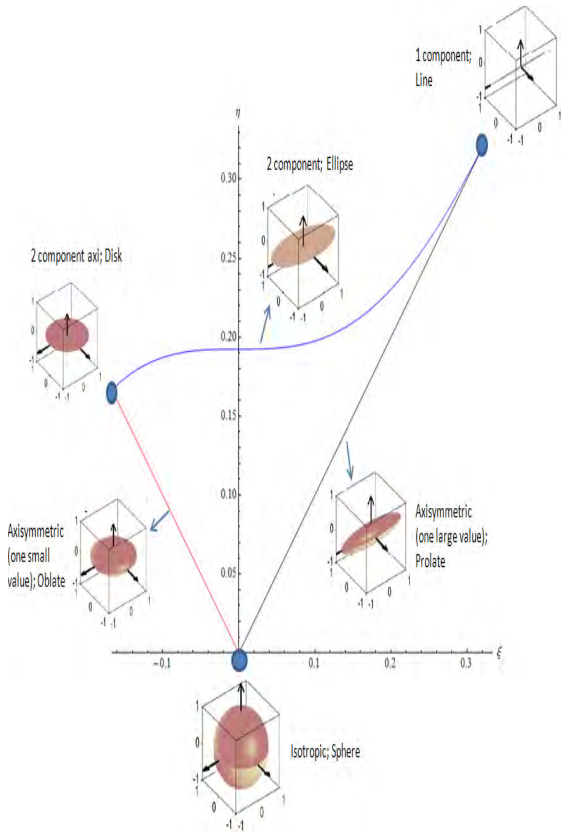

Figure 1: Lumley triangle with its axisymmetric limits showing different turbulence shapes. Source:A.J. Simonsen and P.-A. Krogstad,*Turbulent Stress Invariant Analysis: Clarification of Existing Terminology*

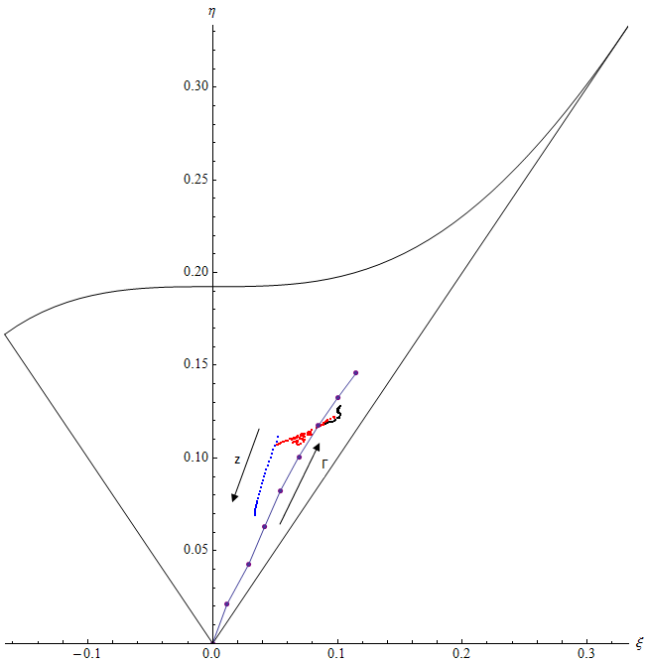

Figure 2: LES data with Mann US model. Black points; Neutral, Red points; Stable, Blue points; unstable, US model; –●–.(Direction of arrows indicates increase of height z for LES stable, unstable and neutral and increase of Γ for Mann model)

compared with unstable LES. The stable LES crosses the curve. The origin in Lumley triangle represents isotropic turbulence where anisotropy tensor is zero ($\xi = \eta = 0$). This state of isotropic turbulence corresponds to $\Gamma = 0$ on the curve.

3 Non-neutral stratification

The application of RDT to flows with both uniform mean shear and constant vertical mean potential temperature gradient has been accomplished in the last decade, but the analysis and focus thus far has mostly been limited to uniform shear plus stable stratification, as in [2].

In this section the buoyancy effect on turbulence structure [2] is discussed against turbulence structure under neutral stratification and eddy life time from [3] .

3.1 Turbulence under uniform stratification and shear

The governing equations of RDT for homogeneous flow with uniform stratification and shear in vertical direction, are,

$$\frac{D}{Dt}dZ_i(\boldsymbol{k},t) = \left(2\frac{k_i k_1}{k^2} - \delta_{i1}\right)\left(\frac{dU}{dz}\right)dZ_3(\boldsymbol{k},t) - \left(\frac{k_i k_3}{k^2} - \delta_{i3}\right)\frac{g}{T}d\Theta(\boldsymbol{k},t), \quad (14)$$

$$\frac{D}{Dt}d\Theta(\boldsymbol{k},t) = -N^2 dZ_3(\boldsymbol{k},t), \quad (15)$$

where N is the Brunt-Väisälä frequency given by $N^2 = (g/T)dT/dz$ (the gradient of the potential temperature) and the Fourier transform of the potential temperature $d\Theta(\boldsymbol{k},t)$ as, $\theta = \int e^{i\boldsymbol{k}\cdot\boldsymbol{x}}d\Theta(\boldsymbol{k},t)$. From equation (14) and (15), the equation for dZ_3 can be solved analytically ([2]). When compared with equation (2), equation (14) has additional term which is due to buoyancy.

Denoting $d\Theta(\boldsymbol{k},t)$ by $dZ_4(\boldsymbol{k},t)$, equations (14) and (15) can also be put in matrix form as,

$$\frac{D}{D\beta}dZ_i(\boldsymbol{k}(\beta),\beta) = M_{ij}(\boldsymbol{k}(\beta),\beta)dZ_j(\boldsymbol{k}(\beta),\beta), \quad (16)$$

where,

$$M_{ij}(\boldsymbol{k}(\beta),\beta) = \begin{bmatrix} 0 & 0 & \frac{2k_1^2}{k^2} - 1 & \frac{1}{\alpha_s}\frac{k_1 k_3}{k^2} \\ 0 & 0 & \frac{2k_1 k_2}{k^2} & \frac{1}{\alpha_s}\frac{k_2 k_3}{k^2} \\ 0 & 0 & \frac{2k_1 k_3}{k^2} & \frac{1}{\alpha_s}(\frac{k_3^2}{k^2} - 1) \\ 0 & 0 & \alpha_s Ri & 0 \end{bmatrix}, \quad (17)$$

$\beta = \alpha_s t$ and Richardson number $Ri = N^2/\alpha_s^2$.

Since from equations (14) and (15), the analytical solution is available for dZ_3 and dZ_4, the spectral tensor Φ_{ij} with $\{i,j\} = \{3,3\},\{4,4\}$ and $\{4,3\}$ has an analytic form

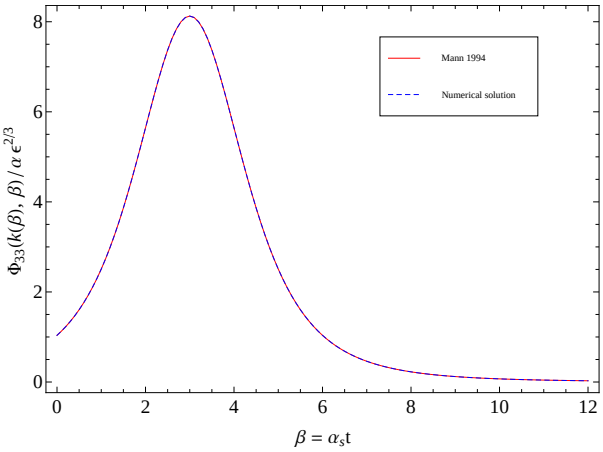

Figure 3: Φ_{33} as function of β from numerical calculation in comparison with $\Phi_{33}(k(\beta),\beta)$ from Mann model

[2]. The initial,isotropic tensor is given as,

$$\Phi_{ij}(\boldsymbol{k}_0,0) = \begin{bmatrix} \frac{k_2^2+k_{30}^2}{4\pi k_0^4} & -\frac{k_1 k_2}{4\pi k_0^4} & -\frac{k_1 k_{30}}{4\pi k_0^4} & 0 \\ -\frac{k_1 k_2}{4\pi k_0^4} & \frac{k_1^2+k_{30}^2}{4\pi k_0^4} & -\frac{k_2 k_{30}}{4\pi k_0^4} & 0 \\ -\frac{k_1 k_{30}}{4\pi k_0^4} & -\frac{k_2 k_{30}}{4\pi k_0^4} & \frac{k_1^2+k_2^2}{4\pi k_0^4} & 0 \\ 0 & 0 & 0 & \frac{2\alpha_s^2 Ri}{4\pi k_0^2}\frac{S(k_0)}{E(k_0)} \end{bmatrix} \times E(k_0)$$

where, $E(k_0)$ (5) and $S(k_0)$ are form of spectral densities such that initial kinetic energy, $\mathrm{KE}_0 = \int_0^\infty E(k_0)\mathrm{d}k_0$ and initial potential energy, $\mathrm{PE}_0 = \int_0^\infty S(k_0)\mathrm{d}k_0$ and $k_0^4 = |\boldsymbol{k}_0|^4$.

The analytic form for the other Fourier components is not available (dZ_1 and dZ_2), and hence for $\Phi_{ij}(\boldsymbol{k}(t),t)$ with $\{i,j\} = \{1,1\},\{1,2\},\{1,3\},\{1,4\},\{2,2\},\{2,3\}$ and $\{2,4\}$. The equations (16) for Fourier components are solved numerically. The values for Φ_{33},Φ_{44} and Φ_{43} as function of $\beta = \alpha_s t$ from the numerical calculation are compared with that from the analytical solution in [2]. The numerics seem to work, but it has to be speed up. Φ_{33} from Mann spectral tensor model is compared with that from numerical solution at $Ri = 0$, which is shown in figure 3.

3.2 Eddy life time and RDT

The linearization imposed by RDT is unrealistic. Eddies are stretched by shear and breaks over a time which is proportional to their life time. Small scale eddies breaks faster due to shear than larger scale eddies. The eddy life time from [3] is given as,

$$\tau(\boldsymbol{k}) \propto \Gamma\alpha_s^{-1} f(kL), \quad (18)$$

where, $f(kL)$ is a function which involve hypergeometric function. The eddy life time given by (18) is proportional to Γ which gives time evolution of spectral tensor from isotropy as shown in figure 2, and inversely proportional to

mean shear α_s, which means that the higher the shear the faster the eddies breaks.

4 Conclusions and future work

The anisotropy tensor of the Mann spectral tensor model for neutral stratification is compared with LES runs from NCAR with different atmospheric stabilities. The deficiency of the model for the stable and unstable cases can be observed. The Γ curve in the Lumley triangle represents a simple way of comparing any other model and the neutral case falls on/near Γ curve for Γ values ranging from 3 to 4 which corresponds to realistic values for a neutral atmosphere in the surface-layer.

It is imperative to develop a stability dependant spatial structure of turbulence. The approach including stratification is discussed. Since all the Fourier components in the RDT equations can not be solved analytically, the RDT equations are solved numerically for all three components and the temperature. The numerical solution for dZ_3 and dZ_4 can be compared with their analytic forms. The future task is to incorporate the eddy life time from the Mann spectral tensor model into the RDT equations to solve and analyse numerically the spectra and co-spectra of all velocity components, and comparisons with data will be made.

I am grateful to Ned Patton (NCAR) for providing the LES data.

References

[1] C. Moeng and J. C. Wyngaard. Spectral Analysis of Large-Eddy Simulations of the Convective Boundary Layer. Journal of the Atmospheric Sciences. Vol. 45, No.23 . 1988.

[2] H. Hanazaki and J. C. R. Hunt. Structure of unsteady stably stratified turbulence with mean shear. J. Fluid Mech. 507: 1-42. 2004.

[3] J. Mann. The spatial structure of neutral atmospheric surface-layer turbulence. J. Fluid Mech. 273: 141-168,1994.

[4] K. R. Sreenivasan. The passive scalar spectrum and the ObukhovCorrsin constant. Phys. Fluids, Vol. 8, No. 1. 1996.

[5] S. B. Pope. Turbulent Flows. Cambridge University Press, 2000.

Wind turbine simulations comparing the actuator disk approach with a fully resolved rotor simulation

Siri Kalvig[1], Eirik Manger[2]
[1]University of Stavanger, Norcowe/StormGeo, Stavanger, Norway
[2] Acona Flow Technology, Skien, Norway
E-mail: siri.m.kalvig@uis.no, eirik.manger@acona.com

Keywords: offshore wind turbines, wakes, CFD, actuator disk, sliding mesh, OpenFOAM, ANSYS/FLUENT.

1 INTRODUCTION

The changing sea state can be seen as a "dynamic roughness" influencing offshore wind turbine wakes and possible also the turbine loads. Computational Fluid Dynamics (CFD) is an efficient and accurate tool for simulating both these effects. Several different approaches can be utilised, ranging from coarse methods only considering the turbine wakes to fully resolved rotor simulations. Presently the open source CFD toolbox OpenFOAM [1] has been used for the general wind-wave simulations, whereas the fully resolved calculations predicting both turbine loads and wakes are done using ANSYS/FLUENT.

2 MOTIVATION

Different sea states affect the wind field in various ways. Wind-waves are often aligned with the local wind. For swells however, which are waves that have propagated away from the source origin, the local wind direction is not necessarily correlated with the swell direction. Occasionally swells will oppose the wind field. Sullivan et al. (2008) performed a CFD experiment simulating wind flow over waves. Using a large eddy approach (LES), they were able to resolve the momentum fluxes and study the different variances, showing that the waves impact the distribution of turbulent energy over the whole marine boundary layer (MBL) [2]. When planning offshore wind farms the possible impact of wave modified turbulence such as the one Sullivan et al. demonstrated, is only briefly considered. It is thus important to investigate if wave modified MBL-turbulence has a significant impact on offshore wind turbines loads and performance. The wave-wind interaction will also influence the offshore turbine wakes. Wakes offshore are expected to be of particular interest because the offshore wind farms are large and the wake can be more persistent due the lower turbulence regime often located in offshore wind sites [3].

3 METHOD

OpenFOAM is an open source computational toolbox containing various applications and utilities for CFD simulations. The main advantages of OpenFOAM are its flexible structure allowing the user to freely access and modify the code, as well as the option to run on multiple processors without additional license costs.

ANSYS/FLUENT is the market leading commercial CFD code, well known within the simulation community. The code is applicable to most CFD problems, and contains sophisticated mesh methods like e.g. sliding mesh together with numerous choices of physical and numerical models.

In order to be able to study wave-wind interactions and possible implications on turbine wakes and loads using open source CFD, the following steps will be addressed;

- Establish methods for wake simulations in OpenFOAM and test the validity of the different methods.
- Develop a set up that are able to simulate atmospheric boundary layer (ABL) conditions in OpenFOAM.
- Establish methods for implementation of a moving wave surface in the ABL domain in OpenFOAM.
- Establish methods for load investigations. This can to some existent be done using OpenFOAM, but the blade element method traditionally used for load and fatigue investigations should also be utilised.

In this work we will concentrate on the first task. An ultimate goal is to include turbines in the CFD domain. For these purposes, a two-folded track is pursued. To simulate loads on turbines, the turbine blades must be resolved in the CFD domain. Acona Flow Technology has studied a fully resolved wind turbines using the sliding mesh capabilities in ANSYS/FLUENT, and the company is currently developing a similar representation within OpenFOAM. For studying wakes it would be interesting to

have multiple turbines present in the wakes, and the simpler actuator disk approach available in OpenFOAM will be used here. The two methods will be compared in analysing the wake from a single turbine.

Both turbine representations will be tested in the NOWITECH/NORCOWE wind turbine blind test in the wind tunnel of NTNU [4]. Here a turbine with a 0.89 m diameter rotor will be tested in uniform wind of 10 m/s and turbulence intensity of 0.3%. The experimental result will be available in October and the organizers will compare the results. In the following, preliminary results for the two different wake-simulation approaches will be compared.

3.1 Actuator disk method and set up

The actuator disk method is based on the simple momentum theory [5], and the turbine with the NREL sb26 air foil is represented by a "disk" which extracts momentum from the flow. Disk area (D), power coefficient (C_P) and trust coefficient (C_T) are input values to the model. Values for C_P and C_T were obtained from a performance test of the wind turbine [6] where these values were measured. The simulations were performed for tip speed ratios (λ) 3, 6 and 10 using a steady-state solver for incompressible, turbulent flow, with an external source in the momentum equation and utilising the standard k-ε model [7].

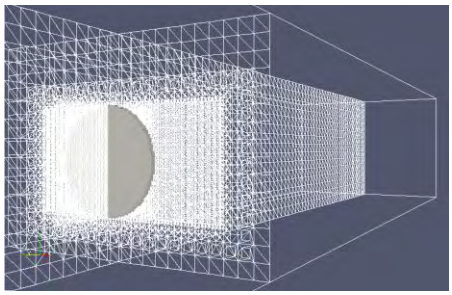

Figure 1: Actuator disk domain, 11.15 m, 2.71 m and 1.851 m. The actuator disk is located 3.66 m downstream the inlet and visualised as a 0.04 m thick disk. The mesh is refined in an area near the disk and in total the number of cell is 1.7 million.

3.2 Resolved turbine with moving mesh

The fully resolved turbine simulations utilise the sliding mesh technology for modelling the motion of the rotor. With this concept, the rotating parts of the turbine are encapsulated in a separate fluid zone which during the simulation is rotated physically according to the rotor motion. The mesh is thus allowed to slide relatively to the rest of the mesh, interacting only through predefined interfaces. This means that transient simulations are required.

Figure 2 shows the mesh, which is created using tetrahedrons, but converted to polyhedrons before the actual simulations to reduce the number of cells and increase calculation speed. After conversion the number of cells just exceeds two million. Since the simulations are transient and quite computer intensive, only the simulations for tip speed ratio (λ) 6 will be reported on.

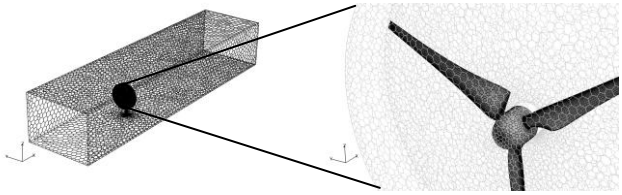

Figure 2: The geometry of the turbine was created based on NOWITECH/NORCOVE input and the mesh generated with ANSYS meshing tools. There is a rotation frame around the rotor, seen in the exploded view to the right.

4 RESULTS

Sample values of the velocity (U) for the two distinct methods were extracted along a horizontal line through the wake centre and through diagonals at positions X/D=1, 3 and 5, together with values for the turbulent kinetic energy (k). While the actuator disk method needs C_P and C_T as input the resolved turbine methods calculates these. Values are extracted and compared with measurements given in [6]. These values also compare well against the predicted level of C_P and C_T from the fully resolved simulation.

4.1 Velocity reductions and turbulence in the wake

Of the three simulated cases with different tip speed ration λ=6 is the most efficient operating speed of the turbine, see Figure 3. The velocity profile obtained from the fully resolved rotor simulation, shown in the same figure, strongly indicates that this simulation has not reached a pseudo-steady state level required to compare correctly against the actuator disk simulations. Due to limited computer resources, this calculation has only been run for approximately 0.5 seconds simulation time. Still, the level in close vicinity behind the rotor shows some promising tendencies.

Indeed, when obtaining velocity profiles along horizontal lines behind the rotor, as shown in Figure 4, the agreement between the actuator disk and the fully resolved rotor simulation is quite good. There is some discrepancy close to the rotor since the actual rotor house is not included in the simulation using the actuator disk approach. Also, at X/D=5 there is some deviations, due to the incomplete pseudo-steady state for the fully resolved rotor simulation.

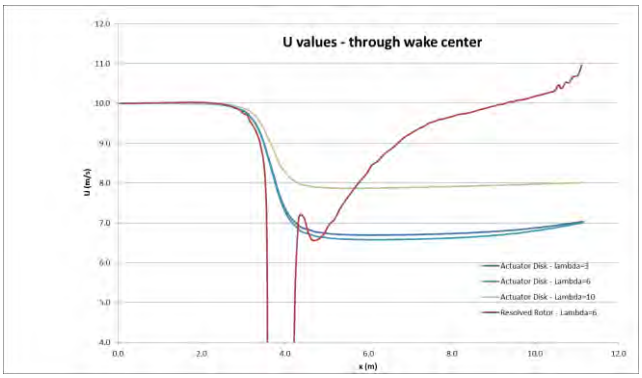

Figure 3: U values through the wake centre of the actuator disk at various tip speed ratios λ, and for the fully resolved rotor simulation at λ=6.

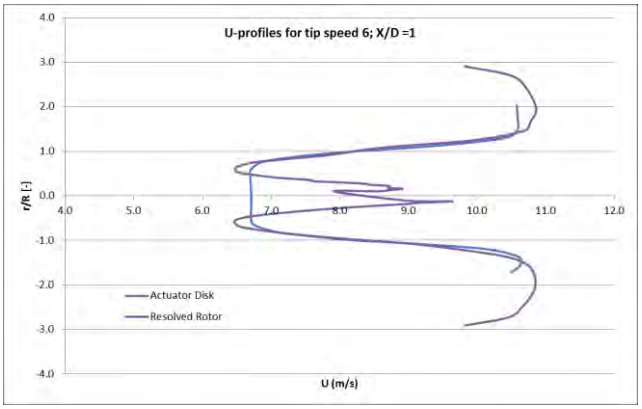

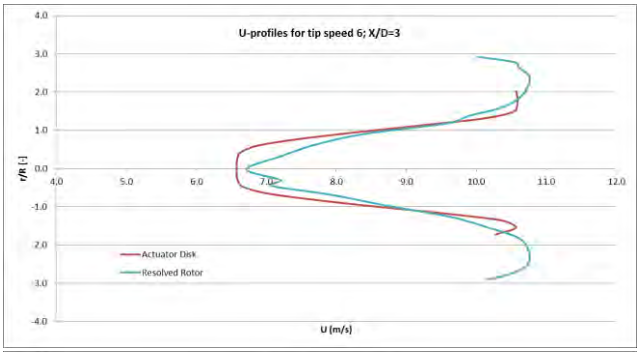

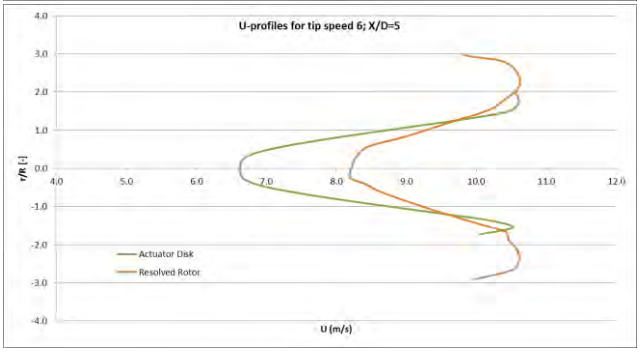

Figure 4: Velocity profiles (U) along horizontal lines through the wake centre for λ=6 at different positions behind the disk.

The profiles for turbulent kinetic energy (k), of which the one at X/D=1 is shown in Figure 5, also underline the lack of reaching pseudo-steady state in the fully resolved rotor simulation, and the turbulence level is too low in the vicinity of the rotor tips. The turbulence profile also shows that an extensive amount of turbulence is produced around the rotor house. This is not captured with the actuator disk.

The turbulent profiles also indicate too much turbulence along the walls of the wind tunnel for the fully resolved rotor simulation. During this work, no effort has been devoted to this part of the calculation domain so far. Thus, the resolution along the walls is too coarse, resulting in high y^+-values and too high turbulence production in this area.

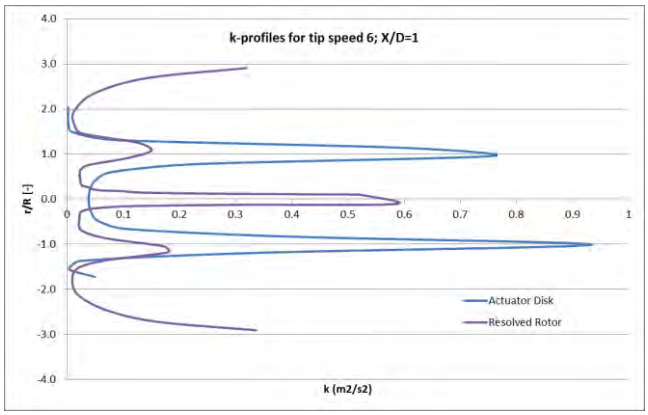

Figure 5: Profiles of turbulent kinetic energy (k) along a horizontal line through the wake centre at X/D=1.

Finally, a contour plots showing velocity and turbulence for the fully resolved calculation is included in Figures 6 and 7. The influence of the rotor is obvious. Also note the influence of the turbine tower, which is the reason for plotting profiles and comparing results along horizontal lines through the wake centre.

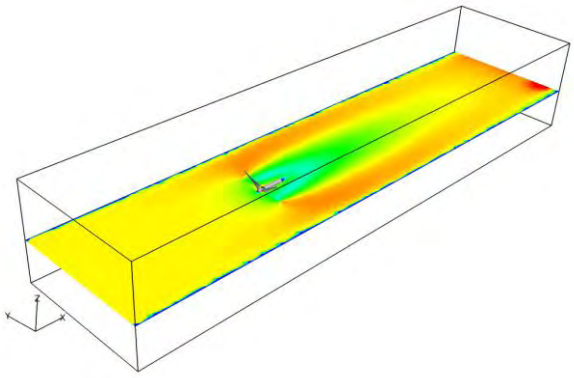

Figure 6: U values through the wake centre of the actuator disk. At the end of the wind tunnel the velocity decrease is 69% of the inlet velocity for λ=6.

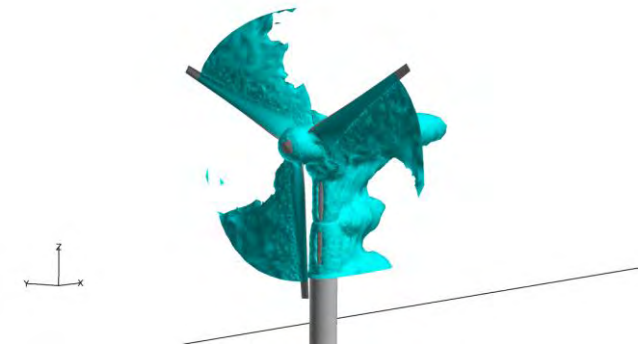

Figure 7: U values through the wake centre of the actuator disk. At the end of the wind tunnel the velocity decrease is 69% of the inlet velocity for λ=6.

5 Discussions and Conclusions

A wind turbine based on the NREL sb26 air foil placed in a wind tunnel has been simulated using an actuator disk approach, and complemented with fully resolved rotor simulations. There are some discrepancies between the predictions of velocity and turbulent kinetic energy in the wake behind the turbine, but the results are promising. Much of the deviations are contributed to the lack of reaching a pseudo-state solution for the fully resolved rotor simulation.

The simulations indicate that the turbulence due to turbine tower and rotor house could be significant and important. This contribution is not included in the actuator disk approach, but might be considered in future work. Assessment of the actuator line method might also be included later.

References

[1] OpenFOAM; http://www.openfoam.com/

[2] Sullivan et al., "Large-eddy simulations and observations of atmospheric marine boundary layers above non-equilibrium surface waves." Journal of the Atmospheric Sciences 65(4): 1225-1245. 2008.

[3] Barthelmie et al. "ENDOW (efficient development of offshore wind farms): modelling wake and boundary layer interactions." Wind Energy 7(3): 225-245., 2004.

[4] Krogstad et al., "Blind test" Workshop, Department of Energy and Process Engineering, NTNU, 30 March 2011.

[5] Manwell et al., "Wind Energy Explained", Wiley, 2002.

[6] Krogstad et al., "Performance of a model wind turbine", 17th Australian Fluid Mechanics Conference, New Zealand, 2010.

[7] Launder and Spalding, "The numerical computation of turbulent flows", "The numerical computation of turbulent flows." Computer Methods in Applied Mechanics and Engineering, 1974

[8] ANSYS/FLUENT; http://www.ansys.com/

Session 3B

Control Systems

LPV Identification of Wind Turbines and Wind Parks
P.M.O. Gebraad, J.W. van Wingerden, M. Verhaegen

A Framework for Structured LPV Control of Wind Turbines
Fabiano Daher Adegas, Jakob Stoustrup, Torben Knudsen

Model Predictive Individual Pitch Control Based on Local Inflow Measurements
Knud A. Kragh, Morten H. Hansen

LPV Identification of Wind Turbines and Wind Parks

P.M.O. Gebraad, J.W. van Wingerden, M. Verhaegen
Delft Center for Systems and Control, Delft University of Technology
Mekelweg 2, Delft, The Netherlands
E-mail: {p.m.o.gebraad, j.w.vanwingerden, m.verhaegen}@tudelft.nl

Keywords: Control Systems, System Identification, Wind Turbine Rotor Dynamics, Wind Parks

1 Introduction

Linear Parameter Varying (LPV) models are linear time-varying model structures that describe the dynamical relation between the input and output signals of a system, where the relation itself depends on scheduling signals. These model structures have great potential in the field of wind energy, as wind turbines can be characterized as LPV systems, with for example wind speed, pitch angle and rotor speed as scheduling signals. It is possible to design an LPV controller that provides guarantees of performance for operating conditions varying throughout the operating region of the scheduling, [1]. Currently, LPV wind turbine control has been restricted to simulation examples based on simplified first-principle models. Part of the development towards applying the LPV control techniques to real-life wind turbines, is the derivation of accurate LPV wind turbine models needed for LPV control synthesis. Deriving these models with identification methods, which estimate models directly from input-output data, provides the possibility to use adaptive control.

LPV system identification techniques are in a state of development. LPV subspace algorithms have great potential in this field, as they derive models in the state-space form suited for LPV control design. This overview paper will discuss the state-of-the-art predictor-based subspace identification algorithm first introduced in [2] in Section 2, and the iterative subspace techniques of [8] in Section 3.

2 LPV Predictor-Based System Identification

The LPV state-space model structure will be explained in more detail in Section 2.1. In Section 2.2, we explain how LPV Predictor-Based System Identification (LPV PSBID) finds the model parameters through solving linear least-squares problems, based on a factorization of predictors which are a function of past input, output and scheduling data. Some contributions regarding dimensionality and regularization issues are treated in Section 2.3 and 2.4. In Section 2.5, 2.6 and 2.7, case studies are presented in which we apply the algorithms in identification experiments on subsystems of the wind turbine.

2.1 Model structure

LPV PBSID finds discrete-time deterministic-stochastic LPV state-space models in the innovation form:

$$x_{k+1} = \sum_{i=1}^{m} \mu_k^{(i)} \left(A^{(i)} x_k + B^{(i)} u_k + K^{(i)} e_k \right), \tag{1}$$

$$y_k = C x_k + D u_k + e_k, \tag{2}$$

where k is the time index, and $x_k \in \mathbb{R}^n$, $u_k \in \mathbb{R}^r$, $y_k \in \mathbb{R}^\ell$, are the state, input and output vectors. The matrices $A^{(i)} \in \mathbb{R}^{n \times n}$, $B^{(i)} \in \mathbb{R}^{n \times r}$, $C \in \mathbb{R}^{\ell \times n}$, $D \in \mathbb{R}^{\ell \times r}$, are the local state, input, output and direct feedthrough matrices. The vector $e_k \in \mathbb{R}^\ell$ denotes a zero mean white innovation process and $K^{(i)} \in \mathbb{R}^{n \times \ell}$ are observer gain matrices. In the state equation (1), the state, input and observer gain matrices, resp. A, B, and K, depend affinely on the time-varying scheduling parameters $\mu_k^{(i)} \in \mathbb{R}$, collected in a scheduling vector $\mu_k \in \mathbb{R}^m$ of the form:

$$\mu_k = \begin{bmatrix} 1, & \mu_k^{(2)}, & \cdots, & \mu_k^{(m)} \end{bmatrix}^T. \tag{3}$$

For notational simplicity, we assume a parameter-independent output equation (2), but the method can be extended to parameter-varying output equations.

2.2 Algorithm overview

LPV PBSID finds the system matrices $A^{(i)}, B^{(i)}, K^{(i)}$ and C, D from signals u_k, y_k, μ_k measured for $k = \{1, \ldots, N\}$. As an intermediate step, the state sequence is found. The algorithm is based on rewriting (1)-(2) in the predictor form:

$$x_{k+1} = \sum_{i=1}^{m} \mu_k^{(i)} \left(\tilde{A}^{(i)} x_k + \tilde{B}^{(i)} u_k + K^{(i)} y_k \right), \tag{4}$$

$$y_k = C x_k + D u_k + e_k, \tag{5}$$

with $\tilde{A}^{(i)} = A^{(i)} - K^{(i)} C$ and $\tilde{B}^{(i)} = B^{(i)} - K^{(i)} D$. Equation (4) can be rewritten using the Kronecker product $\otimes$, as:

$$x_{k+1} = \bar{A}(\mu_k \otimes x_k) + \bar{B}(\mu_k \otimes u_k) + \bar{K}(\mu_k \otimes y_k), \tag{6}$$

with stacked matrix $\bar{A} = \left[\tilde{A}^{(1)}, \cdots, \tilde{A}^{(m)} \right]$, and $\bar{B}$, $\bar{K}$ defined similarly. We can then choose a past window p, and relate the state at time $k+p$ to past input, output and scheduling data:

$$x_{k+p} = \phi_{p,k} x_k + \mathscr{K}_p z_k^p, \tag{7}$$

with transition matrix $\phi_{p,k}$, extended LPV controllability matrix $\mathscr{K}^p$ and regressor vector z_k^p defined as:

$$\phi_{p,k} = \tilde{A}_{k+p-1} \cdots \tilde{A}_{k+1} \tilde{A}_k, \text{ with } \tilde{A}_k = \sum_{i=1}^{m} \mu_k^{(i)} \tilde{A}^{(i)}, \tag{8}$$

$$\mathscr{K}^p = \left[\begin{array}{cccc} \mathscr{L}_p, & \ldots, & \mathscr{L}_1 \end{array} \right] \in \mathbb{R}^{n \times \tilde{q}}, \text{ with} \quad (9)$$

$$\mathscr{L}_1 = \left[\begin{array}{cccccc} \tilde{B}^{(1)}, & K^{(1)}, & \cdots, & \tilde{B}^{(m)}, & K^{(m)} \end{array} \right],$$

$$\mathscr{L}_p = \left[\begin{array}{ccc} \tilde{A}^{(1)}\mathscr{L}_{p-1}, & \cdots, & \tilde{A}^{(m)}\mathscr{L}_{p-1} \end{array} \right],$$

$$z_k^p = \begin{bmatrix} \mu_{k+p-1} \otimes \ldots \otimes \mu_{k+1} \otimes \mu_k \otimes \begin{bmatrix} u_k \\ y_k \end{bmatrix} \\ \mu_{k+p-1} \otimes \ldots \otimes \mu_{k+1} \otimes \begin{bmatrix} u_{k+1} \\ y_{k+1} \end{bmatrix} \\ \vdots \\ \mu_{k+p-1} \otimes \begin{bmatrix} u_{k+p-1} \\ y_{k+p-1} \end{bmatrix} \end{bmatrix} \in \mathbb{R}^{\tilde{q}}. \quad (10)$$

with the size $\tilde{q}$ given by:

$$\tilde{q} = (r+l)\sum_{j=1}^{p} m^j. \quad (11)$$

For a stable predictor, we can choose the past window p large enough such that $\phi_{p,k} \approx 0$, i.e. $x_{k+p} \approx \mathscr{K}^p z_k^p$ and $y_{k+p} \approx C\mathscr{K}_p z_k^p + Du_{k+p} + e_{k+p}$. Now we define the stacked matrices U, Y, and Z:

$$U_p^N = \left[\begin{array}{ccc} u_{p+1}, & \cdots, & u_N \end{array} \right], \quad (12)$$

$$Y = \left[\begin{array}{ccc} y_{p+1}, & \cdots, & y_N \end{array} \right], \quad (13)$$

$$Z = \left[\begin{array}{ccc} z_1^p, & \cdots, & z_{N-p}^p \end{array} \right]. \quad (14)$$

If $\left[\begin{array}{cc} Z^T, & U^T \end{array} \right]^T$ has full row rank, the parameters $C\mathscr{K}^p$ and D can be estimated by solving the following least squares parameter estimation problem in which we minimize the prediction error:

$$\min_{C\mathscr{K}^p, D} ||Y - C\mathscr{K}^p Z - DU||_F, \quad (15)$$

where $||\cdots||_F$ represents the Frobenius norm. From $C\mathscr{K}^p$, we can approximate the product of the extended observability matrix Γ_p of the first local model, defined as:

$$\Gamma_p^T = \left[\begin{array}{cccc} C^T, & \left(CA^{(1)}\right)^T, & \ldots, & \left(C\left(A^{(1)}\right)^{p-1}\right)^T \end{array} \right], \quad (16)$$

and the extended controllability matrix $\mathscr{K}_p$, by constructing:

$$\Gamma^p \mathscr{K}^p \approx \begin{bmatrix} C\mathscr{L}_p & C\mathscr{L}_{p-1} & \cdots & C\mathscr{L}_1 \\ 0 & C\tilde{A}^{(1)}\mathscr{L}_{p-1} & \cdots & C\tilde{A}^{(1)}\mathscr{L}_1 \\ & & \ddots & \\ 0 & & & C\left(\tilde{A}^{(1)}\right)^{p-1}\mathscr{L}_1 \end{bmatrix}. \quad (17)$$

The zeros appear in this equation based on the approximation that $\phi_{j,k} \approx 0$ for all $j \geq p$. Now we can compute $\Gamma^p \mathscr{K}^p Z$, which equals by definition the extended observability matrix times the state sequence, $\Gamma^p X$, where

$$X = [x_{p+1}, \ldots, x_N]. \quad (18)$$

Under the assumptions that X and Γ^p both have full rank and that $p\ell > n$, we estimate the state sequence and the order of the system based on a rank revealing Singular Value Decomposition (SVD):

$$\widehat{\Gamma^p \mathscr{K}^p} Z = \left[\begin{array}{cc} \mathscr{U} & \mathscr{U}_\perp \end{array} \right] \begin{bmatrix} \Sigma_n & 0 \\ 0 & \Sigma \end{bmatrix} \begin{bmatrix} \mathscr{V} \\ \mathscr{V}_\perp \end{bmatrix}, \quad (19)$$

where Σ_n is the diagonal matrix containing the n largest singular values; and $\mathscr{V}$ is the corresponding row space. The system order n is found by detecting a gap between the singular values, and the state sequence is estimated (up to a similarity tranformation) by:

$$\widehat{X} = \Sigma_n \mathscr{V}. \quad (20)$$

Once we have an estimate of the state sequence, the problem of finding the system matrices $A^{(i)}$, $B^{(i)}$, C and D in the model (1)- (2) is a linear least squares problem. Further, we can find the observer gains $K^{(i)}$ stabilizing the predictor (4)-(5) using H_∞ synthesis techniques.

2.3 Kernel method

The method described above suffers from a curse of dimensionality, as $\tilde{q}$, the number of rows in data matrix Z, grows exponentially with the size of the past window p, see equation (11). An effective way to reduce the dimensionality of the regression problem is to use a kernel method. It assumes that the solution to the estimation problem (15) is of the form:

$$\left[\begin{array}{cc} C\mathscr{K}^p, & D \end{array} \right] = \alpha \left[\begin{array}{cc} Z^T & U^T \end{array} \right]. \quad (21)$$

This results into a dual of problem (15), given by:

$$\min_{\alpha} \left(\|Y - \alpha\Phi\|_F^2 \right), \quad (22)$$

where $\Phi = Z^T Z + U^T U \in \mathbb{R}^{(N-p)\times(N-p)}$. When $\tilde{q} > N - p$, using the kernel method improves the numerical efficiency of the identification algorithm, as it reduces the size of the data matrices. In [2], schemes are given to efficiently build the matrix Φ from data, and construct the matrix $\widehat{\Gamma^p \mathscr{K}^p} Z$ from α.

2.4 Regularization techniques and sparse estimation

If the parameter matrix $C\mathscr{K}^p$ or α is estimated with a limited ammount of data N, this leads to an ill-posed parameter estimation problem (15) or (22), making the solution non-unique or sensitive to measurement error. The past window p is an important factor influencing the conditioning of the parameter estimation problem: the bias due to the approximation $\phi_{p,k} \approx 0$ is decreased by choosing a larger p, but by doing this, the number of parameters to be estimated grows exponentially, increasing the variance error due to noise. In principle many types of additional information about the desired solution can be incorporated in order to stabilize the ill-posed problem and make its solution less sensitive to noise.

A) Conventional 2-norm regularization techniques

Conventional 2-norm regularization techniques such as Tikhonov regularization are often used to modify the ill-posed parameter estimation problem. These general-purpose regularization methods give preference to a solution with a small 2-norm.

B) Rank minimizing regularization

An other possibility for regularization is based on a minimum order requirement for the resulting LPV model. This translates into a minimum rank requirement on $\Gamma^p \mathscr{K}^p$, the matrix from which the state sequence is found through (20).

By using the nuclear norm as a heuristic for the rank of this matrix, the problem of finding $C\mathscr{K}^p$ or α remains a convex problem. In [5] we explain the nuclear norm regularization in more detail.

C) Sparse estimation

As a rule of thumb, p can be chosen within a small factor (2 to 4) of the system order n to come to a well-posed problem without using more samples than strictly necessary. However, in general we cannot assume the system order to be known beforehand. Note that for a stable system (4)-(5), $C\mathscr{K}_p$ has a decaying structure, since the blocks $\mathscr{L}^i \to 0$ as $i \to \infty$. Hence, if p is chosen too large, insignificant elements in the left part of matrix $C\mathscr{K}_p$ can be set to zero in order to overcome the problem of overparameterization. This sparsity is imposed by posing the parameter estimation as a Basis Pursuit DeNoise (BPDN) problem:

$$\begin{aligned} &\min \left\| \begin{bmatrix} C\mathscr{K}_p, & D \end{bmatrix} \right\|_{2,1}, \\ &\text{s.t. } \left\| Y - C\mathscr{K}_p Z - DU \right\|_F \leqslant E_0 (1+\varepsilon), \end{aligned} \tag{23}$$

where $\|\cdot\|_{2,1}$ denotes the sum of the two-norms of columns of a matrix, E_0 is the residual norm of the parameter estimation problem without regularization (15), and $\varepsilon > 0$ is a trade-off parameter. In the case study in Section 2.6, we use the SPGL1 solver [6] to solve problem (23).

2.5 Case study: LPV identification of a smart rotor blade.

The LPV subspace identification algorithm is applied to a two-dimensional model of a smart rotor blade in [4]. This is an airfoil with a control surface at the trailing edge. Several studies propose to control loads on the wind turbine by using smart rotor blades, see e.g. [3]. An issue in controlling the smart airfoil is that its dynamics are strongly dependent on the free stream wind speed. In [4] an LPV identification experiment is presented that finds the simplified second order dynamics between the control input, the angle of the control surface, and other mechanical degrees of freedom, being the plunge and pitch of the blade, as outputs. The free stream wind speed and its square is used as scheduling.

2.6 Case study: LPV identification of the flapping dynamics of a rotor blade using sparse estimation.

In Section 3.8.1 of [3] an LPV identification experiment is presented on a second order model that might represent the simplified out-of-plane dynamics of a flexible rotor blade of a fixed-speed wind turbine, using the the blade rotation angle as scheduling. In [3], the order was assumed to be known beforehand, and the past window was chosen accordingly as $p = 8$. Figure 1(a) shows that without regularization, the quality of the identified model may decrease for other choices of the past window p. The quality is expressed in the Variance Accounted For (VAF) for a set of input and scheduling data different from the identification data. The VAF value is defined as:

$$\text{VAF} = \max\left\{0, \left(1 - \frac{\text{var}\,(\hat{y}_k - y_k)}{\text{var}\,(y_k)}\right) 100\%\right\}$$

where $\hat{y}_k$ is the estimated system output, and y_k is the output from the true model. We used a small data set, $N = 50$, and added process and measurement noise with a Signal-To-Noise ratio of 20 dB. When performing the same identification experiment again using the sparse estimation approach of section 2.4.C, the quality of the estimated model remains at approximately the same level for a large range of the past window p, see Figure 1(b). This demonstrates that sparse estimation enables estimating the model without prior knowledge of the model order, or tuning of p.

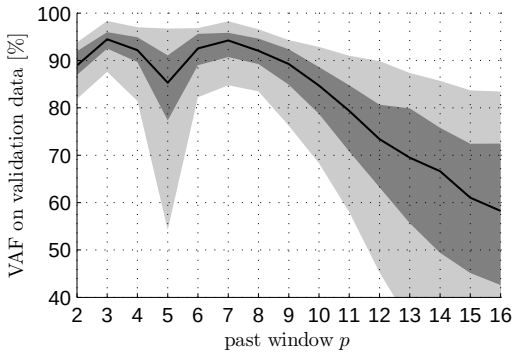

(a) Without regularization

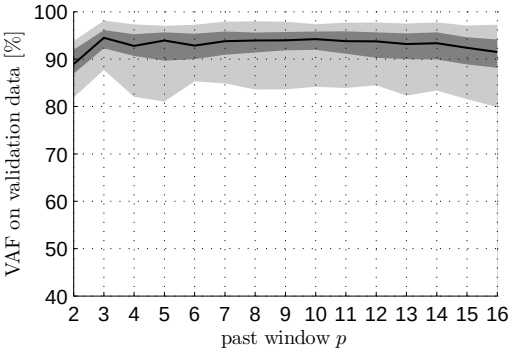

(b) With sparse estimation

Figure 1: Mean VAF (black line) of model estimates in Case Study 2.6 for 80 Monte-Carlo experiments with different realizations of the noise and input sequences, for a range of past windows p. The light gray region are the 5th-95th percentiles, the dark gray region are the 25th-75th percentiles of the VAF values.

2.7 Case study: LPV identification of wind turbine rotor edgewise vibrations.

In [7] we identify from input-output data an LPV model capturing the rotor speed dependent coupled dynamics of the drive-train and the edgewise bending motion of the rotor blades of 3-bladed wind turbines. The rotor blade pitch actuation is used to excite a structural mode pair of the rotor known as the edgewise forward and backward whirling modes. The deflection shapes of these modes are shown in Figure 2. The pure whirling modes consist of oscillations where two blades are bending in opposed directions in the rotor plane, and one blade is standing still. The bending oscillations of the blades are combinations of these pure modes. By applying the Multiblade Coordinate transformation on the bending moments of each blade $\{M_i\}_{i=1}^3$, the bending oscillations of each blade can be expressed in a

ground-fixed (non-rotating) frame:

$$y = \frac{2}{3}\left(M_1 \sin(\phi) + M_2 \sin\left(\phi + \frac{2\pi}{3}\right) + M_3 \sin\left(\phi + \frac{4\pi}{3}\right)\right) \tag{24}$$

where ϕ is the azimuth angle of the first rotor blade. The resulting coordinate y expresses the vertical reaction force of the ground-fixed system. Hence, it expresses how the combined motion of all blades propagates to the fixed system, causing vertical motion of the rotor hub and its supporting structure. The natural frequencies of the whirling modes in the coordinate y are given by $\omega \pm \varphi$, where ω is the natural bending frequency of the blades, and φ is the rotor speed. An LPV model identified from data generated by the GH Bladed wind turbine simulator [9], captures this rotor speed dependency of the rotor dynamics between the pitch input and the output y, see Figure 3. In [7] the results are presented for a similar identification experiment with a real wind turbine.

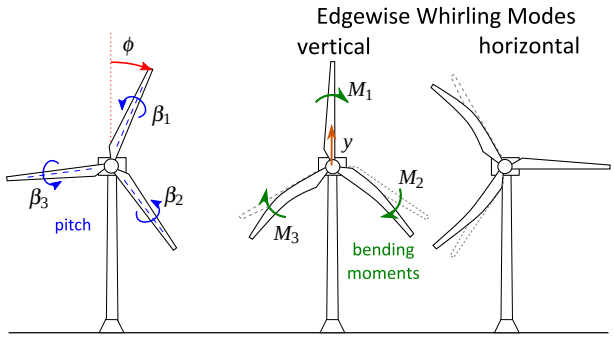

Figure 2: Wind turbine rotor edgewise vibrations

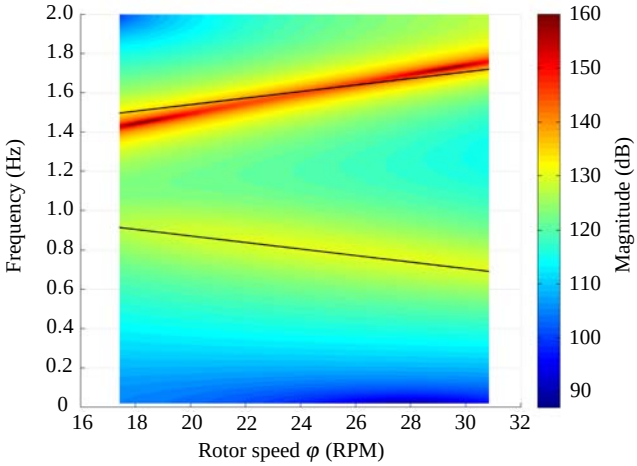

Figure 3: The frequency response of a 4th order LPV model identified from data generated by a GH Bladed wind turbine simulation. The black lines are the natural frequencies of the whirling modes $\omega \pm \varphi$, with the natural bending frequency ω estimated at 1.2 Hz.

3 Iterative LPV System Identification

Another approach to identify LPV state-space models is by iterative methods [8], where in each iteration the identification problem is reduced to an LTI system identification problem:

$$x_{k+1}^{[i]} = A_1 x_k^{[i]} + \bar{A}\left(\bar{\mu}_k \otimes x_k^{[i-1]}\right) + \bar{B}(\mu_k \otimes u_k) + K e_k,$$
$$y_k = C_1 x_k^{[i]} + \bar{C}\left(\bar{\mu}_k \otimes x_k^{[i-1]}\right) + \bar{D}(\mu_k \otimes u_k) + e_k,$$

with $\bar{\mu}_k^T = \left[\mu_k^{(2)}, \ldots, \mu_k^{(m)}\right]$, $\bar{A} = [A_2, \ldots, A_m]$ and $\bar{B}$, $\bar{C}$, $\bar{D}$ defined similarly, and with $x_k^{[i]}$ the state sequence estimate from iteration i. By this reduction, the problem of dimensionality appearing in predictor-based algorithms is circumvented. A disadvantage is that for convergence to a consistent model estimate, it requires certain correlation properties of the scheduling and input excitation signals. In many applications in wind energy, we cannot manipulate these signals to have these properties, and therefore research aims to overcome these restrictions.

3.1 Extension to distributed system identification

We see potential to extend the iterative LPV identification methods to networks of interconnected LPV systems, modelling the aerodynamic interaction between wind turbines in a wind park, as part of the FLOW program [10]. We can use state predictions from neighbouring system estimates, to iteratively model interaction in the network.

References

[1] K.Z. Østergaard. Robust, Gain-Scheduled Control of Wind Turbines, 2008.

[2] J.W. van Wingerden and M. Verhaegen. Subspace identification of bilinear and LPV systems for open- and closed-loop data. Automatica, 45(2), 2009.

[3] J.W. vanWingerden, Control of wind turbines with smart rotors: proof of concept and LPV subspace identification. PhD thesis, Delft University of Technology, 2008.

[4] P.M.O. Gebraad, J.W. van Wingerden, G.J. van der Veen and M. Verhaegen. LPV identification of an aeroelastic flutter model. 49th IEEE Conf. on Decision and Control, Atlanta, USA, 2010.

[5] P.M.O. Gebraad, J.W. van Wingerden, G.J. van der Veen and M. Verhaegen. LPV subspace identification using a novel nuclear norm regularization method. American Control Conf., San Francisco, USA, 2011.

[6] E. van den Berg and M. P. Friedlander. Probing the Pareto frontier for basis pursuit solutions, SIAM Journal on Scientific Computing, 2008.

[7] P.M.O. Gebraad, J.W. van Wingerden, P.A. Fleming and A.D. Wright. LPV subspace identification of the edgewise vibrational dynamics of a wind turbine rotor. IEEE Multiconf. on Systems and Control, Denver, USA, 2011.

[8] P. Lopes dos Santos et al. Identification of LPV systems using successive approximations. 47th IEEE Conf. on Dec. and Control, Cancún, Mexico, 2008.

[9] http://gl-garradhassan.com/en/GHBladed.php

[10] Far and Large Offshore Wind, http://www.flow-windpark.nl

A Framework for Structured LPV Control of Wind Turbines

Fabiano Daher Adegas, Jakob Stoustrup, Torben Knudsen
Automation and Control Section, Aalborg Universitet
Fredrik Bajers Vej 7C 9220-DK, Denmark
E-mail: {fda, jakob}@es.aau.dk

Keywords: wind turbine, structured control, gain-scheduling, linear parameter varying.

1 Introduction

Handling known parameter-dependencies, unknown parameter variations, and faults, constitute the main challenges for the application of wind turbine control, calling for a generic and powerful tool to manage parameter-variations and model uncertainties. The new modeling and controller design procedures presented in this paper are serious candidates for solving a majority of practical wind turbine control problems, provided a sufficiently good model of the wind turbine is available. The procedures are based on a linear parameter-varying (LPV) modeling and control framework. We believe that the resulting controller can be easily implemented in practice due to the following reasons:

1. **Structured controller:** the controller structure can be chosen arbitrarily. Decentralized, dynamic (full or reduced-order) output feedback, static output feedback are among the possible structures.
2. **Low data storage:** the required data to be stored in the control computer memory is only the controller matrices, and scalar functions of the scheduling variables representing plant nonlinearities (aerodynamic gains).
3. **Simple math operations:** the mathematical operations needed to compute the controller gains at each sampling time are look-up tables with interpolation, products between a scalar and a matrix, and sums of matrices.

2 Wind Turbine LPV Model

A linearization-based LPV model is obtained by classical linearization around the operating points. A first order Taylor series expansion of the nonlinear torque and thrust equations leads to the following linearized representations,

$$Q_{\mathrm{a}} \approx \overline{Q}_{\theta_{op}} + \left.\frac{\partial Q_{\mathrm{a}}}{\partial V}\right|_{\theta_{op}} \hat{V}(t) + \left.\frac{\partial Q_{\mathrm{a}}}{\partial \Omega_{\mathrm{r}}}\right|_{\theta_{op}} \hat{\Omega}_{\mathrm{r}}(t) + \left.\frac{\partial Q_{\mathrm{a}}}{\partial \beta}\right|_{\theta_{op}} \hat{\beta}(t) \tag{1a}$$

$$T_{\mathrm{a}} \approx \overline{T}_{\theta_{op}} + \left.\frac{\partial T_{\mathrm{a}}}{\partial V}\right|_{\theta_{op}} \hat{V}(t) + \left.\frac{\partial T_{\mathrm{a}}}{\partial \Omega_{\mathrm{r}}}\right|_{\theta_{op}} \hat{\Omega}_{\mathrm{r}}(t) + \left.\frac{\partial T_{\mathrm{a}}}{\partial \beta}\right|_{\theta_{op}} \hat{\beta}(t) \tag{1b}$$

where $\overline{Q}_{\theta_{op}}$ and $\overline{T}_{\theta_{op}}$ are equilibrium components of the aerodynamic torque and thrust, respectively, $\hat{\Omega}_{\mathrm{r}}(t)$ is the rotor angular speed, $\hat{V}(t)$ is the wind disturbance, $\hat{\beta}(t)$ is the pitch angle, and $\hat{(\cdot)}$ stands for small signal values. The partial derivaties of torque and thrust are hereafter called aerodynamic gains. Aerodynamic torque Q_{a} drives a two-inertial drive train model given by

$$\begin{aligned} J_{\mathrm{r}}\dot{\Omega}_{\mathrm{r}}(t) &= Q_{\mathrm{a}}(t) - N_{\mathrm{g}}B_{\mathrm{s}}\left(N_{\mathrm{g}}\Omega_{\mathrm{r}}(t) - \Omega_{\mathrm{g}}(t)\right) - N_{\mathrm{g}}K_{\mathrm{s}}\delta_{\Omega}(t) \\ J_{\mathrm{g}}\dot{\Omega}_{\mathrm{g}}(t) &= -Q_{\mathrm{g}}(t) - +B_{\mathrm{g}}\left(N_{\mathrm{g}}\Omega_{\mathrm{r}}(t) - \Omega_{\mathrm{g}}(t)\right) + K_{\mathrm{s}}\delta_{\Omega}(t) \\ \dot{\delta}_{\Omega}(t) &= N_{\mathrm{g}}\Omega_{\mathrm{r}}(t) - \Omega_{\mathrm{g}}(t) \end{aligned} \tag{2}$$

where $\Omega_{\mathrm{r}}(t)$ and $\Omega_{\mathrm{g}}(t)$ are the rotor and generator speed, J_{r} and J_{g} are low speed and high speed shaft inertias, N_{g} is the gear ratio, K_{s} and torsion stiffness are torsion stiffness and damping, respectively, $\dot{\delta}_{\Omega}(t)$ is the torsional angle, $Q_{\mathrm{g}}(t)$ is the torque applied to the generator. Friction coefficients are neglected. The thrust T_{a} acting on the rotor introduces fore-aft tower bending described by the axial nacelle linear translation $q(t)$. Sideward tower movements are ignored. The tower translates in the same direction as the wind, therefore aerodynamic torque and thrust are in fact driven by the relative wind speed $V(t) = V_w(t) - \dot{q}(t)$. The tower dynamics is modeled as a mass-spring-damper system,

$$M_{\mathrm{t}}\ddot{q}_{\mathrm{t}}(t) = T_{\mathrm{a}}(t) - B_{\mathrm{t}}\dot{q}_{\mathrm{t}}(t) - K_{\mathrm{t}}q_{\mathrm{t}}(t) \tag{3}$$

where M_{t} is the modal mass of the first fore-aft tower bending mode, B_{t} is structural damping coefficient, and K_{t} is the modal stiffness for axial nacelle motion due to fore-aft tower bending. Hydraulic pitch systems are satisfactorily modeled as a second order system,

$$\ddot{\beta}(t) = -2\zeta\omega_{\mathrm{n}}\dot{\beta}(t) - \omega_{\mathrm{n}}^2\beta(t) + \omega_{\mathrm{n}}^2\beta_{\mathrm{ref}}(t) \tag{4}$$

where the natural frequency ω_{n} and damping ratio ζ specify the dynamics of the model, and $\beta_{\mathrm{ref}}(t)$ is the reference angle.

2.1 Faults

Faults in a wind turbine have different degrees of severity and accommodation requirements. A comprehensive list of wind turbine faults is given in [1]. Linear parameter varying control can be applied in the case of failures that gradually change system's dynamics. As an example consider a failure on the pitch system, usually occasioned by pump wear or pump failure, hydraulic leakage or high air content on the oil. The fault changes the pitch system dynamics by varying the damping ratio and natural frequency from their nominal

values ζ_0 and $\omega_{\mathrm{n},0}$ to their faulty values ζ_f and $\omega_{\mathrm{n,f}}$. The parameters change according to a convex combination of the vertices of the parameter sets,

$$\omega_\mathrm{n}^2(\theta_\mathrm{f}) = (1-\theta_\mathrm{f})\omega_{\mathrm{n},0}^2 + \theta_\mathrm{f}\omega_{\mathrm{n,lp}}^2 \tag{5a}$$

$$-2\zeta(\theta_\mathrm{f})\omega_\mathrm{n}(\theta_\mathrm{f}) = -2(1-\theta_\mathrm{f})\zeta_0\omega_{\mathrm{n},0} - 2\theta_\mathrm{f}\zeta_\mathrm{lp}\omega_{\mathrm{n,lp}} \tag{5b}$$

where $\theta_\mathrm{f} \in [0,\,1]$ is an scheduled indicator for the fault with $\theta_\mathrm{f} = 0$ and $\theta_\mathrm{f} = 1$ corresponding to nominal and faulty conditions, respectively.

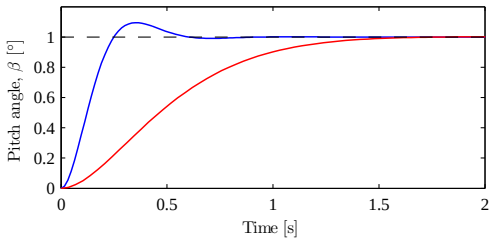

Figure 1: Step responses of hydraulic pitch model under normal (fast) and fault (slow) conditions.

2.2 Uncertainties

Uncertainties are often attributed to the aerodynamics and structural models. Wind turbine aerodynamic properties are commonly computed by Blade Element Momentum (BEM) codes, relying in a simplification of the aerodynamic phenomena and leading to uncertainties. Uncertainty in aerodynamics can be represented as deviations of the nominal aerodynamic gains in a additive way. For example, the pitch to rotor torque gain can be expressed as,

$$\frac{\partial Q}{\partial \beta}(\theta,\alpha) := \left.\frac{\partial Q}{\partial \beta}\right|_{\theta_{op}} + f_l(\alpha) \tag{6a}$$

$$f_l(\alpha) := a_l + b_l\alpha \tag{6b}$$

where a_l, b_l characterizes the additive uncertainty for the l-th aerodynamic gain and α is an uncertainty parameter with lower and upper bounds given by the set,

$$\Lambda = \{\alpha : \underline{\alpha}_i \le \alpha_i \le \overline{\alpha}_i,\, i = 1,\ldots,n_\alpha\}.$$

Figure 2 depicts additive uncertainty on one of the aerodynamic gains.

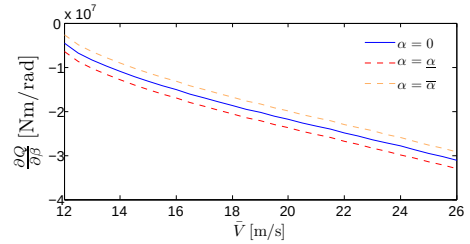

Figure 2: Structured uncertainty on aerodynamic gain.

3 System and Controller Description

The synthesis of LPV controllers are posed similarly to the $\mathscr{H}_\infty$ control of linear systems. The standard state-space interconnections of the LPV model of the plant and the weighting functions is called augmented plant, given by the general continuous-time LPV system description,

$$\begin{aligned}
\dot{x}(t) &= A(\theta(t),\alpha)x(t) + B_w(\theta(t),\alpha)w(t) + B_u(\theta(t),\alpha)u(t)\\
z(t) &= C_z(\theta(t),\alpha)x(t) + D_{zw}(\theta(t),\alpha)w(t) + D_{zu}(\theta(t),\alpha)u(t)\\
y(t) &= C_y(\theta(t),\alpha)x(t) + D_{yw}(\theta(t),\alpha)w(t)
\end{aligned} \tag{7}$$

where $x(t) \in \mathbb{R}^n$ is the state vector, $w(t) \in \mathbb{R}^{n_w}$ is the vector of exogenous perturbation, $u(t) \in \mathbb{R}^{n_u}$ is the control input, $z(t) \in \mathbb{R}^{n_z}$ is the controlled output, and $y(t) \in \mathbb{R}^{n_y}$ is the measured output. $A(\cdot)$, $B(\cdot)$, $C(\cdot)$, $D(\cdot)$ are continuous functions of the time-varying parameter vector $\theta = \begin{bmatrix}\theta_{op} & \theta_f\end{bmatrix}$ and uncertainty parameter vector α. The general case where no restrictions are imposed on the parameter dependence is treated here. It is necessary to choose scalar functions of the varying parameters such that the LPV model of the augmented plant (7) is affine in these functions. That is,

$$\begin{aligned}
\begin{bmatrix} A & B_w & B_u \\ C_z & D_{zw} & D_{zu} \\ C_y & D_{yw} & D_{yu} \end{bmatrix}(\theta,\alpha) &= \begin{bmatrix} A & B_w & B_u \\ C_z & D_{zw} & D_{zu} \\ C_y & D_{yw} & D_{yu} \end{bmatrix}_0 \\
&+ \sum_i \begin{bmatrix} A & B_w & B_u \\ C_z & D_{zw} & D_{zu} \\ C_y & D_{yw} & D_{yu} \end{bmatrix}_i (\rho_i(\theta) + f_i(\alpha)) \\
&+ \sum_m \begin{bmatrix} A & B_w & B_u \\ C_z & D_{zw} & D_{zu} \\ C_y & D_{yw} & D_{yu} \end{bmatrix}_m \theta_{f,m}, \\
i = 1,\ldots,n_\rho, &\quad m = 1,\ldots,n_{\theta_f}.
\end{aligned} \tag{8}$$

where $\rho_i(\theta)$ are scalar functions known as basis functions. The aerodynamic partial derivatives are natural candidates for basis functions related to plant nonlinearities,

$$\rho_1(\theta) := \frac{1}{J_\mathrm{r}}\left.\frac{\partial Q_\mathrm{a}}{\partial \Omega}\right|_{\theta_{op}}, \qquad \rho_2(\theta) := \frac{1}{J_\mathrm{r}}\left.\frac{\partial Q_\mathrm{a}}{\partial V}\right|_{\theta_{op}},$$

$$\rho_3(\theta) := \frac{1}{J_\mathrm{r}}\left.\frac{\partial Q_\mathrm{a}}{\partial \beta}\right|_{\theta_{op}}, \qquad \rho_4(\theta) := \frac{1}{M_\mathrm{t}}\left.\frac{\partial T_\mathrm{a}}{\partial \Omega}\right|_{\theta_{op}},$$

$$\rho_5(\theta) := \frac{1}{M_\mathrm{t}}\left.\frac{\partial T_\mathrm{a}}{\partial V}\right|_{\theta_{op}}, \qquad \rho_6(\theta) := \frac{1}{M_\mathrm{t}}\left.\frac{\partial T_\mathrm{a}}{\partial \beta}\right|_{\theta_{op}},$$

where the division by J_r and M_t is adopted to improve numerical conditioning. The controller synthesis is done in discrete-time. Therefore, the LPV system (7) is discretized resulting in the discrete-time augmented LPV system with state-space realization of the form,

$$\begin{aligned}
x(k+1) &= A(\theta,\alpha)x(k) + B_w(\theta,\alpha)w(k) + B_u(\theta,\alpha)u(k)\\
z(k) &= C_z(\theta,\alpha)x(k) + D_{zw}(\theta,\alpha)w(k) + D_{zu}(\theta,\alpha)u(k)\\
y(k) &= C_y(\theta,\alpha)x(k) + D_{yw}(\theta,\alpha)w(k).
\end{aligned} \tag{9}$$

Assume θ ranges over a hyperrectangle denoted Θ,

$$\Theta = \left\{\theta : \underline{\theta}_i \le \theta_i \le \overline{\theta}_i,\, i = 1,\ldots,n_\theta\right\}.$$

The rate of variation $\Delta\theta = \theta(k+1) - \theta(k)$ belongs to a hypercube denoted $\mathscr{V}$,

$$\mathscr{V} = \{\Delta\theta : |\Delta\theta_i| \le v_i,\, i = 1,\ldots,n_\theta\}.$$

The LPV controller has the form,

$$\begin{aligned} x_{\mathrm{c}}(k+1) &= A_{\mathrm{c}}(\theta)x_c(k) + B_{\mathrm{c}}(\theta)y(k) \\ u(k) &= C_{\mathrm{c}}(\theta)x_{\mathrm{c}}(k) + D_{\mathrm{c}}(\theta)y(k), \end{aligned} \tag{10}$$

where $x_{\mathrm{c}}(k) \in \mathbb{R}^{n_{\mathrm{c}}}$ and the controller matrices are continuous functions of θ with similar type of dependence,

$$\begin{aligned} A_{\mathrm{c}}(\theta) &= A_{\mathrm{c},0} + \sum_{i=1}^{n_\theta} \rho_i(\theta) A_{\mathrm{c},i} + \sum_{i=1}^{n_{\theta_{\mathrm{f}}}} \theta_{\mathrm{f},i} A_{\mathrm{c},n_\rho+i}, \\ B_{\mathrm{c}}(\theta) &= B_{\mathrm{c},0} + \sum_{i=1}^{n_\theta} \rho_i(\theta) B_{\mathrm{c},i} + \sum_{i=1}^{n_{\theta_{\mathrm{f}}}} \theta_{\mathrm{f},i} B_{\mathrm{c},n_\rho+i}, \\ C_{\mathrm{c}}(\theta) &= C_{\mathrm{c},0} + \sum_{i=1}^{n_\theta} \rho_i(\theta) C_{\mathrm{c},i} + \sum_{i=1}^{n_{\theta_{\mathrm{f}}}} \theta_{\mathrm{f},i} C_{\mathrm{c},n_\rho+i}, \\ D_{\mathrm{c}}(\theta) &= D_{\mathrm{c},0} + \sum_{i=1}^{n_\theta} \rho_i(\theta) D_{\mathrm{c},i} + \sum_{i=1}^{n_{\theta_{\mathrm{f}}}} \theta_{\mathrm{f},i} D_{\mathrm{c},n_\rho+i}. \end{aligned}$$

Note that depending on the controller structure, some of the controller matrices may be zero. The controller matrices can be represented in a compact way,

$$K(\theta) := \begin{bmatrix} D_{\mathrm{c}}(\theta) & C_{\mathrm{c}}(\theta) \\ B_{\mathrm{c}}(\theta) & A_{\mathrm{c}}(\theta) \end{bmatrix}. \tag{12}$$

The interconnection of system (9) and controller (10) leads to the following closed-loop LPV system denoted S_{cl},

$$\begin{aligned} S_{\mathrm{cl}} : x_{\mathrm{cl}}(k+1) &= \mathscr{A}(\theta,\alpha,K(\theta))x_{\mathrm{cl}}(k) + \mathscr{B}(\theta,\alpha,K(\theta))w(k) \\ z(k) &= \mathscr{C}(\theta,\alpha,K(\theta))x_{\mathrm{cl}}(k) + \mathscr{D}(\theta,\alpha,K(\theta))w(k). \end{aligned} \tag{13}$$

The iterative LMI optimization algorithm presented next provides the controller matrices $A_{\mathrm{c},i}$, $B_{\mathrm{c},i}$, $C_{\mathrm{c},i}$, $D_{\mathrm{c},i}$, for $i = 0,1,\ldots,n_\rho + n_{\theta_{\mathrm{f}}}$. These matrices, the basis functions, and the value of the scheduling variables are the only required information to determine the control signal $u(k)$ by the dynamic equation (10) of the LPV controller, only involving multiplications and sums.

4 Optimization Algorithm

Robust and structured control problems are naturally formulated as bilinear matrix inequalities (BMI). Instead of attempting to reduce the problem to linear matrix inequalities (LMI), we propose to design the controllers via an LMI-based iterative algorithm [2] which relies on a sufficient conditions extended with slack variables to an upper bound on the induced L_2-gain of the closed-loop system. If there exist $K(\theta)$, $\mathscr{P}(\theta,\alpha) = \mathscr{P}(\theta,\alpha)^T$ and $\mathscr{Q}(\theta)$ satisfying (14) $\forall\,(\theta,\Delta\theta,\alpha) \in \Theta \times \mathscr{V} \times \Lambda$, then the system S_{cl} is exponentially stable and $\|T_{zw}(\theta,\alpha)\|_2 < \gamma$.

The Lyapunov and slack variables are here defined affine functions of the basis functions,

$$\mathscr{P}(\theta,\alpha) = P_0 + \sum_{i=1}^{n_\theta} \left(\rho_i(\theta) + f_i(\alpha)\right) P_i + \sum_{i=1}^{n_{\theta_f}} \theta_{f,i} P_{n_\rho+i} \tag{15a}$$

$$\mathscr{Q}(\theta) = Q_0 + \sum_{i=1}^{n_\theta} \rho_i(\theta) Q_i + \sum_{i=1}^{n_{\theta_f}} \theta_{f,i} Q_{n_\rho+i} \tag{15b}$$

Due to the bounded parameter rate set $\mathscr{V}$ assumed known, the Lyapunov function at $\theta^+ := \theta + \Delta\theta$ can be described as,

$$\mathscr{P}(\theta^+) = P_0 + \sum_{i=1}^{n_\theta} \left(\rho_i(\theta^+) + f_i(\alpha)\right) P_i + \sum_{i=1}^{n_{\theta_f}} \left(\theta_{f,i}^+\right) P_{n_\theta+i}. \tag{16}$$

Conveniently, the basis functions at θ^+ are approximated by a linear function of $\rho(\theta)$ and $\Delta\theta$,

$$\rho_i(\theta^+) := \rho_i(\theta) + f_i(\alpha) + \frac{\partial \rho_i(\theta)}{\partial \theta}\Delta\theta, \tag{17}$$

thereby turning inequality (14) affine dependent on the rate of variation $\Delta\theta$, being sufficient to verify (14) with (16)-(17) only at Vert $\mathscr{V}$. The optimization algorithm iterates between LMI problems by fixing the controller variables at one step and the slack variable $\mathscr{Q}(\theta)$ at another step. We present the concept of an algorithm for the synthesis of controllers with optimal performance level γ. A controller is designed for a gridded parameter space. A gridding procedure consists of defining a gridded parameter subset denoted $\Theta_g \subset \Theta$, designing a controller that satisfies the matrix inequalities constraints $\forall\theta \in \Theta_g$, and checking the inequalities constraints in a denser grid. If the last step fails, the process is repeated with a finer grid.

Algorithm 1 *Given an initial controller $K_1(\theta)$ and a convergence tolerance ε. Set $j = 1$ and start to iterate:*

1. *Find $\mathscr{P}_j(\theta,\alpha)$, $\mathscr{Q}_j(\theta)$, and γ_j that solves the LMI problem,*

   Minimize γ_j subject to (14) *with $K_j(\theta)$ fixed,*
   $\forall(\theta,\Delta\theta,\alpha) \in \Theta_g \times Vert(\mathscr{V}) \times Vert(\Lambda)$.

2. *Find $\mathscr{P}_j(\theta,\alpha)$, $K_j(\theta)$, and γ_j that solves the LMI problem,*

   Minimize γ_j subject to (14)*, with $\mathscr{Q}_j(\theta)$ fixed,*
   $\forall(\theta,\Delta\theta,\alpha) \in \Theta_g \times Vert(\mathscr{V}) \times Vert(\Lambda)$.

3. *If $|\gamma_j - \gamma_{j-1}| < \varepsilon$, stop. Else $K_{j+1}(\theta) = K_j(\theta)$, $j = j+1$ and go to step 1.*

If an initial controller $K_1(\theta)$ (or initial slack matrix $\mathscr{Q}_1(\theta)$) is not readily available, a feasibility version of Algorithm 1 may find one [2].

5 Numerical Example

The proportional and integral (PI) is the most utilized controller by the wind energy industry. At high wind speeds, the PI speed control using pitch angle as controlled input

$$\begin{bmatrix} \mathscr{P}(\theta^+,\alpha) & \mathscr{A}(\theta,\alpha,K(\theta))\mathscr{Q}(\theta) & \mathscr{B}(\theta,\alpha,K(\theta)) & 0 \\ \star & -\mathscr{P}(\theta,\alpha)+\mathscr{Q}(\theta)^T+\mathscr{Q}(\theta) & 0 & \mathscr{Q}(\theta)^T\mathscr{C}(\theta,\alpha,K(\theta))^T \\ \star & \star & \gamma I & \mathscr{D}(\theta,\alpha,K(\theta))^T \\ \star & \star & \star & \gamma I \end{bmatrix} > 0 \qquad (14)$$

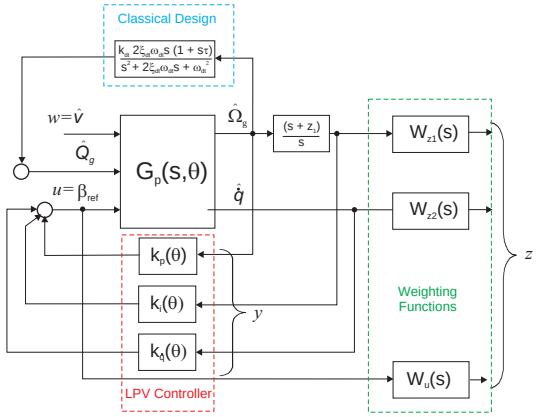

Figure 3: Augmented plant for controller synthesis.

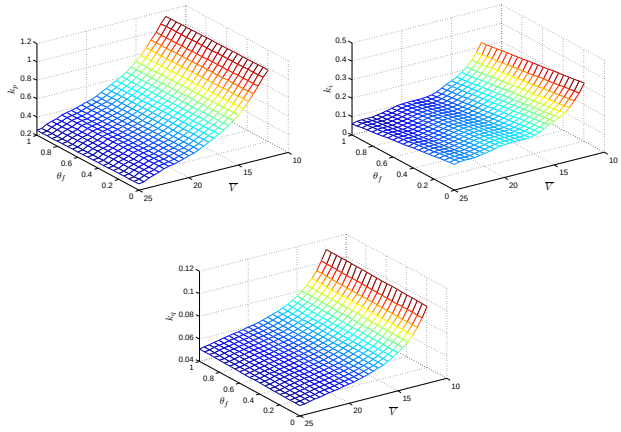

Figure 4: Proportional, integral and tower feedback gains as functions of mean wind speed and fault scheduling.

strongly couples with the tower dynamics, denoting a multivariable problem. For a clear and didactic exposure, the adopted control structure depicted in Fig. 3 is simpler than a industry standard Region III controller.

The drivetrain damper is designed using classical control techniques. A PI controller regulates generator speed and is composed by an integrator filter instead of a pure integrator, where the filter zero z_1 is a design parameter. The tower damper control assumes that tower velocity $\dot{q}$ is available for measurement, by integrating tower acceleration $\ddot{q}$, and is multiplied by a parameter-dependent constant $k_{\dot{q}}(\theta)$ for feedback. The above control structure is in fact a static output feedback. Weighting function W_{z1} shapes rotational speed regulation, W_u is a high-pass filter that penalizes high-frequency content on the pitch angle, and W_{z2} tradeoffs the desired tower damping [3]. An example of the computed LPV controller gains as three-dimensional surfaces of the scheduling parameters $\theta_{\text{op}} = \overline{V}$ (mean wind speed) and θ_{f} (pitch fault) are depicted in Fig. 4. Nonlinear time series simulations with turbulent wind depicted in Fig. 5 shows superior performance of the LPV fault tolerant controller in the case of pitch actuator failure. This is an example of the benefits that the LPV control design framework here presented can bring to wind turbines in closed-loop with industry-standard as well as more elaborate controllers.

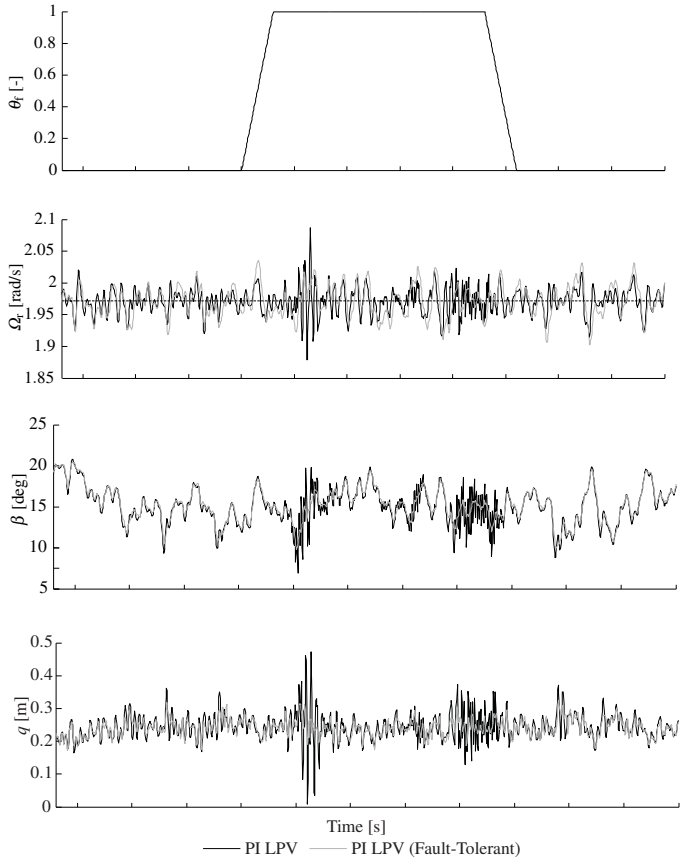

Figure 5: Time series of (a) fault scheduling variable, (b) rotor speed and (c) pitch angle and (d) tower position.

References

[1] Esbesen, T; Sloth, C. Fault Diagnosis and Fault-Tolerant Control of Wind Turbines. Aalborg Univ., 2009.

[2] Adegas, F.D.; Stoustrup, J. Structured Control of Linear Parameter Varying Systems. ACC 2012, to be submitted.

[3] Adegas, F.D.; Sloth, C.; Stoustrup, J. Structured LPV Control of Wind Turbines. Control of Linear Parameter Varying Systems with Applications, Springer-Verlag, 2011.

Model Predictive Individual Pitch Control Based on Local Inflow Measurements

Knud A. Kragh, Morten H. Hansen
Wind Energy Department, Risø-DTU
Frederiksborgvej 399, 4000 Roskilde, Denmark
E-mail: knkr@risoe.dtu.dk

ABSTRACT

As wind turbines become larger, the area swept by the rotor will contain larger variations in wind speed and direction causing varying loads on the turbine. Some of these loads can be alleviated using individual pitch control. In this study, a previous study on individual pitch control is extended to include model predictive control based on preview measurements of the local inflow. The model predictive controller is tested through simulations and the performance of the controller is compared to the performance of a collective pitch controller and a linear quadratic individual pitch controller. The performance of the model predictive controller is tested in both turbulent and deterministic inflow. The results show that in all simulated cases the two individual pitch controllers outperforms the collective pitch controller, but the model predictive controller does not appear to perform significantly better than the linear quadratic.

Keywords: Inflow measurements, load alleviation, Model predictive control, individual pitch

1 INTRODUCTION

The dominating sources of varying loads on wind turbines are the deterministic and stochastic variations in the wind. As the rotor sizes increase, the swept area of the rotor will contain a growing variation in the wind speed and direction due to wind shear, veer, turbulence etc., and due to other effects such as wakes from nearby turbines. These variations in the wind will cause variations in the loads induced on the turbine, which cannot be alleviated using collective pitch control. Hence, more advanced control techniques are required.

Numerous attempts have been made to develop advanced control schemes for alleviating the varying loads. The suggested methods can be categorized in two categories; lifting surface methods such as flaps, and pitch control methods, the latter being the topic of this paper. Early attempts on implementation of pitch control for load alleviation were based on knowledge from the helicopter technology and is referred to as cyclic pitch control [3, 4]. Cyclic pitch is based on using multi-blade transformations on the blade root bending moment signals to gain non-rotating tilt and yaw moments which were used in classical PI control schemes. Control actions were transformed back to the rotating frame of reference using the reverse multi-blade transformation.

Recent work on individual pitch control (IPC) includes further developments of the methods suggested in [3, 4], cf. [2], gust load reduction using nonlinear estimators to estimate inflow parameters based on blade root bending moments [7], and methods based on combining LIDAR wind speed measurements with turbine models[8, 5]. A more thorough review on methods for load alleviation using both individual pitch and lifting surface methods can be found in [1]

The above mentioned methods, except the ones based on LIDAR, are based on structural measurements such as blade root moment and tower bottom moment. Since the structural measurements are effects of varying wind conditions acting on the turbine, using these for control will lead to an inherent time lack. In [10], a control method based on local inflow measurements is suggested. This approach have the advantages of being based on the actual input/disturbance to the turbine. The present work is based on the method suggested in [10]. The objective of this study is to explore the possibility of improving the inflow measurement based method by including preview measurements in the control system. To take advantage of the preview measurements a model predictive controller (MPC) is implemented. The performance of the MPC is compared to the performance of a traditional collective pitch controller and a linear quadratic individual pitch controller without preview (LQR).

2 CONTROL CONCEPT

For full details cf. [10]. The control scheme is based on measurements of angle of attack and relative velocity at some radial position on the blades. These measurements could come from blade mounted pitot-tubes or from other types of transducers such as LIDAR. In this study, it is assumed that perfect measurements of angle of attack and relative velocity are readily available, no modeling of the actual transducer is performed. The basic idea of the control scheme is to split actions based on angle of attack variations from actions based on variations in relative velocity. Control actions due to either type of variation is added to the collective pitch signal and do not affect the average pitch.

The actions based on the angle of attack variations are based on the idea of keeping the angle of attack the same for all

blades. The difference between the angle of attack of one blade compared to the average angle of attack of all blades is used as reference signal for the pitch controller. Hence, the control action based on the angle of attack variations does not affect the collective pitch regulation, which is only concerned with average value. The reference pitch signal based on the angle of attack variations is defined as:

$$\theta_{\delta i,a} = \bar{\alpha} - \alpha_i \tag{1}$$

where $\theta_{\delta i,a}$ is the desired pitch angle increment of blade i, α_i is the angle of attack at a radial position on blade i, and $\bar{\alpha}$ is the average angle of attack of all blades.

The variations in relative velocity cannot be directly translated into reference pitch angles, and are therefore feed to the pitch controller using gains extracted from a cyclic pitch design [10]. The reference pitch signal due to the relative wind speeds is calculated as:

$$\theta_{\delta i,b} = (V_{i,x} - \bar{V_x})K(\omega, \theta_{col}) \tag{2}$$

where $\theta_{\delta i,b}$ is the desired pitch angle increment for blade i, $V_{i,x}$ is the in-plane wind speed of blade i, $\bar{V_x}$ is the average in-plane wind speed of all blades, and $K(\omega, \theta_{col})$ is the pitch gain, which is a function of both rotational speed, ω, and collective pitch angle, θ_{col}. The gain $K(\omega, \theta_{col})$ is obtained from simulations with a cyclic pitch controller. The in-plane wind speeds are calculated as:

$$V_{i,x} = V_{i,rel}\sin(\alpha_i + \theta_i) \tag{3}$$

where θ_i is the current pitch angle of blade i. The total reference pitch increment for each blade is then given as:

$$\theta_{\delta i} = \theta_{\delta i,a} + \theta_{\delta i,b} - \left[\tan^{-1}\left(\frac{\bar{V_y}}{V_{i,x}}\right) - \Theta\right] \tag{4}$$

where $\bar{V_{i,y}}$ is the average wind speed in the out of plane direction, and Θ is defined as:

$$\Theta = \frac{1}{B}\sum_{i=1}^{B}\tan^{-1}\left(\frac{V_{i,y}}{V_{i,x}}\right) \tag{5}$$

where B is number of blades. The last term of Equation (4) is subtracted to subtract the angle of attack variations caused by the actions based on the relative velocity variations.

The pitch reference increment $\theta_{\delta i}$ is added to the collective pitch reference, θ_{col}, and passed to the pitch controller. Hence, the reference pitch for blade i is defined as:

$$\theta_{i,ref} = \theta_{col} + \theta_{\delta i} \tag{6}$$

where θ_{col} is the reference pitch given by the collective pitch controller.

3 Models and Simulation Software

In the present study, simulations are performed using the aeroelastic code developed at Risø-DTU, HAWC2 [9]. The turbulence is simulated using Cartesian boxes with Mann turbulence [11]. The wind turbine model used for the simulations in this study is of a turbine with a hub height of 59 meters, a rated power of 2 MW, and a rated rotor speed of 1.8 rad/s. The pitch servo is modeled as a 2nd order filter given in continuous state space form as:

$$\begin{aligned}\dot{\mathbf{x}} &= \mathbf{A}\mathbf{x} + \mathbf{B}\mathbf{u} \\ \mathbf{y} &= \mathbf{C}\mathbf{x}\end{aligned} \tag{7}$$

where

$$\mathbf{x} = \begin{bmatrix} \dot{\theta}_i \\ \theta_i \end{bmatrix}, \qquad \mathbf{A} = \begin{bmatrix} -2\xi\omega & -\omega^2 \\ 1 & 0 \end{bmatrix}, \tag{8}$$

$$\mathbf{B} = \begin{bmatrix} \omega^2 \\ 0 \end{bmatrix}, \qquad \mathbf{C} = [\mathbf{0} \quad \mathbf{1}] \tag{9}$$

where the eigenfrequency and damping is set to $\omega = 1$ and $\xi = 0.7$, respectively.

4 Control design

In this paper, two different control strategies for tracking the reference pitch are tested; a standard optimal linear quadratic regulator, and a model predictive controller which uses measurement from leading blades as preview measurements.

To enable reference tracking using the LQR, the controller is designed using the pitch servo model given Equation (7) augmented with an integrator. The control gains are calculated using standard linear control theory, c.f. [6].

The preview reference pitch angles for the MPC are available from inflow measurements from the blade leading in the rotation. Hence, if blade 2 follows blade 1 when the rotor spins, the prediction horizon of blade 2, $\theta_{2,ref}$, is found by applying Equation (4) to the angle of attack and relative velocity measured by blade 1 (α_1 and $V_{1,rel}$), see Figure 1. The applied MPC is design in accordance with the description in [12].

5 Preliminary Results

The controller is tested through simulations in both deterministic and turbulent inflows (turbulence intensity: 10%). In both cases a power law vertical wind shear with a power coefficient of 0.5 is imposed on the inflow. In Figure 2 and 3 sections of the resulting time series for the deterministic and

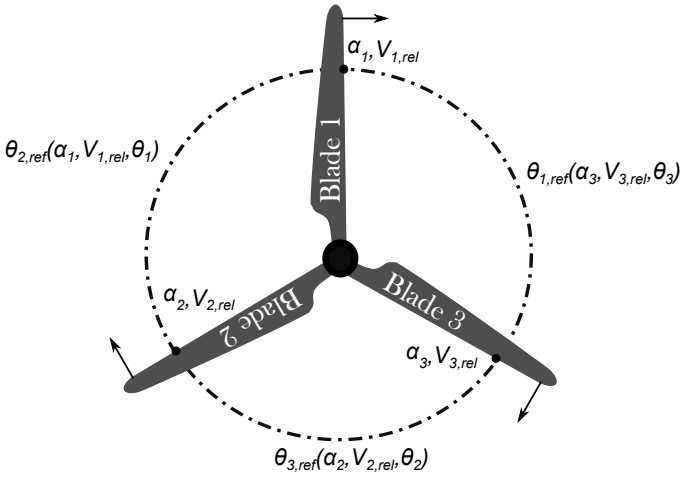

Figure 1: Illustration of the sampling of the prediction horizons

turbulent case is shown. The Figures show angle of attack, pitch and blade root bending moment for situations with both the collective, and the two different individual pitch controllers.

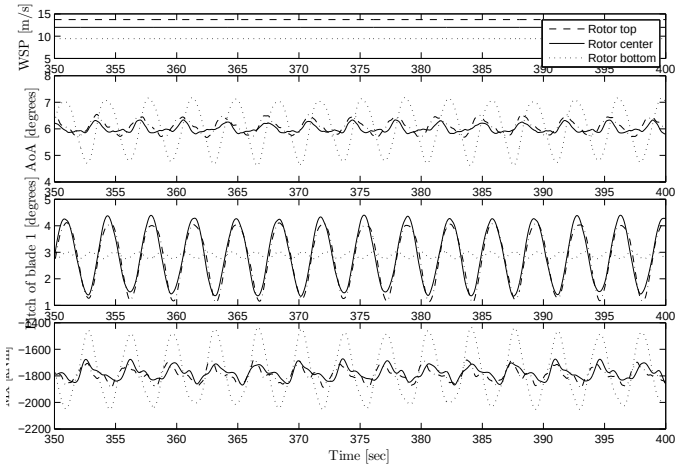

Figure 2: Results of simulations with the three different controllers in deterministic inflow with a power law vertical wind shear with at power coefficient of 0.5. From the top: wind speed, angle of attack, pitch, and blade root bending moment $\cdots$: Collective pitch, $- \cdot -$: LQR, —: MPC.

From Figure 2 it is seen that for the case with a deterministic inflow to the turbine the variations in angle of attack are greatly reduced when using IPC and that the amplitudes of the variations are smallest when applying the MPC. The pitch signal for the IPC controllers are similar, but as expected the signal of the LQR has a slight phase shift compared to the signal of the MPC. Inspecting the blade root bending moment, it is observed that there is very little difference in the signals from the LQR and the MPC, but they both have significantly smaller amplitudes than with the collective pitch controller. Hence, for the deterministic case no benefit are found for the MPC compared to the original

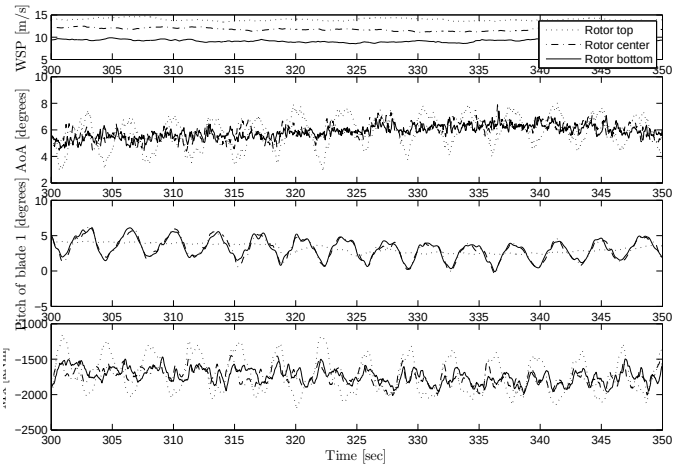

Figure 3: Results of simulations with the three different controllers in turbulent inflow (turbulence intensity: 10%) with a power law vertical wind shear with at power coefficient of 0.5. From the top: wind speed, angle of attack, pitch, and blade root bending moment $\cdots$: Collective pitch, $- \cdot -$: LQR, —: MPC.

LQR.

Inspecting the turbulent case shown in Figure 3 it is seen that the variations in angle of attack now seem to be similar for both the IPC's, however still much smaller than with the collective pitch controller. As expected, the pitch signals for the turbulence cases are more irregular than for the deterministic case, but a slight phase difference between the LQR and the MPC is still visible for the low frequency contents. Finally, inspecting the blade root bending moments for the turbulent case, it is seen that again the amplitudes of both IPC's are much smaller than for the collective pitch controller. Generally, the amplitudes resulting from either IPC are similar. However, some spikes in the LQR blade root bending moment signal are not present in the signal from the case with the MPC, e.g. at $t = 319$, $t = 329$, $t = 332$ and $t = 336$. Anyhow, these reductions might be coincidences, and a larger study is needed to conclude anything in general.

6 Discussion

From the results presented above, it seems that there are only limited benefits from using preview measurements for the local inflow measurement based controller. However, so far only simple cases with and without turbulence have been tested. The preview measurements might provide more benefits in the presences of e.g. gusts or wakes from nearby turbines. In such cases the preview measurements might help alleviate the peak loads. Furthermore, additional benefits of preview measurements might emerge if actual preview measurements were used. In this study, it is assumed that the flow is stationary in the 120 degrees separating the blade at which the flow is measured and the blade being controlled by the model predictive controller. This assumption is not entirely valid, and if it is violated the IPC might increase loads instead of alleviating them. Other upwind pointing

measurement system such as LIDARs could be applied to gain more accurate preview measurements.

7 Conclusions and Future Work

In this preliminary study a model predictive controller for individual pitch control based on the ideas in a previous study was implemented and tested in cases with both deterministic and turbulent inflow. The performance of the controller was compared to the performance of a linear quadratic controller and a baseline collective pitch controller. In the deterministic case it was seen that both of the individual pitch controllers greatly reduced the variations in blade root bending moment. However, no additional benefits were observed for the model predictive controller compared the linear quadratic. In the turbulent case it appears that the model predictive controller might be able to alleviate some of the peaks in the blade root bending moment present in the results from the linear quadratic controller. However, more elaborate studies are needed to investigate this. Further work will include more elaborate simulation studies to better map the performance of the new controller and simulations with wakes and extreme gust. Furthermore, preview measurements from simulated LIDARs will implemented.

References

[1] TK Barlas and GAM van Kuik. Review of state of the art in smart rotor control research for wind turbines. *Progress in Aerospace Sciences*, 46(1):1–27, 2010.

[2] E. Bossanyi and David Witcher. Controller for 5mw reference turbine - upwind report. Technical report, Garrad Hassan and Partners Ltd., 2009.

[3] E. A. Bossanyi. Individual blade pitch control for load reduction. *Journal of Wind Energy*, 6:119–128, 2003.

[4] E. A. Bossanyi. Further load reductions with individual pitch control. *Journal of Wind Energy*, 8:481–485, 2005.

[5] F. Dunne, L. Y. Pao, A. D. Wright, B. Jonkmann, N. Kelley, and E. Simley. Adding feedforward blade pitch control for load mitigation in wind turbines: Non-causal series expansion, preview control, and optimized fir filter methods. In *49th AIAA Aerospace Sciences Meeting including the New Horizons Forum and Aerospace Exposition*, 2011.

[6] E. Hendricks, O.E. Jannerup, P.H. Sørensen, and P.H. Sorensen. *Linear systems control: deterministic and stochastic methods*. Springer Verlag, 2008.

[7] Stoyan Kanev and Tim van Engelen. Wind turbine extreme gust control. *Wind Energy*, 13(1):18–35, 2010.

[8] J. Laks, L. Y. Pao, E. Simley, A. D. Wright, N. Kelley, and B. Jonkman. Model predictive control using preview measurements from lidar. In *49th AIAA Aerospace Sciences Meeting including the New Horizons Forum and Aerospace Exposition*, 2011.

[9] T. J. Larsen. How 2 hawc2, the user's manual. Risø-r-1597(ver. 3-9)(en), Risø-DTU, September 2009.

[10] TJ Larsen, HA Madsen, and K Thomsen. Active load reduction using individual pitch, based on local blade flow measurements. *Journal of Wind Energy*, 8:67–80, 2005.

[11] J. Mann. Wind field simulation. *Probabilistic Engineering Mechanics*, 13(4):269 – 282, 1998.

[12] L. Wang. *Model predictive control system design and implementation using MATLAB*. Springer Verlag, 2009.

Session 4A

Offshore Technology

Monopile 2.0 for Offshore Wind Farm Princes Amalia
M.L.A. Segeren

Dynamics of a floating wind turbine model
S. Rockel, J. Peinke, M. Holling

Fluid Power Transmission Applications in Wind Energy
N.F.B. Diepeveen, A. Jarquin Laguna

Monopile 2.0 for Offshore Wind Farm Princes Amalia

M.L.A. Segeren
Offshore Wind section, Technical University of Delft
Stevinweg 2, The Netherlands
E-mail: m.l.a.segeren@tudelft.nl

Keywords: offshore wind, monopile, support structure

1 Introduction

The support structure of an offshore wind turbine has a significant share (15-25%) in the costs of offshore wind energy[1][2]. In order to reduce the cost of energy(COE) in future wind farm, the support structure designs must be improved. To achieve cost reduction for future wind farms, the support structures of the wind farm Q7/Prinses Amalia are reviewed in this paper. The Prinses Amalia Wind Farm(PAWF) is taken as a example for a desk study in order to illustrate the potential of reduction of COE. This wind farm started to produce power in March 2008 and consists of 60 Vestas V80 2.0MW turbines standing on 4.0m diameter monopiles just 20km off the coast of IJmuiden in the Netherlands. In figure 1 the layout of the support structure design of the PAWF is shown.

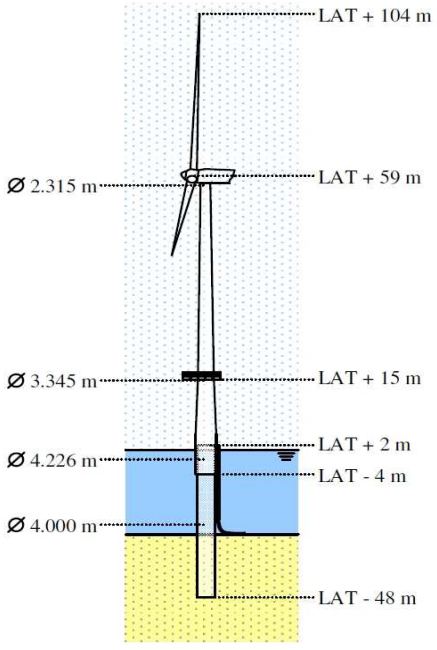

Figure 1: Layout of the monopile based support structure of the Prinses Amalia wind farm

In this paper the monopile designs are reviewed in order to see if the structure could have been design less conservative and its results can be used for the development of future wind farms. This research is part of the FLOW research program, which strives to reduce the costs of energy for offshore wind farms.

2 Approach

The design of the monopile of the PAWF is used as a reference design. A redesign of the monopile is made with the same requirements as has been used for the PAWF. Here the wall thickness of the reference design is used as a starting point and the diameter is reduced until the lower limit of the natural frequency is met. This will result in a different design than the reference. The wave loads on the new designs are calculated to determine how much the loads are reduced or increased. Subsequently, strength checks are performed with the original loads and reduced loads. The masses of the reference design and re-design are then compared. Subsequently conclusions and an outlook on improvement on the design of a monopile is given.

3 Support structures of the Prinses Amalia Wind Farm

3.1 Introduction of the Prinses Amalia Wind farm

The Offshore Windpark PAWF is situated 23 kilometers offshore from IJmuiden, in block Q7 of the Dutch continental shelf. Throughout the wind farm, the individual offshore wind turbines are standing in various combinations of water depth and soil conditions are present. The soil condition vary of which the soil properties of location W8 are the stiffest and the conditions of location W42 are the softest. The water depth is changing through the wind farm area and due to moving sand dunes the water depth is also dynamic, which requires a range of water depth to be investigated per location. Based on the water depths, two pile designs have been made: Pile Type 1 corresponds to the relatively shallow area of the sand bank whereas Pile Type 2 corresponds to the deeper areas. In combination with the soil four design cases have been realized. In table 1 the four combinations of water depth, soil conditions and scour assumptions are given. It also shows which combination will lead to the upper and lower limit of the natural frequency.

3.2 Design aspects

Natural frequency An operational wind turbine has a rotor that revolves through a turbulent wind field. During one

Table 1: Condition combinations for different pile types [3]

Pile Type	Water depth	Scour	Soil Type	Limit F_n
1	19.72 m	0	W 8	Upper
1	21.5 m	1.5	W 42	Lower
2	19.72 m	0	W 8	Upper
2	24.41 m	3	W 42	Lower

rotation a turbine blade passes through several eddies and experiences a short period of higher or lower wind speed. As a result, the wind turbine will experience a load with the rotational frequency of the rotor. This frequency is called 1P and in case of a variable speed turbine this 1P frequency is also variable. Next to loads with the 1P frequency the turbine also experiences loads with the blade passing frequency. In case of a 3 bladed turbine this is called the 3P frequency. To avoid resonance of the structure, the natural frequency of the wind turbine and support structure must lie outside the loading frequency regions of the turbine.
For the Vestas V90 used in the Prinses Amalia wind farm the 1P and 3P frequency regions are located respectively at 0.150-0.317Hz and 0.428-0.906Hz including a 5% safety margin. In figure 2 these frequency regions are given and a wave spectrum is given. The target area for the natural frequency of the whole strucutre lies in between the 1P and 3P region.

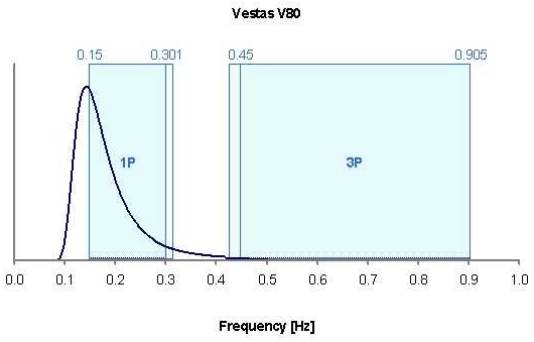

Figure 2: Loading frequency regions

In order to increase a natural frequency a shift to the right in figure 2) the structure must be made stiffer, meaning that material must be added. In order to lower a natural frequency of a structure, it must be made less stiff. In that case material should be reduced in order to realize a lower natural frequency. In order to get cost-effective design, the natural frequency of a wind turbine should ideally be near the 1P region, as that would require the least material and consequently lower cost. The natural frequency of design of Pile Type 1 and 2 are given in table 2. Note that for the lower limit also scour is taken into account. From the table it can be seen that the natural frequency lies near the 3P region. This indicates that there is room to lower the natural frequency by reducing the size of the piles. Table 2 indicates that a scour hole of 3m is considered to occur. This is very conservative as scour protection is also applied to every pile. In the next section it is shown what this conservative approach means for the design of the pile.

Table 2: Natural frequency variation for different pile types and soils in Hz [3]

D=4.0m PileType	Waterdepth	Scour	Soil Type	F_n
1	19.72 m	0	W 8	0.406 Hz
1	21.5 m	1.5	W 42	0.365 Hz
2	19.72 m	0	W 8	0.411 Hz
2	24.41 m	3	W 42	0.359 Hz

4 Result and Comparison

4.1 Introduction

In order to compare the designs of the pile types of reference [3] with redesigns, the original designs were modeled and their natural frequencies calculated to show the minimum difference between the models and design in the reference designs. The natural frequencies of the designs were compared for the four cases shown in table 2. The difference of the models and the design documents are between 0.3 and 4.4%. Therefore it was considered that redesigns can be compared with the reference design.

4.2 Design including/excluding scour to occur

The diameter was reduced until the natural frequency reached the 1P region was reached under the restriction that all piles should have the same diameter. At a pile diameter of 3.5m, Pile Type 2 in combination with soil W42 has a natural frequency of 0.32Hz where 0.317Hz is the upper boundary of the 1P limit. If the scour hole of 3m is not taken into account, because of scour protection, the pile can be reduced to a diameter of 3.3m under the same natural frequency requirements. This is done for the governing cases of the designs of the type 1 and type 2 monopile. The results are given in table 3.

Table 3: Results of the pile diameter reduction to 3.5m and 3.3m

D=3.5m PileType	Waterdepth	Scour	Soil Type	F_n
1	19.72m	0	W 8	0.363Hz
1	21.5m	1.5	W 42	0.336Hz
2	19.72m	0	W 8	0.370Hz
2	24.41m	3	W 42	0.320Hz
D=3.3m				
1	21.5m	0	W 42	0.324
2	24.41m	0	W 42	0.318

Based on the natural frequency requirements it could have been possible to reduce the pile diameter from 4.0m to 3.3m or 3.5m if scour is taken into account. In the next sections, the wave load calculation and the buckling checks on the design will point out if the wall thickness of the reference design is still sufficient.

4.3 Wave load reduction

The wave loads are calculated with the Morison equation, the linear Airy wave theory and Wheeler stretching. The outcomes of the calculation is first checked with the design documents for a pile with a diameter of 4m. In table 4 the calculation parameters are given. The sum of the wave and wind loads have been compared for the 24.42m case at mudline location.

Table 4: Wave load calculation parameters

Pile Type 2 and D=4.0m			
WD	Scour	Marine growth	Load factor
24.41m	3	0.1m	1.35
C_m/C_d	H_{wave}	T	
2.2/0.65	13.80 m	9.62 s	

The calculations outcome of the sum of the force and moment were 1.5 and 3.3 % respectively different than the design document. This indicates that the use of Morison equation, linear Airy wave theory and the calculation parameters give reliable outcomes. Therefore it be assumed that further outcomes may be compared with the reference loads. With this knowledge, the wave loads are calculated for a pile of 3.5m and 3.3m and compared with the sum of wave and wind loads . In table 5 the reduction of the total loads at mudline due to reduction of the wave loads by the use of a smaller diameter pile, are given in percentages.

Table 5: Reduction of wind and wave loads in % at mudline

	Reduction to 3.5m	Reduction to 3.3m	
F	17	23	%
M	9	13	%

4.4 Penetration depth reduction

With the reduction of the loads, the penetration depth can be reduced for the two pile types under equal requirements taken from the rules of Germanischer Lloyd design standard [4].For the piles with a diamter of 3.3m this is only done for the governing cases of the designs of the type 1 and type 2 monopile. The results and comparison with the original penetration depth are given in table 6. The table clearly shows the steel reduction potential.

4.5 Resulting design after frequency checks

The results of the review indicate that a monopile of 3.5m could have been used. In figure 3 the diameter over the height of the original and the review design is given. The tower of the turbine is kept equal to the reference as can be seen. The wall thicknesses are kept equal to reference for most locations. The next paragraph shows what this means for the strength checks.

Table 6: Results Penetration depth [PD]

			D= 4.0m	D= 3.5m	D= 3.3m
Type	WD	Scour	PD(LAT)	PD(LAT)	PD(LAT)
1	19.72	0	**-48m**	**-42m**	
1	21.5	1.5	**-48m**	**-45.5m**	**-44 m**
2	19.72	0	**-52m**	**-43.5m**	
2	24.41	3	**-52m**	**-50.5m**	**-48 m**

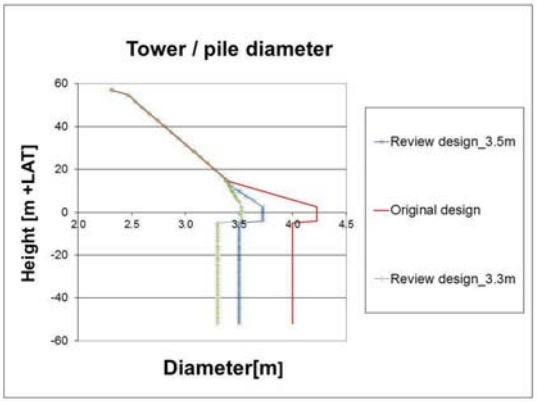

Figure 3: Diameter development along the the structures height

4.6 Strength checks

The design of pile type 2 with a diameter of 3.5m is checked on global and local buckling and yield stress using the rules of Germanische Loyd design standard[4]. For the checks the the original maximum wave and wind loads on the structure were used. The difference in weight, due to diameter reduction, is taken into account in the magnitude of the normal force. The global and local buckling checks are given in figure 4. It can be seen that even without the reduction of the wave loads the unity ratios are less than one, which indicates that no buckling will occur for a monopile of 3.5m. For the monopile 3.3m the unity check fails for buckling under the original loads, as can be seen in and 5. However, if the reduction of the maximum overturning moment is reduced 13%, see table 5, the unity check for buckling is fullfilled. In figure 6 the wall thickness is shown of the pile designs that fullfill the checks with the original loads.

In figure 7 the Stress Reserve Factor SRF] is given. It can be seen that these safety factors are larger than 1 with a minimum of 1.7. This indicates than no yield will occur and using a pile of 3.5m would not have caused any problem regarding these strength checks.

4.7 Weight Comparison

The weight is calculated for the monopile designs of 4.0m and the designs of the monopile of 3.5m and 3.3m with a

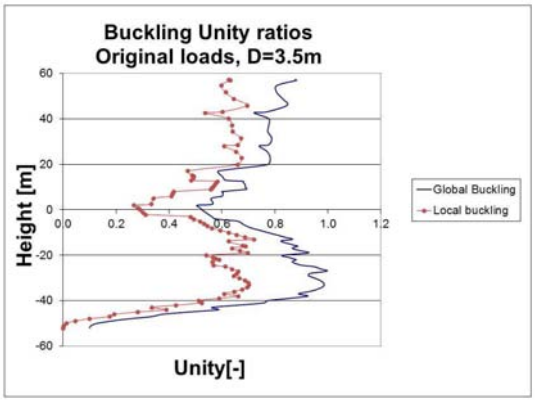

Figure 4: Unity ratios of buckling checks with original loads

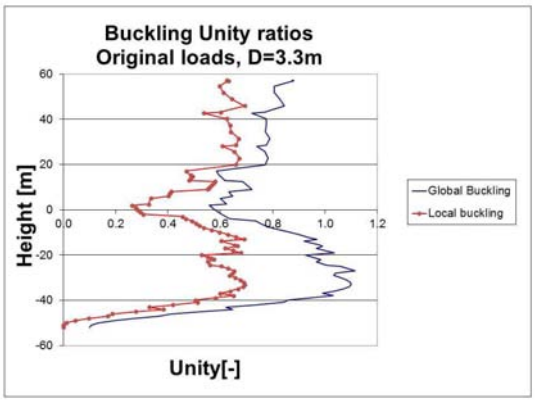

Figure 5: Unity ratios of buckling checks with original loads

shortened penetration depth. In table 7 the difference per pile type and the weight difference of the whole wind farm is given.

Table 7: Weight comparison of the piles in tonnes

	Type 1	Type 2	
D=4.0m	274	326	tonnes
D=3.5m	220	264	tonnes
D=3.3m	208	250	tonnes
Potential			
Total reduction D=3.5	3117	tonnes of steel	
Total reduction D=3.3	3974	tonnes of steel	

This means that if a monopile of 3.5m were used a weight amount of almost 10 pile types 2 could have been saved. The monopiles of the PAWF has 18% or 22% more weight than a offshore wind farm with monopiles of 3.5m or 3.3m in diameter. With the reduction of the pile diameter also the TP becomes smaller. This will save an additional 785 tonnes in case of 3.3m diameter monopiles in comparison with the current design. This makes the total potential steel reduction 26% of the original weight of the support structures of the PAWF..

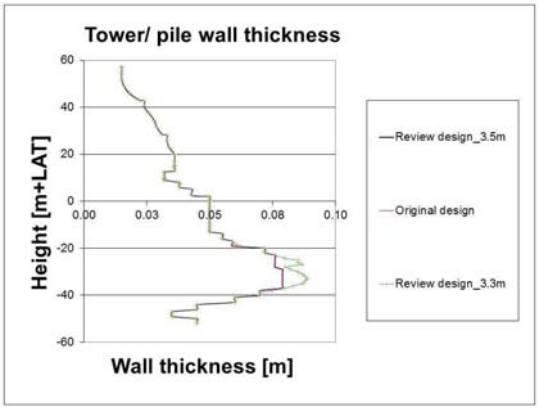

Figure 6: Wall thickness development along the the structures height

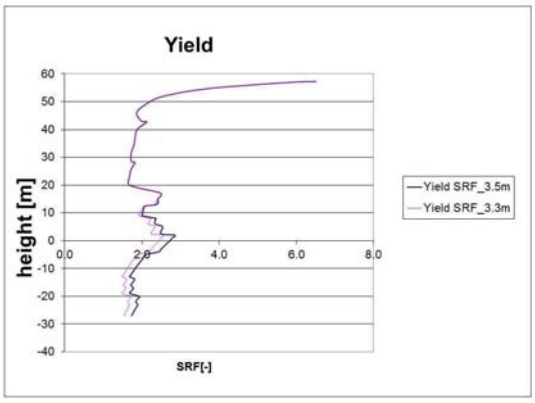

Figure 7: Yield safety factors with original loads

5 Conclusions and Outlook

The designs of the monopile support structures of PAWF can be considered to be over-conservative based on the outcomes of the natural frequency checks and the strength checks shown in this paper. The outcomes of this paper can be used in the optimization process of the support structure and is performed to show where the industry stand and what can be improved using current design regulations and considerations. Fatigue is however not checked in this paper. Fatigue is highly dependent on the damping of different sources and on turbine characteristics. These damping sources will be analyzed in a follow up of this paper.

References

[1] NREL. Energy from Offshore Wind. 2006.
[2] EWEA. Wind energy- the Facts. 2009.
[3] Hessels & van Rooij Engineering B.V. *Design of tower and foundation pile for a V80-2.0MW wind turbine at location Q7-WP.*, 16 February 2005.
[4] Germanischer Lloyds. *Rules and Guidelines, Guideline for the Certification of Offshore Wind Turbines*, edition 2005.

Dynamics of a floating wind turbine model

S. Rockel, J. Peinke, M. Hölling
ForWind - Center for Wind Energy Research, University of Oldenburg
Carl-von-Ossietzky-Str. 9-11, 26129 Oldenburg, Germany
E-mail: stanislav.rockel@uni-oldenburg.de

Keywords: floating turbine, offshore

1 Introduction

By the year 2030 wind energy is projected to contribute up to 350 GW to the energy needs in Europe. The major increase of up to 150 G is expected to be gained from offshore wind energy [11]. Present foundations for offshore wind turbines are cost effective for water depths up to 50 m given that for deeper water the platform becomes a main contributor to the overall costs. Since regions with water depths below 50 m are rare [4] floating platforms for larger water depths are interesting alternatives. Several concepts for floating support structures were suggested by NREL [8]. Research has been done on simulating the behavior of the floating platforms and the turbine performance [5] of which an overview is given in [9]. Investigations on full scale turbines with floating platforms are very costly and the boundary conditions are hard to capture, so the influence of unknown parameter on the performance of the turbine is hard to determine. Wind tunnel experiments with small model turbines are very economical and can be carried out under fixed and reproducible boundary conditions, e.g. laminar and turbulent inflow conditions. Although wind tunnel experiments suffer from scaling problems they are still useful to get a basic understanding of the important parameters for the performance of the turbine. In this work we'll present an experimental setup of a small scale floating turbine. The model turbine is designed after the prototype of the Hywind-Projekt of StatoilHydro and was used in wind tunnel experiments under different wind conditions.

2 Floating turbine model

A model turbine with a rotor diameter of 20 cm and a tower height of 25 cm was mounted to a spar buoy plattform of 25 cm height and 11 cm diameter.(Fig.1). The blades are chosen from airplane models and therefore not optimised to operate on a wind turbine. The center of mass of the turbine is chosen to be as close as possible to the bottom of the buoy, so the turbine was stabilized against overturning. Within the buoy at the center of mass a small DC motor (*Faulhaber 2657W012CR*) is connected to the drive shaft. To connect it to the rotor the drive shaft is turned by 90° in the nacelle by means of a gear box with a ratio of 1:1.

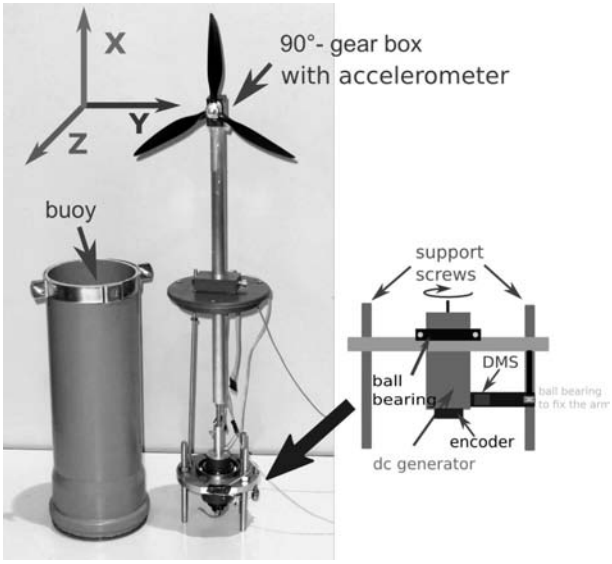

Figure 1: **left:** Final setup for first measurements. Model of floating turbine with an accelerometer, a small DC motor, an encoder for ω and a torque sensor.
right: Scheme of the torque sensor, with ballbeared DC motor, a bending beam and strain gauges.

At the nacelle of the turbine an accelerometer was positioned to measure the acceleration which are induced by the acting wind. The power output of the turbine is also to be measured. According to Kang et. al. [6] measuring the mechanical power is more precise than electrical measurement since electrical losses in a small motor are influencing the measurement. Therefor the torque T and the rotational frequency ω have to be measured, since mechanical power P is given by

$$P = T \cdot \omega. \tag{1}$$

So for the power measurement an encoder (*Faulhaber IE2 - 512*) and a torque sensor are connected to the motor. The encoder has an output of 512 pulses per revolution and is used to measure the rotational frequency ω of the motor. Figure 1 on the right shows the torque sensor developed to measure T at the motor by means of strain gauges (*HBM 1-DK11G-3/350*). Therefore the motor was placed in a ball bearing in a horizontal plate allowing it to rotate freely if a torque is applied. A beam of phosphorus bronze of 32 mm length,

11 mm width and 0,25 mm in thickness is fixed between the housing of the motor and a support screw, which is used for a horizontal alignment of the motor and the sensors. When a torque is applied to the motor the beam prevents it from rotation and is bent. This bending can be measured by strain gauges and the acting torque at the motor can be determined from a linear calibration function. So the mechanical power on the motor is measured, which is more precise. To overcome residual friction in the setup due to the prolonged shaft and it's turning by the gear box the motor was driven actively with a power supply at various voltages. This allows to perform measurements even at low wind speeds.

3 Experimental results

First experiments under different wind conditions were performed in the wind tunnel at the University of Oldenburg.

3.1 Laminar inflow

In order to measure a power curve the turbine was placed non-floating, centered in front of the wind tunnel. The inflow conditions were laminar with a turbulence intensity below 0.3%. The motor was operated at 2.3 V, so the rotor was rotating actively and caused an offset in torque and rotational frequency. The signals were gained to a range of -10 V to 10 V and recorded with an 16bit A/D converter (*National Instruments NI USB-6211*) with a sampling frequency of 1 kHz. The converter was controlled by a program created in *LabView*. The mean values of the signals that were measured 60 s were taken. The offset caused by the motor was measured at 0 m/s wind speed and its mean was subtracted from the signals at higher wind speeds. The wind speed was set from 0 m/s to 6.5 m/s in 0.5 m/s steps. The changes in T and ω caused by the wind were measured with the encoder and torque sensor. The signals are filtered with a Butterworth-Filter [10] of third order at a cutoff frequency of 10 Hz to remove 50 Hz noise and periodic torque changes due to imperfections in the setup, which are explained later. Afterwards the same measurements under same wind conditions were performed with the floating turbine. Therefore the turbine was placed in a water tank centered in front of the wind tunnel outlet. The turbine was fixed to the tank ground with a cord at the center of the buoys bottom, so the turbine was held centered in the tank. With increasing wind speed the floating turbine is inclining in down wind direction up to 12°. Figure 2 shows the mean values and the standard deviations of the power outputs plotted against the wind speed for the fixed case (gray) and the floating case (black). Although the gray curve has some slightly higher values, it can be seen that both curves agree well and the additional dynamics and the inclination of the floating turbine have no influence on the measured power output.

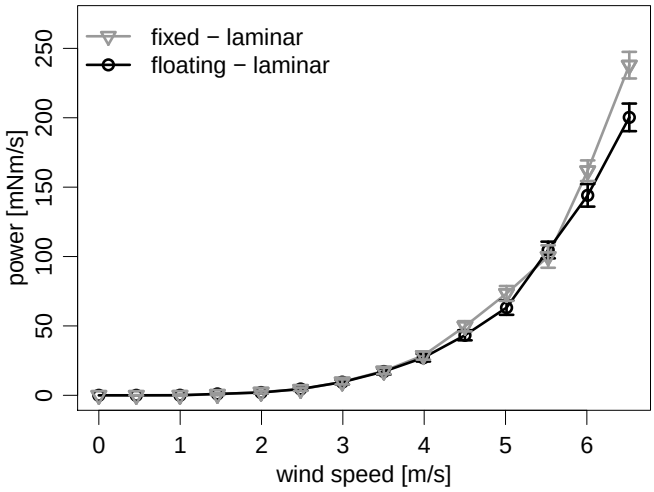

Figure 2: Power curve comparison of fixed and floating turbine under laminar inflow: The triangles in gray are the mean values of the power for the fixed turbine, the black circles for the floating turbine. The respective standard deviations are denoted by the bars. Wind speed is set from 0 m/s to 6.5 m/s in 0.5 m/s steps. The gray curve shows slightly higher values from 4 m/s but the difference between the measurements is not significant.

3.2 Inflow with gusts

Additionally, power measurements were performed under turbulent wind conditions generated by a gust generator. The gust generator consists of ten vertically rotating blades which are driven by an DC motor (Fig. 3). By means of the blades the tunnel nozzle is blocked periodically with a frequency depending on the motor voltage. For described measurements the gusts were created with a frequency of 0.46 Hz.

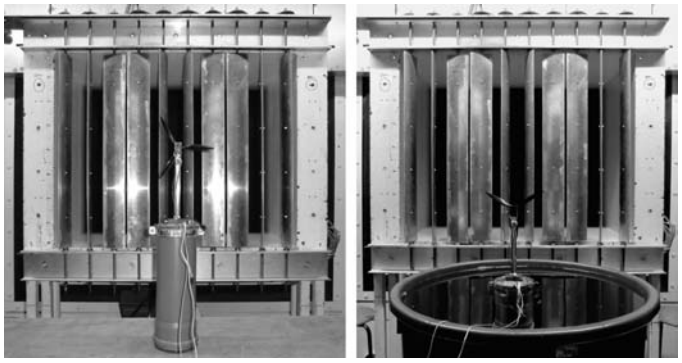

Figure 3: Fixed (left) and floating (right) turbine in front of the gust generator in the wind tunnel at the University of Oldenburg

In order to average over a sufficient number of gust events 180 seconds of torque and frequency data were measured. Figure 4 shows the mean values and the standard deviations

of the power generated under turbulent wind conditions. The torque and frequency signals were recorded at a sampling frequency of 1 kHz for wind speeds from 0 m/s to 6 m/s in 1 m/s steps. Above 2 m/s the power output of the floating turbine (black) is higher than of the fixed turbine. The standard deviations are higher for both signals since a wind speed variation is generated by the gust generator. The standard deviations of the floating turbine data are also higher than those of the fixed turbine which must be caused by the oscillations of the turbine. The comparison of the power outputs shows that under turbulent conditions the power is positively influenced by the dynamics of the floating turbine.

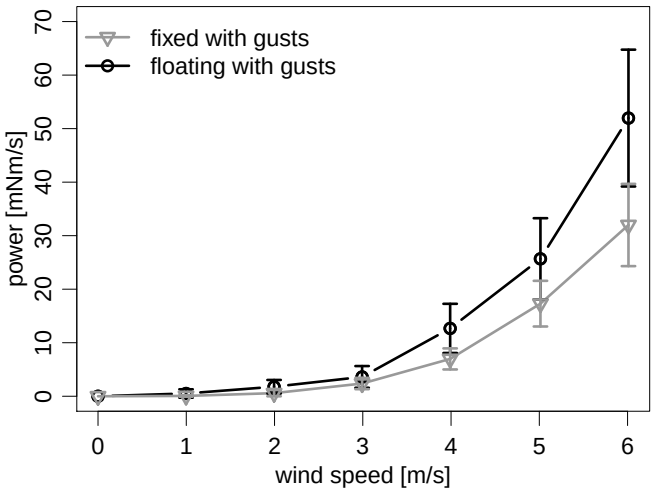

Figure 4: Power curve comparison of fixed and floating turbine under inflow created by a gust generator: The gray triangles are the mean values of the power for the fixed turbine, the black circles for the floating turbine. The respective standard deviations are denoted by the bars. Wind speed is set from 0 m/s to 6 m/s in 1 m/s steps. The measurements in black have higher values over for wind speeds above 2 m/s, which means under gust conditions the floating turbine seems to generate more power. The standard deviations are higher because of the wind speed variations created by the gust generator.

These results are promising, since they indicate that the concept can be used to get a better understanding of the additional dynamics of the floating turbine and its influence on the power output. The method of measuring the power by means of torque and rotational frequency with an active driven motor seems to work. The resulting power has a cubic behavior which is expected ([3]). The prolongation and the 90°-turn in the gearbox of drive shaft create tilts due to high rotational speed, which leads to high periodic torque signals, that are not caused by the wind. Therefore the results have to be taken with care, since these are first measurements that were performed with this setup and further improvements have to be done. To remove these uncertainties an improved setup has to be developed and the measurements have to be reproduced.

4 New model turbine

To obtain more precise results and remove uncertainties, which are dominated by the imperfections of the current model setup, a smaller model of the turbine is to be built.

4.1 Improved setup

The setup will be changed by using a smaller motor and encoder. This allows for a smaller construction of the torque sensor which can be included in the nacelle of the turbine model. The beam has a length of 11 mm, a width of 5 mm and it's thickness is 0.25 mm. Shorter strain gauges with a met length of 1.5 mm are used (*HBM 1-LY11-1.5/350*). The reduced friction losses and the absence of the gearbox may improve the accuracy significally (Fig. 5).

Figure 5: Improved setup of the turbine model: A smaller motor with a smaller encoder are used. The torque sensor is placed in the nacelle since no prolongation of the drive shaft is needed.

The direct connection of the rotor to the motor shaft might lead to reduced tilting since less connections between the parts of the shaft are needed. So less periodic changes in the torque will disturb the signal and the needs of filtering the signal at low frequencies would be reduced. The removal of the gear box may lead to less friction losses and less losses caused by slip at the shaft connections.

4.2 Planned experimental work

Measurements will be performed under laminar and turbulent wind conditions generated by a gust generator and an

active grid. On the improved turbine the same accelerometer (*Bosch BMA 140*) will be used to get acceleration data. To get more information about the dynamics of the turbine recordings of the turbine will be done with a camera. A tracking script based on *OpenCV 2.3* will be used to calculate the position of the turbine with a sampling frequency of 25 Hz. This will give more information about the movement of the turbine in combination with the acceleration data. The data may be used to get a better characterisation of the dynamical movement of the turbine. A stochastic model based on a two dimensional stochastic differential equation, which might be derived from the time series, may be developed. Several parameter on the floating turbine, like the anchoring and damping, will be changed to see how the movement of the turbine is influenced. A stochastic model for the power output, the so called Langevin Power Curve [2, 7, 1], will be applied on the measured power data. The goal is to determine a deterministic and a stochastic behavior in the stochastic driven power output which is caused by the reactions of the turbine on turbulent inflow. Finally the influence of the stochastic movement of the turbine on the power output of the turbine will be investigated. A stochastic model might give a tool for categorising which parameter are important for an optimal power production of the floating turbine and which are negligible.

References

[1] E. Anahua, M. Lange, F. Boettcher, S. Barth and J. Peinke. Stochastic analysis of the power output for a wind turbine. In *Proceedings of the European Wind Energy Conference EWEC*. 2004.

[2] J. Gottschall and J. Peinke. How to improve the estimation of power curves for wind turbines. *Environmental Research Letters*, 3(1):015005 (7pp), 2008.

[3] E. Hau. *Wind turbines: fundamentals, technologies, application, economics*. Springer Verlag, 2006.

[4] A. Henderson, D. Witcher and C. Morgan. Floating support structures enabling new markets for offshore wind energy. In *EWEC 2009 Proceedings*. 2009.

[5] J. M. Jonkman. Dynamics of offshore floating wind turbines—model development and verification. *Wind Energy*, 12(5):459–492, 2009.

[6] H. S. Kang and C. Meneveau. Direct mechanical torque sensor for model wind turbines. *Measurement Science and Technology*, 21(10):105206, 2010.

[7] P. Milan, M. Wächter and J. Peinke. Stochastic modeling of wind power production. In *Proceedings of EWEA 2011*. Brussels, 2011.

[8] W. Musial and S. Butterfield. Future for offshore wind energy in the united states. *EnergyOcean Proceedings, June 2004, Palm Beach Florida, USA*, 2004.

[9] P. Passon and M. Kühn. State-of-the-art and development needs of simulation codes for offshore wind turbines. In *Copenhagen Offshore Wind 2005 Conference and Expedition Proceedings, 26–28 October 2005, Copenhagen, Denmark*. 2005.

[10] J. Proakis and D. Manolakis. *Digital signal processing: principles, algorithms, and applications*, volume 3. Prentice Hall New Jersey, 1996.

[11] A. Zervos and C. Kjaer. Pure power-wind energy scenarios up to 2030. *European Wind Energy Association*, 250, 2008.

Fluid Power Transmission Applications in Wind Energy

N.F.B. Diepeveen, A. Jarquin Laguna
Offshore Wind, TU Delft
The Netherlands
E-mail: {N.F.B.Diepeveen, A.JarquinLaguna}@tudelft.nl

Keywords: hydraulic transmission, wind energy, fluid power, Delft Offshore Turbine

1 Introduction

In the attempt to make wind energy technology more economically attractive, the application of fluid power technology for the transmission of wind energy is being developed by several parties all over the world.

The working principle behind this concept is that rotating mechanical power from the prime mover is transformed into a fluid flow at high pressure, i.e. fluid power, by a positive displacement pump. At the other end of the hydraulic circuit, the fluid power is converted back to mechanical power by a hydraulic motor.

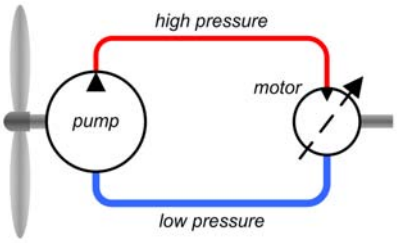

Figure 1: The functioning principle of fluid power transmission for wind turbine application

This paper presents the main players in the field and reveals the differences in configurations and applied technologies.

The use of hydraulic transmissions in wind energy systems is not a novelty. In 1981, The Jacobs Energy Research Inc. (JERICO) submitted a report to the US Department of Energy with the results of using a small wind turbine with hydraulic transmission (one step gearbox coupled to a gear pump) [1]. Testing the system was done by mounting a five meter diameter turbine on a trailer behind a pickup truck and pulling it over the road. The results showed a maximum output of 6.3 kW at a wind speed of 11.1 m/s and a corresponding pressure of 82.7 bar. A lack of precision engineering resulted in an overall low efficient system, which required high start-up torques.

The general conclusion of this project is that for small scale applications, a hydraulic drivetrain is not a practical solution, but that for larger systems “these drawbacks may become less significant and the advantages may be more prominent”.

Since 1981, research on hydraulic transmission for wind turbines has only sporadically been published. One exception is the project on variable transmissions conducted by Luc Rademakers at the Eindhoven University of Technology [2].

Nowadays with the increase of size of commercial wind turbines, and continuing developments in the fluid power industry, the idea of using hydraulics as an alternative solution for power transmission has become particularly attractive compared to the conventional mechanical transmissions.

Advantages of hydraulic drives

1. Continuous variable transmission. This enables speed control with a constant output speed, thus eliminating the need for a gearbox and power electronics

2. High power density. This reduces the overall nacelle mass and hence the support structure dimensions.

3. Increased reliability of components. This is partly due to the damping properties of hydraulic transmissions.

4. Low maintenance requirements

Challenges/disadvantages

1. Lower energy efficiency than conventional transmission.

2. Limited availability of multi-MW components.

Considering all these aspects, there is no doubt that a hydraulic solution can offer solid economic benefits when compared with current geared solutions.

2 Commercial developments

2.1 ChapDrive

ChapDrive is a Norwegian company which has developed a hydraulic transmission with a variable speed control system. The principal characteristic of their concept is the relocation of the major components from the nacelle at the top of the turbine tower to a power unit at the base of the tower using a hydrostatic transmission with a synchronous generator. They have refitted conventional wind turbines (onshore) into 225 and 900 kW functioning prototypes. In 2009, the Norwegian government granted ChapDrive five million euros subsidy for the commercial development of a 5 MW system.

Figure 2: Chapdrive drive train solution for wind turbines [3].

2.2 Artemis Intelligent Power - Digital displacement drive

Artemis is a spin-off company from a wave energy research group at the University of Edinburgh. It has developed a high efficient hydraulic pump/motor by means of computer controlled high speed solenoid valves.

The volumetric displacement of the radial piston drive is changed by controlling poppet valves with high speed actuators. Individual cylinders are thus reconfigured to either pump or idle on each stroke, resulting in high efficiencies over the complete range of operation, with a high level of controllability. These obtained efficiencies are comparable to that of a current wind turbine transmission and the technique is widely regarded as potentially revolutionary for fluid power drives. This technology is also being developed for applications in different industries including hybrid vehicles, off-road vehicles and renewable energy generation.

In December 2010 Artemis Intelligent Power was acquired by Mitsubishi Heavy Industries, which also has a wind turbine manufacturing division. Mitsubishi aims to develop an offshore wind turbine in European waters by 2015.

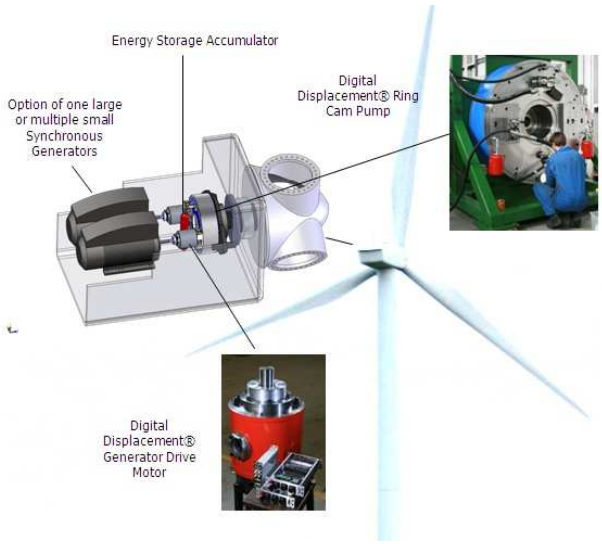

Figure 3: Artemis digital displacement concept [4].

3 Ongoing research

3.1 IFAS

The Institute for Fluid Power Drives and Control at Aachen University in Germany (IFAS) is developing and testing a 1 MW hydrostatic drive train for wind turbines which allows measurements under realistic conditions as experienced by a wind turbine. This is so far the biggest test bench that allows real time simulation of the different components with promising results. Static and dynamic behavior is being explored with overall achieved efficiencies of 85% throughout a wide power range.

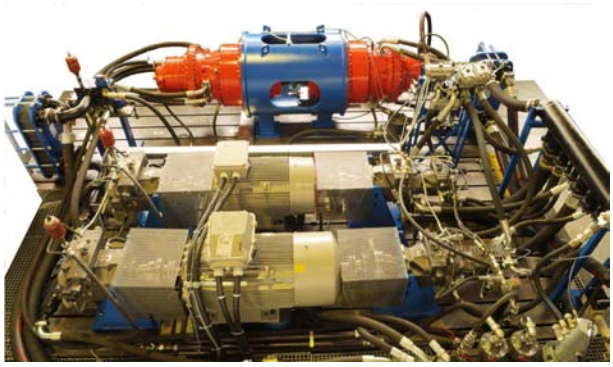

Figure 4: IFAS 1 MW test bench [5].

3.2 CCEFP

The Center for Compact and Efficient Fluid Power (CCEFP) is a research center in the US that is also developing a hydrostatic transmission for mid-size wind turbines; their approach is focused in the combination of system reliability and high efficiency to lower the life cycle cost of wind. At the moment they are constructing a test stand to allow for component testing and development of advanced controls for optimized performance [6].

3.3 Other related applications

The use of fluid power for energy conversion has already been used in other offshore renewable energy technologies, specifically in the wave and tidal energy industry, where transfer of technology becomes a very important aspect to be considered in wind energy applications.

One example is the Oyster wave energy converter, which is being developed by Aquamarine Power Ltd. The Oyster concept consists of a bottom-hinged oscillator that captures the power from near shore waves and it uses an open-loop hydroelectric power take off using fresh water pipelines to transfer the power to shore. Onshore a hydroelectric plant consisting of a variable speed generator coupled to a Pelton turbine delivers electrical power to the grid. A 315 kW full scale proof of concept was successfully installed in Orkney, Scotland in 2009. The next generation Oyster 800 was unveiled in July 2011. One of these 800kW systems will be deployed annually between 2011 and 2013.

The importance of this technology relies in the proof of concept of using water hydraulics for centralized electricity generation; which is one of the key aspects of the Delft Offshore

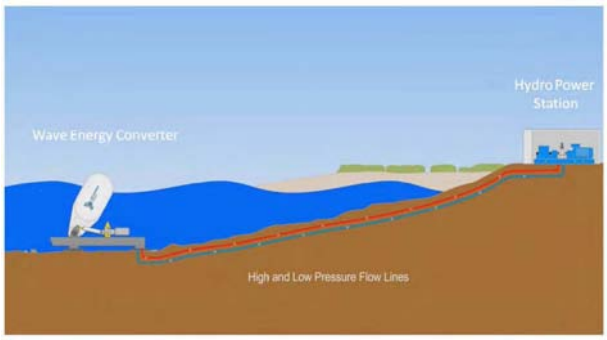

Figure 5: General Outline of the Oyster concept [7].

Turbines, a hydraulic solution proposed by TU Delft for offshore wind.

4 The Delft Offshore Turbine

The "Delft Offshore Turbines" (DOT), is a DUWIND research project which focuses on a cost effective solution for offshore wind by centralizing electricity production using pressurized seawater from individual pumping wind turbines [8].

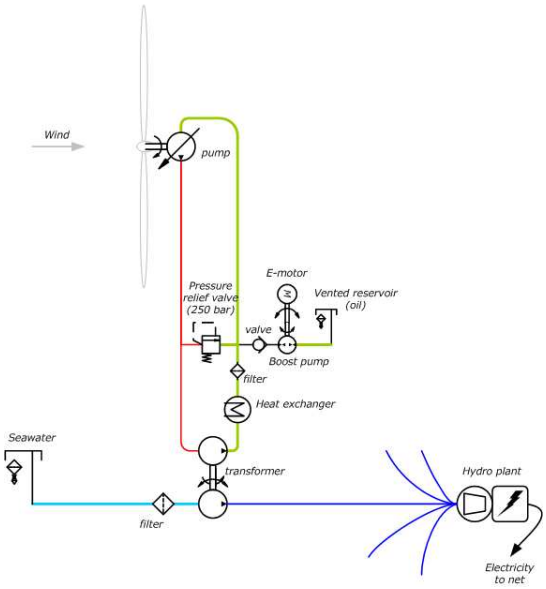

Figure 6: The Delft Offshore Turbines concept.

Each of the Delft Offshore Turbines comprises of a rotor that is directly coupled to a positive displacement pump, therefore converting the kinetic energy form the wind into a high pressure flow. The pressurized flow is contained in a closed-loop circuit together with a hydraulic motor which transfer the mechanical energy from the nacelle to the base of the tower. Here a seawater pump transfers the pressurized seawater in an open-loop to a central generator platform where a hydroelectric plant converts the pressurized seawater into electricity by means of a Pelton turbine which turns a central generator. Furthermore, the Pelton turbine allows the conversion from multiple seawater flows coming from the different turbines in the wind farm, therefore eliminating the need of individual generators and power electronics. A general schematic is presented in figure 6.

Current research at the TU Delft has been focused on the modelling and simulation of the proposed concept. Experimental tests on hydraulic components regarding performance and control have been carried out in collaboration with other research groups in and outside the Netherlands, with promising results. The next key objective is the construction of a scaled prototype for demonstration of the concept and to gain better insight on the dynamics and performance of the system. Development of the first prototype together with a series of experimental test is the first step towards a new fluid power solution for offshore wind.

References

[1] JERICO report. Hydraulic Wind Energy Conversion, 1981.

[2] L. Rademakers. Possibilities of Variable Transmissions in Wind Turbines. M.Sc.Thesis, University of Technology, Eindhoven, the Netherlands, 1988.

[3] ChapDrive. http://www.chapdrive.com

[4] Artemis Intelligent Power LTD. http://www.artemiswind.com

[5] Institute for Fluid Power and Control, RWTH. http://www.ifas.rwth-aachen.de/

[6] Center for Compact and Efficient Fluid Power. http://www.ccefp.org

[7] Aquamarine Power LTD. http://www.aquamarinepower.com

[8] N. Diepeveen, J. van der Tempel. Delft Offshore Turbines, the future of wind energy. Delft University of Technology, 2008.

Session 4B

Electrical Production and Grid Integration

Provision of frequency control with wind turbines

Markus Speckmann, André Baier
Fraunhofer IWES
Kassel, Germany
E-mail: {markus.speckmann,andre.baier}@iwes.fraunhofer.de

Keywords: frequency control, wind farms, probabilistic forecast, tertiary control, available active power

1 Introduction

Because of the increasing installation of renewable energy sources, the energy system in Germany is changing towards a more decentralized and intermittent power production. Consequently in the future renewable energies will have to take over the provision of ancillary services which is nowadays mainly done by conventional power plants. Frequency control is one important ancillary service. As it is described in many studies [1] wind farms will have to provide frequency control in the future. A lot of work has already been done in this field of research. For example the development of control strategies for the provision of frequency control by wind farms [2], [3]. Until now no work has been down concerning the proof of frequency control provision by wind farms. Therefore a concept is presented here (chapter 2). Another field of study which received little attention yet is calculating the amount of available frequency control power. Herein a method based on probabilistic forecasts is described (chapter 3). Closing an economic analysis is made for the German negative tertiary control market for three different wind farms and a virtual power plant (vpp) consisting of theses wind farms (chapter 4).

2 Proof of frequency control provision with wind farms

2.1 State of the art

Nowadays, the proof of frequency control provision is done by comparing the planned power production with the real power production. Usually the transmission system operator (TSO) gets the planned power production at the previous day [4]. If the TSO calls frequency control power, the difference between the planned power production and the real power production must equal the amount of frequency control power. This method is suited for controllable power plants, like coal power plants or biogas plants since they can follow a planned power production made at the previous day.

For wind farms there are only two possibilities to keep a planned power production. One is reducing their planned power production thus increasing the probability of reaching it. This possibility illustrates figure 1. On the y-axis the normalized power of a wind farm is outlined. The graphs in figure 1 illustrate different security levels. The topmost graph resembles a security level of 90%, the lowest graph resembles a security level of 99.9%. Security level of 90% means that the probability is 90% that the real power production is above that 90% graph. The graphs display probabilistic day-ahead forecasts. The area in the background equals the real power production.

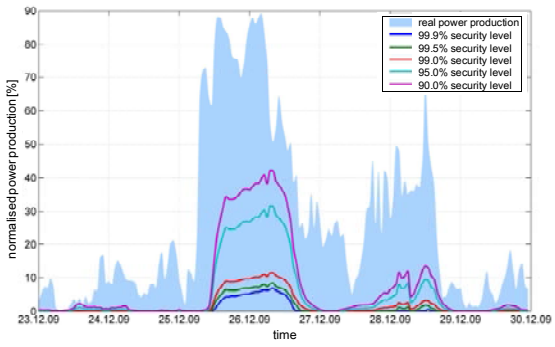

Figure 1: Illustration of probabilistic wind power forecasts (day-ahead) for different security levels and of the real power production of a wind farm [5]

As it can be seen, already for a low security level of 90% a great amount of energy is lost. Therefore, this solution is neither economic nor ecologic.

The second possibility of keeping a planned power production is the combination of a wind farm with storage. This was done in [6]. Here the participation of a vpp consisting of a wind farm, a pumped storage plant and a biogas plant at the negative tertiary control market was investigated. The pumped storage plant was used to balance the forecast error of the wind farm. The result was that the participation of the wind farm has almost no effect on the amount of tertiary control offered by the vpp. This is due to the fact that the amount of power of the pumped storage plant, needed for balancing the forecast error of the wind farms, equals the amount of tertiary control, which

can be provided by the wind farm. It can be expected that the results are different if the vpp consists of more than one wind farm localized in different regions. This would lead to a better wind forecast and thus to a lower amount of power from the pumped storage plant needed for balancing the forecast error. Nevertheless, the disadvantage of optimizing subsystems remains leading to an unnecessary high amount of storage. This is due to the fact that sometimes the pumped storage plant of the vpp will operate in a different direction than the frequency control in the control area. This is always the case, if the forecast error of the wind farm is in a different direction than the call for frequency control in the control area.

2.2 New Concept for Proving the Provision of Frequency Control by Wind Farms

Since both possibilities of keeping a planned power production with wind farms explained in the chapter before have disadvantages this leads to the following conclusion. Wind farms do not provide frequency control or the verification of the provision is changed for wind farms.

In [5] we developed a new proof, which is illustrated in figure 2. This concept has neither the disadvantage of loosing wind power nor the disadvantage of optimizing subsystems leading to an increased amount of storage.

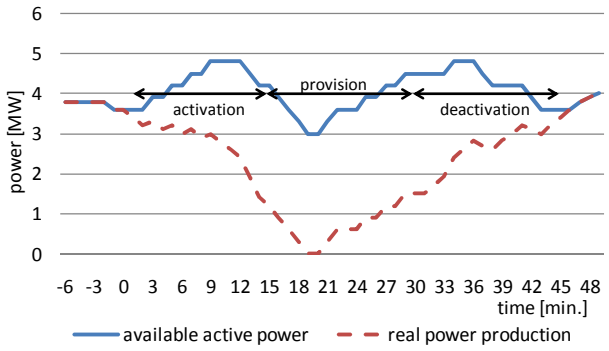

Figure 2: Illustration of the new concept for proving the provision of frequency control, by comparing the available active power (upper graph) with the real power production (lower graph) [5]

The proof is done by comparing the available active power (upper graph) with the real power production (lower graph). The available active power equals the power production of the wind farm if the power was not reduced. Figure 2 illustrates the example of providing tertiary control with the wind farm. In the first 15 minutes the tertiary control is activated (activation). Than the provision of tertiary control is hold constantly for 15 minutes (provision) and afterwards the tertiary control is deactivated within 15 minutes (deactivation).

3. Calculating an Offer for the Provision of Frequency Control

The use of ordinary point wind power predictions is not advisable for calculating an offer for the frequency control market. A failure to fulfill the contracted capacity could be fined and moreover contradicts the meaning of frequency control power. To manage this risk of failure we propose a method to determine an offer based on probabilistic wind power forecasts. Ordinary wind power point forecasts are only able to estimate the amount of wind power which could be expected for the future point in time. In contrast probabilistic wind power forecasts estimate the probability distribution of the wind power feed-in for a future point in time. More precise it is the probability distribution of the random variable X_t at the point at time t. This probability distribution could then be used to determine the probability of occurrence $P(X_t \leq x)$ of any wind power feed-in x. An example for the forecasted probability distribution for wind power feed-in is displayed in figure 3.

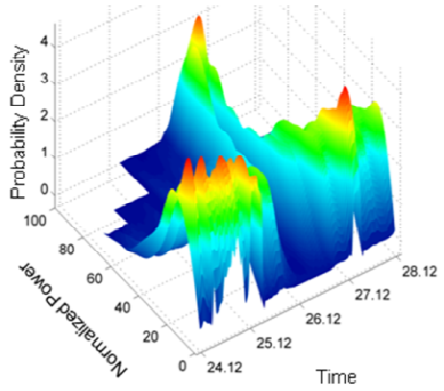

Figure 3: Example for a forecasted probability distribution for wind power feed-in for a certain period of time. Each time step represents a probability distribution function.

For an offer of negative frequency control it is important to know the amount of wind power which could be expected with a certain level of security S. This amount is the wind power x for the security level $S=1-P(X_t \leq x)=P(X_t>x)$. Thus the negative frequency control offered is the (1-S) - quantile of the forecasted probability distribution for the time step t. In other words the wind power for the probability to fail to deliver the offered wind power (1-S).

3.1 Example Negative Tertiary Control Power

The German tertiary control power market is a day ahead market in a four hour time resolution. An offer, therefore, has to be uniform for one four hour block. Thus the maximal possible offer is the four hour minima of the quantile forecast with the security level S or the probability (1-S). An example for an offer is displayed in figure 4.

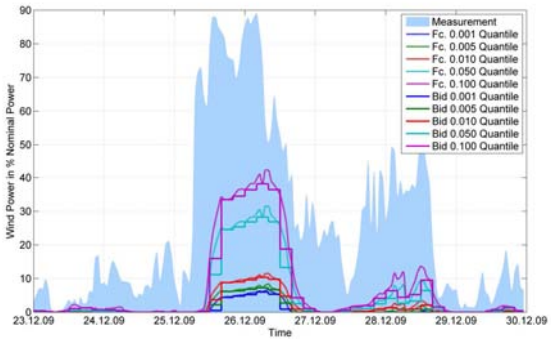

Figure 4: (1-S)-quantile forecast for security levels of 99.9%, 99.5% 99.0%, 95% and 90% and the corresponding offers.

This calculation of offers is done for the whole year 2009 for three wind farms wf north, wf middle and wf south. These wind farms are located in the north, middle and south of the 50Hertz Transmission zone. Additionally offers for a vpp consisting of the three wind farms are analyzed. The probabilistic forecast for the vpp for each time step $P(X_{vpp,t} \leq x)$ is the combination of the three single probabilistic forecasts under the assumption that these wind farms are stochastically independent. Under this assumption the probabilistic distribution function (pdf) of $X_{vpp,t}$ is the convolution of the single pdf of the three wind farms. More general:

$$X_{vpp,t} = \sum_{i=1}^{n} X_{i,t} \quad : \quad f_{vpp,t}(x) = \left(f_{1,t} * \ldots * f_{n,t}\right)(x) \quad t \in [t_{Start}, t_{End}]$$

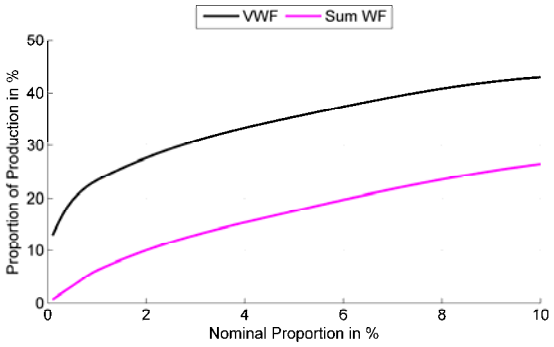

Figure 5: Proportion of the offered negative tertiary control power of the overall production for 2009 against the probability to fail of delivering (1-S).

The result of the analysis for the vpp and the sum of the three different wind farms for 2009 is given in figure 5. Here the proportion of the offered negative tertiary control power of the overall production is displayed.

One obvious result of the analysis is a huge improvement of the available negative tertiary control power for the vpp in comparison to the sum of the three different wind farms. This behavior can be observed over all probabilities to fail from 0.1% to 10% or in terms of security level from 99.9% to 90%. Where the sum of single offers can't provide any noticeable amount of negative tertiary control power for the security level of 99.9% the vpp is able to deliver around 13% of the overall production in 2009. For a security level of 90% the sum of the single offers is 27% and for the vpp 43% of the overall production.

The results show a great influence of spacial balancing effects to the predictability of the volatile wind power. Thus, the offers for negative tertiary control power increase for the vpp in comparison to the sum of the single offers for the same security level.

4. Economic Analysis

With the results from chapter IV an economic analysis was conducted. For the three different wind farms and the vpp the profit was calculated, if they had participated at the German market for negative tertiary control power in 2009. At this market the six four hour intervals of the next day or the following days in case of weekends or public holidays are traded at every working day at ten o´clock in the morning [7].

The analysis was conducted for different security levels of the offer. Since the tertiary control market is a pay as bid market, the calculations were done for three different prices per kW. The low price equals the lowest price in the particular four hour interval. The medium price equals the average price and the high price the highest price in the four hour interval. The prices can be downloaded on the internet platform of the TSO (www.regelleistung.net).

The profit at the negative tertiary control power market equals the income resulting from the price per kW minus the penalty for not providing frequency control power. On the one hand, the income rises with lower security levels, since more tertiary control can be offered. On the other hand, the penalty increases with lower security levels, since the occurrence of times in which the wind farms or the vpp cannot provide the offered tertiary control rises. The income is calculated by multiplying the price per kW of the particular four hour interval with the offered tertiary control. The penalty is calculated according to the regulations in [10].

Prices per kWh were not considered. It was also not considered, at which markets the energy production of the wind farms is sold or if they are paid according to the EEG. For every wind farm and for the vpp 18 scenarios were calculated since six different security levels and three different price levels were considered. It must be mentioned that 2009 was a high price year [8].

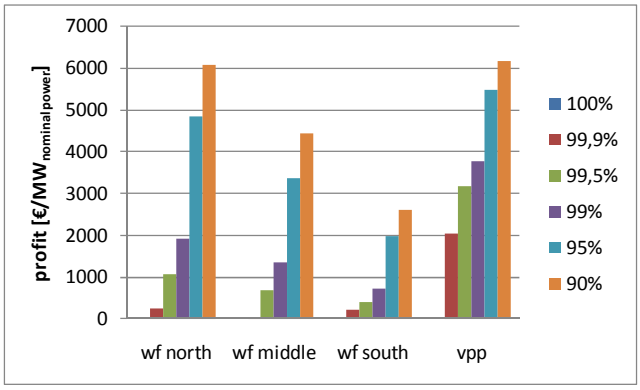

Figure 7: Results of the economic analysis showing the profit of the different wind farms and the vpp for the highest price per kW at the negative tertiary control market in 2009 [5]

For all wind farms and the vpp the profit increases with lower security levels. This means that for the scenarios with the highest price per kW the increase in income from a high security level to the next lower security level is always bigger than the increase of the penalty. This is not the case for the scenarios with the lowest price per kW for all wind farms and the vpp. This is due to the fact that the increase of the penalty from a security level of 95% to a security level of 90% is bigger than the increase of the income.

The vpp has got the best results. This is because of balancing effects between the wind farms, which can only be used if they are combined in a vpp.

5. CONCLUSION

A new concept for proving the provision of frequency control with wind farms based on the determination of the available active power was presented and its advantages compared to the actual method were discussed. Moreover a method for calculating an offer for negative tertiary control based on probabilistic forecast was described. This method was applied to three different wind farms and the combination of these wind farms in a vpp for the year 2009. Here the proportion of the overall production differs from about 0% to 43% depending on the security level with great advantages for the vpp. The results of an economic analysis for the different wind farms and the vpp were presented. The profit differs from nearly 0 €/MW to 6149 €/MW depending strongly on the security level and the price per kW. The combination of the wind farms in a vpp leads to higher profits, due to balancing effects.

REFERENCES

[1] German Energy Agency: “dena-Netzstudie 2 – Integration erneuerbarer Energien in die deutsche Stromversorgung im Zeitraum 2015 – 2020 mit Ausblick 2025“, Berlin, 11.2010

[2] Mauricio, J.M. et al.: ”Frequency Regulation Contribution Through Variable-Speed Wind Energy Conversion Systems”, IEEE Transactions on power systems, Vol. 24, No.1, 2009

[3] Yingcheng, X.; Nengling, T.: ”Review of contribution to frequency control through variable speed wind turbine”, Renewable Energy, Vol.36, Issue 6, pages: 1671 – 1677, 2010

[4] Association of German Grid Operators (VDN): “TransmissionCode 2007 Netz- und Systemregeln der deutschen Übertragungsnetzbetreiber“, Berlin, 8.2007

[5] Speckmann, M.; Baier, A.; Wessel, A.; Weiland, M.: “Begleitstudie zum Vorschlags für einen Anhang zum Transmission Code zur Präqualifikation von Windparks für die Erbringung von Minutenreserve“, Study for Westkapital GmbH, Kassel, 4.2011

[6] Speckmann, M.; Direkvuttikul, K; Schlögl, F.: “provision of tertiary control by a regenerative virtual power plant”, conference paper DEWEK, 2010

[7] Federal Network Agency: “Festlegung zu Verfahren zur Ausschreibung von Regelenergie in Gestalt der Minutenreserve“, AZ-BK6-06-012, 29.8.2006. Available: www.bundesnetzagentur.de/media/archive/7318.pdf, 21.8.2009

[8] BalancePower GmbH: “Minutenreserve – Zusatzerlöse für Betreiber von Notstromaggregaten, Stromerzeugern oder Stromverbrauchern“, march 2011. Available: http://www.energylink.de/dokumente/Minutenreserve_mit_Notstromaggregaten.pdf

[9] “Gesetz für den Vorrang Erneuerbarer Energien (EEG) – Konsolidierte (unverbindliche) Fassung des Gesetzestextes in der ab 1. Januar 2012 geltenden Fassung ”, 2011. Available: http://www.erneuerbare-energien.de/files/pdfs/allgemein/application/pdf/eeg_2012_bf.pdf

[10] 50Hertz: “Rahmenvertrag über die Vergabe von Aufträgen zur Erbringung der Regelenergieart Minutenreserve“, 11.2006

The North Sea Super Grid

Til Kristian Vrana and Olav Bjarte Fosso
Norwegian University of Science and Technology
Trondheim, Norway
E-mail: vrana@ntnu.no

Keywords: North Sea Super Grid (NSSG), Offshore Wind Farm, Offshore Cluster Grid, High Voltage Direct Current (HVDC), Voltage Source Converter (VSC), Current Source Converter (CSC), Hybrid HVDC, Multi Terminal HVDC (MTDC).

INTRODUCTION

The next decades will see large scale deployment of wind turbines in the North Sea. Offshore wind farms that are located near shore can be integrated into the power system with the same technologies as onshore wind farms. More interesting (from an electrical point of view) are the wind farms located far away from shore, which need to be connected with High Voltage Direct Current (HVDC) technology. One farm of this type is already in operation (Bard offshore 1).

The liberalisation of the European electricity markets demands strong interconnectors between the countries. Power output fluctuations of uncontrollable sources are increasing massively, creating the need for long distance transmission to balance regional fluctuations. Some highly needed balancing service can be supplied from the Scandinavian hydro power if transfer capacity is sufficient.

Stricter environmental regulation of the oil&gas industry implies the electrification of offshore rigs. Gas turbines on the platform can be replaced by a power cable to shore. For remote offshore rigs HVDC connections are needed, and one system of this type is already in operation (Troll-field); a second system is under construction (Valhall-field).

The electrical integration of offshore loads and generation is advantageous, since a part of the electric power produced offshore can be consumed locally. This will avoid transmission losses, and platforms supplied by nearby wind parks would be free of carbon emissions.

These developments indicate that the North Sea Super Grid (NSSG) will be essential in the future. The construction of the NSSG is a pioneer project and will pose a lot of technical challenges. In this article (which is based on [1]) an overview of the relevant technologies is given and the challenges of realising the NSSG are discussed.

NSSG STRUCTURE

Generally, the infrastructure of the NSSG can be divided into four levels (shown in Figure 1).

I. Generation and loads
II. Wind farm collection grids
III. Offshore cluster grids
IV. Long distance HVDC transmission

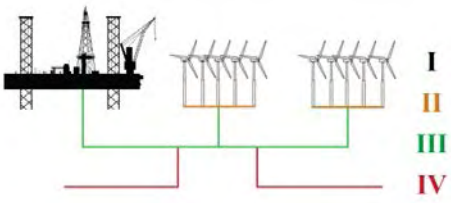

Figure 1: Infrastructure levels of the NSSG

Level I: Offshore generation and loads

The main part of offshore generation will be wind turbines. Wave power plants, stand-by diesel generators, gas turbines and uninterruptible power supply systems are also possible, but will not play a major role.

The main part of the produced power will not be consumed offshore but transported to shore. The loads on connected oil&gas platforms and the wind farm internal loads will be the most relevant offshore loads.

There are significant differences between classical generation units and modern wind turbines. The NSSG will also have a tremendous power surplus. These two issues might lead to power balancing control challenges for the offshore clusters.

Level II: Wind farm collection grids

AC collection grids are applied to all existing wind farms, offering a significant advantage, when the wind farm is directly connected to an AC power system. This advantage disappears for remote offshore wind farms with HVDC connection. For these farms DC collection grids might become a promising option which offers significant benefits. There is very little experience with DC grids, which makes this approach challenging.

The internal electric distribution system of an oil&gas platform also belongs to level II.

Level III: Offshore cluster grids
Offshore cluster grids connect several wind farms together and eventually integrate oil&gas platforms. This type of grid could be either realised in AC or DC. Significant advantages come along with a DC solution, but also the challenges are much larger, due to the earlier mentioned lack of experience.

Level IV: Long distance transmission
AC power transmission is always limited in distance. Significant distances can be handled onshore, but subsea AC cables are much more restricted. The maximum possible distance depends on several factors, but a limit of 100km can be seen as a rule of thumb. Since this limit is exceeded in the North Sea, HVDC transmission is the only realistic option.

HVDC TECHNOLOGY

The offshore cluster grids can be connected to each other and to shore via HVDC links. There are two converter types, which can be applied for HVDC systems: Voltage Source Converter (VSC) and Current Source Converter (CSC). VSC technology is the most promising option for offshore projects nowadays, but CSC technology might also offer good solutions in the future. A combination of both is called hybrid HVDC, which could offer benefits due to its conceptual asymmetry. VSC and CSC HVDC systems are normally symmetric, meaning both sides of the link being equal and power flow possible in both directions. They could also be designed asymmetric, but this has not been applied yet.

VSC HVDC
VSC technology is the most promising option today, due to advantages like compact converter design, black start capability, flexible bidirectional operation and reactive power control. All recent offshore projects (Troll, Valhall, Bard Offshore 1...) are VSC based.

CSC HVDC
With increasing size of the offshore clusters, the demand for stronger interconnection will arise, where CSC technology might offer good solutions, because of its lower losses and higher transmission capability. Most onshore projects are CSC based.

Hybrid HVDC
Hybrid HVDC consists of a VSC on one side and a CSC on the other side of the same DC link, but the concept has until today not been applied. The development of this technology is still at an early stage and it has so far not been tested.

A hybrid HVDC system is (unlike other HVDC systems) asymmetric, which usually is considered a disadvantage. For the NSSG, where the power systems on both ends of the link are totally different (offshore cluster grid and large onshore power system), this asymmetry might actually be beneficial. The VSC terminal is compact and therefore suitable for offshore platforms. The CSC terminal has lower losses and could be placed onshore where size is less important.

Asymmetric HVDC
While Hybrid HVDC is always asymmetric, also VSC and CSC based HVDC systems could be designed asymmetric. This might be beneficial for HVDC links, which are mostly used in one direction (power flow always from wind farm to shore).

HVDC ARRANGEMENTS

Many HVDC systems will be installed in the North Sea. Most existing HVDC systems are simple point to point connectors, but more complex schemes are possible. Series and parallel systems both offer advantages, and a meshed grid would combine the features of both, but it would also be technically more challenging.

Series HVDC
It makes sense to connect several smaller offshore facilities to a single HVDC link, rather than installing one separate cable for each facility. A simple example is a large onshore converter connected by a HVDC cable to a smaller offshore wind farm and another wind farm connected in the middle of the cable. For this system Hybrid HVDC is interesting, with a CSC onshore and two VSC offshore.

With an increasing number of separate offshore electric installations, series connected HVDC will gain importance. These systems are also called Multi Terminal HVDC (MTDC) systems.

Parallel HVDC
Large wind farm clusters are planned for the future, which will need a powerful connection to shore. Parallel HVDC connections could be the only realistic option for this, since it can offer the needed transfer capacities and the important redundancy.

Meshed HVDC grids
A meshed HVDC grid structure would combine advantages of series and parallel connected links, but additional challenges will arise. System protection and power flow control are two of the main fields, where technical progress is necessary to make HVDC grids possible in the future.

NSSG ROADMAP

A variety of topologies for the NSSG have been studied, optimised, proposed and evaluated in several studies. These studies can be taken as a guideline, but many of them are to some extent unrealistic since they are based on a green field approach.

The construction of electric infrastructure in the North Sea has already started. Individual projects are coordinated nationally nowadays, and they do not follow an internationally agreed master plan. By the time, when the NSSG project will be realised, several offshore facilities will exist.

There are three regions in the North Sea, which will play a major role in the deployment of the NSSG. In the German Bight the construction of remote offshore wind farms has started and the first is already in operation. In the Norwegian part of the North Sea a HVDC link to the Valhall-field is under construction. The UK has large plans for wind farms at the Doggerbank, but this project is still in the planning process. Considering these three areas, a simplified topology of the NSSG could look like Figure 2.

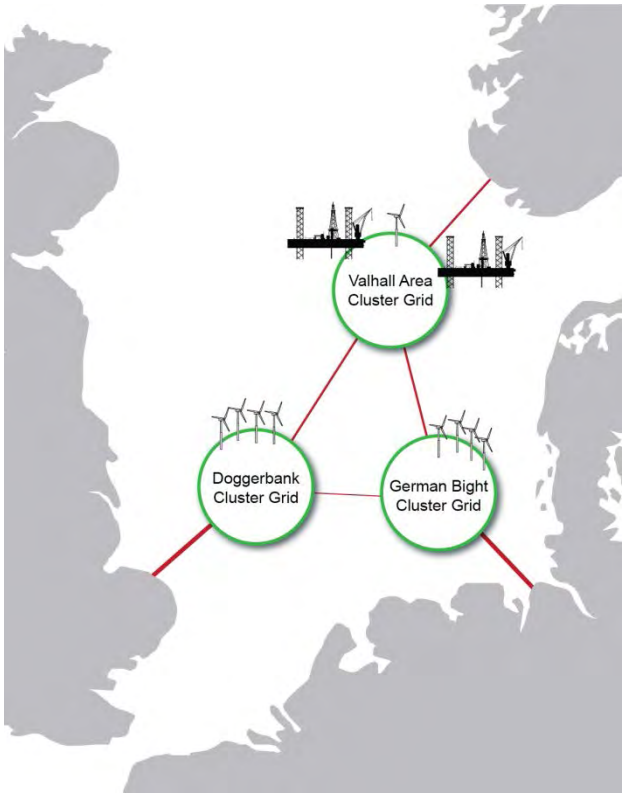

Figure 2: Simplified NSSG topology

The NSSG will not be built in one step as a planned system. It will need to integrate individually and independently planned projects, comprising several DC and AC voltage levels and possibly even different AC frequencies. This flexible and modular approach is different from all existing HVDC projects. It has significant similarity with the evolution of the onshore electric power systems and will lead to a grown rather than an optimised structure.

CONCLUSION

The countries around the North Sea have agreed to build the NSSG. No large power system has ever been created offshore. This is a huge pioneer project and many challenges come along with it.

Building the NSSG with only AC technology is impossible due to the long distances involved. Even though DC is often seen as the solution for the future, many challenges still remain. The wind farms under construction at the moment use a combination of AC and DC technology, AC within the wind farm and DC transmission to shore. Looking far into the future, a gradual shift towards DC technology can be expected.

VSC based HVDC is used today for offshore projects and seems to be the promising solution for the future as well. CSC technology should also be considered since it has some advantages and might gain importance for offshore application in the future. The NSSG might even give application to asymmetric concepts like hybrid HVDC.

The large number of HVDC systems to be constructed for the NSSG indicates the need for smart interconnection of those. While until now almost only point to point connectors have been realised, the NSSG calls for more complex system solutions. Both series and parallel structures will be needed, eventually resulting in meshed HVDC grids.

The planning process of the NSSG is very complex because many technical questions are still unsolved. The coordination of activities is also an issue, due to the large number of countries, companies and parties involved. The future NSSG will therefore incorporate many individually constructed offshore facilities and have a grown rather than an optimised structure.

A once established electric power system always offers significant gains for the covered area. Future offshore projects will have the advantage that they can be connected to the NSSG, avoiding a long connection to shore. All of Europe will benefit from the NSSG, economically and environmentally.

REFERENCES

[1] T.K. Vrana and O.B. Fosso, Technical Aspects of the North Sea Super Grid, Electra, CIGRE, 2011.

Stability Study of Offshore Wind Farm with Long HVAC Transmission System

H. Guo, K. Rudion, Z. A. Styczynski
Chair Electric Power Networks and Renewable Energy Sources, Otto-von-Guericke-University Magdeburg
Universitaetsplatz 2, Magdeburg, 39106, Germany
E-mail: hui.guo@ovgu.de, rudion@ovgu.de, sty@ovgu.de

Keywords: DFIG, grid code, HVAC, offshore wind farm, LVRT, voltage stability, critical fault clearing time (CCT)

1 Introduction

The development of offshore wind power in Europe is recognized as an important potential for helping achieve the European target for renewable energy. There are several proposals for offshore grid development in the North Sea, such as EWEA's 20 year offshore network development master plan [1]. 20 offshore wind farms with a total capacity of approximately 19 GW are in the planning stage for the North Sea, and 5 wind farms with a total capacity of about 2 GW are already under construction. According to EWEA, the cumulative installation capacity of offshore wind power in the EU will reach 40 GW by 2020. It will be a big challenge for grid operators to maintain the stability and reliability of the power system with such a large scale of wind power integrated to it.

There are mainly two types of technologies available to integrate offshore wind farms to the onshore mainland grid. The first one is HVAC (High-Voltage Alternating Current) and the other is HVDC (High-Voltage Direct Current). Both technologies have advantages and drawbacks. Since the network configurations and transmission distance are for the most part different for each wind farm, the connection for an offshore wind farm should be analyzed and optimized case by case. Generally the HVAC system should be the preferred option as long as it is feasible. In fact, HVAC transmission is more competitive than HVDC and has lower investment costs and higher efficacy under a certain transmission distance, even with the investment of additional FACT devices to enhance the system transmission capability and stability. Figure 1 shows a comparison of HVAC and HVDC transmission costs over distance. Until the end of 2009 most of offshore wind farms were connected to the power transmission network by HVAC. For example, the 160 MW Horns Rev I and the 160 MW Rødsand in Denmark as well as the Alpha Ventus in Germany are connected by means of submarine AC cables. As in these cases, AC transmission turns out to be an economically and technically attractive option. The existing offshore wind farms all have rated powers less than 210 MW and the distances to shore are less than 50 km (EWEA statistic: Operational Offshore Wind Farms in Europe, End 2009). In the near future the development of European offshore grid [7] requires international interconnection of large offshore wind farms via very long distances and more power flow controllability between the countries. Thus, the HVDC will be the first choice to fulfill the requirement [8].

In comparison to HVDC transmission, an HVAC cable is characterized by its significant large shunt capacitance. This may cause large charging current evoking reactive power flows and may impact the stability of the system. Therefore, the reactive power compensation become a natural part of the scheme and must be carefully designed to guarantee the system stability, such as voltage stability. The goal of this paper is to investigate the dynamic behavior of offshore wind farms connected by means of high voltage AC (HVAC) cables with regard to fulfilling the grid code specification.

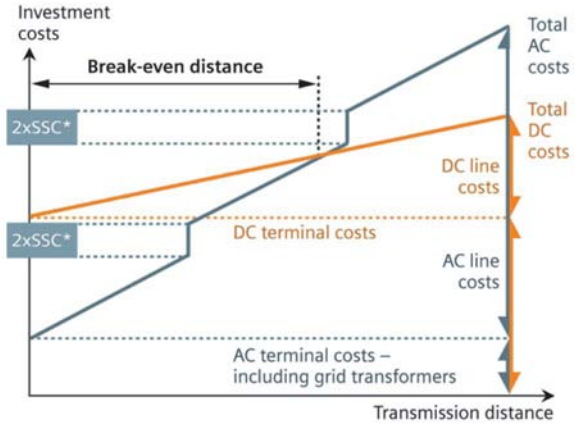

Figure 1: HVAC vs. HVDC transmission cost over distance (*SSC = Series and shunt compensation of AC lines) [9]

Some aspects, like voltage stability, are especially focused on regarding the use of AC technology to integrate offshore wind farms to the power system.

2 TEST SYSTEM MODELING

2.1 General description of the wind farm

The wind farm is based on the Alpha Ventus offshore wind farm, which is located in the North Sea, has an installed capacity of 60 MW and is connected via a 110 kV AC cable to the onshore grid. It is equipped with 5 MW-Class wind turbines. Six of them are based on DFIG (double-fed induction generator), the others are based on PMSG (permanent-magnet synchronous generator) with full-scale power converter. The HVAC cable, which is used to integrate the generated offshore wind power to the onshore power grid, is around 70 km long. Several compensation units are used to compensate for the reactive power of the offshore wind park including the submarine cable.

2.2 Modeling of the test system

The test system has been modeled in the simulation tool PSS®NETOMAC. This model does not represent the real wind farm (alpha Ventus). In order to investigate the transient stability of the offshore wind farm, detailed dynamic simulation models are used. Since the study is focused on the dynamic behavior of DFIG, all the wind turbines are modeled based on DFIG with controllers. The onshore network is modeled as an equivalent synchronous generator with feeder impedance. The topology of the model is shown in Figure 2. It consists of wind turbine transformers, HVAC cable, shunt reactors as compensation units "Comp.1" and "Comp.2", and local load of the onshore grid "Load 1" and "Load 2". T1 (30/110 kV) is the offshore transformer; T2 (110/220 kV) is the transformer on land. In steady state, the HVAC cable can be completely compensated with two shunt reactor banks at both ends, each has 35 Mvar. The power is transferred through the transmission line L2 to node N2, where there is a local load V1 and generation SG. The node N2 is connected to N1 to the Grid through Line L1.

2.3 Control strategy of the offshore wind farm

The reactive power behavior of the offshore wind farm with an HVAC connection system should be carefully studied. The control strategy of the wind farm will be aimed at maintaining the voltage at the PCC (point of common coupling), which is the higher voltage side of the onshore transformer. Under normal operation conditions the steady-state voltage control can be achieved by compensation units. During system contingency such as short-circuit in the grid, the wind turbines will participate on the dynamic voltage control by providing reactive power to the system. According to the grid code [2] requirement on LVRT (low voltage ride through) capability, the wind farms have to remain connected to the grid to help the voltage stability during and after grid faults. This can be done by dynamic reactive power control of the output of the grid-side converter.

2.4 Grid code requirement for LVRT

As more and more wind power is fed into the transmission grid level in Europe, some of the system operators (TSO) have revised their grid code in order to face the challenge of maintaining system stability and controllability [3][4]. Figure 4 shows the German grid code requirement on LVRT for wind farms [2]. The requirement only concerns contingencies such as short circuits occurring in the transmission system, and not short circuits within the wind farm. The red line represents the voltage

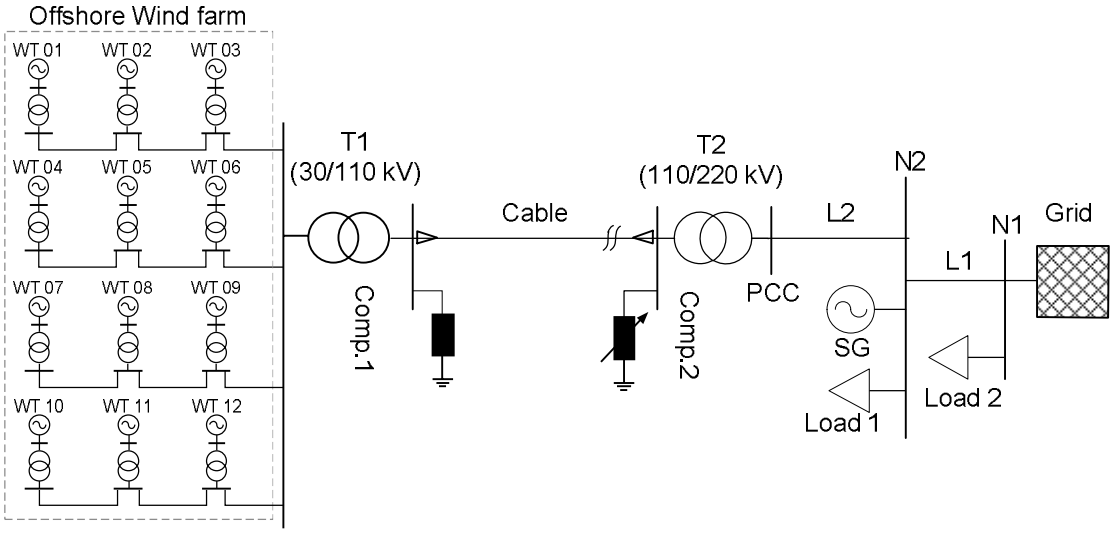

Figure 2: Configuration of the test system

limitation at the PCC (point of common coupling) during and after a grid disturbance, for instance a short circuit fault in the grid. According to the grid code, disconnection of the wind farm is generally not permitted above this limitation line for a specified time (illustrated in Figure 4). The wind farm must withstand voltage dips down to zero for 150 ms and remain connected to the grid and not lead to instability. During the grid fault the wind farm should provide the grid with reactive power to support the dynamic voltage. To ensure this, the parameters for voltage and frequency protection relays of the wind farm have to be chosen appropriately and set carefully. The parameter setting depends on the system configuration, such as voltage level, network structure, strength of the onshore grid with which to be connected and the voltage behavior during grid fault in worst case scenarios. The protective functions of the wind farms shall include settings and time delays meeting the grid code requirements. In this paper the fault clearing time has been estimated for the test system, which gives the information about the delay setting.

3 Case Study and Results

In order to investigate the behaviour of the test wind farm with the aforementioned configuration, a few scenarios were chosen and simulated in the software PSS®NETOMAC. This study concentrates on transient behaviour of the wind farm under specified fault conditions, such as 3-phase short circuit. The test system was simulated in order to study the LVRT requirement. Furthermore, the critical fault clearing time (CCT) was estimated in the case of 3-phase short circuit fault (the worst case) to access the dynamic stability limit of such wind farm configuration. The CCT can indicate the system dynamic stability limit indirectly. In addition, the CCT for different wind farm capacities are estimated, assuming that the wind power increases through the wind farm extension.

3.1 Study case 1: Voltage stability and LVRT

The object of this study case is to investigate the dynamic behavior of the HVAC connected wind farm during and after a severe 3-phase short-circuit on the grid side at the PCC. The obtained simulation results are used to verify the wind farm LVRT-capability according the grid code specification, and to assess the limits of the applied control strategy. The fault occurs at t=1 s and is cleared after 150 ms. The simulation time step is set to 1 ms to capture the transient of the wind turbine generator (WTG).

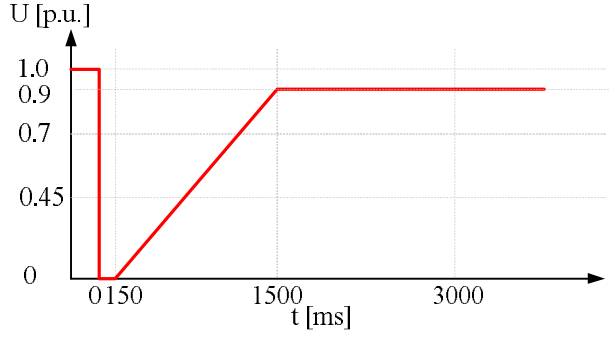

Figure 3: LVRT requirement for wind farms [2]

The simulation results are illustrated in Figure 4 and Figure 4Figure 5. Figure 4 shows the response of the wind farm model at the observed node PCC, during the fault for 150 ms the wind farm remains connected to the grid and no voltage instability is observed. Due to the reactive losses along the AC cable and transformer, during the fault the reactive power at PCC is nearly zero, despite the fact that each WTG in this wind farm supply about 2 Mvar reactive power to the system. Figure 5 shows the dynamic behaviors of the wind turbine generator. It can be observed that, in normal operation before fault occurrence, the reactive power required for the system is balanced by the compensation units, and thus no reactive power is generated by the WTG. During the faults the WTG supplies reactive current to the grid through the control of the line side converter (LSC) and the generator is accelerated. After the fault clearance, the voltage cannot reach the nominal value immediately, because in this moment the generators have to absorb reactive power for its magnetization. At the same time, the active power oscillation can be detected. After about 2 seconds the system becomes stable.

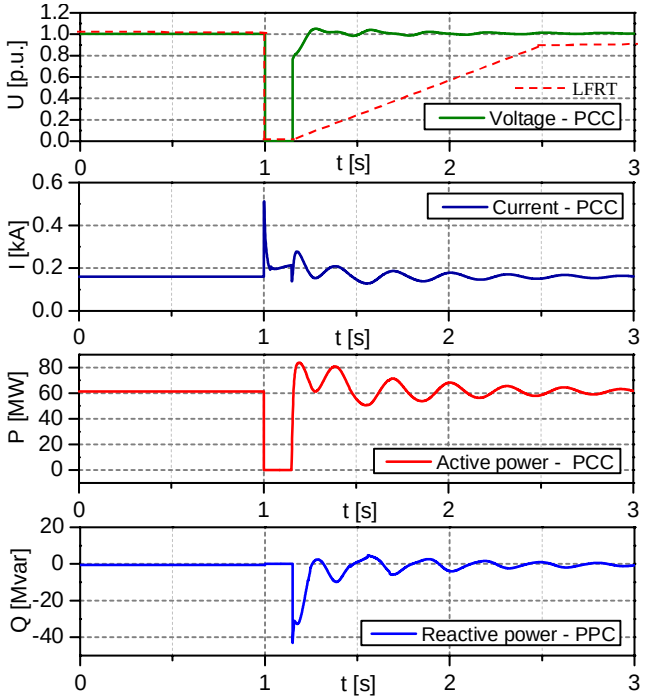

Figure 4: Dynamic response of the test system at PCC during a three-phase short-circuit fault (duration 150 ms)

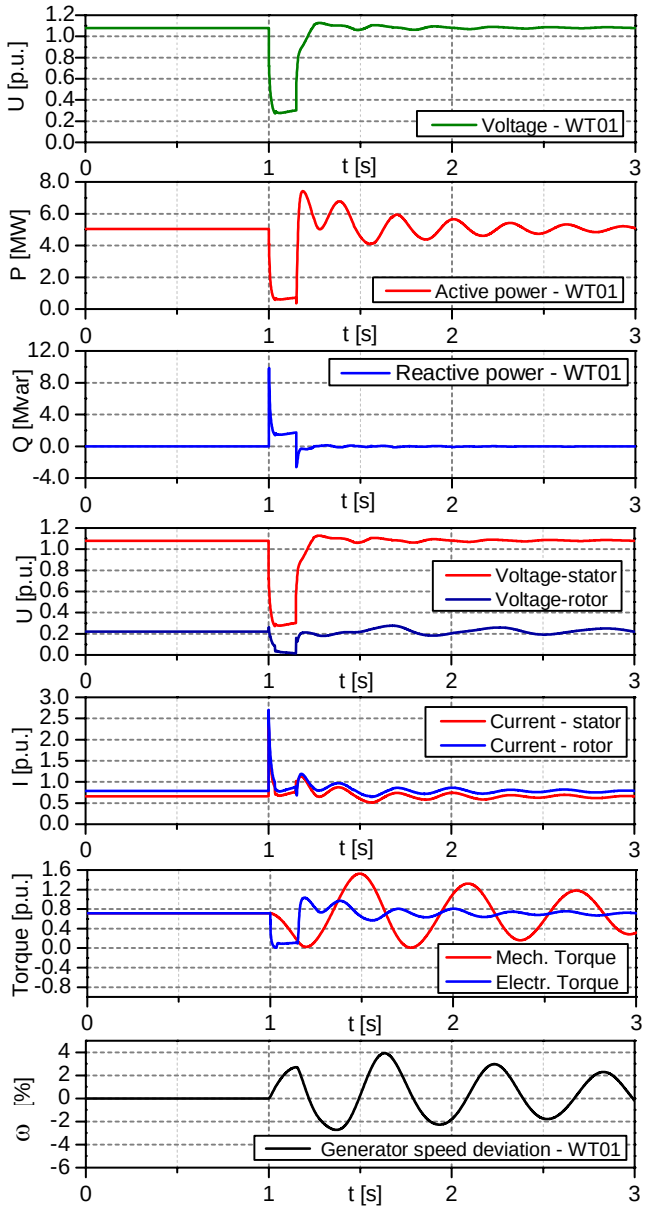

Figure 5: Dynamic response of the wind turbine generator WT01: generator terminal voltage, active-/reactive power output, rotor-/stator voltage and current, generator torque, and generator speed deviation.

3.2 Study case 2: stability limit - Critical fault clearing time (CCT)

In this study case, the critical fault clearing time of the test wind farm for different wind power capacities is obtained by means of dynamic time domain simulation. If a 3-phase short-circuit fault at PCC (causes voltage down to 0) is not cleared within the CCT, the System cannot remain stable anymore. As can been seen in Table 1 the CCT decreases as the wind farm capacity increases. This indicates that the stability limit of the system declines and the system tends to be more likely unable to keep stability under contingency.

Table 1 CCT of the wind farm for different capacity

P(MW)	60	120	180	240	300	360	420
CCT(ms)	2362	793	63	60	19	10	<0.1

4 Conclusions

From the case study results we can conclude that the LVRT requirement for the wind farm with a long HVAC cable can be fulfilled by appropriate dynamic control of WTGs. But the voltage support at PCC is limited obviously, due to the long HVAC connection and substation. Moreover, the stability limit, which can be indicated by CCT, decreases with the increasing power capacity. To avoid this situation, the onshore grid has to be enhanced, and FACTs devices may help to increase the stability of the HVAC connected wind farms.

References

[1] "Oceans of Opportunity – Harnessing Europe's largest domestic energy resource", A report by the European Wind Energy Association, EWEA, 2009.

[2] Verband der Netzbetrieber VDN. "TransmissionCode 2007 – Network and System Rules of the German Transmission System Operators", August 2007.

[3] "Requirements for Offshore Grid Connections in the Transpower Grid", Transpower Stromübertragung GmbH, 30 April 2010. http://www.tennettso.de/pages/tso_de/Transparenz/Veroeff-entlichungen/Netzanschluss/Netzanschlussregeln/PDF_seeseitige_Anforderungen_en.pdf

[4] Nordic Grid Code: Grid Code for Nordel (Denmark, Finland, Iceland, Norway and Sweden), 2007. Online available: https://www.entsoe.eu/

[5] M. Tsili, Ch. Patsiouras, S. Papathanassiou: "Grid code requirements for large wind farms: a review of technical regulations and available wind turbine technologies", EWEC08, Brussels, Belgium, April 2008.

[6] T. Bublat, T. Gehlhaar, "Comparison on high technical demands on grid connected wind turbines defined in international Grid Codes", 7th International Workshop on Large Scale integration of Wind power and on Transmission Networks for Offshore Wind Farms, 26-27 May 2008, Madrid.

[7] ENTSO-E, „Offshore Grid Development in the North Seas ENTSO-E views", 2011, online available, http://ing.dk/modules-/fsArticle/download.php?fileid=727

[8] H. Guo, K. Rudion, C. Heyde, Z. Styczynski, "Stability study of offshore wind farms", 5th International Conference on Critical Infrastructure, 20-22 Sept. 2010.

[9] Siemens Energy Sector, "Power Engineering Guide", 5th Edition, 2008 Published by Siemens, Germany. Online available: http://www.energy.siemens.com/

Session 5A

Wind Modelling, Forecasting and Resource Assessment II

The Anisotropic Multifractal Model and Wind Turbine Wakes

G. Fitton[1], I. Tchiguirinskaia[1], D. Schertzer[1] & S. Lovejoy[2]
[1]Universitè Paris Est, Ecole des Ponts ParisTech, LEESU,
6-8 avenue B. Pascal, Citè Descartes, 77455, Marne-la-Vallée cedex 02, France;
tel.: +33 1 64 15 36 07, fax: +33 1 64 15 37 64
McGill University, Physics department, 3600 University street, Montreal, Quebec, Canada
E-mail: fittong@cereve.enpc.fr

Keywords: Universal Multifractals, Spectral Analysis, Wind Velocity Fluctuations and Power Estimation.

1 Introduction

A typical routine in wind field resource assessment, at the most basic level, consists of first to third order statistics of times series data. The quality of the time series data can range between 0.05 to 600 seconds. More often than not the frequency of data will be the latter of the two since it is the cumulative power over long periods of time that define the financial return from turbines and thus high-resolution data is deemed unnecessary. It is now evident that such coarse time series data are no longer sufficient for a representative assessment of the wind and that estimations based on such data are associated with inaccurate power curve prediction and turbine damage. In particular it has been suggested that such problems are due to a lack of understanding of the somewhat intermittent nature of the wind velocity fields and the small-scale fluctuations thus associated. In order to address this there has been a significant increase in research involving coupled mesoscale-microscale models and stochastic downscaling methods. Our contribution is a demonstration that a good knowledge of small-scale variability is essential for a better understanding of the atmospheric boundary layer. We discuss the applicability of the stochastic anisotropic multifractal model to the complex conditions of wind farm potential and operational sites.

2 Data

Available to us is six-months of wind velocity and temperature measurements at the heights 22, 23 and 43m.

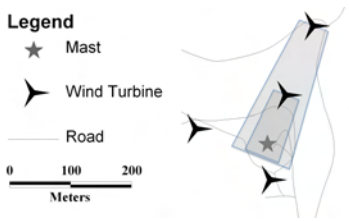

Figure 1: Schematic of turbine positions and wake effect due to North-Westerly winds (map courtesy of Julien Richard).

The measurements came from 3D sonic anemometers with a 10Hz data output rate positioned on a mast in a wind farm test site subject to wake turbulence effects (see Fig. 1). The quality of the data was of utmost importance so thorough pre-processing and verification was implemented to assure the reliability of the results.

3 Analysis

3.1 The Energy Spectrum and Scaling

A typical first-step-method to determine the overall scaling behaviour is the transformation of the velocity field into Fourier space. We 'should' then be able to observe power-law behaviour of the spectrum such that

$$E(\omega) \equiv A\omega^{-\beta} \tag{1}$$

where ω is the frequency, $E(\omega)$ is the energy at a given frequency, A is a coefficient of proportionality and β is the scaling exponent. The review of [Marusic et. al., 2010] discusses the existence of a -1 power law sub-range over small frequencies, adjoined by a classical Kolmogorov inertial sub-range with $\beta = 5/3$.
We will present shortly a more in-depth discussion on how our results compare to Kolmogorov's predictions however before this we would like to discuss the fact that there is no unique scaling regime i.e. there are three common scaling features, instead of the predicted universal law (see Figs. 2 and 3 also), that are:

- **High frequency scaling range** (R_{HF}:$\sim$ 0.1 secs to $\sim$5 mins) in which all three velocity components, u, v and w, follow (approximately) the same scaling law.
- **Mid-frequency w-component departure** from scaling at $\sim$5 minutes. Mid-Frequency, R_{MF}, corresponds to the ranges $\sim$ 5 mins to $\sim$1 hour.
- **Low frequency scaling reunification** (R_{LF}:$\sim$ 1 hr to $\sim$1 day) for all three velocity components at about an hour. The power law is not the same as that for small scales as will be discussed later.

The focus therefore of our more in-depth analysis is the behaviour of the horizontal u- and v-components over the mid-frequency-ranges i.e. $\sim$5 mins to $\sim$1 day. In fact what we

found was that our data fell into two categories; days (i.e., independent samples of 2^{19} measurements [$\approx$ 14.5 hours] per day) *without* a mid-frequency perturbation (Fig. 2) and days *with* a mid-frequency perturbation (Fig. 3). In the next section we will consider the simpler of the two regimes that are the non-perturbed days.

3.2 Non-perturbed Days & The Anisotropic Multifractal Model

The results from spectral analysis on non-perturbed days confirm a unique power law for all three velocity components over higher frequencies up to approximately 40 seconds at which the vertical wind w-component shows a clear scaling break followed by a -1 power law subrange as described in the previous section.

Moreover, such a clear separation of power law subranges allows us to obtain an estimate of the integral length scale for the vertical wind component as suggested in [Monin & Yaglom, 1975], which in turn leads to an estimate of the Reynolds number of about 60,000. Thus, from dimensional analysis one may obtain a minimum Reynolds number of about 14,000. These estimates confirm that the investigated wind field exhibits fully developed turbulence.

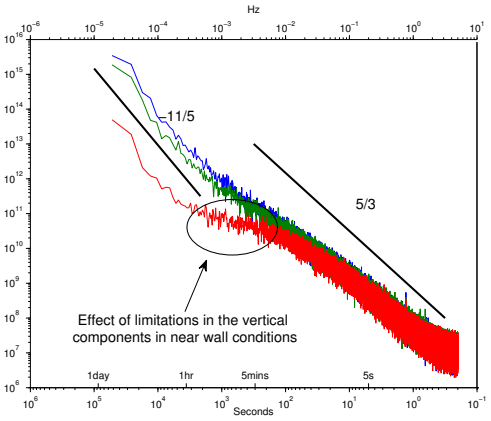

Figure 2: Averaged spectra for 11 non-perturbed days where the velocity component u is blue, v is green and w is red. The high-frequency range from ~ 0.1 sec to 5 mins has spectral slope ~ 1.4, less than the predicted 5/3. In addition we have highlighted the -1 adjoining range, from 5 mins to an hour, with the scale break being predictable based on the mast height (see [Fitton et. al., 2011] for more details). Low frequency scaling region is compatible with the -11/5 scaling law.

Over the high-frequency range Fig. 3 displays spectral exponents that differ from Kolmogorov's -5/3 law. The difference corresponds to an intermittency correction of spectral slopes and can be taken into account using the universal multifractal framework (Schertzer and Lovejoy, 1987), where:

- the energy density flux is a conserved (at any scale ratio λ) multifractal field proportional to a power law with singularity, γ, i.e.

$$\varepsilon_\lambda \propto \lambda^\gamma, \tag{2}$$

- the statistical moments of the energy density flux are defined by:

$$\langle \varepsilon_\lambda^q \rangle \propto \lambda^{K(q)}, \tag{3}$$

- and the scaling moment function $K(q)$ is defined by:

$$K(q) = \frac{C_1}{\alpha - 1}\left(q^\alpha - q\right). \tag{4}$$

Here, q, is the order of moment, C_1 is the codimension of the mean singularity and α is the multifractal Lévy index. The spectral exponent of Eq. 1 now becomes

$$\beta = 2H + 1 - K(2) \tag{5}$$

where $H = 1/3$ quantifies the degree of non-conservation of velocity increments. For spectra (i.e. for second order statistics), we estimated $K(2) = 0.27$. Such high intermittency corrections are expected over high frequencies in areas with high Reynolds numbers and complex terrain.

In addition we observed the Bolgiano-Obuhkov -11/5 power law at low frequencies illustrating the influence of large-scale vertical motions specific to the topography of our wind farm test site [Faggio & Jolin, 2003].

To take into account the dominant role of the vertical motion of large scale atmospheric structures, one may consider that the buoyancy force variance flux, ϕ, plays the same role as the energy flux, ε, in 3D turbulence but only along the vertical [Schertzer & Lovejoy, 1984]. This is contrary to the classical 'buoyancy subrange' that postulates an isotropic turbulence [Bolgiano, 1959, Obukhov, 1959] with two different (horizontal and vertical) scaling regimes. Thus we have the coupled sets of scaling equations [Schertzer & Lovejoy, 1984, Lazarev et. al., 1994]:

$$\left.\begin{aligned} \Delta V(\Delta x) &\stackrel{d}{=} (\varepsilon(\Delta x))^{1/3}\Delta x^{1/3} \\ \Delta V(\Delta z) &\stackrel{d}{=} (\phi(\Delta z))^{1/5}\Delta x^{3/5} \end{aligned}\right\} \tag{6}$$

$$\Longrightarrow (\varepsilon(\Delta x))^{1/3} \approx (\phi(\Delta z))^{1/5} \text{ when } \Delta x^{1/3} \approx \Delta z^{3/5} \tag{7}$$

where $\Delta V(\Delta x)$ and $\Delta V(\Delta z)$ denote the horizontal and vertical shears of the horizontal wind respectively and the symbol $\stackrel{d}{=}$ means equality in probability distribution.

Because the scaling fluctuations of both fluxes are not neglected (due to their explicit scale dependency) we can define anisotropic scaling (as defined by the anisotropic multifractal model [Schertzer & Lovejoy, 1984]) at all significant scales instead of two isotropic regimes, separated by a scaling break (see [Fitton et. al., 2011] for more details).

3.3 Perturbed Days, Wakes and Power Estimation

In [Fitton et. al., 2011] we put forward the argument that the non-perturbed days were a result of lack of influence of wind turbines justified by the low frequency power law (cross-diagonal mean wind) of the integrated cospectral analysis. The same argument allowed us to select days that were highly perturbed. By this we mean days where the mid-frequency range, R_{MF}, in which the scaling of horizontal

velocity components remained the same as described in the previous section, now have significant fluttering (see below [Fig. 3]).

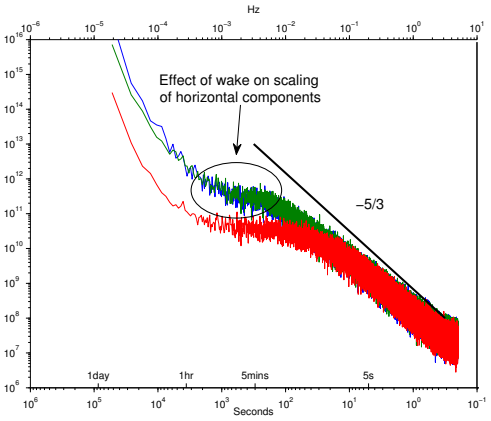

Figure 3: Averaged spectra for 11 perturbed days where the velocity component u is blue, v is green and w is red. The high-frequency range from ~ 0.1 sec to 5 mins has spectral slope ~ 1.6 which is much closer to the predicted 5/3. We have highlighted the fluttering for the horizontal components over R_{MF}. We can also see the fluttering of the vertical component is accentuated to a plateau. The 11/5 low frequency scaling regime remains, although with a lower coefficient of proportionality A (Eq. 1).

To see the effect of the turbines we can do a direct comparison of the integrated spectra, $\omega E(\omega)$, in log-linear coordinates of perturbed and non-perturbed days (11 of each see Fig. 4).

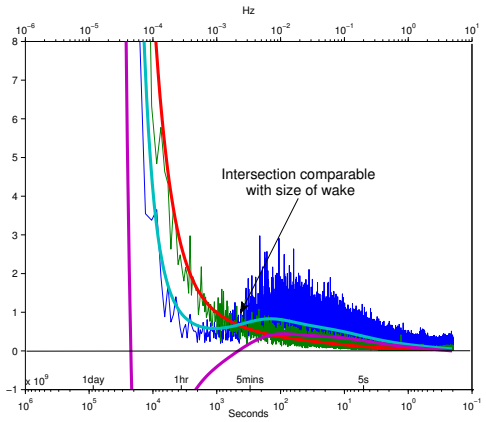

Figure 4: Comparison of perturbed and non-perturbed, u-component averaged integrated spectra, $\omega E(\omega)$, in log-linear coordinates; blue is perturbed days with light-blue moving average, green is non-perturbed with red moving average and purple is the differences of the moving averages.

This gives us a quantification of the energy per frequency increment making the overall evaluation of the energy gains and losses much easier. We have selected the horizontal u-component since there is no -1 adjoining range for non-perturbed days making it easier to make the comparison. Note the behaviour of the horizontal v-component is very similar (evidence of asymmetry at larger scales). From Fig. 4 we can draw the following intermediate conclusions based on the ranges defined in §3.1:

- **High frequency scaling range** (~ 0.1 secs to $\sim$5 mins) has an injection of energy since perturbed days (blue integrated spectra, light-blue moving average in Fig. 4) have more energy than the unperturbed days (green integrated spectra, red moving average in Fig. 4). This is confirmed by the positive difference of the moving average of the integrated spectra (purple curve of Fig. 4). If we consider the most basic approximation to a turbine, the actuator disc, then we can assume any eddy larger than the disc will be split into smaller eddies. This may explain the increase in high frequency energy. In fact, we can further confirm this idea since the transition of energy peaks at $\sim$ 5 mins highlighted again in Fig. 4 correspond to the size of the wake shown in Fig. 1.

- **Mid-frequency u-component** ($\sim$ 5 mins to $\sim$3 hours) shows evidence of energy pumping from the turbines for the perturbed days. This is more obvious when looking at the negative difference of the two integrated spectra over this range.

- **Low frequency** ($\sim$ 3 hours to $\sim$ 1 day [mesoscales]) shows that although there is similar scaling behaviour the energy for the perturbed days (red curve) is greater than the non-perturbed (light-blue curve) since the difference of the two (purple line) is positive. In [Fitton et. al., 2011] we suggested this was because the two particular types of wind the site was typically subject were strong North-Westerlys and weak South-Easterlys. This meant only the stronger winds would interact with the turbines (see Fig. 1).
  In addition we see at $\sim$ 3 hours the energy of the non-perturbed days becomes greater than perturbed. In the previous section we discussed how topographical features can change the scaling power law over the lower frequency data. This suggests there are similar topographical influences causing the loss of energy e.g. higher mean winds dissipate more energy over complex terrain.

Fig. 5 displays a schematic diagram that illustrates the corresponding inter-relations of different scaling ranges of the energy spectra. Over each of these ranges, two distinct power laws describe the corresponding scaling behaviour, with and without wake effects. Thus, from Eq. 5 we get:

$$E_1(\omega) = A_1 \omega^{-\beta_1}, \tag{8}$$

$$E_2(\omega) = A_2 \omega^{-\beta_2}. \tag{9}$$

Since the estimates of the multifractality parameter, α, remain stable for both perturbed and non-perturbed fields, the

ratio of the energy spectra is defined by the second order structure function:

$$\frac{E_1(\omega)}{E_2(\omega)} = \frac{A_1}{A_2}\omega^{-\zeta_\Delta(2)} \quad (10)$$

where $\zeta_\Delta = 2(\Delta H) - (\Delta C_1/(\alpha-1)) \cdot (2^\alpha - 2)$ from Eqs. 4 and 5.

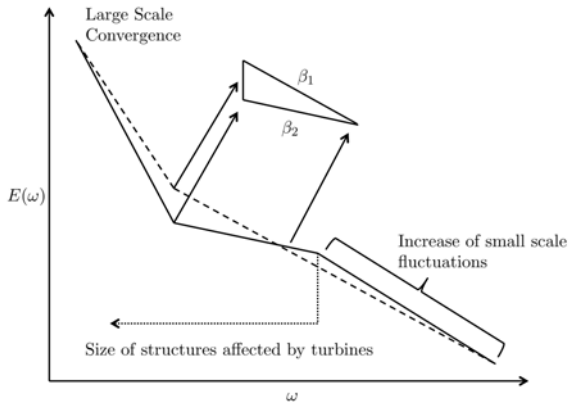

Figure 5: Schematic of the inter-relations of different scaling ranges of the energy spectra in a log-log plot.

From Fig. 5, Eq. 4 and the above equation (Eq. 10) we see an empirical spectral exponent closer to the theoretical values of $\beta = 5/3$ (over small scales) or $\beta = 11/5$ (over large scales), correspond to a smaller intermittency correction $K(2)$. Figs. 4 and 5 therefore suggest that by taking the energy over large scales, wind turbines create additional small-scale eddies and re-inject them as part of the energy over smaller scales, making the turbulence more homogeneous.

4 Conclusion

The aim of this study was to explore the scaling behaviour of atmospheric velocity measurements in a wind farm test site subject to wake turbulence effects. Based on this study we can make the following conclusions:

- Using long time series, 10Hz data, we identified (depending on the direction of the mean wind) two or three scaling sub-ranges.
- Through spectral analysis we found possible relations between wind velocity scaling breaks and associated theories of fully developed turbulence in the atmospheric surface-layer and used the universal multifractal framework to deal with the strong intermittency of the field.
- We have discussed how the anisotropic multifractal model can be applied to near wall atmospheric turbulence over complex terrain how it can be fully validated for days with no interaction with the wind turbine wakes.
- We found empirical evidence of the influence of wakes and suggested reasoning and scaling techniques that enable us to quantify the loss of energy with the potential of taking this into account using the anisotropic multifractal model.
- And finally, we discussed how the pumping of energy from wind turbines over mid-frequency scales, creates additional small-scale eddies which are re-injected as part of the energy over smaller scales. This makes the turbulence more homogeneous over the smaller scales in an analogous way to grid-generated homogeneous turbulence.

References

[Bolgiano, 1959] Bolgiano, R. 1959 Turbulent spectra in a stably stratified atmosphere, *J. Geophys. Res.* **64**, 2226.

[Faggio & Jolin, 2003] Faggio, G. & Jolin, C. 2003 Suivi ornithologique sur le parc dèoliennes dErsa- Rogliano (Haute Corse) - Rapport final-SIIF/AAPNRC-GOC, 100p.

[Fitton et. al., 2011] Fitton, G. F., Tchiguirinskaia, I., Schertzer D., & Lovejoy, S. 2011 Scaling Of Turbulence In The Atmospheric Surface-Layer: Which Anisotropy?, *Journal of Physics: Conference Series* (in review) Warsaw, ETC13.

[Lazarev et. al., 1994] Lazarev, A., Schertzer, D., Lovejoy, S. & Chigirinskaya, Y. 1994 Unified multifractal atmospheric dynamics tested in the tropics: part II, vertical scaling and generalized scale invariance, 115-123.

[Marusic et. al., 2010] Marusic, I., McKeon, B. J., Monkewitz, P. A., Nagib, H. M., Smits, A. J. & Sreenivasan, K. R. 2010 Wall-bounded turbulent flows at high Reynolds numbers: Recent advances and key issues *Phys. Fluid.*, **22**, 065103.

[Monin & Yaglom, 1975] Monin, A. S. & Yaglom, A. M. 1975 *Statistical Fluid Mechanics*, Cambridge, MIT-Press, Vol. 2, pp. 874.

[Obukhov, 1959] Obukhov, A. N. 1959 Effect of Archimedian forces on the structure of the temperature field in a temperature flow, *Sov. Phys. Dokl.* **125**, 1246.

[Pinus et. al., 1967] Pinus, N. Z., Reiter, E. R., Shur, G. N. & Vinnichenko, N. K. 1967 Power spectra of turbulence in the free atmosphere, *Tellus* **19**, 206.

[Schertzer & Lovejoy, 1984] Schertzer, D. & Lovejoy, S. 1984 On the Dimension of Atmospheric motions. In: T. Tatsumi (Editor), Turbulence and Chaotic phenomena in Fluids, Amsterdam, Elsevier Science Publishers B. V., pp. 505-512.

[Yaglom & Kader, 1989] Yaglom, A. M., Kader, B. A., & Zubkovskii, S. L. 1989 Spatial Correlation Functions of Surface-Layer Atmospheric Turbulence in Neutral Stratification, *Bound.-Lay. Meteorol.* **47**, pp. 233-249.

Classification of Lidar measurement errors in complex terrain conditions

Fernando Borbón [1], Paula Gómez [1], Javier Sanz Rodrigo [1], Alvaro Cuerva [2], Mike Courtney [3]
[1] National Renewable Energy Center (CENER), [2] Technical University of Madrid (UPM), [3] National Laboratory for Sustainable Energy (RisoDTU)
Contact: fborbon@cener.com; Ciudad de la Innovación 7, 31621 Sarriguren, Spain

Keywords: Remote sensing, lidar, complex terrain, measurement uncertainty, wind resource.

INTRODUCTION

The present work shows the results observed from a measurement campaign in complex terrain conditions using the same lidar equipment and compared to standard cup anemometry. The campaign has being performed at the Cener's Alaiz text site which is locate on the top of a mountain, followed by a flat plateau at the north side. The main sources of lidar uncertainty are studied and special attention is paid to the sources of non-uniform wind flow caused by the terrain shape, which has been accredited to play a major role on lidar uncertainty.

LIDAR PERFORMANCE IN COMPLEX TERRAIN

The performance of two lidar devices has been assessed in flat and complex terrain conditions, by means of installing the two lidars close to well instrumented meteorological masts, and comparing the wind speed measurements of lidars and calibrated cup anemometers at different heights. In order to make the results from both test sites comparable, similar filtering criteria have been applied in both cases, following the practices indicated by Gosttschall [1].

The influence of the terrain conditions can be revealed when plotting lidar bias as function of the wind direction, as shown in the graphs from table 1. For the case of flat terrain, there is a wind direction sector from which the lidar bias is more obvious (saw shape). It was identified that from this direction region, the presence of turbine wakes affected both the cup and lidar measurements. Depending on the direction angle, the wake could be impacting only the cup anemometer and not the lidar and vice versa, therefore the big positive or negative differences in the wind speed values sensed by them. Other issue is that the lidars are scanning a perimeter whose diameter length scale is comparable to the one of the turbine wake, while the cup anemometer can be considered as a point in space. As consequence, the wind field where they measure can have significant differences.

some variables are difficult to separate when studying the bias sources. During the measurement campaign at Høvsøre, it was found that most of the low cloud presence was precisely when wind was blowing from the sector with turbine wakes. Therefore, the influence of clouds in the lidar measurements (especially in the continuous wave lidar) was difficult to separate from the turbulence and speed deficit due to the turbine wakes.

In order to study the different sources of lidar bias, the wind data is analyzed when preferably belongs to a clean wind direction sector. This sector has been selected following the next conditions:

- It is free of big obstacles or structures and the roughest terrain conditions in the surroundings.
- It contains the predominant wind direction at the test site.
- It includes the sectors where the met mast effects over the cup anemometers and wind vanes are minimized.

This free sector helps to reduce the presence of those error sources different from the ones of interest. Then, the individual isolation of possible lidar bias sources becomes more feasible. From field visits, data analysis and map studying, these sectors have been identified as follow:

- Mainly west [225º, 315º] for the flat terrain campaign.
- North and south +/- 45º for the complex terrain campaign.

At the complex terrain site Alaiz, observe that the wind blows in mainly from north (at 0º with uphill wind) and south (at 180º and downhill wind) directions. Here, the lidars tend to underestimate the wind speed since the bias is mainly negative. Nevertheless, for the region between 180º and 360º, there are enough data to identify a curve

shape in the plot revealing the terrain effects since the lidars tend to underestimate the wind velocity from northern and southern sectors, precisely where the there is more tilt in the flow due to the alignment with the mountain slope. As the wind direction changes and the tilt angle is reduced as wind flows parallel to the mountain flatten top (eastern and western sectors), the lidar bias is reduced. At 270º there is a group of data revealing the mast effect. Here the cup anemometer might be sensing a reduced wind speed due to the wind flow obstruction caused by the mast.

For the complex terrain case, the influence of the wind tilt angle over the ratio of horizontal wind speed obtained from the lidar and the met mast instrumentation has been studied. In the latter case, the vertical and horizontal wind speed sensed by the propeller (w) and cup anemometer (u) respectively, were used to compute the tilt angle as tan-1(w/u). This relation is shown in Figure 1 (right) for the 118 m height. As can be appreciated, when the wind flow presents a vertical component (and therefore a tilt angle different from zero) the lidars mostly underestimate the horizontal wind speed compared to cup anemometer. On the contrary, when the tilt angle is nearly zero, the lidars sense a velocity closer to the measurement from the cup anemometer or even higher. The lidar bias can reach up to 5 %, and is in accordance with the values indicated by Bingöl [2].

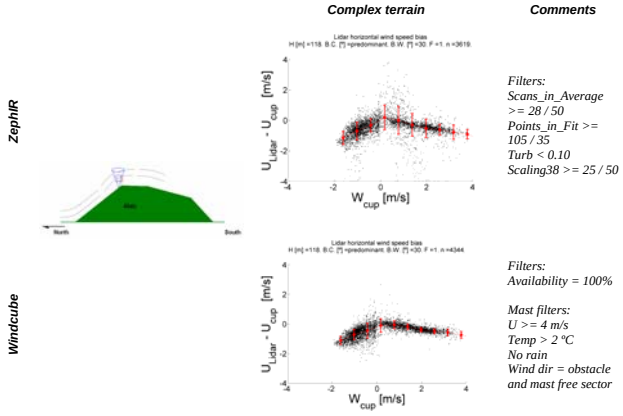

Figure 1: Lidar bias as function of the vertical component of the wind velocity.

ATMOSPHERE STABILITY

There is special interest in assessing the influence of the atmosphere stability conditions over the lidar bias for the complex terrain conditions. The Froude number (Fr) is used as an indicator of the stability conditions and the coupling of the air natural frequency with the wind velocity and the Alaiz mountain dimensions. In stable conditions, the wind regime is controlled by the Froude number and is given by Stull [3] as:

$$Fr = \frac{\pi U_0}{N_{bv} L} \qquad \text{eq. 1}$$

For very stable conditions and slow winds (i.e. Froude << 1), the lower layer of the ABL is colder than the upper layer and therefore, when there is a considerable obstacle like the Alaiz mountain, the wind is constricted to flow around the obstacle and not upon it. As the stability is reduced and higher wind speeds are present, more and more flow is able to overpass the mountain and lee waves are formed behind it. At some point, the amplitude of the air vertical oscillation and the wave length matches the height and with dimensions of the mountain and then the resonance point is achieved (Froude = 1).

As the atmospheric conditions become neutral and higher wind speeds are present, there is boundary layer separation behind the mountain and a turbulent wake can be created. The wind flow is highly accelerated, especially at the mountain top and the streamlines change in angle and separation whether they are seen before or after crossing over the mountain top. This is an important difference and has to be taken into account when analyzing lidar data at Alaiz from different directions. As has been mentioned before, lidar errors are largely dominated by the presence of non-uniform wind conditions over the measurement volume scanned by the lidar. When measuring near to the hilltop of Alaiz, at MP5 position, the curvature of the streamlines over the mountain depend on the atmospheric stability.

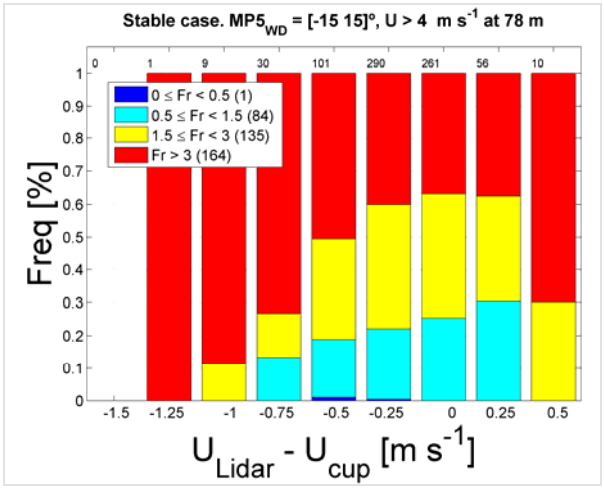

Figure 2: Atmosphere stability influence on lidar bias based on the Froude number. Complex terrain site and stable conditions. Wind from north direction [-15º, 15º] and above 4 m/s. Lidar bias in the horizontal wind speed at 78 m height in MP5 met mast position.

For the present analysis, the wind speed at 118 m is used as the reference velocity and a hill length of L = 2000 m is considered as the approximate dimensions of the Alaiz mountain ridge. The Brunt-Väisälä frequency Nbv is obtained from the potential temperature gradient between 81 and 113 m. Figure 2 shows the mean velocity profiles for different stability classes and the associated mean velocity error at 78 m level in the MP5 position.

In strongly stable conditions, with very low Fr, the air rather flows around the mountain than over it. At weaker stabilities a larger portion of the air flows above the mountain. In neutral and unstable conditions the boundary layer is dominated by well mixed turbulence and the wind profiles observed at MP5 show less scatter with very low wind shear. All these regime switching mechanisms affect the curvature of the flow above the Alaiz mountain and, consequently, the difference between the velocities sensed by the cup and lidar anemometers. A negative bias is generally observed with larger errors as the atmosphere becomes more neutrally stratified.

WASP CORRECTION METHOD

As explained previously, WAsP engineering tool integrates a script to predict the lidar bias at several heights for a desired location. Both CW and pulsed lidar measurements are emulated. These predictions can be compared with field results for the Alaiz test site in order to validate its effectiveness.

Firstly, a level curve map is necessary for the Alaiz location. The script manual recommends a domain with at least 5 x 5 km and a minimum resolution of at least 10 m. Still, it suggests having a 10 x 10 km domain with 5 m of minimum resolution in order to have better results.

Then, the map is loaded in WAsP and the locations of the met mast (obligatory named M) and the lidars (mandatory named L) are introduced through the “Insert new site” option. Then, the desired heights to be simulated are introduced through the “Insert new height” option. Then, the script can now be executed. The output is written into an Excel document with several sheets (one per height) where the horizontal and vertical wind speed components are detailed for every 12º degrees of wind direction. There the simulated results for the met mast and the lidars are shown in columns and a graph is plotter showing the ration of wind speed lidar/cup as function of the wind direction. The script manual indicates these results correspond to a wind speed of 12 m/s, measured at the met mast location at 45 m.

For the Alaiz measurement campaign, the lidar/cup wind speed ratio obtained from the field measurements and the predictions given by the WAsP Engineering tool are shown in figures 3 and 4. As can be seen, the field measurements present a high dispersion despite applying several data quality filters. Nonetheless, when averaging all the data per wind direction bin, a tendency line is obtained showing the main sinusoidal behaviour. This average line presents similar shape and magnitude as that one predicted by the WAsP Engineering script. From these results two significant conclusions can be derived. The first one is that the general lidar bias behaviour can be predicted with WAsP Engineering tool with reasonable good results.

The second conclusion is that since there is a high variability in the field data, applying the same correction factor (e.g. based on WAsP Engineering) to each individual measurement will not correct properly the lidar bias for all the cases. Also it is important to mention that obtaining the general trend for the field measurements required nearly 9 months of continuous measurements; and still not all the wind direction bins have statistically representative data. Therefore it is not always easy to obtain enough data to validate the prediction obtained from a computational tool.

From previous conclusions, it can be derived that there are useful tools available that can help to predict the general tendency of the lidar bias at a given site. However, there is still room for further research in terms of reducing the lidar uncertainty for individual measurements (i.e. instantaneous data or 10 min averages) since not always met mast data is available from a near location.

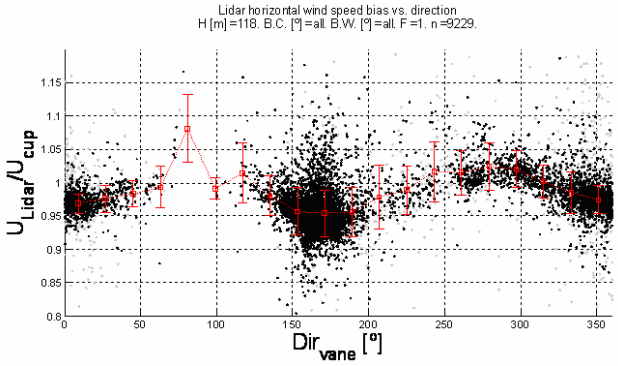

Figure 3: Lidar/cup anemometer horizontal wind speed ratio vs. wind direction, at 118 m height. Field measurements from Windcube and cup anemometer at Alaiz test site. Black dots represent all the measurements while the line indicates the averages per wind direction bin. The error bars represent the standard deviation for each direction bin.

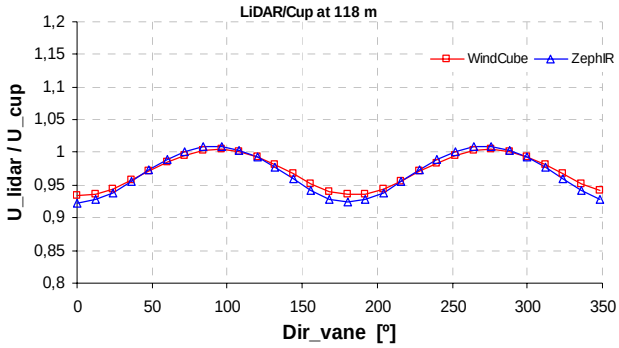

Figure 4: Lidar/cup anemometer horizontal wind speed ratio vs. wind direction, at 118 m height. WAsP Engineering script prediction for Windcube and ZephIR at Alaiz test site; using a 2.5 km x 2.5 km map with 5 m resolution.

CONCLUSIONS

Identifying the main sources of lidar uncertainty (assuming lidars and cups are properly calibrated) is a difficult task since the studied bias sources can affect the measurements simultaneously and identifying their individual contribution is sometimes not possible.

It was shown that the variation of the vertical component of the wind velocity plays an important role in the lidar bias occurrence for the Alaiz campaign. It is still necessary to verify if this relationship is causal or if at the lidar siting (mountain edge) the vertical velocity gradient dW/dx scales with W.

The WAsP Engineering tool gives good results to characterize the general bias behavior at the Alaiz test site. Nevertheless, to correct individual measurements (10 min periods), a new methodology would also be of high value too.

ACKNOWLEDGEMENT

It is acknowledged the financial support of the European research projects SAFEWIND and WAUDIT for the realization of this paper as well as the technicians at both Høvsøre and Alaiz test sites for their valuable contribution to set up and maintain the sensing equipment.

REFERENCES

[1] Gosttschall, J; Courtney, M., 2010. Verification test for three WindCube WLS7 lidars at the Høvsøre test site. Report number Risø-R-1732(EN)

[2] Bingöl, F. et al. Lidar performance in complex terrain modeled by WAsP Engineering. EWEC 2009 Proceedings. Marseille, March 2009

[3] Stull R.B. An Introduction to Boundary Layer Meteorology, Kluwer Academic Publishers, 1988

Table 1. Lidar horizontal velocity bias vs. wind wane direction.

	Flat terrain	Complex terrain	Comments
ZephIR	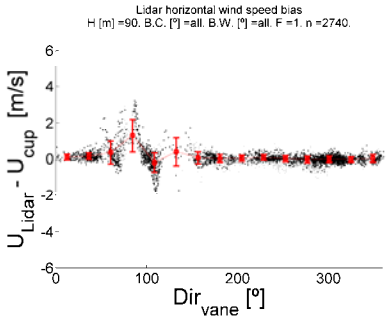	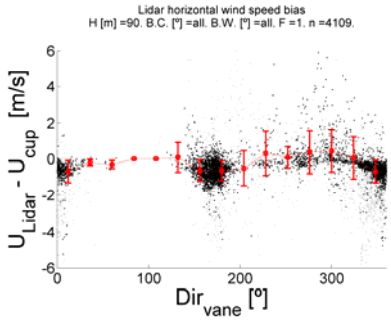	Lidar filters: Scans_in_Average >= 28 / 50 Points_in_Fit >= 105 / 35 Turb < 0.10 Scaling38 >= 25 / 50
Windcube	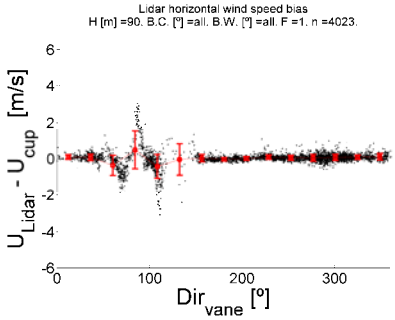	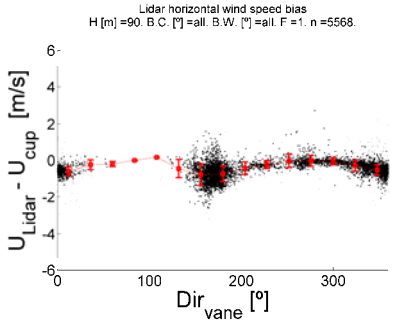	Lidar filters: Availability = 100% Mast filters: U >= 4 m/s Temp > 2 ºC No rain Wind dir = obstacle and mast free sector

Comparing the sphere anemometer to standard anemometers for wind energy

Hendrik Heißelmann, Joachim Peinke, Michael Hölling
ForWind, Center for Wind Energy Research, University of Oldenburg
D-26111 Germany
E-mail: hendrik.heisselmann@uni-oldenburg.de

Keywords: wind measurements, sensor, anemometer

1 Introduction

The most common anemometers for wind energy applications are cup anemometers and ultrasonic anemometers. Nevertheless, both sensors suffer from a variety of drawbacks. While cup anemometers are available for a reasonable price, they provide only wind speed information with limited temporal resolution of about 1 Hz and tend to de-calibrate due to wearing bearings. To obtain wind direction information as well, cup anemometers have to be complemented with an additional sensor, e.g. a wind vane.
In contrast, higher resolving ultrasonic anemometers can provide up to three components of the wind vector with a typical temporal resolution of 30 Hz. However, ultrasonic anemometers are fairly expensive and the wakes from their transducers and mounts result in systematic errors, which cannot be entirely corrected [1].
In this contribution, we present the sphere anemometer as a robust alternative to cup anemometry without any wearing parts. Based on the previous anemometer described in [2], the design of the latest sphere anemometer was improved towards operation under harsh environmental conditions such as off-shore applications.

2 The sphere anemometer

2.1 Measuring principle

The newly designed sphere anemometer makes use of the velocity-dependent deflection of a flexible tube. As sketched in fig. 1, the deflection s is a result of the forces F_s acting on the sphere and F_t acting on the tube. It is given by

$$s = \frac{l^3}{E \cdot J} \cdot \left(\frac{F_s}{3} + \frac{F_t}{8} \right), \tag{1}$$

with tube length l, elasticity modulus E and second moment of the area J. F_s and F_t are described by the general expression of the drag force acting on a body

$$F = \frac{1}{2} \rho \cdot A \cdot c_D(Re) \cdot u^2, \tag{2}$$

with the cross-section A of the sphere and the tube, respectively. ρ is the air density, $c_D(Re)$ is the drag coefficient of the respective body and u denotes the wind speed. The drag coefficient c_D of a smooth sphere as well as of a cylinder can be considered constant for Reynolds numbers in the range of about 1,000 up to 200,000 [3]. In this range of the calibration function, the wind speed is expected to be proportional to the square-root of the deflection s

$$u \propto m \cdot \sqrt{s}. \tag{3}$$

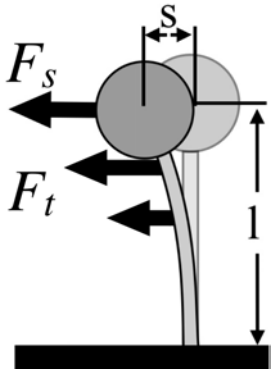

Figure 1: Drag forces acting on a sphere attached to the top of a flexible tube.

The general principle of drag-based sphere anemometers has already been published several decades ago [4] and since then, several different approaches have been undertaken to develop a robust and reliable anemometer. Unlike using strain gauges or proximity sensors as described in previous works by Green et. al. [5] and Smith [6], the new sphere anemometer makes use of the light pointer principle in order to detect the deflection of the sphere. This fast and highly resolving technique is known from atomic force microscopy and has already been applied in a miniaturized flow sensor for laboratory use, namely the Laser-Cantilever-Anemometer [7].

2.2 Anemometer setup

The sphere anemometer (figure 2, left) consists of a lightweight sphere which is attached to the tip of a flexible tube of 8 mm diameter. The lower end of the tube is fixed to the streamlined anemometer housing. A sphere diameter of 7 cm was chosen to match the assumption of constant drag

coefficient c_D for a wind speed range of 0.2 m/s up to 43 m/s, which is reasonable for wind energy applications. In order to detect the deflection of the sphere, a laser diode is mounted on top of the tube as sketched in figure 2, right. Through the tube, the laser is aimed onto a two-dimensional position sensitive detector (2D-PSD) at the bottom of the measurement unit. Once the tube is bending due to the acting drag forces, the laser spot is displaced and its changing position on the detector's active area of $4 \times 4\,\mathrm{mm}^2$ can be determined from the induced photo currents of the 2D-PSD. These displacements are converted to wind speeds via calibration.

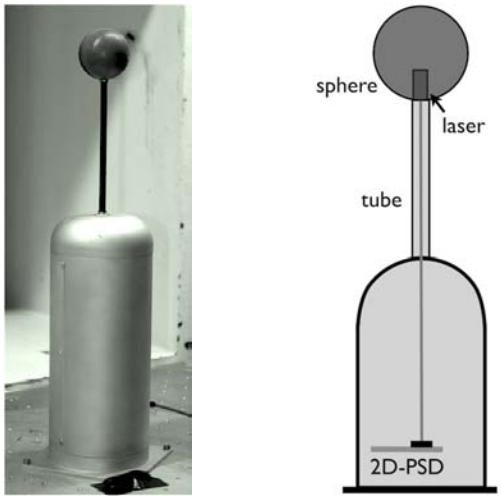

Figure 2: *Left:* Photograph and *right:* sketch of the sphere anemometer setup using a light pointer to detect the deflection of the sphere. A laser is aimed onto a two-dimensional position sensitive detector (2D-PSD) and the wind speed can be calculated from the deflection of the spot.

The usage of this sensitive measurement technique, which permits the detection of deflections in the order of micrometers, allows for a sphere anemometer setup which is robust and highly responsive at the same time. Additionally, this setup permits the simultaneous measurement of wind speed and direction within one sensor, since the displacement of the laser spot is detected in two dimensions. In contrast to ultrasonic anemometers, which suffer from the wakes generated by its transducers and mounts, the sphere anemometer has no supporting structures outside of the sphere-tube-combination. Thus, the undisturbed flow is measured by the anemometer.

3 Wind tunnel tests

Wind tunnel experiments have been carried out at the University of Oldenburg in order to obtain a calibration function for the new sphere anemometer and to characterize the behavior of the sensor. The used wind tunnel with an outlet cross-section of 100 cm × 80 cm has an open test section and can provide wind speeds up to 50 m/s at a turbulence level of less than 0.2%.

3.1 Sensor calibration

For the calibration procedure, the sphere anemometer was placed on a turntable with stepping motor. Wind speeds u were varied between 0 m/s and 20 m/s and the output signals of the 2D-PSD were recorded for flow angles Φ of 0° up to 350° in steps of 10°. The top graph of figure 3 shows the resulting two-dimensional calibration function for the sphere anemometer. The x-axis corresponds to the x-output of the 2D-PSD while the y-axis is its y-output signal. Each of the points corresponds to the position of the laser spot on the 2D-PSD for a certain combination of wind speed and angle Φ. In this representation, the flow angle Φ increases counter-clockwise and values belonging to the same angle are connected. The wind speed increases in radial direction with 0 m/s being in the center and 20 m/s being the outermost circle. Each of the connected lines corresponds to an one-dimensional calibration function as exemplarily shown for $\Phi = 220°$ in figure 3, top. In this graph, the wind speed is plotted against the anemometer's output magnitude $\sqrt{x^2 + y^2}$. The data was fitted with a square-root function as expected according to equation (3).

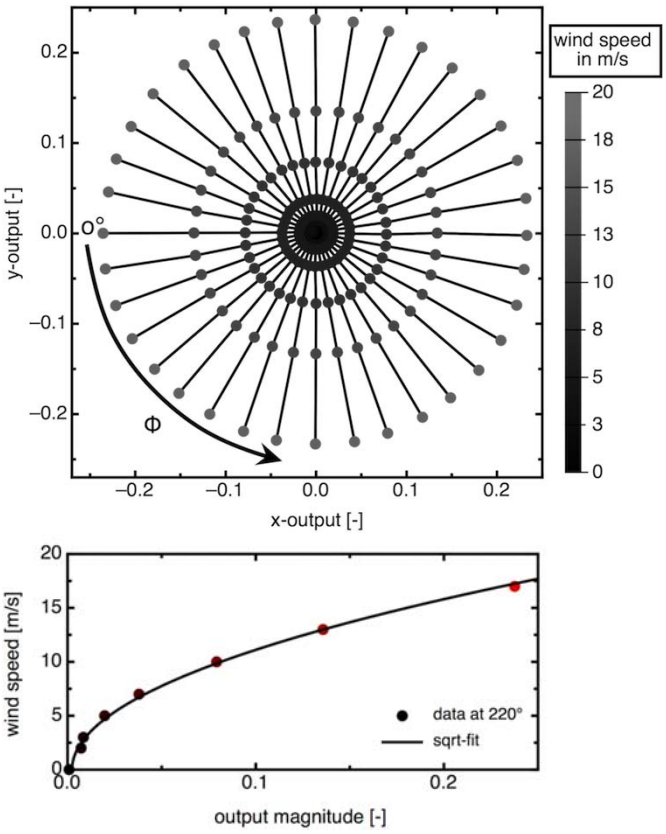

Figure 3: *Top:* 2D-calibration function of the sphere anemometer. The y-output of the 2D-PSD is plotted against its x-output signal. The angle Φ increases counter-clockwise and connected points belong to the same angle. The wind speed increases in radial direction with the outermost circle corresponding to 17 m/s. *bottom:* 1D-calibration for $\Phi = 220°$. The measured data is fitted with a square-root function.

Previous sphere anemometer realizations used to have the power supply cables for the laser diode attached to the outside of the tube. This caused an angle-dependent change of the exposed cross-section of the tube and the 2D-calibration featured a slightly asymmetric system of rings. Even though the effect was small, it could clearly be identified [2]. In contrast to the previous sphere anemometer setup, the 2D-calibration of the latest setup shows an almost perfect system of concentrical circles as it is theoretically expected for a symmetrical sphere and tube setup. This improvement can be assigned to the fixation of the cables and the used steel tube which is more isotropic than the former glass fiber material.

3.2 Comparison to cup anemometry

Wind tunnel experiments on the dynamical behavior of the previous sphere anemometer setup have been carried out. The sphere anemometer and a cup anemometer were exposed to artificially created wind gusts, while a highly resolving hot-wire anemometer served as a reference. The results of these investigations were already described in [2] and have shown the ability of the sphere anemometer to match the accuracy of state-of-the-art cup anemometers. Furthermore, the cup anemometer's temporal resolution is significantly exceeded by the sphere anemometer since it is only limited by the eigenfrequency of the sphere-tube-combination (about 40 Hz).

4 Atmospheric measurements

As a further step in the characterization of the new sensor, measurements under atmospheric wind conditions were performed with the new sphere anemometer and the commercially available 3D ultrasonic anemometer *Gill WindMaster Pro*. Both sensors were installed with their respective north spar aligned northwards on the roof of an university building in Oldenburg (figure 4) and three continuous hours of measurement data were collected.

The *Gill WindMaster Pro* was operated at its maximum output frequency of 32 Hz and the internal calibration procedure was switched on. Due to the limited channels of the used A/D converter, only the analogue signals of the horizontal wind magnitude (range: 0 - 40 m/s) and the horizontal wind direction were recorded for the ultrasonic anemometer. All signals from sphere anemometer and *WindMaster Pro* were sampled simultaneously at 200 Hz with a resolution of 16 Bits.

An excerpt of 100 seconds from the recorded time series with both anemometers is shown in figure 5. The reference data from the ultrasonic anemometer is displayed in black, while the data from the sphere anemometer is drawn in gray. Qualitatively, both datasets are in very good agreement although the sphere anemometer time series exhibits slightly more pronounced extreme values indicating a higher sensitivity. The choice of a different part of the three-hour time series may result in a similar level of agreement as this exemplary part shows, but it has to be mentioned that this is not the case for the entire dataset from both anemometers.

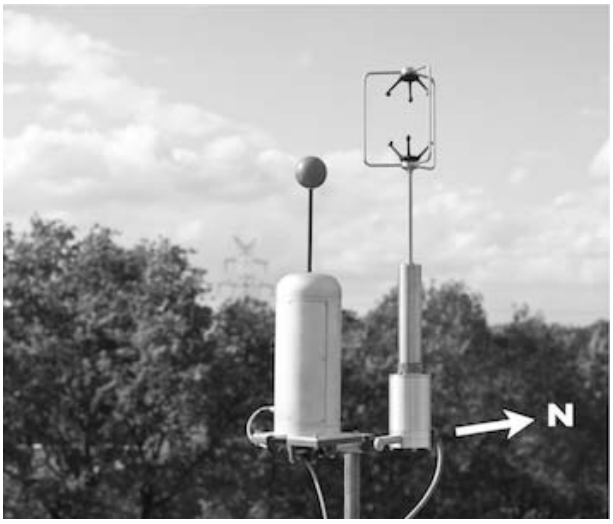

Figure 4: Photograph of the sphere anemometer (left) and the Gill WindMaster Pro ultrasonic anemometer (right) installed on the roof of an university building in Oldenburg.

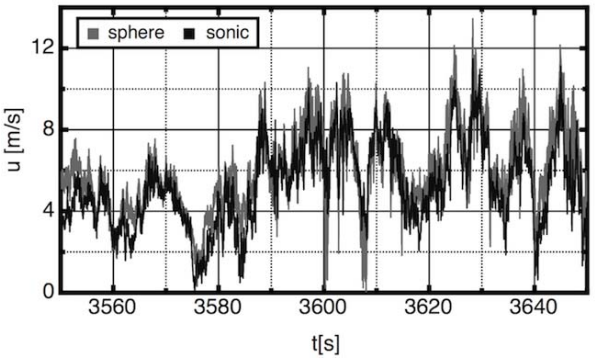

Figure 5: 100 seconds excerpt of the three-hour time series measured on the roof of an university building with sphere anemometer (gray) and ultrasonic anemometer (black). A general agreement of the time series is observed.

The histogram of measured wind speeds, given in figure 6, is plotted in black for the ultrasonic anemometer and in gray for the sphere anemometer. While the general shape of the histogram looks similar for both tested sensors, the histogram of the sphere anemometer measurement seems to be shifted towards higher wind speeds. This impression is supported by the comparison of the measured horizontal mean wind speeds $\bar{u}$, which is about 14% higher for the sphere anemometer data, as denoted in table 1. As we did not condition the analyzed data on the wind direction to ensure undisturbed inflow conditions for both anemometers, one possible reason for these deviations could be wake effects of one anemometer affecting the other one. The sphere anemometer indicates wind directions around 180°

(southerly winds) for the treated measurement data. This may cause the observed deviations as the wind passes the sphere anemometer first and afterwards reaches the ultrasonic anemometer. The hypothesis of the ultrasonic anemometer being located in the wake of the sphere anemometer could explain both, the lower horizontal wind speed $\bar{u}$ as well as the higher turbulence intensity $TI = \sigma_u/\bar{u}$ measured for the analyzed interval (table 1).

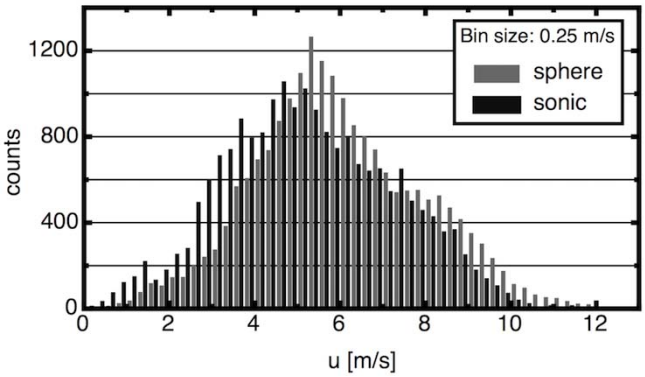

Figure 6: Histogram of the wind speed data shown. The sphere anemometer (gray) seems to over-estimate the wind speed compared to the ultrasonic anemometer (black).

Table 1: Measured mean wind speeds $\bar{u}$, standard deviations σ_u and turbulence intensities TI for both anemometers.

	sphere	**sonic**
$\bar{u}$ [m/s]	5.99	5.24
σ_u [m/s]	2.0	2.0
TI [%]	33	38

5 Conclusion

The current setup of the sphere anemometer was subject to several improvements regarding used materials and sensor design. The two-dimensional calibration function of the anemometer became more symmetric and each of the one-dimensional calibration functions is in agreement with the theoretically expected square-root function, which can be considered a cornerstone of accurate wind speed and direction measurements.

After an earlier version of the anemometer was tested against a state-of-the-art cup anemometer, the latest sphere anemometer was used in comparative experiments with an ultrasonic anemometer. The data from real wind measurements on the roof of an university building were in fairly good agreement for the chosen excerpt of the measured dataset. Possible wake effects could be identified, but further careful analyses of the entire measurement have to be carried out. Overall it has to be admitted, that the wind conditions on the flat roof may be strongly affected by the building and surrounding structures such as trees and railings. Nevertheless, they were tolerable for first anemometer testings, because they permitted fast access to the sensors. Future measurement campaigns will include the installation on a met station and a wind turbine.

Acknowledgements

The presented work was financially supported by the German Federal Ministry for the Environment, Nature Conservation and Nuclear Safety (BMU) under grant no. 0325207.

References

[1] A. Wiesner et. al.. The influence of the sensor design on wind measurements with sonic anemometer systems. J. Atmos. Oceanic Technol., 18:1585-1608, 2001.

[2] H. Heißelmann, M. Hölling, J. Peinke. Using the sphere anemometer for wind speed and direction measurements. TORQUE 2010: The Science of Making Torque from Wind, pp.13-18, 2010

[3] D.J. Tritton. Physical Fluid Dynamics, 2nd Ed. Oxford Science Publications, New York, 1988.

[4] W.H. Reed III and J.W. Lynch. A simple fast response anemometer. J. Appl. Meteorol., 2:412-416, 1963.

[5] A.E. Green et. al.. A rapid-response 2-D drag anemometer for atmospheric turbulence measurements. Bound. Lay. Met., 57:1-15, 1991.

[6] S.D. Smith. Evaluation of the Mark 8 thrust anemometer-thermometer for measurement of boundary-layer turbulence. Bound. Lay. Met., 19:273-292, 1980.

[7] S. Barth et. al.. Laser-Cantilever-Anemometer A new high resolution sensor for air and liquid flows. Rev. Sci. Instrum. 76 075110, 2005.

Session 5B

Operation, Condition Monitoring and Maintenance

Dynamic analysis of wind turbine tower at different operating and non-operating conditions.

Francesco Poggi,
DICAT, University of Genoa
Via Montallegro, Genoa ITALY
E-mail: francesco.poggi@unige.it

Keywords: dynamic analysis, aerodynamic damping

1 INTRODUCTION

With the fast development of the wind turbine orienting to the large-scaled and flexible and in order to ensure the system working reliably, we should keep it in good inherent characteristics. During rotor's rotating, if the incentive frequency produced by rotation approaches the inherent frequency of the tower, it will cause the tower in great vibration or even in resonance. Vibration can make the tower causing greater dynamic stress , structure fatigue so that it will also shorten the service life of the machine. Therefore, it has profound significance of the research on the inherent characteristics of the wind turbine tower. Currently the research on the inherent characteristics of the wind turbine tower mostly adopts the methods of analytic mechanics, multi-body dynamics and the theory of finite element. However the report of the inherent characteristics based on the field measurements is hardly to be available. Since the wind turbine tower is always situated in severely changeable environment with the special structure that at the top of the tower there is an installed rotor, therefore , the field measurement is an comparatively reliable way to obtain the inherent characteristics of the wind turbine tower, as well as way to provide the forceful verification for the theoretical analysis. The paper deals with the inherent characteristics of wind turbine tower at different operating condition (idling, parking, power production, stop) The measured data include acceleration at various levels and strain gauges to estimate tower-top bending moment and torsion, and tower-root bending moment. In order to evaluate the atmospheric conditions at the turbine site are used a cup anemometer, located at a met. mast at hub height . This paper presents a part of the ongoing experimental program concerning the on-site long-term measurements to be performed on the steel tower. The following objectives were established for the information to be extracted from the measured data:

- the dynamic behavior of the tower and an accurate modal identification;
- the estimation of the aerodynamic damping;
- the section loads acting on the top and bottom of the tower at different condition

Gust and Fatigue Load Alleviation of Smart Wind Turbine Blades Using Piezo-Driven Tabs

Lars Oliver Bernhammer
Wind Energy Research group, TU Delft
Kluyverweg 1, 2629HS Delft, The Netherlands
E-mail: l.o.bernhammer@tudelft.nl

Keywords: Aeroservoelasticity, wind turbine, smart blade Piezoelectric actuators, Gust load alleviation, flutter suppression

1 INTRODUCTION

The most recent work has been carried out by Heinze et al. proposing to implement trailing edge tabs on the control surfaces for load alleviation for gust load reduction [6,7] and drag reduction [4,5]. These studies are concerning a very slender, low frequency wing structure with a control surface and a trailing edge tab.

Barlas et al. [1] identify this type of tabs as potential candidate for load alleviation for wind turbines. Wingerden et al. [9], Basualdo et al. [2] and Rice et al. [8] have demonstrated load alleviation for gust loading in wind tunnel experiments.

This paper will illustrate how the successful wind tunnel research for flutter control of vertical tail plane rudders might be used to alleviate the load of smart wind turbine blades. The schematic set-up of the rudder model is given in Figure 1. The piezoelectric bender will actuate a lever that will deflect the trailing edge tab. It is fully mounted in the rudder.

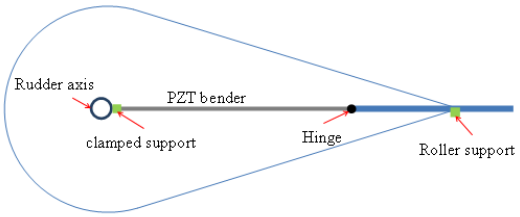

Figure 1: Piezoelectric bender design

2 NUMERICAL MODEL

The structural model has been created within Nastran. The model has been idealized using shell elements. Lumped masses have been allocated at the tip of the wing to reduce the bending frequency of the wind tunnel model.

An eigenmode analysis has been run to reduce the computational requirements. The first 5 modes have been taken into account, as higher frequency modes display strong plate vibration behavior.

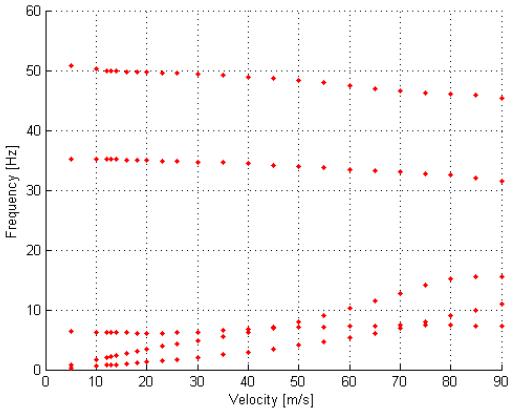

Figure 3: Frequency vs Velocity of tailplane model in Nastran

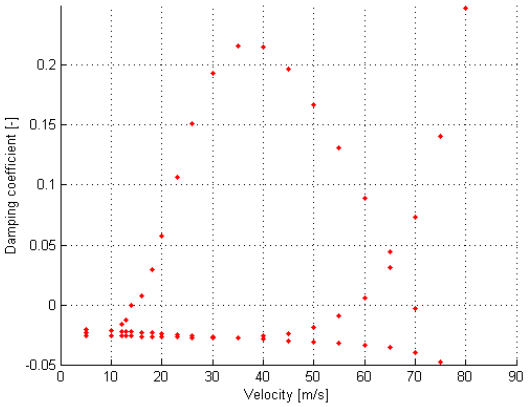

Figure 4: Damping vs Velocity of tailplane model in Nastran

Consequently an aeroelastic analysis has been done using the P-K method Figure 3 and 4 show the Frequency and damping plots, respectively. A very low design flutter speed of 14 m/s is reached, when the rudder deflection starts to interact with the bending of the wing. These results have been confirmed with a K-method using

ZAERO. Five frequencies can be identified in Figure 3. Two modes start at zero frequency. These are the rudder deflection modes, which are strongly damped, therefore their frequency increases at higher wind tunnel speeds. Already at low speeds interaction with the first bending mode of the vertical tail plane occurs. Control surface induced flutter is the result. At higher speeds of about 60 m/s the second bending mode develops into a second flutter mode. Figure 4 manifests those observations.

3 Controller Design

The controller design was kept as simple as possible as the focus was on the technology demonstration.

The aerodynamics of the numerical model have been restated in terms of a minimum state-space approximation. This system was augmented with the rudder deflection such that a plant for a controller could be established. This controller uses an accelerometer at the wing tip as input and the tab deflection as output.

The system was defined by:

$$s\{x_{ae}\} = [A_{ae}]\{x_{ae}\} + [B_{ae}]\{u_{ae}\} + [B_{aw}]\{w_g\}$$

Where x is the state vector, A is the state matrix, B is the input matrix and u the input vector. W represents the gust vector.

The system is combined with a feedback equation such that the system becomes:

$$\{\dot{x}\} = [A]\{x\} + [B]\{u\}$$
$$\{y\} = [C]\{x\} + [D]\{u\}$$

The state-space system in plant format has been integrated between a low-pass filter to reduce the measurement noise. Notch pass filters for the eingenfrequencies have been added.

This simple closed loop controller has been implemented in ZAERO to obtain a prediction of the flutter properties with the controller switched on. Figures 6 and 7 give the damping and the frequency plots respectively.

The flutter speed increases to 48 m/s. This clearly shows the potential of the piezoelectric actuator usage in controller design of wings or blades. As one can see from the frequency curves, the first bending moment mode is experiencing an increase in frequency, therefore it does not interact anymore with the rudder deflection.

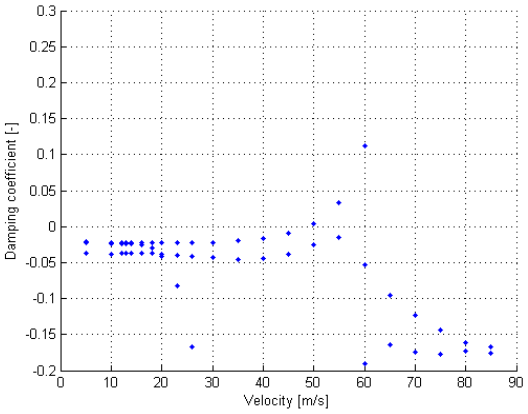

Figure 5: Damping vs Velocity with closed-loop control system evaluated by ZAERO

Additionally it can be seen that the outboard control surface experiences a much stronger damping. Therefore it can be concluded that the control surface effectiveness is significantly higher.

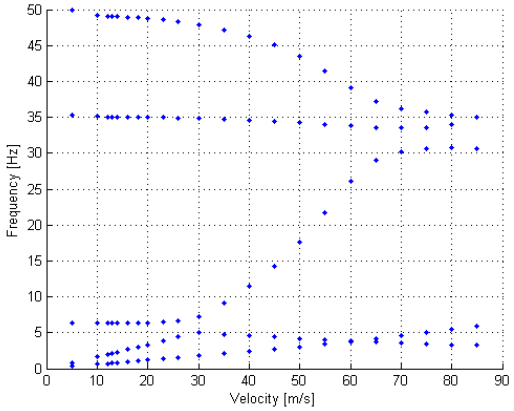

Figure 6: Frequency vs Velocity with closed-loop control system evaluated by ZAERO

4 Piezoelectric Actuator

The trailing edge tabs are driven by piezoelectric actuators, which are mounted within the rudder. The maximum voltage that the benders can handle is 110 volts. Therefore a saturation limit of 100 volts has been included in the controller design.

As shown in Figure 1, the bender is clamped to the rotation axis of the rudder. At the other end it is hinged to a quasi rigid bar that drives the control tab.

Dunsch et al. [3] give the deflection of a bimorph bender:

$$\delta(L) = \frac{3 d_{31} L^2}{8 h^2} U$$

Combining with the flat plate aerodynamics, the tab

deflection can be evaluated to:

$$\alpha = \frac{\frac{3d_{31}L^2}{8h^2}U}{d + \rho V^2 S\pi \frac{L^3}{3EI}\frac{b}{d}}$$

It can be concluded that over the entire operational range of the wind tunnel up to 30 m/s, at least a tab deflection of 1 degree can be reached with 70 volts.

5 Wind Tunnel Experiment

The first step in the wind tunnel experiments was the identification of the actual model. During the construction some adjustments needed to be made. The most notable is that the attachment to the balance needed to be changed. In the wind tunnel model, the wing was clamped to a bar that ran through an aerodynamic panel. This bar was attached to the balance. Due to the addition in length the stiffness of the model decreased, thus the eigenfrequency also decreased.

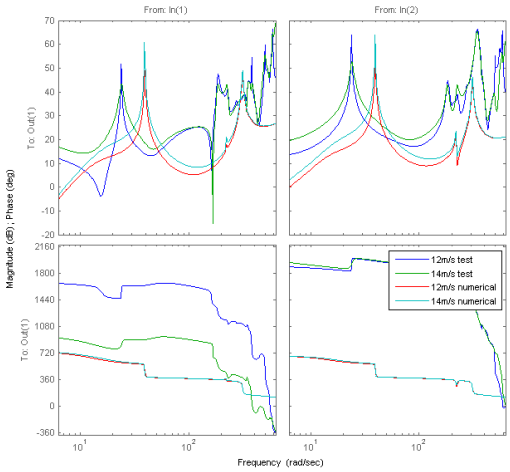

Figure 7. Bode rudder Tip acceleration vs frequency: Inboard tab (left) and outboard rudder (right), magnitude (top) and phase angle (bottom)

Figure 7 shows the acceleration of the tip as a function of the frequency of the trailing edge tab actuation. Clearly a peak can be spotted just below 4 Hz for the real model. As expected, this is a lower frequency compared to the numerical model. However the peaks display the same magnitude. Those peaks correspond to the eigenfrequency of the structure. At higher frequencies of more than 20 Hz, the identification is strongly polluted with noise of the accelerometer. Therefore higher frequencies are filtered out in the controller.

It is believed, that the numerical model is not fully applicable anymore because of the alterations that needed to be made when attaching the structure to the balance.

Load alleviation of the model has been tested by a gust simulation. For that purpose the inboard control surfaces has been used to excite the model in a periodic fashion, while the outboard surface has been used to damp that motion. Figure 8 shows the root bending moment amplitude as a function of wind speed. While the effect is small, for low velocities, the effect becomes more pronounced when approaching the flutter speed. At low speeds the forces generated and thus the moments are not high enough to overcome the friction of the system and therefore a reduction cannot be achieved. At higher speeds the loading can be increased to less than a quarter of the original value.

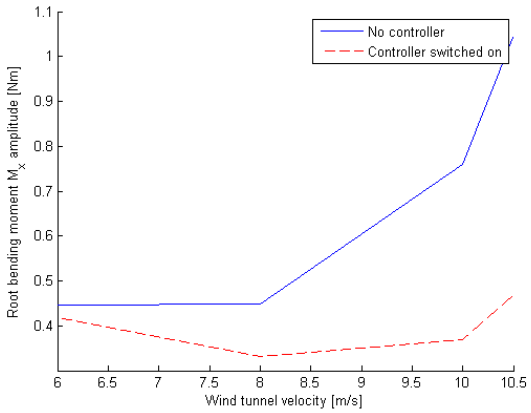

Figure 8. Load alleviation of bending moment as function of speed

An important challenge of the wind tunnel tests was to demonstrate the ability of the control system to increase the flutter speed. For that purpose the tests have been repeated with the controller switched on. Figure 9 illustrates the pole trajectories of the controlled model compared to the numerical solution.

The damping plot sees a very strong increase in damping starting at 11 m/s with a peak at 14 m/s. After that point the damping reduces again. The steep increase is explained by the increasing separation of the frequencies of the associated modes. The strong reduction is connected to the saturation limit of the controller. Figure 10 shows the tip accelerations and the input send to the piezoelectric actuators sent by the controller. The controller output jumps between the saturation limit in both directions. Consequently the required control signal cannot be modeled accurately anymore.

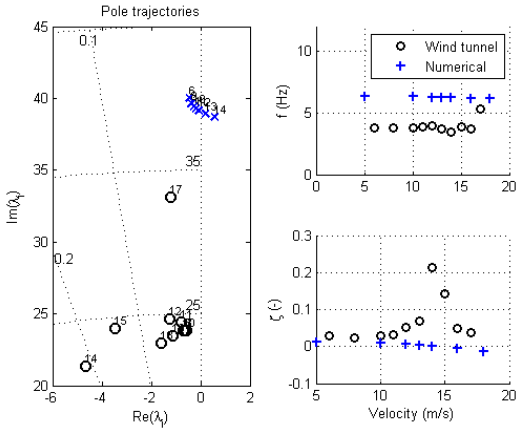

Figure 9. Pole trajectories of model post flutter, Nastran (blue) vs Controlled model (black)

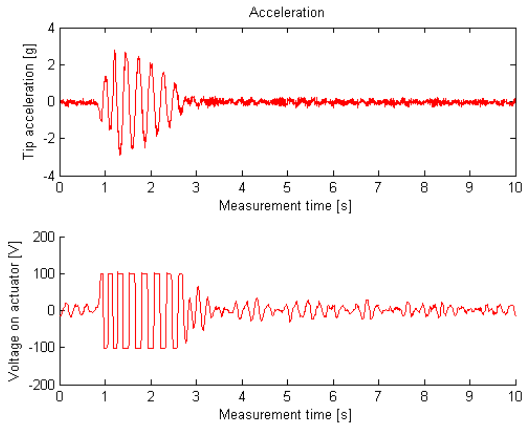

Figure 10. Comparison voltage input of control to tip acceleration at 16 m/s

Still the controller is able to suppress flutter until a speed of 21.5 m/s. Despite the inaccurate modeling, the controller causes the rudders to oscillate out of phase with the motion of the vertical tail plane, thereby reducing the energy of the system.

6 Future research

Nowadays, state-of-the art wind turbines operate with variable rotor speed. Their wind turbine blades can be pitched as whole to regulate the power output. Individual pitch control has emerged and slowly finds application in technology demonstrations. However the technology to pitch the full span has important short comings as the frequency bandwidth required. Another problem is wear of bearing and actuators.

Therefore an alternative approach has been devised based on active control using piezoelectric actuators. This technology is now transferred to the full scale design of 'Smart rotors' of wind turbines in the multi-MW range. Active controllers are designed measuring loads and accelerations to determine the aerodynamic loading. Not only the fatigue load is taken into account, but also extreme loads. For full control authority, the trailing edge will be equipped with flap-tab combinations such that the loading profile can be tailored to the desired state.

A 3 blade model will be built with a diameter of 7 m to demonstrate the technology onwind turbines and their rotary aerodynamics. Besides that technology demonstration, a reliability and producibility analysis will be carried out to show the cost saving potential for customers.

References

[1] Barlas, T.K., van Kuik, G.A.M., 2010, "Review of state of the art in smart rotor control research for wind turbines", *Progress in Aerospace Science*, 46, 1-27.

[2] Basualdo, S., 2005, "Load alleviation on wind turbine blades using variable airfoil geometry", Wind engineering, 29, 169-182.

[3] Dunsch, R., Breguet, J.M., 2006, "Unified mechanical approach to piezoelectric bender modeling", Sensors and Actuators A.

[4] Eller, D., Heinze, S., 2005, "An approach to induced drag reduction with experimental evaluation", Aeroelastic concepts for Flexible Wing Structures, ISSN 1651-7660.

[5] Heinze, S., Borglund, D., 2005, "On the influence of modeshape variations in robust flutter analysis", Aeroelastic concepts for Flexible Wing Structures, ISSN 1651-7660.

[6]…Heinze, S., Karpel, M. 2005, "Analysis and wind tunnel testing of a piezo-electric tab for aeroelastic control applications", Aeroelastic concepts for Flexible Wing Structures, ISSN 1651-7660.

[7] Karpel, M., Moulin, B., 2005, "Dynamic response of aeroservoelastic systems to gust excitation", Journal of Aircraft, 42 (5), 1265-1272.

[8] Rice, J.K., Verhagen, M., 2009, "Robust and distributed control of a smart blade", Wind energy, 13, 103-116.

[9] Wingerden, J.W., Hulskamp, A.W., Barlas, T.K., van Kuik, G.A.M., Verhagen, 2008, "On the proof of a concept of a 'smart' wind turbine rotor blade for load alleviation", Wind energy, 11, 265-280

A Dynamic Model for Supporting Decisions Regarding the Operation and Maintenance of Offshore Wind Farms

G. Wilson, A. Zitrou, F. Quail
Wind Energy DTC, University of Strathclyde
Royal College Building, 204 George Street, Scotland
E-mail: {Graeme.Wilson.100,Athena.Zitrou,Francis.Quail}@strath.ac.uk

***Index Terms* — Bayesian Belief Networks, Condition Monitoring, Diagnostics, Prognostics.**

1. INTRODUCTION

Access to an offshore wind turbine is greatly limited by the environment; consequently operation and maintenance (O&M) can become more sporadic and infrequent. This reduces the turbine availability, thus decreasing the generated output [1]. O&M is already a large part of the life costs of a turbine, but with offshore turbines, this will increase greatly with the inclusion of vessel hire costs [2]. Due to these factors it is extremely important to have adequate operation and maintenance procedures to ensure the offshore wind farms function effectively and efficiently.

Wind turbines are usually maintained in two ways: preventative and corrective [2]. The latter is reactive maintenance which occurs in response to a failure. The former aims to maintain the condition of the system at an acceptable level to avoid failure. Preventative maintenance can potentially be a more economical and practical option as vessels can be booked in advance, specific components can be ordered and this can be planned in fair weather periods. There are two types of preventative maintenance: time-based maintenance and condition-based maintenance. This paper will focus on condition based maintenance.

2. BAYESIAN NETWORKS

This section gives an introduction to Bayesian Networks. More detailed information can be found in [3] and [4].

2.1 Bayesian Belief Networks

Bayesian Belief Networks (BBNs) are probabilistic graphical models, based on Bayes' Rule, which allow for reasoning under uncertainty and show the interdependencies of a system.

Fig 1. BBN of an observation ***O***, and a variable ***X***.

A fictitious example of a BBN is shown in ***figure 1*** for illustrative purposes. The system contains observation ***O***, and variable ***X***; the state of ***X*** can only be observed through ***O***.

It is important in this case therefore to find the probability of the variable ***X*** in a certain state; given the observation ***O***. This updates our belief about the state of ***X*** and is calculated using Bayes' Rule as shown in ***equation 1***.

$$P(X|O) = \frac{P(O|X)P(X)}{P(O)} \quad (1)$$

Knowing the probability of the state of the variable in the case of a wind turbine would allow an engineer to assess the probable condition of a turbine component taking into account only the observation from a condition monitoring sensor.

2.2 Dynamic Bayesian Networks

As BBNs only take account of the observations made at a given point in time they are considered to be static models [5]. A Dynamic Bayesian Network (DBN) can be used to dynamically model a system over a finite number of time slices. A DBN is formed by interconnecting BBNs over time slices. DBNs can be used for basic inference tasks [6]:

- *Filtering or Monitoring* – using historical observations, to predict the state of the variable in the present.
- *Prediction* – using historical observations to predict the state of the variable at a defined point in the future.
- *Smoothing or Hindsight* – using present and past evidence to get an accurate definition of the state of a variable at a point in the past.
- *Most Likely Explanation* – The likely sequence of states which have generated a sequence of observations.

Filtering, Smoothing and Most Likely Explanation have the potential to be used in diagnosis, while Prediction may be used in prognosis [7].

The software GeNIe, models DBNs and is used throughout this paper in carrying out inference tasks and modelling the system.

3. WIND TURBINE GEARBOX DBN EXPLANATION

Shown in ***figure 2***, is a DBN representing an example of wind turbine gearbox containing two components. The DBN consists of:

- Two observation nodes – Iron content and Temperature
- Two component nodes – Bearing and Gear Tooth Condition
- A decision node representing the degradation at time $t = 0$.
- Two maintenance nodes.

This section aims to explain how the DBN was constructed and used to simulate component failures.

3.1 Observations

A major indicator of gearbox condition is the gearbox lubricant [8]. In the gearbox there is a great deal of contact between components. When these components wear down, particles are liberated and become suspended in the lubrication [9].

Both observations are discretised into three states – *High*, *Medium* and *Low*. The probabilities for these observations are calculated using Gaussian Mixture Modelling, which is described in more detail in ***section 3.3***.

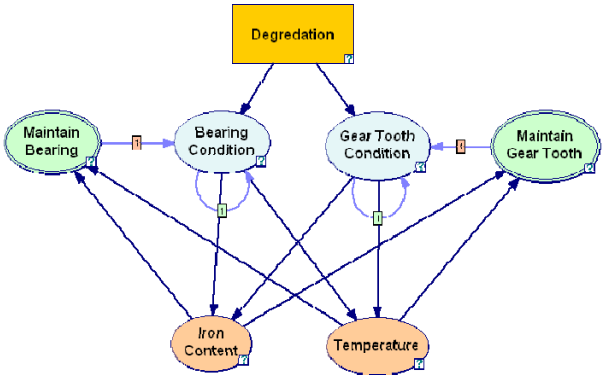

Fig 2. Wind Turbine Gearbox DBN

3.1.1 Iron

Iron is an element which normally features in gearbox components, it can therefore be inferred that an increase in ferrous particle content in the lubricant oil is due to increased wear of a gearbox component. Condition monitoring sensors can observe iron particles by using Electromagnetic Detection (EMD) [10].

3.1.2 Temperature

Fluctuations in oil temperature can be due to a number of factors. Thermal degradation can also cause the additives in the lubricant to become unstable and less efficient [11]. An increase in temperature is therefore a clear indication of a failure somewhere within the system. Thermocouple sensors can be used to monitor the temperature of the oil.

3.2 Components

The components have three states, *OK*, *Poor* and *Failure Mode*. There are two failure modes. The first, *FM1*, is a bearing failure; the second, *FM2*, is a gear tooth failure. Detailed information on these failure modes can be found in [11].

3.3 Failure Modes

The failure modes used as examples come from [12] and [13]. ***Figure 3*** shows the failure mode for bearing failure.

Condition monitoring sensors continuously measure the iron content and temperature of the oil. To represent the probability of all possible values from the failure curve, a continuous probability density function can be used. To do this, the failure mode data is broken up into regions which represent states of the component (*OK*, *Poor* and *FM*) and are each represented by a Gaussian. This is called Gaussian Mixture Modelling (GMM). The regions are shown in ***figure 3***; the continuous probability density function for iron content is shown in ***figure 4***.

In GMM, the Gaussians are combined by applying a mixture weight so that the GMM represents the data accurately and so that the combined areas of all the Gaussians equal 1. If $e_j(\boldsymbol{O})$ represents the probability of observation $\boldsymbol{O}$, while in state j , M is the number of mixtures, and v_{jm} is the mixture weight for the mth mixture of state j [11]:

$$e_j(\boldsymbol{O}) = \sum_{m=1}^{M} v_{jm}\, g(\boldsymbol{O}|\mu_{jm}, c_{jm}) \qquad (2)$$

Using this method and applying ***equation 2***, it is possible to train the model to recognise what state the system is in based on an observation.

The GMM's are also used to calculate the observational probabilities i.e. the likelihood of an observation, given the states of the two independent components.

3.4 Maintenance

Maintenance nodes are used to represent a maintenance strategy. They have two states, *Fix* and *Don't*. If the component is fixed, it returns to its original condition, whereas if it is not, it remains at its current state. This is used to simulate the replacement of faulty components in a wind turbine. Maintenance strategies can be set in the maintenance nodes which decide the observations that trigger a component replacement. In this case the maintenance strategy was to replace a component if at any point a *High* reading was observed.

3.5 Degradation Node

A decision node is used to represent the level of degradation experienced by both the gearbox teeth and bearings at time step 1. Degradation is assumed to be in a constant state in this model. Degradation is modelled in the

components using their Conditional Probability Tables (CPT). The degradation has three states, *Excellent*, *OK* and *Poor*. The probabilities for the CPT are based upon judgement on the behaviour of the failure modes.

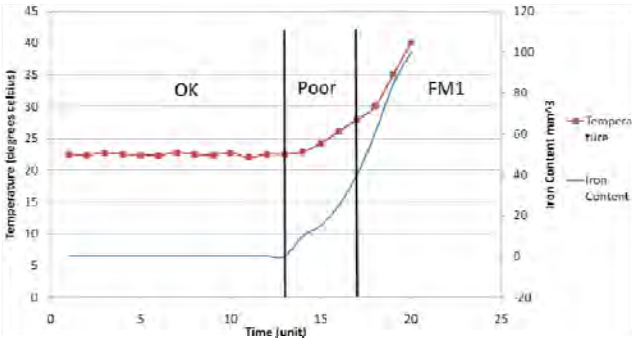

Fig 3. Bearing failure mode

4. RESULTS

The model shows the condition of the two components over time, based on the initial degradation state and maintenance regime. GeNIe was configured to show 20 time steps. ***Figure 5*** shows the condition of the bearing and gear tooth over the 20 time steps when the degradation is *Excellent* and the maintenance regime discussed in ***section 3.4*** is employed.

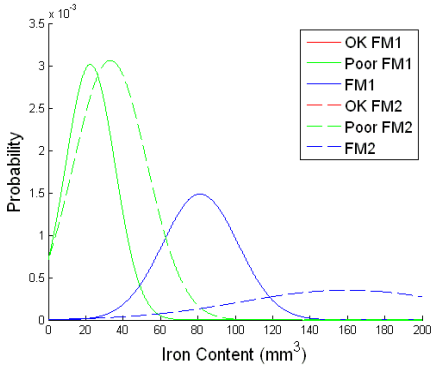

Fig 4. GMM for iron failure mode

Figure 5 shows that initially the condition of the gear tooth is 50% likely to be in the *OK* or *Poor* state. However as the degradation state is excellent the likelihood of the condition of the gear tooth being in an *OK* state increases over time. This data could be used to make a decision based upon the type of maintenance regime to employ. If no maintenance regime is employed the condition of the components over the 20 time slices changes to as shown in ***figure 6***.

If no maintenance strategy is employed, the condition of both the gear tooth and the bearing declines as the *Failure Mode* states become more likely over time and the *OK* conditions become less likely. A maintenance decision can be made based upon this information from the DBN. Different maintenance regimes can be tested until an optimum is found that satisfies performance and cost.

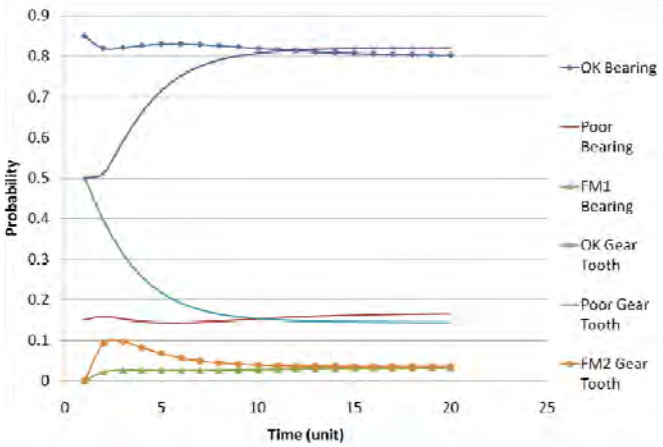

Fig 5. Component condition probabilities for maintained gearbox experiencing excellent degradation state

Decisions can also be made about the future state of the components based on the chosen maintenance regime and the degradation state by considering the predictions made in GeNIe. This could be used in deciding the best maintenance strategy for an offshore wind turbine.

As shown in ***figure 7***, when the gearbox is in a *Poor* degradation state and is not maintained, it fails very quickly.

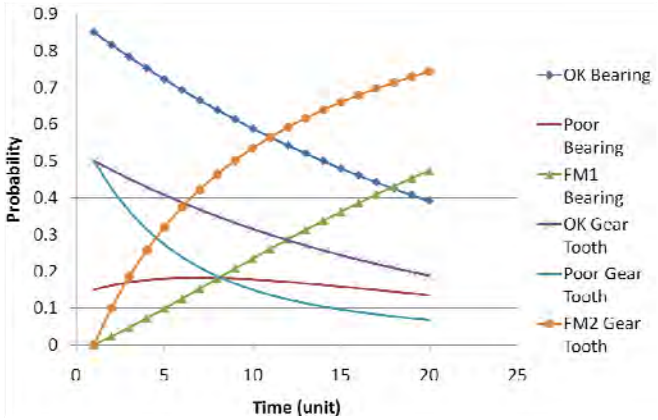

Fig 6. Component condition probabilities for non-maintained gearbox experiencing excellent degradation

However as demonstrated in ***figure 8***, when a maintenance strategy is applied its components fair better.

5. DISCUSSION

The results show that the GeNIe DBN model is useful in making maintenance decisions based on observations from condition monitoring sensors. The model can be further extended to account for more observations from other sensors and visual inspections, as well as external factors such as the weather. This could be used to make a more

holistic decision, taking into account the availability and cost of vessel hire as well as the sea state.

The most important elements of the model are the observation nodes and the probabilities contained within their CPTs. More research must be undertaken to make the process of calculating these probabilities quicker and more efficient as this takes a considerable amount of time and could not be carried out on a larger scale effectively.

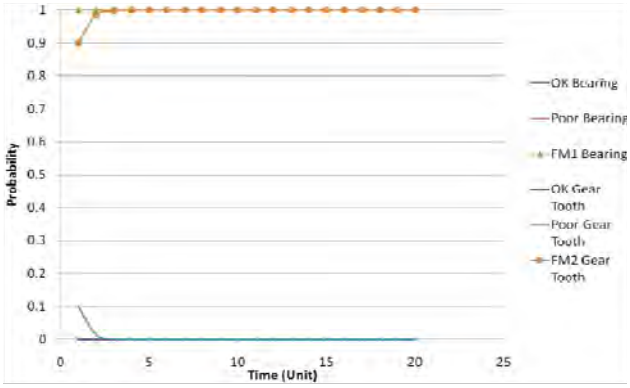

Fig 7. Component condition probabilities for an unmaintained gearbox experiencing poor degradation.

To improve the model further a new software program which is more advanced than GeNIe would have to be designed. GeNIe is very limited and requires observations and states to be discrete rather than continuous. In reality it is not satisfactory to simplify a variety of complex failures to just three states as it may not give a fair reflection of the state of the system. GeNIe is also limited by its incapability to handle large quantities of data. By using GMM it is possible to determine continuous probabilities and therefore make more accurate decisions. In future the same GMM process could be used within the new software program to model a variety of components using training data.

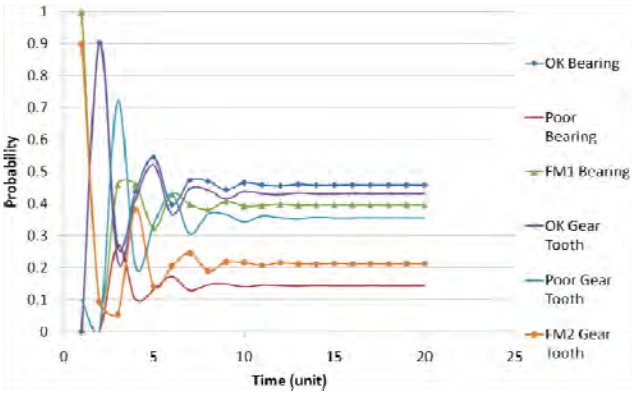

Fig 8. Component condition probabilities for a maintained gearbox experiencing Poor degradation.

The degradation of the gearbox components could be improved by determining actual degradation rates rather than judging them according to their failure curves. To do this more research would have to be carried out on the degradation process with the possibility of using hazard functions and failure rates.

Retrofitting of GMM curves to aged turbines is also a point for consideration, as if a system like this was employed, many existing turbines could have it applied retrospectively after a degree of aging. This retrofitting could be programmed into new software.

Finally and most importantly, the economics of using such a decision making tool has to be investigated to ensure that it can reduce the costs of operation and maintenance effectively.

6. CONCLUSION

This is an area of special interest in research due to the pressure to reduce operation and maintenance costs for the growing numbers of offshore wind turbines. DBNs may offer a means of reducing costs by making accurate diagnosis and prognosis of component states using information gathered from observations made by condition monitoring sensors.

ACKNOWLEDGEMENTS

The authors would like to thank the EPSRC for funding this project.

REFERENCES

[1] S. Faulstich, B. Hahn and P.J. Tavner, “Wind turbine downtime and its importance for offshore deployment,” *Wind Energy*, vol 14, pp 327-337, 2011.

[2] J. D. Sorensen, “Framework for risk-based planning of operation and maintenance for offshore wind turbines,” *Wind Energy*, vol 12, pp 493-506, 2009.

[3] P. M. Lee, *Bayesian Statistics: an Introduction 2nd Edition*. London, UK: Arnold, 1997.

[4] J. H. Sigurdsson, L. A. Walls and J. L. Quigley, “Bayesian belief nets for managing expert judgement and modelling reliability,” *Quality and Reliability Engineering International*, vol 17, pp 181-190, 2001.

[5] C. P. Robert, *The Bayesian Choice*. New York, Springer, 2001.

[6] S. J. Russel, P. Norwig, *Artificial Intelligence: a modern approach.* Upper Saddle River, N.J., Prentice Hall, 2010.

[7] A.K.S. Jardine, L. Daming and D. Banjevic, “A review on machinery diagnostics and prognostics implementing condition-based maintenance,” *Mechanical Systems and Signal Processing*, vol 20, pp1483-1510, 2006

[8] D. J. Lekou, F. Mouzakis, A. Anastasopoulos, and D. Kourousis, Emerging Techniques for Health Monitoring of Wind Turbine Gearboxes and Bearings, Proc. EWEC 2009, Scientific Track – Operation and Maintenance, Marseille, France, March 16-19, 2009

[9] L. A. Toms, Machinery Oil Analysis - Methods, Automation & Benefits 3rd Edition, STLE, Virginia Beach, 2008.

[10] C.J. Crabtree, Survey of Commercially Available Condition Monitoring Systems for Wind Turbines, Durham University, 2010.

[11] A. Hamilton and F. Quail, “Detailed state of the art review for the different on-line/in-line oil analysis techniques in context of wind turbine gearboxes,” *in Conf. Rec.* 2011 *ASME Expo*

[12] Gear Foundation Course Notes, 2009, Version 2, David Brown Gear Academy.

[13] Rao, B. K. N., 1996, Handbook of Condition Monitoring (1st Edition), Elsevier Advanced Technology, Oxford. (use this to reference wear profiles)

Poster Session 1

Electrical Production and Grid Integration

Control Strategies of VSC HVDC Transmission Link Connected to Offshore Wind Farm with Regard to Grid
Cuong Nguyen-Mau, Krzysztof Rudion, Zbigniew A. Styczynski

Characterization and reduction of wind power fluctuations
S. Martın-Martınez, A. Vigueras-Rodrıguez, E. Gomez-Lazaro

Aerodynamic Optimisation of a Small Scale Wind Turbine Blade
David Ferguson, Francis Quail, Peter Jamieson

Offshore Technology

Dynamic Simulation of Mooring Lines for Floating Wind Turbines
J. Azcona Armendariz, X. Munduate Echarri, T. Anders Nygaard, D. Merino Hoyos

Integrated Modelling of Off-shore Wind Turbines
Dimitris Manolas, Vasilis Riziotis, Spyros Voutsinas

Jacket dynamics validated against alpha ventus measurements
Peter Schaumann, Jan Dubois (speaker)

Operation, Condition Monitoring and Maintenance

Bearing Currents in Wind Turbines Generators
Matthew Whittle, Jon Trevelyan, Li Ran, Junjie Wu

Loads on DFIG wind turbines due to unbalanced voltage faults
Braulio Barahona, Christian Wessels, Anca D. Hansen, Poul Sørensen

Condition Monitoring Using Wind Turbine Generator Control Loop Signals
M.N. Zaggout, P. J. Tavner, Li Ran

Rotor and Wakes Aerodynamics

Interaction of Offshore Wind Farms through Large Eddy Simulation
H. Sarlak, J. N. Sørensen, R. Mikkelsen

Prediction of wake effects on wind farm power production using a RANS approach. Offshore case studies from the UPWIND project
D. Cabezón, R. García, J. Sumner, A. Crespo

Comparison between Actuator Disc and BEM models for a floating wind turbine rotor in periodic surge motion
J.B. de Vaal, M.O.L. Hansen, T. Moan

Experimental investigation of 3D separation on an airfoil
Marinos Manolesos, Spyridon Voutsinas

Characterization of a model wind turbine
Francesco Cuzzola

Wind Modelling, Forecasting and Resource Assesment

Modelling forest canopy flow dynamic phenomena, informing steady CFD models with unsteady measurements or/and unsteady CFD models
Ilda Albuquerque, Javier Sanz, Lars Landberg, Simon Watson

Validation of a Vector Auto-regressive Model for Wind Modelling and Synthesis of the UK Wind Field
C. Plumley, D. Hill, D. McMillan, K. Bell, D. Infield

The wind field in the marine boundary layer
Olav Krogsæter, Gard Hauge, Joachim Reuder

Turbulence Modelling of Flow around a Single Tree
Cian Desmond, Simon Watson

Implementation and calibration for atmospheric turbulence of an EARS model
T.Ternisien, J.Prospathopoulos,P.K.Chaviaropoulos

WRF mesoscale modelling and measurements of the diabatic offshore wind profile at FINO1
D. Munoz-Esparza, B. Canadillas, J. van Beeck

Wind Turbine Structural Design and Materials

Axial Capacity of Grouted Joints for Offshore Wind Energy Converters regarding Interlocking Effects
Peter Schaumann, Anne Bechtel (speaker),

Tensile and Fatigue Properties of Carbon Fabric T-joints as a Structural Element of Wind Turbine Blade
Amirhossein Hajdaei, Paul Hogg

Control Strategies of VSC HVDC Transmission Link Connected to Offshore Wind Farm with Regard to Grid Code - Abstract

Cuong Nguyen-Mau, Krzysztof Rudion, Zbigniew A. Styczynski
Chair Electric Power Networks and Renewable Energy Source (LENA), Otto-von-Guericke-University Magdeburg
Universitaetsplatz 2, D-39106 Magdeburg, Germany
E-mail: mau.nguyen@ovgu.de, rudion@ovgu.de, sty@ovgu.de

Keywords: Control strategy, fault ride through (*FRT*), high voltage direct current transmission (*HVDC*), offshore wind farms, voltage source converter (*VSC*).

INTRODUCTION

The goal of this paper is to investigate control strategies in future offshore wind farms interconnected by means of *VSC HVDC* transmission in order to fulfill the grid codes.

STATE OF THE ART AND TASK DEFINITION

In the future many large wind farms (*WF*) will be built offshore at distances over 100 km from the grid connection point. Voltage Source Converter based High Voltage Direct Current (*VSC HVDC*) transmission systems should be utilized for this application due to the self-commutating capability of *IGBT* valves and the resulting features such as rapid and independent control of active and reactive power, no need for reactive power compensating units.

Wind power will play an important role in the stability of the German and European power system. In some cases, *WF* has to act like the conventional generators in steady-state modes and in fault modes. If the offshore *WF* is connected to the power grid by *VSC HVDC* technology, the performance of its control system plays a vital role in fulfilling the grid code.

MODEL DEVELOPMENT

The simulated case presented here consists of a 200 MW wind farm based on full-sized converters, which is connected to a 100 km *VSC HVDC* transmission link via a 35/110 kV transformer. The *DC* rated transmission voltage is ±100 kV. The *IGBT* of both converters are controlled by means of Pulse Width Modulation (*PWM*) at switching frequency of 1350 Hz. The topology of these two converters is a two-level bridge.

If there is a fault at the *AC* side of a converter, the unbalanced active power between the two sides of a converter causes the *DC* voltage of the *VSC HVDC* link to continuously increase. According to [1], the protection of *VSC HVDC* will be active when there is a *DC* over-voltage of about 30% within a period of 5 to 10 ms, while grid codes require that the wind turbine remains connected to the grid for a period up to 150 ms, even if the voltage at the point of common coupling drops to zero [2]. To avoid the *DC* over-voltage, the *WF* must reduce its generated power. This paper will discuss the control strategy of reducing the output power of the *WF* by increasing the frequency on the *WF* grid.

STUDY CASES ANALYSIS

To evaluate the effectiveness of the method, a three phase fault that lasts 150 ms is simulated at the 220 kV side of the converter connected to the power grid. The *DC* voltage on the *VSC HVDC* transmission link and other important signals of both converters before, in and after fault will be recorded to assess the efficiency of the proposed control strategy in enhancing the *FRT* capability.

CONCLUSIONS

By applying this method the over-voltage on the *DC* side of both converters is kept in an acceptable range. With this strategy, the cost of a full rated *DC* chopper may be saved while the stability of the system is not jeopardized.

REFERENCES

[1] L. Harnefors, Y. Jiang-Häfner, M. Hyttinen, and T. Jonsson. Ride-Through Methods for Wind Farms Connected to the Grid via a *VSC-HVDC* Transmission. Available electronically at: www.abb.com.

[2] Transpower, Grid Connection code – Extra high voltage. Available electronically at: www.transpower.de/pages/tso_de/Transparenz/.

[3] C. Feltes, H. Wrede, F. W. Koch, I. Erlich. Enhanced Fault Ride-Through Method for Wind Farm Connected to the Grid through VSC-Based HVDC Transmission, *IEEE Transactions on Power Systems*, vol. 24, no. 3, August 2009.

Characterization and reduction of wind power fluctuations

S. Martín-Martínez[1] , A. Vigueras-Rodríguez[2], E. Gómez-Lázaro[1]
Renewable Energy Research Institute
[1]Dept. of Electrical, Electronic and Control Eng. EPSA
[2]Dept. of Applied Mechanics and Project Engineering EPSA
Universidad de Castilla-La Mancha
02071 Albacete (SPAIN)
E-mail: {sergio.martin, antonio.vigueras, emilio.gomez}@uclm.es

Keywords: Smoothing effect, power fluctuations, wind integration, grid codes, system operation.

1 Abstract

Power fluctuations could have a remarkable impact on power system operation and costs, according with the increasing production of wind power worldwide. In systems with weak interconnections, as Iberian Peninsula Power System, these fluctuations could be a security issue. Large amount of wind power installed in Spain and future expansion give rise to concerns about the adverse effects of wind farms on power operations and its stability. Wind penetration in Spanish is expected to go on rising up to 29000 MW installed capacity according to Ministry of Industry energy plan for 2016, [1]. Power fluctuations from this great amount of wind power generation not only requires an increase of reserves caused by uncertainty in the wind energy production but, at the same time, the consequent reduction on dispatchable power units leads to a reduction in the proportion of units that could follow demand variations or system events, [2], [3].

In order to characterise the worst effects on power systems of wind power fluctuations, the most negative wind power ramp rates can be used. With the aim of estimating these increases in allocated reserves, two statistical measures have been proposed to characterise the variability of wind energy: the standard ramp deviation [4] and the 99% Percentile Negative Ramp Rate (PNRR-99) [5]. The main difference between these estimates is that the standard ramp deviation gives a value that includes positive and negative ramps. While the PNRR-99 focuses on the worst drops. Sorting all ramp rates within a interval from the greatest positive one to the greatest negative, the value whose position includes the 99% of the ramps achieved is the PNRR-99. Therefore, only 1% of the time, wind power drops exceed such value. Traditionally, the use of standard deviation has been more extended. In fact, if ramp rates distribution is considered to be Normal, both parameters would be equivalent. However, as the aggregated power series of WFs are often dependent, distribution of ramp rates can be different from Normal. Therefore, PNRR-99 is more conservative and it also has a greater and direct influence on reserves, which is the variable that the TSOs can control.

In this work, geographical smoothing effect is evaluated regarding negative wind power ramp rates. Futhermore, several control strategies are suggested to reduce the resulting aggregated negative ramps. For each strategy, the controlled power is compared with the uncontrolled power output, studying the achieved reduction in negative ramps. The results give a comparison of such strategies, regarding energy losses and the improvement for power system operation.

References

[1] AEE. Asociación empresarial eólica. [Online]. Available: www.aeeolica.es

[2] P. Sørensen, N. Cutululis, A. Vigueras-Rodríguez, L. E. Jensen, J. Hjerrild, M. H. Donovan, and H. Madsen, "Power fluctuation from large wind farms," *IEEE Transactions on Power Systems*, vol. 22, no. 3, pp. 958–965, August 2007, special Section on Power System Perfomance Issues associated with Wind Energy.

[3] P. Sørensen, N. Cutululis, J. Hjerrild, L. Jensen, M. Donovan, L. Christensen, H. Madsen, and A. Vigueras-Rodríguez, "Power fluctuations from large offshore wind farms," in *Proceedings of the Nordic Wind Power Conference*, Espoo (Finlandia), 2006.

[4] H. Holttinen, M. Milligan, B. Kirby, T. Acker, V. Neimane, and T. Molinski, "Using standard deviation as a measure of increased operational reserve requirement for wind power," *WIND ENGINEERING*, vol. 32(4), pp. 445–451, 2008.

[5] A. Vigueras-Rodríguez, P. Sørensen, N. Cutululis, A. Viedma, and M. H. Donovan, "Wind model for low frequency power fluctuations in offshore wind farms," 2009, accepted in Wind Energy.

Aerodynamic Optimisation of a Small Scale Wind Turbine Blade

David Ferguson, Francis Quail, Peter Jamieson
Wind Energy DTC, University of Strathclyde
Glasgow, UK
E-mail: davidferguson@strath.ac.uk

Keywords: Reynolds numbers, small HAWT, aerofoil, optimization.

1 Introduction

For low Reynolds numbers (less than 500,000) aerodynamic performance of aerofoils change. Small scale wind turbines operate at low Reynolds numbers which can lead to severe degradation of performance if correct aerofoil selection is not made. [1]

A low Reynolds number regime is defined as that for which laminar separation dominates the drag and although there is no fixed range it is normally for Reynolds numbers less than 500,000.In high Reynolds number regimes the boundary layer transition occurs before laminar separation. In low Reynolds number regimes the laminar separation is dominant. [1] High Reynolds numbers usually have thick aerofoils where the range of supercritical flow is large compared to thin aerofoils designed specifically for low Reynolds numbers.

Difficulty arises when designing and optimizing a blade for a stall regulated wind turbine due to the uncertainty in the aerodynamic stall characteristics.

This project will consider potential aerofoil designs optimised for low Reynolds number operation, to be proposed for an existing small scale stall regulated wind turbine designed in the DTC.

2 Aerofoil selection

The aim was to select an aerofoil which can operate at low Reynolds numbers. In Selig and McGranahan [1] six aerofoils for use on small wind turbines were tested and the resulting drag polars for each of the aerofoil were used to make a selection of the aerofoil. The aerofoil selection was based on a number of drag polar characteristics, such as the shape of the drag polar, maximum lift-to-drag ratio and corresponding lift coefficient, the size of the drag bucket and also the maximum lift coefficient.

3 Blade optimization

Following the calculations to determine chord length and twist distribution along the span of the blade, blade optimization was carried out using the GH Bladed design software package. Steady Power Curve calculations were performed to determine the electrical power output. Unlike pitch regulated power curves, the power curve for a stall regulated wind turbine cannot be curtailed as accurately. Optimization therefore required careful design to insure stall occurs at the required wind speed.

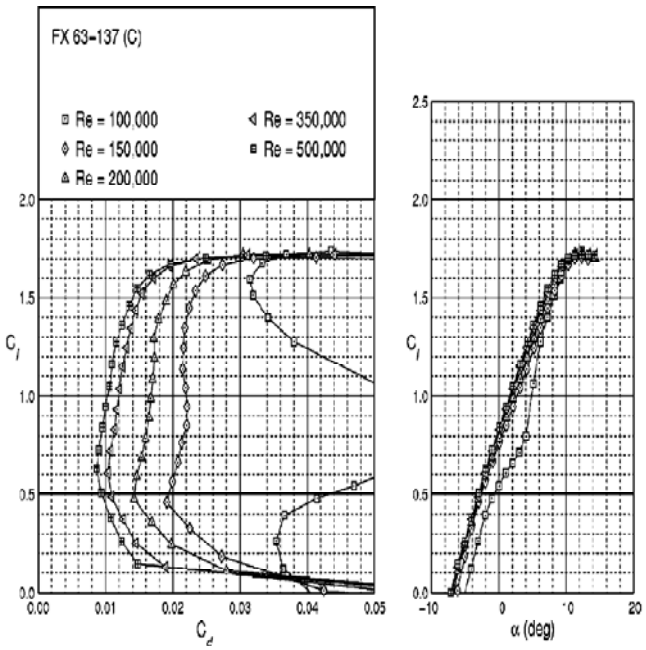

Figure 1: Drag Polar for FX63-137 aerofoil [1]

4 Conclusions

Selecting the correct aerofoil for the Reynolds number that the blades operate at is crucial in order to optimize performance. The optimized blade design for the small HAWT will allow a new set of blades to be manufactured and used on the small HAWT that will be used for educational purposes.

References

[1] **Selig, M.S.** *Wind Tunnel Aerodynamic Tests of Six Airfoils for use on Small Wind Turbines* - 2004.

[2] **Giguère, P. and Selig, M.S.** *Low Reynolds Number Airfoils for Small Horizontal Axis Wind Turbines* - 1997.

Dynamic Simulation of Mooring Lines for Floating Wind Turbines

José Azcona Armendáriz[1], Xabier Munduate Echarri[1], Tor Anders Nygaard[2], Daniel Merino Hoyos[3]
[1]Renewable Energy National Centre, CENER
Ciudad de la Innovación 7, 31621 Sarriguren, Navarra, Spain
[2]Institute for Energy Technology, IFE
Instituttveien 18, NO-2007 Kjeller, Norway
[3]Acciona Energía
Avenida Europa 6, Parque Empresarial La Moraleja, 28108 Alcobendas, Madrid, Spain
E-mail: {jazcona, xmunduate}@cener.com

Keywords: mooring, floating platforms

1 Introduction

This work is part of the PhD that the first author is developing at "Universidad Politécnica de Madrid".
The mooring system of a floating wind turbine is made of several cables attached to the platform, with the lower ends anchored to the seabed, holding the structure in the desired location. A code based on finite elements for the dynamic simulation of mooring lines has been developed at CENER. The motion equations are integrated in time using an explicit scheme [1]. After verifying the results of CENER's stand alone code, it has been loosely coupled with the FAST code [2] for the simulation of floating wind turbines.

2 Code Development

Three translational degrees of freedom per node are defined in this dynamic model. The effect of inertias, added masses, gravity, hydrostatics and axial elasticity is considered. Normal and tangential drags between the line and the water are introduced using the drag term of Morison's equation. A contact model of the line with the seabed has been implemented using bi-linear springs. Also, a line-seabed friction model has been developed and introduced into the model. It considers interaction in axial and normal directions independent. Static friction is modelled using horizontal springs that introduce forces when the node is not sliding. Dynamic friction depends on the vertical contact force and the friction coefficient.
A first verification of the stand alone code was performed comparing free oscillation simulations with theoretical natural frequencies of the line. Then, several load cases were defined and compared with SIMO-RIFLEX including regular and irregular waves and friction and no friction simulations. Results have been satisfactory.

3 Coupling with FAST

Original FAST mooring lines model uses a cuasi-static formulation. In order to introduce new dynamic capabilities into the FAST code for the simulation of moored floating platforms, CENER's code has been coupled with FAST using a loose scheme. FAST uses an Adams-Moulton-Bashforth predictor-corrector integrator and CENER's mooring lines code uses an explicit scheme. Each time FAST equations of motion are evaluated, the mooring lines code reads the position of the platform and provides the forces at the fairleads. Once the predictor and corrector steps are completed, both integrators advance one time step. A second verification of the coupled tool has been performed and comparison between CENER's code coupled with FAST and results from SIMO-RIFLEX have shown good agreement. A more extensive verification of the coupled tool will be performed in the future, including comparisons with different codes.

4 Conclusions

A new stand alone code for the dynamic simulation of mooring lines have been developed and verified. The code has been coupled with FAST, improving its capabilities for simulation of floating platform wind turbines. CENER's mooring line code introduces new features into FAST as: damping, inertia, water drag and normal seabed friction, providing a more accurate description of floating wind turbine dynamics.

5 Acknowledgements

We want to thank Ingemar Carlen from Teknikgruppen AB. for his guidance and support at the beginning of this study. This work has been performed within a project funded by Acciona Energía.

References

[1] J. Lindahl, A. Sjöberg, *Dynamic analysis of Mooring Cable*, Chalmers University of Technology, 1983

[2] J. M. Jonkman. *Dynamics Modeling and Loads Analysis of an Offshore Floating Wind Turbine.* Technical Report NREL/TP-500-41958, 2007.

Integrated Modeling of Off-shore Wind Turbines

Dimitris Manolas, Vasilis Riziotis, Spyros Voutsinas
Laboratory of Aerodynamics, National Technical University of Athens
9 Heroon Polytechneiou str., GR15780 Athens, Greece
E-mail: {manolasd,vasilis,spyros}@fluid.mech.ntua.gr

Keywords: offshore wind turbine, monopile, tripod, jacket, floating wind turbine

INTRODUCTION

The work aims at concluding an integrated design tool for off-shore wind turbines by implementing the additional effect of hydrodynamic loading into GAST, NTUA's servo-aero-elastic tool. The additional modules leading to hydro-GAST concern the modeling of the effect of water waves and currents as well as the modeling of the moorings and the foundation. The approach followed consists of concurrently solving all of the dynamic equations of the entire system: the servo-aero-elastic equations for the complete wind turbine, the dynamic equations of the submerged structure and of the moorings. The integrated tool should be able to model different concepts for the submerged structure: monopile, jacket, spar floater etc.

DESCRIPTION OF hydro-GAST

The formulation of the problem is carried out in the context of multi-body dynamics resulting in coupled equations of the entire wind turbine configuration. Couplings are defined at the connection points of the different components; namely the blades-to-hub connections; the connection between the drive train and the tower; the connection of the tower to the submerged structure; and the connection of the mooring lines on the floater in case of a floating wind turbine. At all connections, one of the connecting components delivers the kinematics (position and orientation given by the displacements and rotations as well as the associated velocities and accelerations) while all other contribute their loading so that full continuity is insured.

The numerical implementation involves: the aerodynamic modeling of the rotor; the elastic modeling of the blades, the drive train, the tower and the submerged structure (in case of a sea-based concept); the hydrodynamic loading on the submerged structure; the modeling of the mooring lines (in case of floating concepts); and the modeling of the control system.

Aerodynamic modeling: There are two options in GAST: a Blade Element Momentum model and a free-wake vortex type model. Both models use the generalized ONERA dynamic inflow model in order to calculate the aerodynamic loading. A basic difference is that in the free-wake model the so called "attached" circulation is directly derived from the flow solver.

Structural modeling: All solid components are modeled as 3D Timoshenko beam structures and discretized by means of the Finite Element Method. The beams are considered in combined bending (in two directions), tension and torsion. In order to account for large displacements and rotations, the components can be divided into non-linearly connected sub-bodies.

Hydrodynamic loading: The wave and current loads acting on the submerged structure are calculated on the basis of Morisson's approximation for both linear (regular and irregular) and non-linear wave solutions (stream function). In the case of a floating system, the hydrodynamic loading on the floater is calculated by solving the first order hydrodynamic problem (diffraction, radiation). The linear memory effect is captured in the time-domain by means of time-convolution of the radiation impulse-response functions (i.e. the wave-radiation-retardation kernel), with the floater velocities.

Mooring lines: The mooring is modelled as a line of truss elements transmitting axial loads. The interaction with the sea bed is modeled by introducing non-linear springs that prevent the mooring elements to get bellow the mud line.

hydro-GAST is currently under evaluation within the IEA Task 30 Annex. Code-to-code comparisons have been also carried out for the test cases defined in IEA Task 23 Annex.

CONCLUSIONS

An integrated hydro-servo-aero-elastic design tool for offshore wind turbines has been concluded and is currently under evaluation. The paper will provide a brief description of the modeling principles as well as indicative comparative results.

Jacket dynamics validated against alpha ventus measurements

Peter Schaumann, Jan Dubois (speaker)
ForWind – Centre for Wind Energy Research,
Institute for Steel Construction, Leibniz University Hannover
Appelstrasse 9A, 30167 Hannover, Germany
E-mail: dubois@stahl.uni-hannover.de

Keywords: alpha ventus, offshore test field, jacket dynamics, integrated load simulation

INTRODUCTION

The German offshore test field ´alpha ventus´ provides a valuable opportunity to validate integrated simulation results of 5 MW wind turbines with jacket or tripod substructure. The REpower av04, a 5 MW wind turbine with jacket is equipped with hundreds of sensors to measure SCADA signals, meteorological conditions and structural responses. Within the research project OWEA, funded by the Federal Ministry for the Environment, Nature Conversation and Nuclear Safety, the evaluation of measurement data started, since first time domain measurements are recently available.

MODEL AND BENCHMARKING

An essential subtask of the OWEA project was the development of an integrated simulation tool. Therefore, the Endowed Chair of Wind Energy (SWE), University of Stuttgart, and the Institute for Steel Construction, Leibniz University Hannover, coupled existing tools Flex 5 and POSEIDON. As a result, a aero-servo-hydro-elastic tool can be deployed for subsequently performing integrated simulations. The overall model of the wind turbine with jacket support structure has been build up as Figure 1 shows schematically. The model is successfully benchmarked due to the fact that essential measured natural frequencies are matched well.

SIMULATIONS AND MEASUREMENTS

Special measurement periods with wind conditions around rated wind speed and slightly lower than cut-off wind speed are chosen. The meteorological and environmental simulation parameters are adapted according to the described measurement conditions and integrated simulations are performed subsequently. In addition, the measurement data is prepared by converting strain signals into resulting member forces in order to distinguish between global and local structural responses for following validation works.

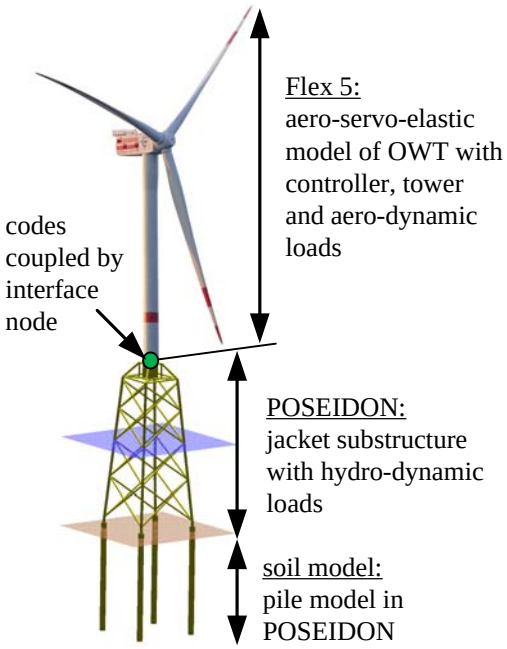

Figure 1: Simulation model in Flex 5 – POSEIDON of the REpower 5M with jacket at alpha ventus.

Validation

The validation is currently carried out. The model benchmark showed good agreement to measurements and first time domain investigations appear promising. This contribution will present the results of validation activities focussed on global and local structural responses.

REFERENCES

[1] Böker, C. (2010): Load simulation and local dynamics of support structures for offshore wind turbines. Dissertation Thesis, Leibniz Universität Hannover.

[2] Schaumann, P., Dubois, J., et al. (2010): Integrated simulation of the REpower 5 MW offshore wind turbine with jacket support structure validated by alpha ventus measurement data, , Proceedings of the 10th German Wind Energy Conference DEWEK, Bremen, November 17th – 18th, 2010.

[3] Kaufer, D., et al. (2009): Integrated Analysis of the Dynamics of Offshore Wind Turbines with Arbitrary Support Structures. Proceedings of EWEC 2009. Marseille, 2009.

Bearing Currents in Wind Turbines Generators

Matthew Whittle, Jon Trevelyan, Li Ran, Junjie Wu
Energy Group, University of Durham
School of Engineering and Computing Sciences, South Road, Durham, UK
E-mail: {m.w.g.whittle,jon.trevelyan,li.ran,junjie.wu}@durham.ac.uk

Keywords: bearing currents, generator failure, reliability

1 INTRODUCTION

Improving the reliability of wind turbines is an essential component in the bid to minimise the cost of energy, especially for offshore wind due to the difficulties associated with access. Numerous studies have shown that wind turbine generator failure rates are unacceptably high, particularly given the long downtime incurred per failure [1-3]. However, generator failures have, to date, received relatively little attention in the wind industry with the focus generally having been on the blades and the gearbox. There is evidence that the bearings are the most important source of generator failures [4]. There are many possible root causes for bearing failures; one important root cause is bearing currents which flow as a result of the common-mode voltage associated with the pulse-width modulation (PWM) of the power electronic converter.

2 COMPUTATIONAL STUDY

The parasitic capacitive coupling, by which HF leakage currents give rise to bearing currents, has been investigated and the general principles are now quite well understood. A range of coupling models has been proposed in the literature [5-7], but all incorporate a very simplified model of the bearing. An improved model of the bearing capacitance is presented here by using both Hertzian contact mechanics and the Hamrock-Dowson film thickness equation. By considering a typical 2MW DFIG the capacitances of the HF stray circuit were calculated from the machine geometry and a range of simulations and sensitivity studies were undertaken.

3 CONCLUSIONS

It was found that the dielectric strength of the grease lubricant was exceeded upon each switch of the converter, resulting in electrostatic discharge machining (EDM) of the bearing balls and raceway. Because the converter switching frequency is in the *kHz* range this results in a very large number of current discharge events taking place, which may lead to very rapid damage of the bearings.

It was also found that the winding-rotor coupling capacitance was an order of magnitude greater when the converter fed the rotor (as in a DFIG), rather than the stator. Therefore, for rotor-fed machines (very common in wind turbines) the bearing voltages are much greater, leading to an increased probability of EDM.

4 FURTHER WORK

A test rig is under construction to carry out further investigation. The test rig will serve two purposes:

- It will be used to validate and, if necessary, improve the stray HF model
- It will allow accelerated ageing of bearings subjected to a specified electrical stress regime.

A description of the rig is provided in the paper.

REFERENCES

[1] S. Faulstich, Windenergie Report Deutschland. Kassel: Institut fur solare Energieversorgungstechnik, 2008.

[2] Landwirtschaftskammer Windenergie. [Online] http://lwksh.de/cms/index.php?id=2875

[3] B. Hendriks, Reliawind Design for Reliability. Warsaw: EWEC, 2010.

[4] W. Chen, and K. Alewine, Wind turbine generator failure modes analysis and occurrence. Dallas: WindPower, May 24-26, 2010.

[5] S. Ogasawara, and H. Akagi, Modeling and Damping of High-Frequency Leakage Currents in PWM Inverter-Fed AC Motor Drive Systems, IEEE Transactions on Industry Applications, 32(5): 1105-1114,1996.

[6] S.. Chen, T. A. Lipo, D. Fitzgerald, Modeling of Motor Bearing Currents in PWM Inverter Drives, IEEE Transactions on Industry Applications, 32(6): 1365-1370, 1996.

[7] A, Muetze, A. Binder, Calculation of Motor Capacitances for Prediction of the Voltage Across the Bearings in Machines of Inverter-Based Drive Systems, IEEE Transactions on Industry Applications, 43(3): 665-672, 2007.

Loads on DFIG wind turbines due to unbalanced voltage faults

Braulio Barahona[1,*], Christian Wessels[2], Anca D. Hansen[1], Poul Sørensen[1]

1) Wind Energy Division, Risø DTU, Technical University of Denmark
399 Frederiksborgvej, 4000 Roskilde, Denmark

2) Institute for Power Electronics and Electrical Drives,
Faculty of Engineering Christian-Albrechts-University of Kiel
Kaiserstrasse 2, D-24143 Kiel, Germany

*E-mail: {brab}@risoe.dtu.dk

Keywords: unbalanced voltage fault, wind turbine loads, DFIG wind turbine, integral dynamic analysis.

ABSTRACT

Wind turbines are generally required to stay connected to the power system during a voltage fault (i.e. fault ride-through). Typically, studies of the dynamic behavior of the wind turbine, and the power system during such faults, address only the balanced (or symmetrical) voltage faults (i.e. three-phase short-circuit to ground) because in most of the cases they represent the worst case. Also in this trend, the grid codes enforced by power system operators in different countries outline fault ride-through requirements in terms of balanced faults.

However, unbalanced voltage faults (i.e. single-phase-ground, two-phase-ground, phase-phase) are more common in power systems, and in some cases they can be worst than the symmetrical case [1, 2]. Therefore, the interest on developing models capable of handling unbalanced faults for power system stability studies [1, 2]. Furthermore, investigations of structural loads on wind turbines due to voltage faults only consider the balanced case [3].

This work studies the dynamic response of a DFIG wind turbine due to unbalanced voltage faults. The focus is to investigate the impact on the structural loads, and the potential for load reduction given a single-phase voltage fault, while the generator power converter controls the shaft speed, and the blade angle control limits the aerodynamic power. The model used consists of a 2 MW wind turbine, where the aeroelastic, structural, electrical, and control dynamics are simulated in HAWC2-Matlab/Simulink. It was observed that the loads imposed by the unbalanced fault are not prohibitive.

REFERENCES

[1] J. Fortmann, S. Engelhardt, J. Kretschmann, C. Feltes, and P. I. Erlich, "Validation of an rms dfig simulation model according to new german model validation standard fgw tr4 at balanced and unbalanced grid faults," in *8th International Workshop on Large-Scale Integration of Wind Power int Power Systems as well as on Transmission Networks for Offshore Wind Farms*, 2009.

[2] V. Akhmatov, B. Andresen, J. N. Nielsen, K. H. Jensen, N. M. Goldenbaum, J. Thisted, and M. Frydensbjerg, "Unbalanced short-circuit faults: Siemens wind power full scale converter interfaced wind turbine model and certified fault-ride-through validation," in *European Wind Energy Conference & Exhibition*, 2010.

[3] A. D. Hansen, N. A. Cutululis, H. Markou, and P. Sørensen, "Impact of fault ride-through requirements on fixed-speed wind turbine structural loads," *Wind Energy*, 2010.

Condition Monitoring Using Wind Turbine Generator Control Loop Signals

M.N. Zaggout, P. J. Tavner, Li Ran
Energy group, Durham University
South Road, Durham, DH1 3LE, UK
E-mail: {m.n.zaggout,peter.Tavner,li.ran}@durham.ac.uk

Keywords: condition monitoring, DFIG wind turbine, generator control loops.

INTRODUCTION

In recent years renewable energy sources have grown throughout the world. Wind energy is growing to be the largest of these sources. Wind turbine technology has undergone rapid enhancements in the last three decades with increasing turbine sizes up to 7 MW. However, the wind turbines are also subjected to faults due to the turbulent operating conditions from the wind and weather, lowering their availability and raising the cost of energy. By condition monitoring, faults can be detected and corrected before failure bringing significant benefits from reduced downtime, increased capacity factor and availability.

RESEARCH METHOD

Conventional condition monitoring techniques require the deployment of a variety of costly sensors and computationally intensive analysis techniques. This research aims to develop condition monitoring techniques for a modern large wind turbine based upon observing the wind turbine generator's control loop, particularly in the offshore environment based on the concept that faults have a large impact on control loop signals, this impact depending on type and strength of the faults. These signals are available at no cost, requiring no new sensors, and can be used to detect wind turbine faults reliably. This research focuses on the generator control loop in a DFIG wind turbine. Firstly, determining which control loop signal is most likely to yield monitoring signals, which can determine the deterioration of condition. Secondly, simulation will be carried out of a real large wind turbine using Matlab. Representative faults will be applied and the effects on the control loop signals observed. Thirdly, A comprehensive model of the 30 kW Test Rig established in the school will be constructed in Matlab and Labview to monitor the wind turbine drive train. Then, develop the Test Rig to close loop and representative faults will be applied and observed. Finally, develop the real Test Rig into a closed loop and testing those theories experimentally.

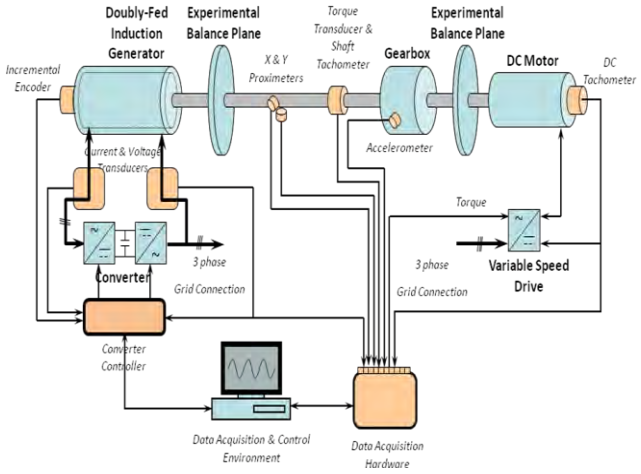

Figure 1: Future diagram of Test Rig with DFIG closed loop control

CONCLUSIONS

The presence of a DFIG fault has a notable effect inside the generator control loop signal. The type and strength of fault as well as the control strategies have been used lead to decide which signal inside the controller should be used for diagnostic purpose.

REFERENCES

[1] A. Bellini, F. Filippetti, G. Franceschini, and C. Tassoni, "Closed-Loop Control Impact on the Diagnosis of Induction Motors Faults", IEEE Transactions on Industry Applications, Vol. 36, No. 5, September/October 2000.

[2] A. Stefani, A. Yazidi, C. Rossi, F. Filippetti, D. Casadei, and G. A. Capolino, "Doubly Fed Induction Machines Diagnosis Based on Signature Analysis of Rotor Modulating Signals", IEEE Transactions on Industry Applications, Vol. 44, No. 6, November/December 2008.

[3] Bianchi, F, Battista, H. and Mantz, R. Wind Turbine Control System; Principles, Modelling and Gain Scheduling Design. Springer. 2007

Interaction of Offshore Wind Farms through Large Eddy Simulation

H. Sarlak, J. N. Sørensen, R. Mikkelsen
Fluid Mechanics Section, Technical University of Denmark
Bdg. 403, Nils Kppels Alle, 2800 Kgs. Lyngby, Denmark
E-mail: {hsar,jns,rm}@mek.dtu.dk

Keywords: offshore wind farms, LES, Heat Equation, ABL

Abstract

nteraction of wind farm turbulence and atmospheric flows based on large eddy simulation of Navier-Stokes equations is the aim of this project. Wind turbines are modeled as equivalent actuator disks. On each actuator disk, body forces (i:e:, aerodynamic loads) based on calculated angle of attack, are determined from tabulated aerodynamic lift and drag coefficients. The actuator disk technique is a very powerful method for this type of computations because resolving blade boundary layers can be prevented, and therefore it demands much less computational effort than direct simulation, while preserving the accuracy and resolution of simulations satisfactorily. Modifications of the current actuator disc is being done so that it can be controlled to operate more realistically in all kinds of operational conditions. The focus on ambient flow will be on modeling different atmospheric turbulence scenarios such as stable, thermally stratified and unstable boundary layers.

Introduction

Simulation of flow around wind turbines and in wind farms have been carried out recently (see[1]-[5]). The current project, however, aims at modeling large scale interactions between neighboring wind farms taking into account different atmospheric turbulence scenarios. This kind of simulation enables to predict the effect of wind farms in terms of velocity deficit and turbulent recovery length and may lead to an optimized placement of wind farms in high potential sites. fig 1 shows the very famous photo illustrating wake effects generated behind wind turbines in Danish offshore wind farm Horns Rev 1.

Figur 1: wake effects in Horns Rev 1 wind Farm. [Photographer Christian Steiness]

References

[1] N. Troldborg; M. Gaunaa; R. Mikkelsen, Actuator Disc Simulations of Influence of Wind Shear on Power Production of Wind Turbines, EWEA Proceedings, 271-297, 2010.

[2] S. Ivanell, J. N. Sørensen, R. Mikkelsen, D. Henningson, Analysis of Numerically Generated Wake Structures, Wind Energy, Volume 12, Issue 1, p63-80, 2009.

[3] N. Troldborg; J. N. Sørensen; R. Mikkelsen, Numerical simulations of wake characteristics of a wind turbine in uniform inflow, Wind Energy, vol: 13, issue: 1, 86-99, 2010.

[4] Y. Wu and F. Porte-Agel, Large-Eddy Simulation of Wind-Turbine Wakes: Evaluation of Turbine Parametrisations, Boundary-Layer Meteorology, V 138, No 3, 345-366, 2011.

[5] M. Calaf, C. Meneveau, and J. Meyers, Large eddy simulation study of fully developed wind-turbine array boundary layers, Phys. Fluids 22, 015110, 2010.

Prediction of wake effects on wind farm power production using a RANS approach. Offshore case studies from the UPWIND project

D. Cabezón[1], R. García[2], J. Sumner[2], A. Crespo[3]

[1]Wind Energy Department, National Renewable Energy Centre (CENER), Madrid (Spain)
e-mail: dcabezon@cener.com

[2]Department of Mechanical Engineering, École de Technologie Supérieure (ÉTS), Montreal (Canada) e-mail: rgarcia@cener.com; jonathon.sumner.1@ens.etsmtl.ca

[3]Departamento de Ingeniería Energética y Fluidomecánica, Escuela Técnica Superior de Ingenieros Industriales, Universidad Politécnica de Madrid (UPM), Madrid (Spain)
e-mail: antonio.crespo@upm.es

keywords: wake effects, actuator disk, CFD wind farm modeling, turbulence modeling

ABSTRACT

Clearly, the estimation of power losses due to wind turbine wakes is crucial to understanding overall wind farm economics. This is especially true for large offshore wind farms, as it represents the primary source of losses in available power. With respect to onshore installations, wake effects have relatively greater importance here given the regular arrangement of rotors, their generally larger diameter and the lower ambient turbulence level, all of which conspire to dramatically affect wake expansion and, consequently, the power deficit.

Simulation of wake effects in offshore wind farms (in reasonable computational time) is currently feasible using CFD tools. An elliptic CFD model based on the actuator disk method and various RANS turbulence closure schemes is tested through the open CFD solver OpenFoam 1.7.1 and validated using power ratios extracted from Horns Rev and Nysted wind farms, collected as part of the EU-funded UPWIND project [3].

The primary focus of the present work is on turbulence modeling, as turbulent mixing is the main mechanism for flow recovery inside wind farms. Higher-order approaches, including an anisotropic RSM model [6], are tested to better take into account the imbalance in the length scales inside and outside of the wake, this not being well reproduced by current two-equation closure schemes.

A second focus involves the method by which the reference wind speed is determined, as this has been shown to have an impact on predicted power deficits [7].

This approach represents the starting point for future releases based on numerical parabolization techniques together with more advanced turbulence models feasible at offshore sites, without affection of streamwise wind speed gradients produced by the ground.

REFERENCES

[1] Vermeer L.J. et. al., 2003, "Wind turbine wake aerodynamics". Prog. Aerosp. Sci. 39, 467-510

[2] Crespo A., Hernández J., Frandsen S., "A survey of modelling methods for wind-turbine wakes and wind farms", Wind Energy 2 (1999) 1–24.

[3] Barthelmie, R.J., Frandsen, S.T., Rathmann, O., Politis, E., Prospathopoulos, J., Rados, K., Hansen K., Cabezón D., Schlez W., Phillips, J., Neubert, A., van der Pijl, S. and Schepers, G., “Flow and wakes in large wind farms in complex terrain and offshore”. European Wind Energy Conference, Brussels, March 2008 (Scientific track)

[4] Réthoré P., Sørensen N., Zahle F., Bechmann A., "Study of the wake turbulence of a CFD actuator disk model compared with a full rotor CFD model", Proceedings of the European Wind Energy Conference 2009, Marseille (France)

[5] Cabezón D., Sanz J., Martí I., Crespo A., "CFD modelling of the interaction between the Surface Boundary Layer and rotor wake. Comparison of results obtained with different turbulence models and mesh strategies". European Wind Energy Conference and Exhibition 2009, Marseille, March 2009.

[6] Gibson M.M. and Launder B. E. “Ground Effects on Pressure Fluctuations in the Atmospheric Boundary Layer” J. Fluid Mech., 86:491–511, 1978

[7] Prospathopoulos J., Cabezón D., Politis E.S., Chaviaropoulos P.,K., Rados K.,G., Schepers J.,G., Hansen K., Barthelmie R.J., Simulation of wind farms in flat and complex terrain using CFD, Proc. of ‘The Science of Making Torque form Wind’ Conference, Athens (Greece), June 2010

Comparison between Actuator Disc and BEM models for a floating wind turbine rotor in periodic surge motion

J.B. de Vaal, M.O.L. Hansen, T. Moan
Centre for Ships and Ocean Structures, Norwegian University of Science and Technology
Trondheim, Norway
E-mail: jacobus.b.de.vaal@ntnu.no, molh@mek.dtu.dk, torgeir.moan@ntnu.no

Keywords: Floating offshore wind turbine, blade element momentum theory, actuator disc theory, induced velocity.

ABSTRACT

This paper aims to investigate the best practice for aerodynamic modelling of a floating wind turbine (FWT) rotor in periodic surge motion using the blade element momentum (BEM) theory. Comparisons are made between simulations using different BEM implementations and an actuator disc (AD) model.

In the codes that are typically used to verify the stability of the wind turbine structure and its ability to withstand environmental loads (e.g. Bladed [1], HAWC2 [5] or FLEX [9]), the aerodynamics is based on the so called BEM method [2], further improved by including various engineering models [6, 7, 8]. In its most basic form, the BEM model calculates induced velocity as a ratio of the thrust to two times the mass flow through the rotor. An interesting question arises when the wind turbine is oscillating in and out of the wind – as is the case in a periodic surge motion of an offshore FWT. The blades will experience the surge velocity as an apparent wind, increasing/decreasing the relative velocity when the rotor is moving up-/downstream of the free wind. When evaluating the lift and drag forces that yield the rotor thrust, this structural velocity must be considered. Also, if the wind turbine is moving up-/downstream with a constant velocity, the structural velocity must be considered when estimating the mass flow through the rotor. For an oscillating surge movement, however, the structural velocity component integrated over an oscillation period is zero so that the mean mass flow is determined only from the free wind speed and the induced velocity. Here it is not obvious whether the movement of the structure should be included when calculating the mass flow through the rotor.

To investigate this question, for different surge frequencies and amplitudes, a so called AD model was implemented in FLUENT. Since FLUENT solves the Navier-Stokes equations directly, the results naturally include the dynamic reaction of the incoming wind to the changes in rotor loading and can therefore be compared to the BEM method to answer the question of how to model the mass flow correctly. The model for the investigation is an NREL 5-MW reference wind turbine [3] mounted on a catenary moored spar-buoy type floating platform on which extensive dynamic modelling has been done previously and for which time series data of nacelle surge motion under realistic operating conditions are available [4].

REFERENCES

[1] GHBladed, http://www.http://gl-garradhassan.com/en/GHBladed.php.

[2] H. Glauert, Airplane Propellers, Aerodynamic Theory, W. F. Durand, ed., 1963.

[3] J.M. Jonkman, S. Butterfield, W. Musial and G. Scott, Definition of a 5-MW Reference Wind Turbine for Offshore System Development, TP-500-3806, NREL, February 2009.

[4] M. Karimirad and T. Moan. Wave and wind induced dynamic response of a spar-type offshore wind turbine. *Journal of Waterway, Port, Coastal, and Ocean Engineering*, 1(1):55, 2011.

[5] T.J. Larsen and A.M. Hansen. How 2 hawc2, the user's manual. Risø-R-1597 (ver. 3-1)(EN), Risø, 2007.

[6] J.G. Schepers, H. Snel, G.J.W. van Bussel, et al. Dynamic inflow: yawed conditions and partial span pitch control. ECN-C--95-056, ECN, Petten, October 1995.

[7] H. Snel and J.G. Schepers. Joint investigation of dynamic inflow effects and implementation of an engineering method. ECN-C-94-107, ECN, Petten, 1995.

[8] S. Øye. Dynamic stall-simulated as time lag of separation. In *Proceedings of the 4th IEA Symposium on the aerodynamics of wind turbines*, 1991.

[9] S. Øye. Flex4 simulation of wind turbine dynamics. In *Proc. 28th Meeting of Experts, International Energy Agency, Annex XI*, pages 71–77, 1996.

Experimental investigation of 3D separation on an airfoil

Marinos Manolesos, Spyridon Voutsinas
Laboratory of Aerodynamics, National Technical University of Athens
9 Heroon Polytechneiou str., GR15780 Athens, Greece
E-mail: marinos@fluid.mech.ntua.gr

Keywords: stall cells, tuft flow visualization.

INTRODUCTION

The final aim of our research is to experimentally study the flow behind solid vortex generators (VG) on an airfoil optimized for pitch-regulated wind turbines. During the study of the baseline flow, i.e. airfoil without VGs, unsteady three dimensional vortical structures of separated flow known as stall cells (SCs) were observed after a certain angle of attack (α) depending on the Reynolds (Re) number.

The airfoil used in the experiments is an 18% thickness airfoil experiencing trailing edge separation. Airfoils of this type have been reported to give rise to SC in the past [1]. The number of cells for a specific wing appears to decrease as the wing aspect ratio (AR) decreases [2], but no research has been published for AR less than two. Contrasting reports appear with regards to the effect of α, see [3], [4]. The present paper reports on the initial findings of this campaign as well as the future steps to be taken.

EXPERIMENTAL SET UP

All experiments were carried out at the National Technical University of Athens wind tunnel. The tunnel is of the closed-return type and the turbulence intensity in the test section is 0.2%. The wing model had a chord of 0.6m and spanned the test section vertically, a distance of 1.4m. The width of the test section was 1.8m, so that this model orientation minimized the blockage. The suction side of the model was fitted with No.60 threads in a staggered manner.

To minimize the wind tunnel boundary layer effect and at the same time control the aspect ratio we used two fences which could move along the model span, see Figure 1. The test matrix included tripped and untripped flow cases for Re numbers from 0.5×10^6 to 1.5×10^6 and AR 1.5 and 2.0. To trip the flow we used 0.4mm thick zig-zag tape with 60deg angle.

RESULTS

It was found that the SCs that appeared on the suction side of the wing were not only dynamic but also, on occasions, highly unstable. The flow was forced to select one of the stable modes by tripping the boundary layer over a small amount of its span. This resulted in the creation of a single stable SC, the geometrical characteristics of which were studied. The campaign will continue with the Stereo-PIV measurement of both the baseline flow and the VG flow. Finally it will be attempted to computationally reproduce the experimental results using an in-house RANS code.

CONCLUSIONS

By locally tripping the flow it was made possible to force the creation of a single stabilized SC. The effects of Re number and AR on this coherent stable structure were studied and some qualitative findings are presented.

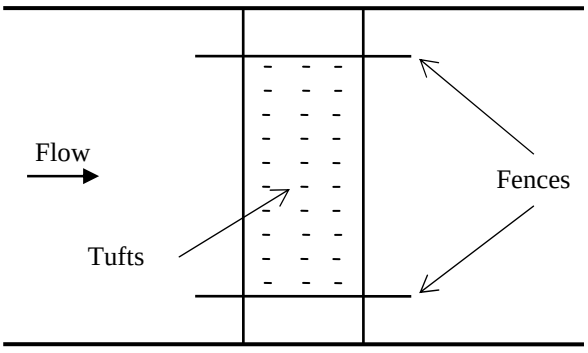

Figure 1: Side view of the test set up.

REFERENCES

[1] Broeren, A., & Bragg, M. (2001). Spanwise Variation in the Unsteady Stalling Flowfields of Two-Dimensional Airfoil Models. *AIAA Journal, Vol. 39, No. 9* , 1641-1651

[2] Yon, S. A., & Katz, J. (1998). Study of the Unsteady Flow Features on a Stalled Wing. *AIAA Journal vol.36 no.3* , 305-312

[3] Winkelman, A. E., & Barlow, J. B. (1980). Flowfield Model for a Rectangular Planform Wing beyond Stall. *AIAA Journal vol.18 no.8* , 1006-1008

[4] Gregory, N., Quincey, V. G., O'Reilly, C. L., & Hall, D. J. (1971). *Progress Report on Observations of Three-Dimensional Flow Patterns obtained during Stall Development on Aerofoils.* London: A.R.C.C.P. No. 1146

Characterization of a model wind turbine

Francesco Cuzzola
Enviromental Wind Tunnel Laboratory, University of Hamburg
Bundesstr. 55 D-20146 Hamburg, Germany
E-mail: francesco.cuzzola@zmaw.de

Keywords: wind tunnel, wind turbine, wake, velocity, LDA

Within the scope of the FP7 funded European project WAUDIT a model wind turbine is being developed at the University of Hamburg to investigate wake behavor in a physically modelled atmospheric boundary layer flow.

The turbine model is a three-bladed rotor. The blades have been designed using a self developed code based on the Blade Element Momentum theory. The airfoil used is the Jedelsky EJ85 airfoil, which is commonly used in the model airplane community due to its performances at low Reynolds number. The model is equipped with a Faulhaber DC motor 3268 G024 BX4 which allows the rotational velocity to be controlled.

Before starting the experimental campaign in the boundary layer wind tunnel, a full characterization of the model is required. This paper focuses on this characterization which consists of measuring the velocity profile, using Laser Doppler Anemometry, in the near wake for several operative conditions. These measurements allow for a comparison of the turbine performance as well as the effects of dimensionless parameters on the behaviour of the wake. The aim of this paper is to deliver guidelines on how to operate a model wind turbine in the wind tunnel.

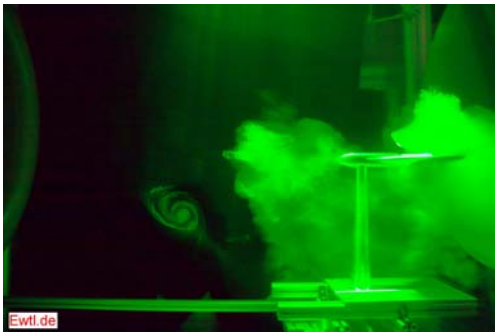

Figure 1: Tip Vortex visualization

REFERENCES

[1] L.J. Vermeer, J.N. Soerensen and A. Crespo. Wind Turbine Wake Aerodynamics. Prog. In Aerospace Sciences, 39:467-510, 2003.

[2] S. Aubrun. Modelling wind turbine wakes with porosity concept. Proceedings of the Euromech colloquium 464b. Wind Energy pp 265-270. J Peinke, P. Schaumann, S. Barth (eds), 2005.

[3] D.E. Neff, R.N. Meroney, E. McCarthy,E. Davis. Upstream and lateral wake effects on wind turbine performances. Journal of Wind Engineering and Industrial Aerodynamics 36, pp 1405-1414, 1990.

[4] G.P. Corten, P. Schaak, T. Hegberg. Turbine interactions in large offshore wind farms - wind tunnel measurements.ECN report ECN-C-04-048, 2004.

Modeling forest canopy flow dynamic phenomena, informing steady computational fluid dynamic models with unsteady measurements or/and unsteady computational fluid dynamic models.

Ilda Albuquerque, Javier Sanz, Lars Landberg, Simon Watson
WAUDIT – PORTUGAL, CENER – SPAIN, Garrad Hassan – DENMARK, CREST - UK
E-mail: {elimd@lboro.ac.uk, jsrodrigo@cener.com, Lars.Landberg@gl-garradhassan.com, S.J.Watson@lboro.ac.uk}

Keywords: Canopy, Computational Fluid Dynamics, Forest

INTRODUCTION

Modeling of wind flow within forest canopies had been done in more or less complex ways, ranging for a deep physical insight to a bulk description of the flow behavior; nevertheless, models have been mainly empirical. These flows are characterized by highly unsteady phenomena from which the most relevant are the canopy size coherent structures originated in the roughness layer.

SECTION 1

As the forested area represents a semi-obstacle to the flow allowing part of the flow to entrain within the forest, the streamwise velocity profile has an inflexion point near the canopy top. A shear layer develops in the upper region of the forest [1] connecting a relative high mean velocity region in which the more energetic wake processes occur, with the slower bleed flow at the lower levels. Raupach [2] established a parallel between canopy flow and the plane mixing flow, in which a plate with finite length separates two streams with different velocities. Downstream of the plate the two streams interact which originates vortical coherent structures. In [3], it is reported a preference for sweeps ($u>0$, $w<0$) below $z/h_c = 1.25$, and for ejections ($u<0$, $w>0$) at higher elevations, being h_c the forest's height. He also verified using Particle Image Velocimetry (PIV) measurements and conditional sampling based on signs of velocity fluctuations, that during sweeps the downward flow generates a narrow, highly turbulent shear layer containing multiple small-scale vortices just below canopy height. This provokes narrow peaks just below canopy height in the turbulent kinetic energy, Reynolds stresses, production and dissipation rates. During ejections, the upward flow expands this shear layer and the associated small-scales flow structures to a broad region located above the canopy. In the other hand sweep events, correspond to high dissipation rate values. At middle and low canopy heights, the mean wind velocity is relatively small, and there are frequent periods of calm or very low wind intensities. Intermittent large eddies produce the so-called inactive motion, gusts on scales bigger than h_c increasing variances in the u and v directions but not in the vertical direction. In fact forest represents both a turbulence enhanced medium as a dissipation one, the latter case for the larger scales, as eddies are separated into smaller ones and dissipate quicker. This phenomenon is visible in the canopy spectrum and it is denominated as spectral short cut of the turbulent energy cascade.

CONCLUSIONS

Based in measurement campaigns corroborated by LES simulations it becomes evident that turbulence levels within and above canopies are not produces locally, being transported by phenomena as the ones described above. It is purposed the study of the spatial variation of the turbulence levels within and above forest canopies using techniques such as two-point spatial correlation, conditional sampling of data, quadrant analysis amount others applied to time resolved data. Allowing information from time resolved phenomena to be incorporated into forests' steady state computational fluid dynamic models.

REFERENCES

[1] Boldes, U., et al (2003) Characteristics of some organized structures in the turbulent wind above and within a spruce forest from field measurements. Journal of Wind Engineering and Industrial Aerodynamics, 91(10), 1253-1269.

[2] Coutts M. P. & Grace J. Eds. (1995). Wind and Trees. Cambridge University Press, Cambridge

[3] Zhu, W. H., et al (2007). On the flow structure and turbulence during sweep and ejection events in a wind tunnel model canopy. Boundary-Layer Meteorology, 124(2), 205-233.

Validation of a Vector Auto-regressive Model for Wind Modelling and Synthesis of the UK Wind Field

C. Plumley, D. Hill, D. McMillan, K. Bell, D. Infield
Wind Energy Systems Doctoral Training Centre, University of Strathclyde
Glasgow, UK
E-mail: charles.plumley@strath.ac.uk

Keywords: vector auto-regressive model; validation of wind simulation; time series modelling; integration of wind

INTRODUCTION

As wind penetration increases in the UK important decisions need to be made regarding investment in energy infrastructure. To create a scientific foundation for these decisions, an understanding of the underlying statistical nature of the UK wind resource is required. To this end a vector auto-regressive (VAR) model is being developed.

MOTIVATION

When looking at the integration of wind energy into the electricity network certain characteristics of the wind resource are of particular importance: the long-term wind distribution helps predict typical power flows and output; the occurrences of calm periods and the duration of these calms, as well as the times of high wind penetration, aid analyses of maximum power flows on the transmission network; and the variability of the wind resource, especially at look-ahead times of up to 48 hours, allow decisions to be made about dispatch and day ahead scheduling of generation. For a model of the UK wind field to be of use, it is important to understand how well the model describes these phenomena. A previous analysis conducted by Sturt & Strbac of a univariate auto-regressive model is used as a source for this study and results from it can be used for comparisons [1].

MODEL DESCRIPTION

The VAR model being developed is a second order multivariate auto-regressive model. It takes account of the correlation between sites and, through a method of de-trending, also the annual and diurnal (24 hour) variations. The diurnal variations are also a function of the season. [2]

VALIDATION OF VAR MODEL

Calibration

Initially 14 sites spread across the UK were selected and a 2 year data set used to calibrate the model. The synthesised data was then compared to the original historical data to assess the accuracy of the model.

Wind speed distributions

The probability distributions of hourly wind speeds were calculated and plotted. An initial analysis shows that the model under estimates extreme wind speeds. The shapes of the distributions differ, with the synthesised data having a closer to normal distribution compared to the Weibull distribution of the historical wind data.

Occurrences of calm periods

The occurrences of calm periods, where the wind speed was below 4m/s, were recorded along with the duration of these calms. The distribution of the duration of the calms is correct; however the number of calm periods is under predicted in the model.

Variability

The variability is a measure of the rate of change of wind speed. This was accurate on short time scales up to about 4 hours ahead, which is useful as the start-up time of a Combined Cycle Gas Turbine is approximately 4 hours, but the variability is underestimated by the model on longer time scales.

CONCLUSIONS

The VAR model creates data similar to the historical data and key characteristics are present. The analysis conducted shows the limitations of the model so that it can be used with confidence and further work can be conducted to optimise it. The VAR model could then be used to guide decisions regarding investment in energy infrastructure.

REFERENCES

[1] A.Sturt and G. Strbac; “Time-series modelling of power output for large-scale wind fleets,” Wind Energ. DOI 10.1002/we.459

[2] D. Hill, D. McMillan, K. Bell, D. Infield, G. W. Ault; “Application of Statistical Wind Models for System Impacts,” Universities’ Power Engineering Conference, 2009

The wind field in the marine boundary layer

Olav Krogsæter[*,**], Gard Hauge[*], Joachim Reuder[**],
[*]StormGeo, Nordre Nøstekaien 1, 5011 Bergen, Norway.
[**]University of Bergen, Geofysisk Institutt, Allé gaten 70, 5020 Bergen, Norway
E-mail: {olav.krogsaeter, gard.hauge}@stormgeo.com, Joachim.Reuder@gfi.uib.no

Keywords: Marine Boundary Layer (MBL), wind field, turbulence, waves, Weather Research and Forecasting Model (WRF), German research platform FINO1.

INTRODUCTION

Here we will show some results on important atmospheric parameters connected to offshore wind energy in the MBL. To perform these sensitivity tests we have run the WRF-model [1] for a whole year with five different Planetary Boundary Layer (PBL) schemes. The results are primarily compared with observations from the German research platform FINO1 [2] in Southern North Sea. From this platform there exists meteorological observations for every 10th meter from 30 m to 100 m above sea level.

RESULTS

The main task in this work is to study the behaviour of the different PBL schemes in WRF over pure offshore conditions. WRF3.2.1 has eight different PBL schemes to choose among. We have tested five of the most relevant ones. Two of them are so-called non-local closure schemes (YSU [3] and ACM2 [4]), while the others are local closure schemes (MYJ [5] , MYNN2 [6] , and QNSE [7]).

QQ-plots

A QQ-plot is a plot of the quantiles of two datasets against each other, and is an easy way to get an overall view of the model performance. The PBL-schemes give quite different results. In the QQ-plot for January-05, the YSU scheme comes up with rather large deviations from the measurements, while both the ACM2 and MYJ have a much better behaviour. The YSU scheme is clearly overestimating the wind speed. We get similar results when looking at the QQ-plots for the whole year.

Objective hit Score, OhitS

A new method is developed called Objective hit Score, OhitS, which is a method for statistically comparing several model runs with point observations. The OhitS method uses the median, mean error (bias), mean absolute error, standard deviation, and 1st and 3rd quantile to the model variables and observations. The method show that the MYJ and MYNN2 schemes have the highest score, while the YSU scheme clearly has the lowest score.

CONCLUSIONS

Already at an early stage of this study we see that the PBL schemes gives rather different results regarding wind speed. More detailed studies on the PBL-parametrization schemes, drag coefficient, turbulence, atmospheric stability, wind shear, and how ocean waves influences the wind field will be carried out. In a short time we will also have a coupled atmosphere-wave modelling system up and go (WRF-SWAN), and it will be very interesting to see how that will influence the mean wind and turbulence in the MBL compared with the stand alone atmospheric WRF model.

REFERENCES

[1] W.C. Skamarock, J.B. Klemp, J. Dudhia, D.O. Gill, D.M. Barker, W. Wang, J.G. Powers. A Description of the Advanced Research WRF Version 2. NCAR Technical Note, 2005.

[2] T. Neumann, K. Nolopp, K. Herklotz. First operating experience with the FINO1 research platform in the North Sea. DEWI Magazin, 24, 2004.

[3] S-Y. Hong, Y. Noh, J. Dudhia. A New Vertical Diffusion Package with an Explicit Treatment of Entrainment Processes. Monthly Weather Review, 134:2318-2341, 2006.

[4] J.E. Pleim. A Combined Local and Nonlocal Closure Model for the Atmospheric Boundary Layer. Part I: Model Description and Testing. Jour. of Appl. Meteorology and Climatology, 46:1383-1395, 2007.

[5] Z.I. Janjić. Nonsingular Implementation of the Mellor-Yamada Level 2.5 Scheme in the NCEP Meso model. National Centers for Environmental Prediction. Office Note 437,2001.

[6] M. Nakanishi, H. Niino. An improved Mellor-Yamada level-3 Model: Its numerical stability and application to a regional prediction of advection fog. Boundary-Layer Meteorology, 119:397-407, 2006.

[7] S. Sukoriansky, B. Galperin, V. Perov. Application of a new spectral theory of stably stratified turbulence to the atmospheric boundary layer over sea ice. Boundary-Layer meteorology, 117:231-257, 2005.

Turbulence Modelling of Flow around a Single Tree

Mr. Cian Desmond, Prof. Simon Watson
CREST, Loughborough University
Leicestershire, UK LE11 3TU
E-mail: {c.desmond,s.j.watson}@lboro.ac.uk

Keywords: CFD, CFX, SST, k-ɛpsilon, wind tunnel

INTRODUCTION

In a previous paper [1], CFD simulations of mean horizontal flow in the wake of a series of single trees were validated against wind tunnel experiments. This paper will extend the analysis to include turbulence intensity data and thus provide a more rigorous examination of the numerical simulation of forest canopy flows.

WIND TUNNEL DATA

An open-return, nominally closed jet wind tunnel with the dimensions 2 m wide x 1.5 m high x 20 m long was used for the experiments. An atmospheric boundary layer was simulated with a turbulence grid and castellated wall at the inlet and a series of roughness elements on the tunnel floor.

5 No. architectural model trees of varying porosity and height (*Hc)* of approx 175 mm were place individually in the tunnel. These models are composed of etched brass and wire with rough ground silicon to simulate foliage, were sourced from the 4D Modelshop Ltd. (London, UK) and are realistic in both appearance and texture.

Velocity measurements were taken in the wake of the model trees by means of a rack of 100 No. pitot tubes. The arrangement of the tubes and a view down the tunnel are shown in Figure 1. The rack was placed at distances *Hc* to *9 Hc* behind the specimen perpendicular to the mean flow. Thus a total of 900 measurements were taken in the wake of each model tree.

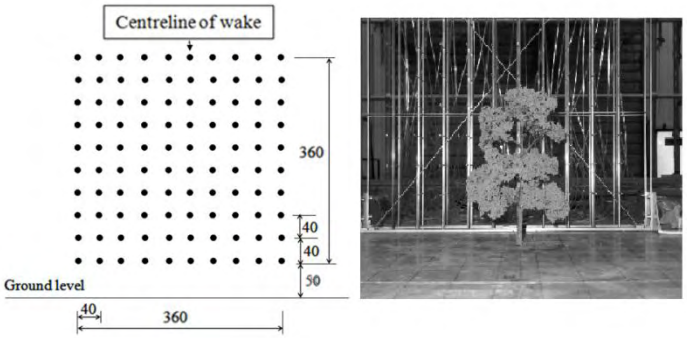

Figure 1: Schematic of pitot rack and view downwind.

The mean and standard deviation of the horizontal pressure at each point was recorded thus allowing mean velocity and turbulence intensity (TI) to be calculated.

CFD SIMULATION

The commercially available CFD software ANSYS CFX 12.1 was used for this study. This software is a generalised fluid dynamics solver and thus requires modifications in order to simulate flows within the atmospheric boundary layer.

Modifications are also required to include the effect of the canopy by the inclusion of source and sink terms [2]. The equations for these terms require an understanding of the canopy structure which was acquired by use of the Tree Analyser [3] photographic analysis software.

A steady state solution was produced by the CFX software and the resulting turbulent kinetic energy, k, at each measurement point examined to provide a value for TI.

CONCLUSIONS

Conclusions will be drawn from analysis of the data and will aim to answer the following questions:

- It was found in [1] that increasing the level of canopy detail in the CFD significantly improves simulation of mean horizontal velocity. Does the simulation of TI follow this trend?
- It was found in [4] that the SST turbulence model out performs k-epsilon in simulating horizontal mean velocity. Is this also true for TI?

REFERENCES

[1] C. Desmond and S. Watson. Wind Flow Around a Single Tree. Proceedings of ICWE 13.
[2] A. Sogachev. A Note on Two-equation Closure Models of Canopy Flow. Boundary-Layer Meterol, 130:423-435, 2009.
[3] J. Phattaralerphong and H. Sinoquet. A Method for 3D Reconstruction of tree crown volume from photographs. Tree Physiology, 25,:1229-1242, 2005.
[4] S. Wylie and S. Watson. A CFD Study of Wind Flow around a Model Forest. Proceedings of EWEA 2011.

Implementation and calibration for atmospheric turbulence of an EARS model

T.Ternisien, J.Prospathopoulos,P.K.Chaviaropoulos
Wind Department of CRES (Center for Renewable Energy Sources)
19th km Marathonos Ave, 19009, Pikermi, Attiki,Greece
E-mail: {ternisien@cres.gr, jprosp@cres.gr, tchaviar@cres.gr}

Keywords: CFD, Turbulence modeling, Anisotropy, Complex Terrains, WT Wakes

1 Introduction

As all turbulent closure models based on the Boussinesq approximation, the k-ω one cannot account for the anisotropic part of the Reynolds stress tensor and, thus, cannot properly split the turbulent kinetic energy to its diagonal components. The objective of the proposed work is, therefore, to implement and calibrate an atmospheric Explicit Algebraic Reynolds Stress Model (EARSM) building upon a k-ω model.

2 Defaults of two-equation models

Linear two-equation models present certain weaknesses when modeling of complex atmospheric flows, like wind turbine wakes, is attempted [1]. For better estimations of the turbulence, more realistic models are necessary. However, to be of practical interest, computational cost must be kept reasonable. According to a hierarchy of turbulent models proposed by Gatski and Jongen [2], the EARS model is considered as a good compromise between complexity and realism.

3 Implementation of an EARSM in a two-equation model

In an Explicit ARSM, the anisotropy tensor a_{ij} is represented as a polynomial of the mean strain rate tensor S_{ij} and the vorticity rate tensor Ω_{ij} [3]. Due to its non-linearity, a_{ij} is split into linear and non-linear parts. The linear part is embedded directly in the two-equation by the introduction of an effective eddy viscosity [4]. The non-linear part accounts for extra-forces in the momentum equation and extra-sources of production into the turbulent scales (k and ω or ε) equations [5].

4 Calibration

Because most of the EARSM models have been calibrated for a variety of engineering flows, when applied to the atmospheric boundary layer, the coefficients of the model need to be readjusted. These readjustments should be consistent with the logarithmic layer relations and the values of the anisotropy of the Reynolds stress tensor obtained experimentally for atmospheric flows. Calibration of the coefficients for atmospheric flows is done using the ratios of the standard deviations of wind velocity in the three directions, given by the standards on wind turbine design [6].

$$\frac{\sigma_z}{\sigma_x} = \sqrt{\frac{R_{33}}{R_{11}}} = 0.5, \quad \frac{\sigma_y}{\sigma_x} = \sqrt{\frac{R_{22}}{R_{11}}} = 0.8 \tag{1}$$

5 Some Prelimary Results and Conclusions

An EARSM based on the model of Jones and Musonge [7] has been calibrated for atmospheric flows and implemented on the existing k- model of the CRES-FlowNS code. A first test case in flat terrain shows a good agreement between the newly implemented model and the k-ω model, with results differing by 0.1%. The components of the anisotropy tensor are found to be correct and constant in flat terrain. When a slightly more complex terrain (a Gaussian hill), is simulated, significant differences appear in the profiles of the turbulent kinetic energy k (around 15 %) due to an increased impact of the secondary flows. Numerical and qualitative studies of the 2D version of the code are in progress.

References

[1] Réthoré, P.E.M. Wind Turbine Wake in Atmospheric Turbulence. PhD Thesis Technical University of Denmark, Risø , Wind Energy Division, 2009.

[2] Gatski, T.B, Jongen, T. Nonlinear eddy viscosity and algebraic stress models for solving complex turbulent flows. Progress in Aerospace Sciences, 36(8):655-682, 2000.

[3] Hellsten, A., New two-equation turbulence model for aerodynamics applications. PhD thesis, Helsinki University of Technology, Laboratory of Aerodynamics. 2004.

[4] Wallin, S. Engineering turbulence modelling for CFD with a focus on explicit algebraic Reynolds stress models. KTH Doctoral thesis, 2000.

[5] Wilcox, D.C, Turbulence modeling for CFD. DCW Industries, Inc. La Caada,California, 1998.

[6] International Standard IEC 61400-1, , Wind Turines - Part 1:Design requirements., 3rd edition, 2005-2008

[7] Jones, W.P., Musonge, P., Closure of the Reynolds stress and scalar flux equations, Physics of Fluids, 31:3589-3603,1988.

WRF mesoscale modelling and measurements of the diabatic offshore wind profile at FINO1

D. Muñoz-Esparza[1,*], B. Cañadillas[2], J. van Beeck[1]
[1]Environmental and Applied Fluid Dynamics, von Karman Institute for Fluid Dynamics
Chaussée de Waterloo 72, B-1640 Rhode-St-Genèse, Belgium
[2]Deutsches Windenergie-Institut GmbH
Ebertstrasse 96, D-26382 Wilhelmshaven, Germany
[*]E-mail: domingo.munoz.esparza@vki.ac.be

Keywords: WRF model, FINO1 offshore platform, PBL parameterization, Marine Boundary Layer, stability, wind profile.

ABSTRACT

Numerical Weather Prediction (NWP) models are currently employed as an operational tool by the wind energy community. They are used, among others, to perform dynamic downscaling of wind conditions over a limited area where the wind resource needs to be evaluated. One limitation of such models arises from the representation of microscale processes on a coarse grid, normally on the order of kilometers. For wind energy applications, the structure of the wind profile is an essential aspect and it is strongly related to the ability of the model to reproduce the turbulent fluxes on the lower part of the Boundary Layer. Moreover, the atmospheric stability plays a major role on the vertical fluxes and thus on the distribution of the wind profile.

The importance of the turbulent flux parameterization has been pointed out previously by the authors [1, 2]. In the present study, the ability of different turbulent flux parameterizations in WRF is thoroughly evaluated at FINO1 offshore research platform. Firstly, we developed a comprehensive database of field measurements at FINO1 for validation. Different types of measurements were combined to accomplish this objective. Turbulent fluxes and surface stability related parameters, as friction velocity and Obukhov length, are calculated with sonic anemometers. Together with cup anemometrs, LiDAR wind profiling and other standard meteorological sensors (temperature, humidity, . . .), a complete representation of the Marine Boundary Layer (MBL) is given. Then, different stability scenarios based on the previously generated FINO1 database were selected.

We tested different WRF-PBL schemes for the turbulent flux parameterization. The horizontal grid spacing in the modeled area was refined through three nested domains reaching a high resolution of 1km at the most inner one. In this study we compared two first order closure schemes: Yonsey University and Asymetric Convective Model v2, and four one-and-a-half order (or TKE closure schemes): Mellor-Yamada-Janic, Mellor-Yamada- Nakanishi-Niino, Quasi-normal Scale Elimination and Bougeault-Lacarrre. The analysis is focused on how the vertical momentum eddy diffusivity affects the turbulent flux and the shear of the wind profile under different atmospheric stability conditions, as well as the surface representation of offshore conditions. We took advantage of the recent LiDAR measurement campaign carried out at FINO1 to validate our conclusions up to 250 m height, encompassing the rotor swept area of the tallest wind turbines.

REFERENCES

[1] D. Muñoz-Esparza, J. van Beeck, B. Cañadillas. Impact of turbulence modeling on the performance of WRF model for offshore short-term wind energy applications. 13th International Conference on Wind Engineering. Amsterdam, The Netherlands, July 2011.

[2] D. Muñoz-Esparza, B. Cañadillas, J. van Beeck, T. Neumann. Turbulent flux parameterizations in WRF mesoscale model with a focus on wind energy purposes: stability dependence and its influence on the Marine Boundary Layer structure. 11th EMS Annual Meeting / 10th European Conference on Applications of Meteorology. Berlin, Germany, September 2011.

Axial Capacity of Grouted Joints for Offshore Wind Energy Converters regarding Interlocking Effects

Peter Schaumann, Anne Bechtel (speaker),
ForWind - Center for Wind Energy Research,
Leibniz University Hannover, Institute for Steel Construction,
Appelstr. 9A, 30167 Hannover, Germany
E-mail: bechtel@stahl.uni-hannover.de

Keywords: offshore wind energy, grouted connection, axial capacity, shear key, interlocking effect

Introduction

Grouted joints are used for Offshore Wind Energy Converters to connect the substructure to the foundation. In jacket substructures this hybrid pile-sleeve connection is primarily exposed to alternating axial loads. The legs of the jacket are placed inside the foundation pile and the annulus between inner and outer pile is filled with high-performance grout (see Figure 1).

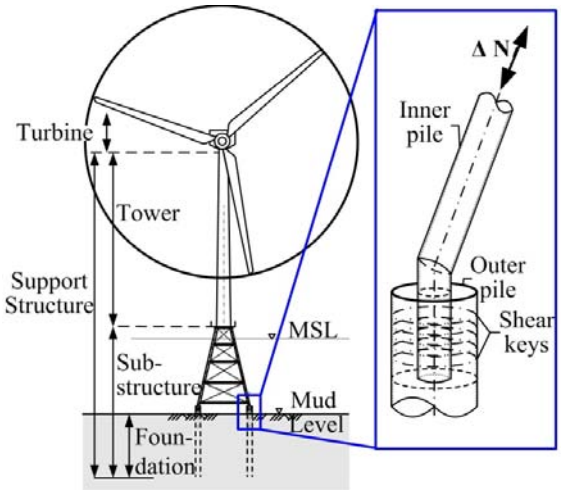

Figure 1: Jacket substructure with close-up of axially loaded grouted connection.

Structural Behaviour of Grouted Connections

The axial loads in the grouted connections are transferred by shear and friction forces between the surfaces of grout and steel. The load capacity can be increased by installing additional mechanical interlocks as weld beads in circumferential direction [1]. These so-called shear keys are adjusted on the facing surfaces of the overlapping steel sections within grouted joints. Due to valid offshore standards as EN ISO 19902 [2] shear keys are to be arranged with a certain distance between opposed welds. Consequently arising diagonal compression struts transfer predominantly occurring loads within grouted joints with shear keys. The load capacity due to interlocking can be effected by geometrical dimension and installation imperfections or early age cycling. Therefore investigations focus on the influence of interlocking to the axial load capacity of grouted connections.

Investigations concerning Interlocking Effects

Regarding geometrical dimensions as the shear key width to height ratio (w/h) and the shear key height to distance ratio (h/s) the influence within the ultimate and fatigue limit state is investigated. Numerical simulations are conducted showing arising stress concentrations at the shear keys provoking significantly affected fatigue behaviour. Besides, different installation positions are modelled to analyse the effect of occurring compression strut inclinations to the axial load capacity. The effect of early age cycling will be taken into account. Numerical simulations are benchmarked on large-scale tests of grouted connections conducted at the Institute for Steel Construction of the Leibniz University Hannover.

Conclusions

The position of the jacket leg influences arising compression struts especially the inclination angle leading to a reduced load capacity. Arising stress concentrations depict a notch effect regarding the steel tubes and therefore influence the fatigue behaviour.
Beside the investigations focussing on the interlocking an outlook on future challenges regarding the axial load capacity of grouted connections connecting jacket substructure to the foundation will be given which will be dealt with in a new research project.

References

[1] Schaumann, P., Bechtel, A., Lochte-Holtgreven, S.. Fatigue Performance of Grouted Joints for Offshore Wind Energy Converters in deeper waters, Proceedings of the Twentieth ISOPE, Bejing, China, 2010.

[2] EN ISO 19902, “Petroleum and natural gas industries - Fixed steel offshore structures,” CEN - European Committee for Standardization, Brussels, Belgium, 2007.

Tensile and Fatigue Properties of Carbon Fabric T-joints as a Structural Element of Wind Turbine Blade

Amirhossein Hajdaei, Paul Hogg
Northwest Composite Centre, University of Manchester
Paper science building, Sackville street, Manchesterm M13 9PL, UK
E-mail: amir.hajdaei@manchester.ac.uk

Keywords: Fatigue, Tensile, Wind Turbine, T-Joint

INTRODUCTION

Wind turbines are recognized as classic examples of structures where the operating lifetime of the structure is controlled by the fatigue properties of the materials. This is exacerbated by the 2D nature of the composite materials forms used in blade construction which are typically fabrics in a variety of formats (e.g. NCF, uniweave, woven). The formation on internal detailed shapes within the blade, allowing features such as spars, shear webs and other connections, inevitably requires these 2D material forms to be formed into 3D shapes such that there are positions within the structure where load transfer occurs across regions with no fibre reinforcement that act as areas of weakness and natural positions for the initiation of fatigue damage that can occur well before fatigue damage would be expected in the basic material subject to simple in-plane loading.

The aim of this study is to modify and improve the blade structure in order to extend the working life of blade and minimize geometry related fatigue problems. To achieve this goal T-sections has been made as representative elements of the blade's Spar. T-sections have been made of carbon fabric and epoxy resin and it have been modified with different toughening technique, such as the use of veil layers and the use of nano and rubber particles. The changing parameters in samples are, the addition of the veil layer to the composite structure, number of veil layers, veil material, and the addition of the rubber modified or nano-particle modified epoxy system to the composite.

Samples with different toughening methods have been evaluated for tensile properties using an Instron 8802 mechanical testing machine equipped with 100kN load cells. Maximum tensile strength of the samples has been compared and the samples with highest ultimate tensile strength have been chosen. In next stage because of fundamental differences in fatigue and tensile strength, four samples with highest tensile strength have been fatigue tested in one stress level of 6 MPa.

From the results it has been found that the rubber modified sample has got the highest tensile strength among the samples. In addition similar results have been found for fatigue testing and the rubber modified sample went through the highest number of cycles before failure. Another interesting point was that despite the difference of ultimate tensile strength of samples with different number of same material veil layer, no significant difference was observed in their fatigue life.

Poster Session 2

Control Systems

A comparison of linear models for the design of pitch controllers
Daniel Duckwitz, Martin Shan, Boris Fischer

Efficiency of kite power systems in pumping operation
Uwe Fechner, Rolf van der Vlucht, Roland Schmehl, Wubbo Ockels

Control oriented modeling in wind farms by using Sequentially Semi-Separable matrices
Patricio Torres, Jan-Willem van Wingerden, Michel Verhaegen

Electrical Production and Grid Integration

New Principles of Access for Wind Generation Curtailment Scheme in Active Network Management
Laura Kane, Graham Ault, Simon Gill

Analysis of Investment in Great Britain's Transmission Capacity with High Wind Penetration
S. McLaren-Gow, T. Houghton, K. Bell

Effect of Wind Turbine Wakes on Wind Induced Motions of Wood-Pole Overhead Lines
C. MacIver, A. Cruden, W.E. Leithead

Operation, Condition Monitoring and Maintenance

Stochastic modeling of wind turbine characteristics
Philip Rinn, Patrick Milan, Matthias Wachter and Joachim Peinke

Damage Model for Reliability Assessment of Solder Joints in Wind Turbines
Erik E. Kostandyan, John D. Sørensen

Wind Turbine Condition Monitoring Based on SCADA Data
Y. Wang, D.G. Infield

Rotor and Wakes Aerodynamics

Wind Farm Operation Planning
N. Moskalenko, K. Rudion, Z. A. Styczynski

Wake effects of large offshore wind farms - a study of mesoscale atmosphere and ocean feedbacks
P.Volker, J. Badger, A.Hahman

Bolund-site RANS simulations for several inflow directions using the validated CFDWind1.0
R. Garcia, C. Masson, D. Cabezón

Parallel vortex method on GPU for VAWT aerodynamics
Giuseppe Tescione

Wind Modelling, Forecasting and Resource Assessment

Challenges for wind resource assessment of mountainous terrain in the wind tunnel
Boris Conan, Jeroen van Beeck, Sandrine Aubrun

Intermittent spatial and temporal structure of wind fields
Fatima Keshtova, Joachim Peinke

Improving the wind power prediction in the European Transmission System Operator Zones with the wind power prediction based on the COSMO-EU model
Nicole Stoffels, Dr. Luder von Bremen

Downscaling the wind energy resource in complex terrain using coupled mesoscale and microscale models
Venkatesh Duraisamy Jothiprakasam , Eric Dupont, Bertrand Carissimo

Modification of CFD code to model the atmospheric boundary layer
T. W. Koblitz, A. Bechmann, A. Sogachev, N. N. Sørensen

Load estimation using Lidar data
O. Bischoff,J. Anger, M.Hofsäß ,A. Rettenmeier, D.Schlipf

Finite Elements CFD Model for Wind Resource Assessment
A.Bonanni, T.Banyai, T.Quintino, H.Deconinck, C.Lacor

Wind Turbine Structural Design and Materials

Two-dimensional fluid-structure interaction
Knut Nordanger, Trond Kvamsdal, Runar Holdahl

Uniaxial loading on in-plane hexagonal chiral structure with negative Poisson’s ratio: adaptive structures for rotor blades
Oscar Castro, Fernando Casanova, Yesid Aguilar

A comparison of linear models for the design of pitch controllers

Daniel Duckwitz, Martin Shan, Boris Fischer
Division Control Engineering and Energy Storages, Fraunhofer IWES
Königstor 59, Kassel, Germany
E-mail: {daniel.duckwitz, martin.shan, boris.fischer} @iwes.fraunhofer.de

Keywords: identification, pitch control, control design, load calculation, model comparison.

INTRODUCTION

Pitch control is present in most new WEC. The design of the pitch control loop has to be done in an early stage of the development of a WEC. A linear model is required for this task. This work will compare different ways of obtaining this model. The necessary effort and possible uncertainties will be evaluated.

OBTAINING LINEAR MODELS

A common WEC type is under investigation, while several ways to obtain linear models will be compared, including identification from a number of aeroelastic codes. The first and second approach are causing additional effort for modeling and parameter fitting, while the third approach is the most time efficient. The fourth approach is applicable to any WEC model, which allows to derive linear models even if no linearization feature is available.

Linear model based on linear multibody approach and linear subsystems

This model is suitable for designing the pitch control loop as well as controls for load reduction, including individual pitch control. However, considerable effort is necessary to setup the model parameters and overall structure, in addition to the model for load calculation. For accurate modeling, parameters may have to be derived from more complex models (FEM, detailed drivetrain model, ...).

Simple linear model

Only the most basic effects (aerodynamics, tower bending and rotor inertia) are considered here. The effort to create a set of parameters is reduced significantly.

Linear model from aeroelastic code

The model used for load calculation usually is quite detailed. To obtain linear models, some aeroelastic codes offer the extraction of linear models.

Linear model from identification

On the other hand, identification of the pitch control loop can be done by analyzing the input and output signal under steady operating conditions. Using test input signals with small amplitudes is possible in any load calculation software. Using common system identification methods, the linear model can be obtained by the same method for different aeroelastic codes.

Comparing the linear models will reveal the degree of uncertainty caused by the choice of the model. The necessary level of detail could be evaluated based on this comparison.

OUTLOOK / CONCLUSION

This work will help to judge the necessary effort for pitch control design. It will also give an initial guess on modelling uncertainties. As a result from model uncertainty, the robustness of the control loop will be analyzed.

In the future, closed loop identification methods shall be investigated. This would also allow to verify the models against a real turbine.

Efficiency of kite power systems in pumping operation

Uwe Fechner, Rolf van der Vlucht, Roland Schmehl, Wubbo Ockels
ASSET Institute, TU Delft
Kluyverweg 1, The Netherlands
E-mail: {U.Fechner,R.vanderVlugt,R.Schmehl,W.J.Ockels}@tudelft.nl

Keywords: Airborne Wind Energy, AWE, kite power, pumping operation, jojo operation, winch, efficiency

Introduction

Airborne Wind Energy (AWE) systems are a novel way to harvest wind energy without the need for a heavy tower and foundation. During the last decade the number of companies and research groups involved in the development of AWE systems increased from three to sixty. AWE systems are expected to work with a very high capacity factor, because the wind-speed at increasing altitudes is higher and steadier. In many applications they also promise a substantial decrease of costs per kWh. However, the practical challenges to develop reliable AWE systems, which are operated automatically are high. The principle of operation of the AWE demonstrator of TU Delft will be explained. A simplified mathematical system and efficiency model will be presented.

Principle of operation

Kite power systems combine one or more computer-controlled inflatable membrane wings with a motor-generator unit on ground using a strong and lightweight cable[1]. Each pumping cycle consists of an energy generating reel-out phase, in which the kites are operated in figure-eight flight manoeuvres to maximize the pulling force, and a reel-in phase in which the kites are depowered and pulled back towards the ground station using a small fraction of the generated energy (see figure 1).

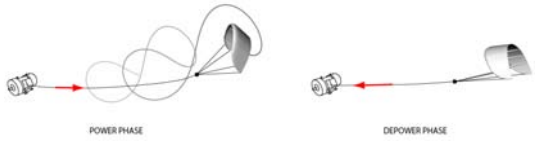

Figure 1: Pumping Kite

To reach a high efficiency of the wind harvesting mechanism, a high reel-out and a low reel-in force are required. A high reel-out force is achieved by flying crosswind, a low reel-in force is realized by de-powering the kite. The current demonstrator achieves a harvesting efficiency of about 80%.

Measuring results

In the upper diagram the mechanical and electrical power output of the generator is shown, and the quotient of them, the generator efficiency. In the lower diagram you can see the power consumption of the spindle motor and the brakes, that must be released, when the system is active.

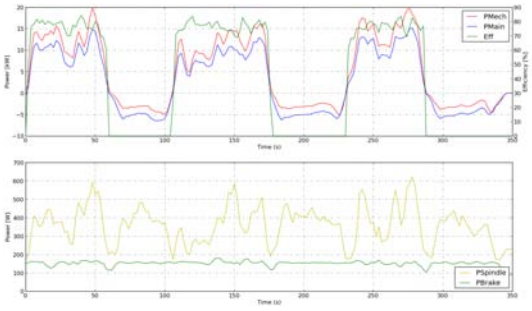

Figure 2: Power during three cycles

Mathematical model

A simplified mathematical model was developed to optimize the operation parameters and the winch. It combines an analytical framework with empirically derived performance factors. It takes into account the aerodynamic performance of the kite, the drag of the tether, the elevation angle of the tether and the increase of the wind-speed at higher altitudes. The most important mechanical performance factors are the duty cycle, the harvesting efficiency, the crest factor of the reel-out speed and the crest factor of the reel-out force. For the reel-in phase it takes into account, that the elevation angle of the kite rises, when the kite is depowered. By means of global optimization the optimal elevation angle, tether length, reel-out speed and reel-in speed as a function of the wind speed can be calculated.

Conclusions

The mean mechanical output of the system could be improved from about 2 kW to 6 kW in the time from June 2010 to June 2011. For a much higher mechanical power and a better electrical efficiency a new winch is currently in the design phase. The current goal is to increase the mean mechanical power to 25 kW and the mean electrical output to about 20 kW, using a kite with a size of 25 to 35 m^2.

References

[1] P. Williams, B. Lansdorp, and W. Ockels, Optimal Crosswind Towing and Power Generation with Tethered Kites, Journal of Guidance, Control, and Dynamics, vol. 31, Jan. 2008, pp. 81-93.

Control oriented modeling in wind farms by using Sequentially Semi-Separable matrices

Patricio Torres, Jan-Willem van Wingerden, Michel Verhaegen
Delft Center for Systems and Control, Delft University of Technology
Mekelweg 2, 2628 CD, Delft, Netherlands
E-mail: {p.i.torrestapia, j.w.vanwingerden, m.verhaegen}@tudelft.nl

Keywords: wind farm, distributed wind model, subspace identification, sequentially semi-separable matrices

1 Introduction

In this work, the first steps towards the development of a general identification technique for the wind within farms resulting on a distributed model suitable for control synthesis is presented. Firstly, a cluster of turbines located in a row is considered. Every turbine is fully oriented in the wind direction and modeled by using the actuator disc approach. A dedicated Computational Fluid Dynamic (CFD) model of the wind based on the numerical solution of the 2D Navier-Stokes equation [1] is available for data. The method consist in to divide the row of turbines in consecutive rectangular regions, each one containing one turbine. By assuming the flow is oriented in a fixed direction along the row, the identification can be performed separately over each region by using subspace methods for LTI systems [2] and order reduction techniques. Thus, the resulting distributed model can be recovered by connecting the individual state-space models in cascade by using the wind speed at the consecutive borders as interconnection variables. Such model can be represented by lifted matrices with sequentially semi-separable structure (SSS) [3]. This fact can be used to speed up the involved matrix operations (linear complexity). Besides, we plan to propose a distributed controller that exploit the SSS structure of the obtained model.

2 Identification procedure

We collect the data of the wind velocity in every point of the discretized domain resulting from the numerical solution of the 2D Navier-Stokes equation [1]. In Fig.1 we show an example of three turbines aligned in a row.

In this case, $\{\Omega_s, \beta_s\}$, $s \in \{1,2,3\}$ are the rotational speed and pitch angle of the s-th turbine, $\{z_s\}$ is the vector that contains all the velocities within the s-th region, $\{u_2^m, u_3^m\}$, are the interconnection vectors, that contains the velocities at the right hand border of the regions 1 and 2 respectively and $u_0^m = u_B$ is the velocity of the incoming wind. Notice that the interconnection variables are oriented in just one direction. This is because we assume that the velocity before does not depend on the velocity after the flow. By taking this into account, we can treat each region independently. Therefore, we apply the subspace identification method [2] over each region separately using as input $u_s = [u_{s-1}^m, \Omega_s, \beta_s]^T$ and output $y_s = [z_s, u_{s+1}^m]^T$ for $s \in \{1,2,3\}$. Order reduction techniques are applied too in order to obtain state-space models with minimal order - complexity and suitable for control design. From the subspace identification step, we obtain for every region a model of the form:

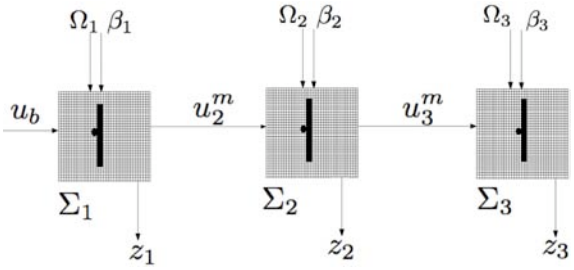

Figure 1: Row of three turbines.

$$\begin{aligned} x_s(k+1) &= A_s x_s(k) + B_s u_s(k) \\ y_s(k) &= C_s x_s(k) + D_s u_s(k) \end{aligned} \tag{1}$$

Then, by splitting the matrices C_s and D_s in:

$$C_s = \begin{bmatrix} C_s^m \\ C_s^1 \end{bmatrix} \tag{2}$$

$$D_s = \begin{bmatrix} W_s^m & L_s^m & V_s^m \\ J_s^m & D_s^{11} & D_s^{12} \end{bmatrix} \tag{3}$$

according to the sizes of $z_s, u_{s+1}^m, u_{s-1}^m, \Omega_s$ and β_s, the whole system can be represented as a lifted model whose characteristic matrices have SSS structure, (for more detail see [3]) .

References

[1] P. Torres, J. W. van Wingerden and M. Verhaegen. Modeling of the flow in wind farms for total power optimization. submitted to IEEE ICCA, Chile, 2011.

[2] M. Verhaegen and V. Verdult. Filtering and System Identification, A Least Squares Approach. Cambridge university press, 2007.

[3] J.K. Rice. Efficient algorithms for distributed control: a structured matrix approach. Ph.D. Thesis, Delft University of Technology, 2010.

New Principles of Access for Wind Generation Curtailment Scheme in Active Network Management

1, Laura Kane 2, Graham Ault 3 Simon Gill
Wind Energy Systems DTC, University of Strathclyde
Glasgow, UK
E-mail: laura.kane@strath.ac.uk,g.ault@eee.strath.ac.uk,
simon.gill@eee.strath.ac.uk

Keywords: Curtailment, Wind Generation, Distribution Network, Active Network Management

INTRODUCTION

The growth of wind generation in distribution networks is leading to the development of Active Network Management (ANM) strategies. These aim to increase the capacity of Distributed Generation (DG) that can connect to the network. One such strategy is generation curtailment where DG is given a non-firm connection under which the network operator instructs the generator to reduce its power output under specified conditions. Currently in the UK the Orkney distribution network operates a curtailment scheme for wind and other renewable generation and a further ANM scheme is planned for the Shetland Islands. Principles of Access (PoA) for generators connected to the power network under these schemes is of serious concern for generators, network operators and other stakeholders. This paper describes possible approaches and presents the outcomes of detailed analysis of alternative PoA for wind generation integration into distribution networks.

SECTION 1

There are a number of contractual arrangements that can be applied to curtailment schemes in ANM [1]. A common one, and the one implemented in Orkney, is the Last in First Out (LIFO) policy. This means that the first generator to sign a contract for network access is always the last generator to be curtailed under the specific conditions when curtailment is required.

This paper investigates alternative curtailment policies such as ‘Shared Percentage’, ‘Market Based’ methods and ‘Technical Best’ methods.

In order to analyse different access and curtailment policies, the Orkney distribution system is analysed using MatPower to simulate different curtailment schemes and access arrangements. The benefits of each approach are assessed with reference to the different stakeholders including wind turbine owner/operators and network operators.

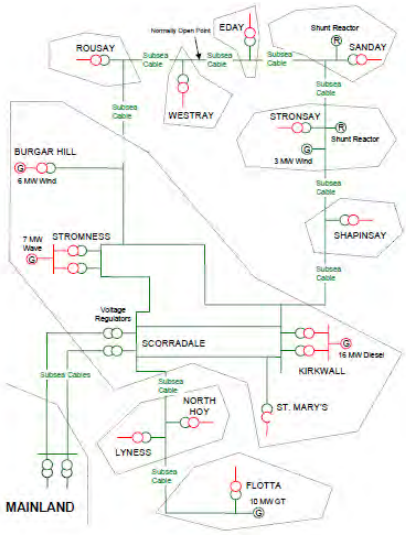

Figure 1: Existing network layout of the Orkney 33kV network [2]

CONCLUSIONS

This paper provides evidence to suggest a market based POA would be the most appealing solution to congestion for both network operators and generators. By allowing generators to bid a price to remain connected during periods of constraint they are in control of their own generating ability, and the network benefits from increased profits. This market approach can be expanded to include advantages of other POA such as shared percentage in order to create the most efficient network operation during periods of constraint.

REFERENCES

[1] Currie, R. (2011). Commercial arrangements to facilitate active network management 21st International Conference on Electricity Distribution. Frankfurt**:** 4.

[2] Scottish & Southern Energy (2004) Facilitate Generation Connections on Orkney by Automatic Distribution Network Management.

Analysis of Investment in Great Britain's Transmission Capacity with High Wind Penetration

S. McLaren-Gow, T. Houghton, K. Bell
Wind Energy Systems Doctoral Training Centre, University of Strathclyde
204 George Street, Glasgow, United Kingdom
E-mail: scott.mclaren-gow@strath.ac.uk

Keywords: Monte Carlo simulation, power system economics, wind generation, transmission network investment

INTRODUCTION

In line with European Union Directives, the British Government has set aggressive targets for renewable electricity generation. There is significant controversy surrounding the consequences of meeting these targets, largely due to the fact that wind turbines are expected to make up the majority of new renewable generation [1]. Concern is often focused on the effect of wind power's intermittency on the transmission network, which can be costly to reinforce.

Despite the importance and prominence of the debate, there is a lack of clear information on the levels of power system utilisation with high wind penetration and therefore on the required transmission network capacities. This study intends to investigate these issues using a model of Great Britain's power system.

MODELLING TOOL: ANTARES

ANTARES [2] is a sequential Monte Carlo simulator suited to modelling simplified country or continent wide generation and transmission systems. Two types of simulation are possible: adequacy, where the aim is to predict values such as loss of load probability and expectation; and transmission efficiency, where the aim is to estimate the extent to which a transmission system restricts the economically optimal use of generation.

Simulations in ANTARES are based partly on the use of historical time series for load, wind generation and hydro generation. These are scaled to their predicted future values and analysed to provide probability distributions for their underlying stochastic processes. Many year long time series are then generated which represent a set of possible futures; for example, the year being simulated has some chance of being windy and some chance of being calm. The optimal dispatch of thermal generation can then be found for each of the possible futures, thereby allowing the utilisation of each transmission system link to be calculated.

STUDY

This study will seek to extend a pre-existing model of Great Britain's power system in ANTARES. The model consists of nine areas in which generators can be placed, while the transmission system is represented by transfer capacities at the borders between areas. This simplified model is expected to provide a reasonable representation of transmission constraints as the borders correspond to the weakest links in the transmission system.

Data with which to populate the model must be selected as a first stage of this study. This includes: historical load data; locations, capacities, reliability and costs of thermal generation; rainfall data for hydro schemes; wind speed time series; and transmission network transfer capacities. Once a baseline model has been completed, work will be undertaken to determine the impact of an increased level of wind penetration.

CONCLUSIONS

A model of Great Britain's power system will be set up using ANTARES. A study will then be undertaken to investigate the need for transmission investment with high wind penetration.

REFERENCES

[1] Department of Energy & Climate Change. UK Renewable Energy Roadmap. 2011.

[2] M. Doquet, R. Gonzalez, S. Lepy, E. Momot, F. Verrier. A new tool for adequacy reporting of electric systems: ANTARES. Paper C1-305, CIGRE 2008 Session, Paris, August 2008.

Effect of Wind Turbine Wakes on Wind Induced Motions of Wood-Pole Overhead Lines

C. MacIver, A. Cruden, W.E. Leithead
Wind Energy Systems Doctoral Training Centre, University of Strathclyde
R336, 204 George Street, Glasgow, United Kingdom
E-mail: callum.maciver@strath.ac.uk

Keywords: wake, conductor vibration, overhead line

INTRODUCTION

Wind farms are being proposed close to existing wood-pole overhead lines. There are concerns about possible deleterious wake effects on conductors behind a wind turbine. Previous and current studies have focused on large scale transmission lines. The effects on wood-pole medium voltage lines at lower heights and with shorter spans have not been studied despite the fact that wood-pole lines are much more numerous than tower lines.

Two potential problems for conductors are:

i. Increased time spent in low wind speeds could result in an increase in Aeolian vibrations

ii. Turbulent flow could result in high-amplitude low-frequency oscillations.

WIND INDUCED CONDUCTOR MOTION

Wind induced vibrations and oscillations in overhead electricity lines have been widely documented and are recognised as a leading contributor to fatigue and failure of conductors. There are a number of different phenomena which can occur and the most important are outlined as the main focus for investigation:

i. Aeolian vibrations – Vortex induced, high-frequency, low-amplitude vibrations. Normally occur in low wind speeds up to 7m/s [1] and can cause long term fatigue damage to conductor strands especially at support points

ii. Galloping (ice induced) – High amplitude, low-frequency oscillations. Asymmetry introduced in certain iced conditions can lead to aerofoil like behaviour of the conductor. Can lead to outright failure or add to fatigue.

iii. Turbulent Buffeting – Highly turbulent winds can introduce forcing effects which excite some low order natural frequencies of the conductor. Similar effects to galloping.

How these phenomena might be influenced or altered as a result of the presence of wind turbine wakes will be determined.

An understanding of how a wind turbine wake will propagate and what its influence will be at these low levels will be explored through literature [2] as well as by the analysis of test data.

The outcome is of interest because although mitigation against such effects, through dampers or other means, is common on large scale transmission line towers, this is not the case at distribution level on wood-pole overhead lines.

WIND FARM DATA

Several tests have been carried out on a test wind farm site and data is available for analysis. Measurements of wind parameters at different distances and positions upstream and downstream of the turbine have been collected at a height of 6m which corresponds to that of a standard wood-pole line.

A full analysis of this data will be carried out to determine the mean wind speed and turbulence intensity as a function of position downstream of the turbine. This will allow the identification of any potential ‘danger zones’ where the influence of the wind turbine or farm could cause or add to the wind induced motion of overhead lines.

CONCLUSIONS

Research is currently ongoing and conclusions will be available at the time of presentation.

REFERENCES

[1] EPRI: Transmission Line Reference Book: Wind Induced Conductor Motion. Electric Power Research Institute, Palo Alto California, 1979.

[2] L.J. Vermeer, J.N. Sørensen and A. Crespo. Wind Turbine Wake Aerodynamics. Progress In Aerospace Sciences, 39:467-510, 2003.

Stochastic modeling of wind turbine characteristics

Philip Rinn, Patrick Milan, Matthias Wächter and Joachim Peinke
ForWind – Center for Wind Energy Research, University of Oldenburg
26111 Oldenburg, Germany
E-mail: philip.rinn@uni-oldenburg.de

Keywords: stochastic modeling, monitoring

Abstract

While wind energy converters (WEC) become larger and the exploration of wind energy resources increases there is still a lack of fundamental research on the effects of turbulent wind inflow on the operation lifetime of the WEC as well as on its electric power production. Short-scale as well as long-scale turbulent effects lead to a ever-changing intermittent loading on the WEC and thus to ever-changing power signals fed into the grid. A stochastic model that includes turbulent effects is proposed as an alternative to standard tools in wind energy research. Based on the Langevin equation it can characterize and simulate complex systems such as the electric power production or deflections of the WEC. It is an interesting tool for wind energy applications such as monitoring, availability prediction or grid integration as the proper statistics can be reproduced. An expansion to fatigue loads is planned.

Stochastic Analysis

A wide range of dynamic systems can be described by a stochastic differential equation, the Langevin equation (1). The time derivative of the system trajectory $\dot{P}(t)$ can be expressed as a sum of a deterministic part $D^{(1)}$ and the product of a stochastic δ-correlated Gaussian white noise with zero mean $\Gamma(t)$ and a weight coefficient $D^{(2)}$[1, 2].

$$\dot{P}(t) = D^{(1)}(P(t),u(t)) + \sqrt{D^{(2)}(P(t),u(t))}\,\Gamma(t) \qquad (1)$$

$$D^{(n)}(p,u) = \frac{1}{n!}\lim_{\tau\to 0}\frac{1}{\tau}\langle (P(t+\tau)-p)\rangle|_{P(t)=p}\,,\; n\in \mathrm{N}$$

To characterize the power output of a WEC we cut the wind speed in 0.5 m/s broad bins and calculate the drift and diffusion for each bin. From the drift in each wind speed bin we derive the fixed point which is the stable operation point in this bin. Figure (1) shows these fixed points along with arrows denoting the direction and strength the system is pushed towards these points.

Once we characterized the WEC by means of drift and diffusion coefficients we can model the power output of the WEC from a given wind speed time series. From equation (1) we integrate the power output. Figure (2) shows the quite good agreement between measured and modeled time series.

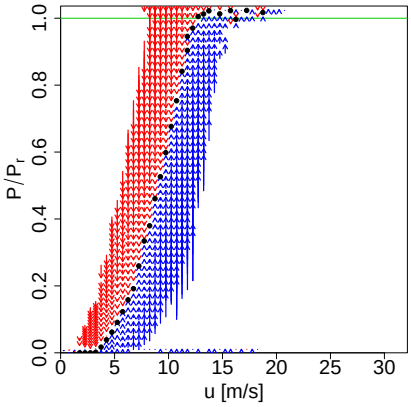

Figure 1: Dynamic Power curve with fixed points (black dots).

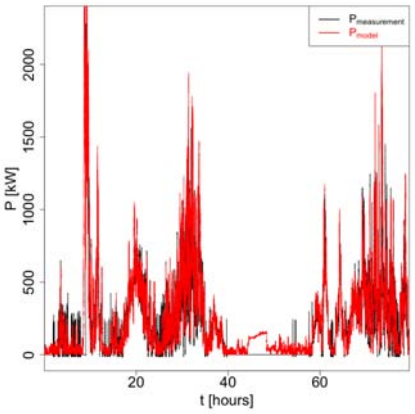

Figure 2: Comparison between measured and modeled time series.

References

[1] S. Siegert et al. Analysis of data sets of stochastic systems. Phys. Lett. A, 243:275–280, 1998.

[2] R. Friedrich et al. Extracting model equations from experimental data. Phys. Lett. A, 271:217–222, 2000.

Damage Model for Reliability Assessment of Solder Joints in Wind Turbines

Erik E. Kostandyan, John D. Sørensen
Department of Civil Engineering, Aalborg University
Sohngaardsholmsvej 57, Aalborg, Denmark 9000
E-mail: { ek, jds}@civil.aau.dk

Keywords: Wind Turbines Electrical Components Reliability, IGBT Damage Model, SnAg Solders Damage Model.

1 Introduction

Electrical components are inseparable part in many products. The environment, under which the electrical components are utilized, directly influences the reliability of electrical components. Such influences might be loads and stresses from turbulence, temperature, humidity and many other environmental factors. Reliability assessment for such type of products conventionally is performed by classical reliability techniques based on test data. Usually conventional reliability approaches are time and resource consuming activities. Thus in this paper we choose a physics of failure approach to define damage model by Miner's rule. Our attention is focused on crack propagation in solder joints of electrical components due to the temperature loadings. Based on the proposed method it is described how to find the damage level for a given temperature loading profile. The proposed method is discussed for the application at Wind Turbines electrical components reliability assessment.

2 Motivation and Procedure

Power Semiconductor Devices (PSD) are electronic switches that are widely used in electronic applications as well as at Wind Turbine's (WT) electronic modules. Insulated Gate Bipolar Transistor (IGBT) is a three terminal PSD. IGBT has advantages because of its switching speed and practically it is used in most WTs. WT's components suppliers and producers offer IGBT as a solution to the increased voltage peaks within the generator that might harm the coils, also the IGBT is used in WT's control systems.

IGBT and PSD are complicated electronic devices that are mainly comprised from semiconductors, aluminum, copper and ceramics. These components are linked together by soldering, wirebonds and other manufacturing techniques.

Lifetime prediction models for solders are based on methods defined by strain ranges, accumulated creep/plastic strain and accumulated strain energy density during a temperature-loading cycle. We propose a method that accounts both initial accumulated plastic strain from temperature mean and temperature range as well as crack propagation in solder joints. By this method, it is possible to estimate damage level during degradation process. A schematic layout of the proposed method is depicted in Figure 1.

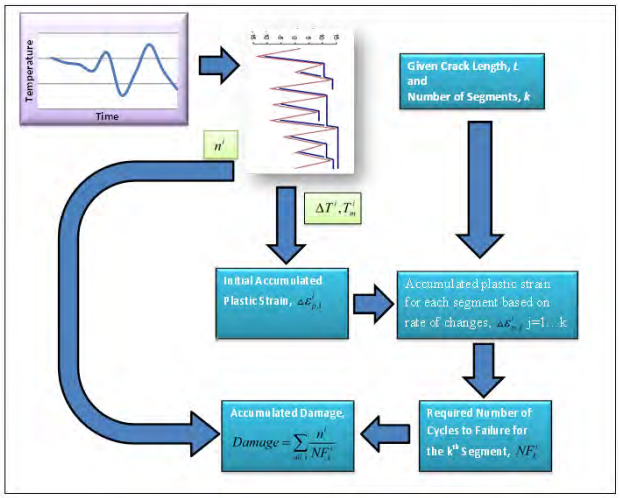

Figure 1: Layout for Damage Accumulation Procedure Based on Crack Propagation.

3 Conclusion

The physics of failure for electrical components due to temperature loading is described. The main focus is on crack propagation in solder joints and damage accumulation model based on the Miner's rule. The model is proposed that describes the initial accumulated plastic strain from temperature mean and temperature range. Constants in the model are estimated as well as the model error. The proposed method is useful to predict damage values for solder joint in electrical components. This method might be used to calculate damage in electrical components (e.g. IGBT) of Wind Turbines.

Wind Turbine Condition Monitoring Based on SCADA Data

Y. Wang, D.G. Infield
Institute for Energy and Environment, Department of Electronic and Electrical Engineering, University of Strathclyde
204 George St, Royal College Building, Glasgow G1 1XW, UK
E-mail: {y.wang, david.infield}@eee.strath.ac.uk

Keywords: wind turbine, condition monitoring, SCADA data, pitch system, yaw system, NSET.

INTRODUCTION

The excellent UK offshore wind resource and the need for the UK to reduce carbon emissions from electricity generation is driving policy to install 33GW of new offshore wind generation capacity by 2020. Access and maintenance offshore can be difficult and will be more costly than onshore and availability correspondingly lower, and as a result there is a growing interest in wind turbine condition monitoring and condition based rather than responsive and scheduled maintenance.

CONDITION MONITORING FOR PITCH AND YAW SYSTEM

This paper will report on research being undertaken to extract component condition indicators from standard 10 minute SCADA data. In this section, particular attention is being paid to condition monitoring of the wind turbine pitching system and the yaw system, based on regularly updated power curves that are compared with a standard curve for the turbine (this can be taken as the IEC Standard power curve as supplied by the manufacturer). [1]

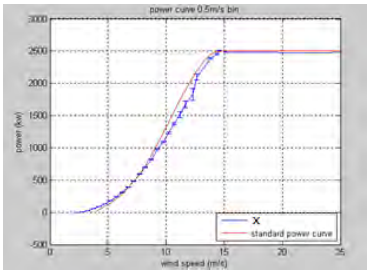

Figure 1: Power curve comparison

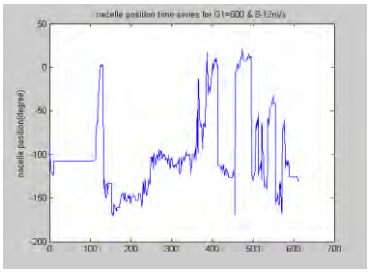

Figure 2: Nacelle position time series

NONLINEAR STATE ESTIMATE TECHNIQUE

The Nonlinear State Estimate Technique (NSET), used successfully in nuclear power plant condition monitoring, is proposed here to construct a normal behaviour model of the wind turbine. By properly choosing data in the state memory matrix, the model is capable of capturing the characteristics of the system and hence achieving expected performance. [2]

According to the statistics of turbine failure and downtime results in [3], gearbox shows the highest downtime compared to other components in wind turbine although its failure is not as frequent as others. Therefore, a wind turbine gearbox NSET model is constructed here in order to detect anomalies associated with gearbox as early as possible.

CONCLUSIONS

The gearbox NSET model in this paper is capable of detecting system anomalies prior to the final failure, thus saving the downtime costs. Future work will involve more turbines of different types and in different locations, and other models with regards to each specific component will be constructed as well to test the robustness of this proposed method.

REFERENCES

[1] J.F. Manwell, J.G. McGowan, A.L. Rogers and Dawsonera, Wind energy explained: theory, design and application (2nd ed), Chichester: John Wiley, 2007.

[2] F.K. Bockhorst, K.C. Gross, J.P. Herzog, and S.W. Wegerich, MSET modeling of crystal river-3 venturi flow meters, International Conference on Nuclear Engineering, San Diego, CA, 1998.

[3] C.J. Crabtree, Y. Feng and P.J. Tavner, Detecting incipient wind turbine gearbox failure: a signal analysis method for on-line condition monitoring, European Wind Energy Conference 2010, warsaw, Poland.

Wind Farm Operation Planning - Abstract

N. Moskalenko, K. Rudion, Z. A. Styczynski
Chair Electric Power Networks and Renewable Energy Sources, Otto-von-Guericke-University Magdeburg
Universitaetsplatz 2, Magdeburg, 39106, Germany
E-mail: natalia.moskalenko@ovgu.de, rudion@ovgu.de, sty@ovgu.de

Keywords: energy yield, pitch angle, wake effect, wind energy, wind farm, yaw angle.

INTRODUCTION

The main task of this paper is to investigate the possibilities of optimal operation planning to maximize the energy production from a wind farm.

STATE OF THE ART AND TASK DEFINITION

During the wind farm planning process an important task is to minimize the area utilized by the planned wind farm while producing as much energy as possible from the minimal number of wind turbines and with a minimal space between the turbines due to the economy of land resources. Minimization of the distance between single wind turbines within a wind farm causes an increase of the wake effect, which is introduced by the shadowing of some wind turbines by the other units in the wind farm and, consequently, causes a turbulent flow. This leads to a reduced energy yield in the shadowed units. Thus, the resulting layout of a wind farm in the planning phase is a compromise taking into account the mentioned issues, and generally is optimized for one main wind direction that is most probable for the considered site. However, during real operation the wind direction can change and does not always correspond to the main direction assumed in the planning process. In such a situation it is still important to get the maximal possible energy yield from the farm.

The maximization of energy yield could be reached through the adjustment of the yaw angle of individual wind turbines as discussed in [1] or by the appropriate adjustment of the pitch angle in different wind turbines within the farm. The current status of this work is to investigate and compare the influence of these two methods on the overall energy yield of the wind farm.

MODELING AND SIMULATION

Approach Characterisation

The approach proposed in this paper assumes on the one hand changing the yaw angle at the individual wind turbines from the optimal value, which corresponds to the perpendicular position of the rotor plane to the wind direction and minimization of wake effect within the farm.

On the other hand, the paper considers the method of changing the pitch angle in the individual wind turbines from the optimal value, which corresponds to the maximal power coefficient and maximal utilization of kinetic energy from the wind flow, and it also assumes a minimization of the wake effect within the farm due to the thrust coefficient dependence on the pitch angle. The goal is to find both the optimal yaw angle patterns as well as pitch angle pattern for different wind speeds in order to maximize the overall energy yield of the farm.

Model Development and Study Cases

This paper presents the developed model, which is based on Jensen's wake model [2]0, and includes required extensions to investigate both the yaw angle influence and the pitch angle influence on the energy yield. The methodology of the optimization of wind farm operation in order to minimize the wake effect as well as increase the energy yield will be discussed in the second step. Finally, the simulation results for chosen scenarios will be presented and evaluated. Initial results have shown that optimizing the yaw and pitch angle can improve the overall energy yield of a wind farm.

CONCLUSIONS

This paper presents the method that is based on Jensen's wake model and includes required extensions to investigate the pitch angle influence as well as yaw angle influence of a wind turbine on the overall energy yield of the wind farm.

REFERENCES

[1] N. Moskalenko, K. Rudion: Optimal Operation Planning for Wind Farms; Proceedings of the 6th EAWE PhD Seminar, Trondheim, Norway, 30.09.-01.10.2010.

[2] N.O. Jensen: A Note on Wind Generator Interaction; Technical Report RISO-M-2411, Denmark, Nov. 1983.

Wake effects of large offshore wind farms - a study of mesoscale atmosphere and ocean feedbacks

P.Volker, J. Badger, A.Hahman
Risø DTU
Address, Country
E-mail: {pvol, jaba, ahah}@risoe.dtu.dk

Keywords: Offshore wind farms, Mesoscale, Wake effects

ABSTRACT

In this poster the outline and some first results of a PhD project titled "Wake effects of large offshore wind farms - a study of mesoscale atmosphere and ocean feedbacks" started in October 2010 will be presented.

The PhD project objectives are to investigate and develop methods for prediction of wind resources, including wake effects and atmospheric feedbacks at mesoscale, for scenarios where large portions of the sea are covered with wind farms such that a significant feedback to the wind climate must be expected. At present there exist a range of models for calculating the wake from turbines singly and as part of a wind farm, however these are not yet incorporated in mesoscale models, which simulate the atmosphere circulation and physics at the regional scale (2 - 30km).

The aim of the first part of the project will be to develop a physically justified parameterisation of a wind-farm and to implement it in a mesoscale model (WRF). The offshore wind-farm parameterisation has to account for the wake creation caused by the momentum deficit, which is induced by the extraction of energy, as well as turbulence generated by the turbines and its transport. These two processes are responsible for the transformation of mean kinetic energy into turbulent kinetic energy and for the spectral short circuiting of turbulence, which increases the turbulence dissipation. For the extraction of momentum the actuator Disk approach will be used which is valid in the near wake region, where the mass is conserved and the wake is still evolving. In the far wake region where the velocity deficit is conserved the self-preserving nature of the wake region will be used. The approach will take further into account the influence of atmospheric stability effects on the entrainment rate. Also an additional source term of turbulence kinetic energy caused by the wind turbines is added in the wake region. Since the sub-grid scale transport is 1D in mesoscale models, due to the large horizontal grid size compared to the length scales of the processes, we have to introduce in the downwind direction of the wind-farms the horizontal advection of turbulence has also to be introduced.

In the second part of the project the wind-farm description will be used to investigate eventual climate impacts due to large wind-farms. It will address to what extent the wind climate and the surface ocean circulation are affected by large wind farms. Furthermore it will develop techniques for upscaling the effects simulated by turbine and wind farm wake models into mesoscale atmospheric planetary boundary layer (PBL) parameterisations and perform simulations using these parameterisations to understand the feedbacks between the wind farms and the regional wind climate. The work will extend the current knowledge about wake effects from observations and small-scale models to the feedbacks that could occur in the atmospheric boundary layer, the atmosphere and the upper ocean.

Bolund-site RANS simulations for several inflow directions using the validated CFDWind1.0

R. Garcia[1], C. Masson[1], D. Cabezón[2]

[1]Department of Mechanical Engineering , École de Technologie Supérieure (ÉTS), Montréal (Canada).
e-mail: rgarcia@cener.com; Christian.Masson@etsmtl.ca

[2]Wind Energy Department, National Renewable Energy Centre (CENER), Madrid (Spain).
e-mail: dcabezon@cener.com

keywords: speed-up factor, normalized turbulent kinetic energy, inflow directions

ABSTRACT

CFD Wind flow models has become during the recent years a powerful tool for predicting wind speed and turbulent intensity, which represent significant quantities for the wind resource assessment process for the wind energy industry. Nevertheless CFD results need estimates of their uncertainty under different conditions such that final users get better knowledge before their use.

One of the best ways to get uncertainty estimates consists of validating CFD wind flow models through extensive field measuring campaigns particularly focused on validation purposes. This implies the installation of a comprehensive set of meteorological masts along different main flow directions to take into account average and turbulent properties.

This study aims to analyze the speed-up factor and the normalized turbulent kinetic energy for four different wind directions (270º, 255º, 239º and 90º) at the Bolund test site [1,2]. To this end, the results of the different simulations and measurements obtained in the case of Bolund will be compared. The CFDWind1.0 model [3] developed by CENER and based on the opensoruce CFD solver OpenFOAM 1.7.1 [4] at the site of Bolund is used. The model is based on the adaption of the Reynolds-averaged Navier-Stokes approach and the two-equation k-ε turbulence closure to the solution of the Surface Boundary Layer (SBL) [5].

The validation demonstrates that RANS-based models with two-equation k-ε closure, properly modified for the simulation of the surface boundary layer, can provide fairly accurate flow predictions over complex terrain in reasonable time.

REFERENCES

[1] Risø DTU, 'The Bolund Experiment: Blind comparison of CFD codes – Wind in complex terrain', http://www.risoe.dk/da/Research/sustainable energy/wind energy/projects/VEA Bolund/Bolund Blind Comparison.aspx?sc lang=en.

[2] Bechmann A., Berg J., Courtney M., et al., 'The Bolund experiment: Overview and background', Risø-R-1658(EN), July 2009.

[3] Cabezón D., Sumner J., García B., Sanz Rodrigo J., Masson C., “RANS simulations of wind flow at the Bolund experiment”, EWEC 2011 scientific proceedings, Brussels, Belgium, March 2011

[4] OpenCFD, 'OpenFOAM: The Open Source CFD Toolbox – Programmer’s Guide v1.6', 2009.

[5] El Kasmi, A., Masson, C., 'Turbulence modeling of atmospheric boundary layer flow over complex terrain: A comparison of models at wind tunnel and full scale', Wind Energy, 2010. In press.

A GPU-accelerated Vortex Particle Method for VAWT Aerodynamic Simulation

Giuseppe Tescione
DUWIND, Delft University of Technology
Kluyverweg 1, 2629HS Delft, The Netherlands
E-mail: G.Tescione@tudelft.nl

Keywords: Vertical Axis Wind Turbine, Aerodynamics, Vortex Particle Method, GPGPU, CUDA

Introduction

A Vortex Particle Method (VPM) is used for the aerodynamic analysis of a Vertical Axis Wind Turbine (VAWT). The code is run in parallel on a Graphics Processing Unit (GPU) to speedup the computation. The nature of the physical problem (VAWT aerodynamics), the numerical model (VPM) and the computing process (GPU) creates a perfect synergy which shows very interesting potential. The present report illustrates the reasons behind this synergy and the methodology which will be used to achieve an effective research tool.

Background

Vertical Axis Wind Turbines (VAWTs) are experiencing a renewed interest, both in the industry and in the research community. There is, however, a lack of extensive and updated research on the physical phenomena characterizing VAWT aerodynamics. This is a major issue since VAWT aerodynamics is more complex and, in some basic aspects, different from HAWT aerodynamics. VAWT aerodynamics is inherently unsteady and tridimensional with multiple blade-vortex interactions and dynamic stall. The fact that the energy conversion is based on the variation of the blade circulation results in a wake composed of shed and trailing vorticity. This complex aerodynamics and the lack of knowledge led to inaccurate aerodynamic models. Design tools belonging to the HAWT field are currently being used for VAWTs with small modifications, without considering the different nature of the energy extraction process. What if the claimed lower efficiency of the VAWT was a result of a less deep understanding of its physics and of a lack of proper analysis and design tools rather than an inherent characteristic of the machine?

In order to resolve this dearth of physical understanding and absence of proper models, computational fluid dynamics can be used as a tool for basic aerodynamic research. However, because of the important role that vorticity plays in VAWT aerodynamics, the commonly used grid-based methods, with their intrinsic numerical diffusion, fail to provide a good simulation tool for this application. Conversely, Vortex Particle Methods (VPMs), based on a Lagrangian formulation of the Navier-Stokes equations in terms of vorticity, represent a more promising approach in the simulation of VAWT aerodynamics. Their effectiveness is due to several features, but primarily their grid-less nature implies the lack of numerical diffusion and requires no time-expensive grid generation. However, VPMs have encountered a limited success in numerical aerodynamics so far, mainly because of their high computational cost. Indeed the use of particles, with the need of calculating the mutual interaction of each of the N elements, leads to an N^2 problem.

The use of a distributed computing environment is a direct way to reduce the computational time while preserving the level of accuracy. In the field of parallel computing, a recent breakthrough has been achieved by using graphic cards for scientific computing, a technique known as GPGPU (General Purpose computation on Graphic Processing Units).The GPUs are high-performance many-core processors capable of very high computation and data throughput; their special architecture makes them ideal for problems where the same operation is performed on multiple data which have a low level of communication. VPMs belong to this class of problems, as the interaction of all the elements on each particle can be computed independently.

Preliminary Results

A GPU version of a vortex method has been implemented with the use of the NVIDIA's parallel computing architecture CUDA. Simulations of the 2D code on an NVIDIA Quadro4000 (256 CUDA Cores) showed, over a quad-core CPU, a specific (peak) speedup of the self-induction function of 500x and an overall speedup of the full code of 30x for N=30000.

References

[1] Cottet, G.H. and Koumoutsakos, P.D. Vortex Methods, Cambridge University Press, 2000.

[2] NVIDIA. NVIDIA CUDA C Programming Guide Version 4.0, Tech. rep., NVIDIA Corporation, 2011.

Challenges for wind resource assessment of mountainous terrain in the wind tunnel

Boris Conan[1,2], Jeroen van Beeck[1], Sandrine Aubrun[2]
1. Enviroment and Applied Fluid Dynamics, von Karman Institute for Fluid Dynamics
72 chaussée de Waterloo, Rhode-Saint-Genèse, Belgique

2. Institut PRISME, Orléans University
8 rue Léonard de Vinci, 45072 Orléans, France
E-mail: {conan, vanbeeck}@vki.ac.be, sandrine.aubrun@univ-orleans.fr

Keywords: physical modelling, wind tunnel, wind resource assessment, micro-siting, complex terrain

INTRODUCTION

The Energy-Climate work-package of the European Union aims at reaching 20% of electricity consumption generated by renewable energy in 2020. Wind energy is one of the most promising sectors for producing “green” energy. Predicting the wind resource in mountainous terrain at the scale of a wind farm (micro-siting) is a complex but major issue for evaluating the profitability of a wind farm. The EU aims at less than 3% uncertainty in the local wind conditions forecasting regardless of the terrain complexity.

THE WIND TUNNEL ALTERNATIVE

Historically, the assessment of local wind conditions has been performed mainly by CFD computations and validated by field measurements. In very complex terrains, physical modelling in the wind tunnel is also an alternative and can provide precise validation data. This tool is not very widespread but is certainly a valuable help in assessing wind in very complex terrains.

A number of obstacles are associated to the simulation of atmospheric phenomena in a wind tunnel: the modelling of the atmospheric boundary layer, the choice of the mock-up scale (balance between reproducing a large area and keeping a reasonable scaling factor), the Reynolds number, the reproduction of the terrain roughness. Additionally, and specific from wind tunnel testing, measurement techniques have to be implemented.

The aim of the thesis is to gain deeper insight into the physical modelling of atmospheric flows for wind turbine micro-siting by tackling the above-mentioned issues.

PARAMETRIC STUDY

Several test campaigns have been performed in the wind tunnel using different complex terrains test cases: Alaiz mountain (Spain) and Bolund hill (Danemark).

Adapted measurement techniques have been implemented and parametric studies are being performed to gain experience and to try to validate the approach.

The Alaiz test campaign [2] (fig. 1) performed at the scale 1/5000 is to be validated with field measurements.

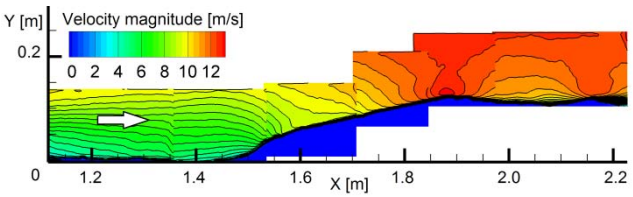

Figure 1: Experimental results (PIV) of the velocity field above the Alaiz hill.

The paper will discuss a selection of parametric studies performed in the wind tunnel.

CONCLUSIONS

Wind resource assessment by physical modeling in the wind tunnel is currently under validation for the assessment of wind potential in complex terrain

REFERENCES

[2] TP Wind http://www.windplatform.eu/

[2] B. Conan , S. Buckingham, J. van Beeck, S. Aubrun, J. Sanz-Rodrigo, Feasibility of Micro Siting in Mountainous Terrain by Wind Tunnel Physical Modellign, *European Wind Energy Conference, Brussels, March 2011*

Intermittent spatial and temporal structure of wind fields

Fatima Keshtova, Joachim Peinke
ForWind, Center for Wind Energy Research, Institude of Physics, Carl von Ossietzky University Oldenburg, Germany
E-mail: fatima.keshtova@uni-oldenburg.de;peinke@uni-oldenburg.de

Keywords: wind field model, stochastic modeling, turbulence, wind gusts

INTRODUCTION

The IEC standard 61400-1 specifies different wind field models to simulate the turbulent inflow conditions for wind turbines. These models are generating purely Gaussian statistics for the wind variations, which is in contrast to experimental data. The current analysis of measured turbulent wind data reveals a statistics of velocity increments that are not Gaussian but highly intermittent.

The main idea of this work is the simulation of stochastic 3-dimensional wind fields considering advanced characterisation of turbulence on scales ranging from a few meters to some hundred meters. For simulation Continuous Time Random Walk (CTRW) theory is used. The model enables to adapt parameters in order to accurately reproduce time dependent statistical features of wind turbulence. Current challenges include the proper implementation of spatial gusty structure. For this purpose the multi met masts measurement campaign GROWIAN is being used.

REFERENCES

[1] Tanja Muecke, David Kleinhans and Joachim Peinke. Atmospheric turbulence and its influence on the alternating loads on wind ruebines. Wind Energy, 2010.

[2] A.Morales, M. Waechter and J. Peinke. Characterization of wind turbulence by higher-order statistics. Wind Energy, 2010.

[3] D. Kleinhans and R. Friedrich. Simulation of intermittent wind fields: a new approach. DEWEK 2006 – Proceedings, Bremen(Germany) 2006

Improving the wind power prediction in the European Transmission System Operator Zones with the wind power prediction based on the COSMO-EU model

Nicole Stoffels, Dr. Lüder von Bremen
Wind Energy Meteorology, Carl von Ossietzky University Oldenburg
Ammerländer Heerstraße 136, D-26129 Oldenburg, Germany
E-mail: nicole.stoffels@forwind.de

Keywords: COSMO-EU model, wind power prediction, Taylor Plots, forecast error distributions

INTRODUCTION

Wind power forecasting on a large scale becomes more important aspiring an energy market with 80% renewable energy by 2050. For this purpose the COSMO-EU model of the German Weather Service (DWD) is taken for prediction scenarios such as forecast error smoothing or probabilities of forecast errors in certain regions over Europe. However as a first step the model outcome for wind power has to be evaluated and improved. This is done by comparing it on a statistical basis to other models, mainly commercial models. Afterwards ways are found how to improve the forecast accuracy and decrease the forecast errors. If the statistical values are similar the wind power prediction of the DWD model will serve for further prediction scenarios.

STATISTICAL EVALUATION

Northern Ireland Test Cases

For the evaluation of the wind power prediction derived with the COSMO-EU model it was compared to other wind power prediction models. First the error statistics were tested for two Northern Ireland wind farms, Altahullion and Elliott's Hill. In this case the comparative model was the Spanish wind power prediction model developed by CENER, a Spanish wind power Research Institution. In case of the Cener model the data was validated against the actual wind farm data provided by SONI, the Northern Ireland Transmission System Operator. The DWD wind power forecast was validated against the DWD wind power analysis data. Moreover the DWD analysis data and the SONI data were compared to each other. If only the closest grid points to the two wind farms were taken into account the DWD model statistics outperformed the Cener model statistics for various reasons. This can be seen in the several statistical parameters calculated. These include Taylor Plots [1], a graphical way of summarizing how close the statistics of different models are, presenting the correlation, standard deviation and RMSE in one plot, as well as forecast error distributions with statistical tests.

German TSO Test Cases

As a second step the DWD model was tested against the wind power prediction models of the four German Transmission System Operators (TSO) EnBW, 50 Hertz, Amprion and Tennet. These are mixtures of commercial wind power prediction models which are more complex. In the first run all grid points in the TSO zones were linearly averaged. The TSO models were validated against the wind power production in the TSO zone. The same statistical analyses as before were performed including Taylor Plots and distributions. In case of the German TSO zones the DWD model statistics were outperformed by the other models. This gives reason to improve the wind power forecast of the DWD model.

Improvements

This time the grid points were not simply averaged over the whole zone. Instead another mechanism of averaging was taken, which comes closer to the real spatial distribution of installed wind power capacity. The grid points were weighed giving more weight on the grid points close to wind farms than the grid points far away from wind farms. This leads to an improvement as the DWD model is now comparable to the published TSO forecast data.

CONCLUSIONS

For single grid point predictions the error statistics between the models differ quite much and are not satisfactory. However simple averaging over the zone does not provide the optimal forecast results either. The error statistics get adequate if the spatial capacity distribution is considered. With the changes in the run, the DWD model based wind power prediction serves as well as the commercial wind power prediction.

REFERENCES

[1] K.E. Taylor. Summarizing multiple aspects of model performance in a single diagram. J. Geophys. Res., 106: 7183-7192, 2001.

Downscaling the wind energy resource in complex terrain using coupled mesoscale and microscale models

Venkatesh Duraisamy Jothiprakasam[1] , Eric Dupont[1], Bertrand Carissimo[1]
[1]EDF R&D / CEREA,
6 Quai Watier, 78401 Chatou, Cedex, France
E-mail: {venkatesh.duraisamy, eric.dupont, bertrand.carissimo}@edf.fr

Keywords: Coupling mesoscale and microscale modeling, complex terrain, wind resource assessment.

INTRODUCTION

The development of wind energy generation requires precise and well-established methods for wind resource assessment, which is the initial step in every wind farm project. Linear flow models are unable to predict the accurate wind speeds in complex terrain. Non-linear CFD models are able to give better prediction in atmospheric flows for complex terrains. The goal of the research work carried out is to reduce the uncertainty in the prediction of wind resource in a complex terrain using the CFD code Code_Saturne developed at EDF-R&D and CEREA (joint laboratory EDF-R&D / Ecole des Ponts). This work is performed in the framework of the FP7/ITN Marie Curie project WAUDIT.

CASE DESCRIPTION

One of the main causes of the uncertainty is due to the usage of theoretical wind profile conditions in the atmospheric CFD flow, which don't include the real features of the actual boundary condition. To overcome this, the lateral boundary conditions of the local scale simulations are provided by coupling the CFD model with the mesoscale model (Météo-France model Aladin). This coupling is combined to an assimilation of field measurements (wind speed and direction). A one-year field measurement campaign was led by EDF R&D and EDF Energies Nouvelles between June 2007 and June 2008 on a site of the South of France. The instrumental set-up included 2 sodars, two 50 m masts equipped with cup anemometers and vanes, and a 82 m mast equipped with cup and sonic anemometers, vanes, temperature and humidity sensors. The k-mean clustering method was used to reduce the number of situations to be simulated, reducing dramatically the computational time.

METHODOLOGY

A previous work performed with Code_Saturne with a preliminary version of this new methodology showed a significant reduction of the error simulation compared to WAsP simulation [1]. In order to improve this methodology, a detailed comparison with the measurements of wind and turbulence on some situations selected by the clustering method, a statistical error analysis over the whole data set, and an analysis of the situations which leads to the larger errors were carried out. Improvements of this methodology based on a better coupling with mesoscale model outputs are presented. A sensitivity to the grid and to the domain of simulation are also presented.

CONCLUSIONS

Further works will consist especially in taking into account the data assimilation [2], thermal stratification, and to couple the flow simulation with a wake modeling, in order to better optimize the turbines layout and to reduce the uncertainty in the annual energy production estimation.

REFERENCES

[1] Laporte L, Dupont E, Carissimo B, Musson-Genon L, Secolier C, Atmospheric CFD simulation coupled to mesoscale analyses for wind resource assessment in complex terrain, Proceeding of European Wind Energy Conference, Marseille, France, 2009

[2] Sue Ellen Haupt, Frank J.Zajaczowski, Kerrie J.Schmehl, A preliminary study of assimilating numerical weather prediction data intp computational fluid dynamics model for wind prediction, Journal of Wind Engineering and Industrial Aerodynamics, 99, 320-329, 2011

Modification of CFD code to model the atmospheric boundary layer

T. W. Koblitz, A. Bechmann, A. Sogachev, N. N. Sørensen
Wind Energy Dep., Risø DTU National Laboratory,
Frederiksborgvej 399, DK-4000 Roskilde, Denmark
E-mail: {tiko,andh,anso,nsqr}@risoe.dtu.dk

Keywords: atmospheric stability, CFD, wind resource assessment, RANS.

INTRODUCTION

In contrast to typical 'wind engineering' flows, the wind flow within the atmospheric boundary layer (ABL) takes place at other spatial and temporal scales, and depends on more complex physical processes that cannot be ignored in modeling. These are for example the Coriolis force, buoyancy forces, sensible and latent heat transport. Surface forcing has also complex temporal and spatial variations. For wind resource assessment, the industry is increasingly relying on Computational Fluid dynamics (CFD) methodology, based mostly on the solution of the Reynolds Averaged Navier-Stokes (RANS) equations, where, however, above mentioned processes are mostly ignored. To improve existing models for wind resource assessment, these effects should be included in the models. The starting point for the present work is the existing in-house CFD code (Risø DTU) EllipSys3D, that was developed for modeling of 'engineering' flows inside a limited, neutrally stratified domain. To model the flow within the ABL, the finite-volume code is modified to account for neutral, stable and unstable conditions. Therefore the effect of buoyancy will be included into the EllipSys3D code. This represents a promising approach to reduce uncertainty in predicting the geophysical transport phenomena, and is essential to understand the effect of buoyancy on the shear flow in the ABL. Within the present study the effect of Coriolis forcing is considered, and a length-scale-limited k- ε model, earlier proposed by [1], is employed. It limits the global maximum mixing length, while still being consistent with the logarithmic law close to the ground. Additionally, ambient floor values for the turbulence variables are imposed, in order to improve convergence for small mixing lengths [2]. Computational tests prove the applicability of the modifications, and the results are compared against previous results and observations [1,3], including data from the famous Leipzig wind profile and from the Cabauw site. The object of the first part of this study is to validate the modifications that were made to the flow solver EllipSys3D. Finally, the simulation of non-neutral ABL conditions is considered. The second part therefore focuses on flow over flat terrain, subjected to non-neutral temperature stratifications. Following previous works, the temperature equations and a further modified turbulence model are implemented into the code. These modifications enable us to simulate temporally varying non-neutral ABL conditions, as described for example in [4].

CONCLUSIONS

The present work presents modifications to the EllipSys3D code to model the wind flow within the ABL more appropriately. The implementation of the Coriolis forcing, as well as a length-scale limited k- ε turbulence model into the EllipSys3D code are successfully validated. Additionally, ambient floor values for the turbulence variables were used, and specific lower and upper bounds for these ambient values and the eddy viscosity have been determined. Finally, simulations of non-neutral conditions are considered. Further modifications that should be included into the existing model are evaluated, based on previous studies.

REFERENCES

[1] Apsley, D.D., Castro I.P., 1997. A limited-length-scale k–ε model for the neutral and stably-stratified atmospheric boundary layer. Boundary-Layer Meteorol, 83:75–98.

[2] Spalart, P.R., Rumsey, C. L., 2007. Effective Inflow Conditions for Turbulence Models in Aerodynamic Calculations. AIAA Journal, Vol. 45, No. 10, pp. 2544-2553.

[3] Sogachev, A., Panferov O., 2006. Modification of two-equation models to account for plant drag. Boundary-Layer Mete-orol., 121:229–266. doi:10.1007/s10546-006-9073-5.

[4] Mellor, G.L., Yamada T., 1974. Ahierarchy of turbulence closure models for planetary boundary layers. J Atmos Sci, 31:1791–1806.

Load estimation using Lidar data

O. Bischoff [1],J. Anger [1], M.Hofsäß [1] ,A. Rettenmeier [1], D.Schlipf [1]
Endowed Chair of Wind Energy (SWE), University of Stuttgart, Germany
Allmandring 5B, 70569 Stuttgart, Germany
E-mail: bischoff@ifb.uni-stuttgart.de

Keywords: LIDAR, fatigue, load estimation, turbulence

Introduction

This abstract and the corresponding paper present results and future work tasks that are planned related to Lidar measurements and corresponding load and fatigue evaluations of wind turbines. The measurements are taken at on- and offshore test-sites which are all also suited with standard measurement devices for validation purposes.

First results of load analyses based on data measured at AREVA M5000 wind energy turbines will be presented. These measurements are analysed and evaluated by on- and offshore measurements with Lidar systems which are enhanced with multi-purpose scanning devices [1] installed on the top of the nacelles of the wind turbines. This work is carried out within two research projects related to the German RAVE initiative.

Data Analysis & First Measurement Results

Wind turbines are highly dynamic loaded machines which are exposed to large numbers of load cycles during their fatigue life. Load and fatigue evaluations are generally carried out on the basis of wind data captured by measurement devices on a met mast. The main disadvantage of such devices is the lack of information about the entire incoming wind field.

Lidar systems and especially nacelle based Lidar systems offer the possibility to take a more detailed look on the wind conditions influencing a wind turbine.

The purpose of this work is to investigate and develop strategies to improve statistical load evaluations and also to research effects of transient events on the wind turbine and its mechanical components by not only regarding point measurements of the incoming wind but by introducing the whole incoming wind field into the analysis.

First measurement results taken with a nacelle based Lidar system and an attached scanner unit (Fig 1), with which it is possible to scan defined trajectories, indicate deviations to measurements taken with standard measurements devices especially regarding the turbulence dependency of loads [2].

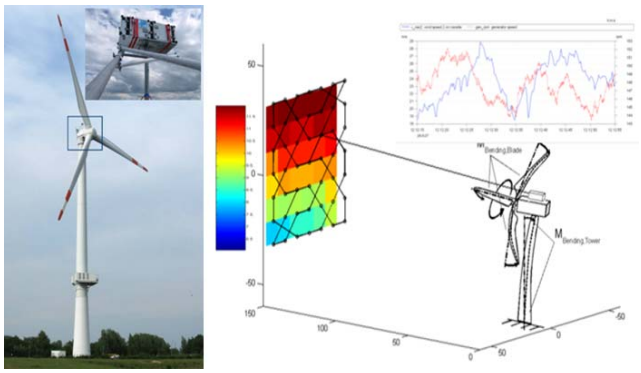

Figure 1: (a) AREVA M5000 with attached Lidar system, (b) sketch of the mode of operation of the Lidar-Scanner system

Future Work

Next worksteps will include a research of the effects of vertical and horizontal shearing on the fatigue of a wind turbine. It is planned also to define special criteria and areas of the incoming wind field which are of a considerable relevance for the wind turbine. Additionaly effects on the loads of transient events such as gusts shall be looked at.

Conclusions

First results and ongoing studies clearly indicate the benefit which is gained by introducing measurement data from the whole incoming wind field into the analysis of mechanical loads. It is expected that in the course of this work some parameters, as for example the turbulence influence, which are important for the dimensioning of wind turbine parts regarding fatigue issues can be defined.

References

[1] Rettenmeier, A. et al., Wind field analyses using a nacelle-based Lidar system, EWEC, Warsaw, 2010.

[2] Bischoff, O et al., Statistical load estimation using a nacelle-based Lidar system, DEWEK, Bremen, 2010

Finite Elements CFD Model for Wind Resource Assessment

A.Bonanni, T.Banyai, T.Quintino, H.Deconinck, C.Lacor
CFD Research group Von Karman Institute, Bruxelles
Mechanical Dep. of VUB University, Bruxelles
E-mail: {bonanni,banyai,quintino,deconinck}@vki.ac.be, clacor@vub.ac.be

Keywords: CFD, RANS, Wind Resource Assessment

1 Introduction

With the fast development of wind energy we are experiencing nowadays, it is not surprising that there is a rising demand for optimization tools that can improve the wind farm design and improve the evaluation of business opportunities. Optimization tools rely on numerical simulations of the atmospheric flow. The aim of this PhD is to develop a RANS CFD model for wind farm simulation and use it as a basis for a wind farm optimization tool.

2 CFD model development

The first objective of this PhD was the development of a CFD tool for exploring new simulation strategies for wind resource assessment over complex terrains. We now report on this development experience, focusing on the most important steps.

2.1 Finite Elements CFD RANS solver

A CFD RANS solver [3] has been adapted to make it suitable for Atmospheric Boundary Layer simulations [4]. This solver, called COOLWinD, has been developed inside the VKI simulation framework COOLFluiD. It presents an element of novelty for wind engineering applications since it uses a Finite Elements technique. This choice was justified by the experience that Finite Elements schemes revealed to be generally more accurate compared to other numerical techniques with unstructured grids (like the ones used for this project). The adaptation of the solver was mostly focused on the implementation of inlet conditions and wall functions suitable for ABL simulations. In particular, the original formulation of the wall-functions [1] needed to be recast to be successfully used in the FEM framework [5].

2.2 Ad-hoc mesh generator

Aside the CFD model, a new software for unstructured mesh generation has been developed [6]. This mesh generator allowed to test novel meshing strategies for complex terrains (mesh refining strategies, round domain boundaries, terrain surface smoothing, customized cell expansion factor in the vertical direction, etc..). The possibility to easily fine tune the mesh design revealed important implications in the results.

2.3 Actuator disk model

Finally, a wind turbine model has also been developed within the COOLWinD solver [7]. This model is based on the actuator disk principle . To simulate a wind turbine, the issue of the interaction of different atmospheric turbulence scales has to be addressed. In particular, the RANS closure model have to be modified. For our solver we chose the correction proposed by Kasmi-Masson [2].

2.4 Results and testcases

To validate the whole model we went through a series of testcases. We firstly simulated the empty-fetch to check the ability of the solver to keep the inlet profiles constant along the computational domain. We then simulated the Askervein testcase and finally we tested the actuator disk model against the data from the NIBE experiment.

3 Conclusions

The developed finite elements CFD solver has shown very good performances in all the testcases. In particular, from the Askervein testcase, it was clear that the numerics plays an important role and the problem of the underestimation of the turbulent kinetic energy in the lee-ward side of the hill can be significantly improved.

References

[1] P.J. Richards and R.P. Hoxey. Appropriate Boundary Conditions for Computational Wind Engineering Models Using k-eps Turbulence Model. J. Wind Eng. Ind. Aerodyn., 145-153, 1993.

[2] A.E. Kasmi, C. Masson. An Extended K-Eps model for turbulent flow through horizontal-axis wind turbines. Int Journal of Wind Engineering 96, 103-122, 2008.

[3] T.Banyai and D.V.Abeele and H.Deconinck. A Fast Fully-Coupled Solution Algorithm for the Unsteady Incompressible Navier-Stokes Equation. Conference on Modelling Fluid Flow (CMFF06), 2006.

[4] A.Bonanni. Adaptation of a generic CFD Solver to Atmospheric Boundary Layer Simulations. Technical report VKI-TN210, 2011.

[5] T.Banyai, A.Bonanni, T.Quintino, C.Lacor, H.Deconinck. Finite Element Technique for CFD Simulations of Atmospheric Boundary Layer Flows. Accepted for publication at ICWE13 conference, 2011.

[6] A.Bonanni. Development of a Mesh Generator for Atmospheric Boundary Layer Simulations. Technical report VKI-TN212, 2011.

[7] A.Bonanni. Wind Turbine Models in COOLFluiD. Technical report VKI-TN213, 2011.

Two-dimensional fluid-structure interaction

Knut Nordanger[1], Trond Kvamsdal[1], Runar Holdahl[2]
[1]Department of Mathematical Sciences, Norwegian University of Science and Technology
7491 Trondheim, Norway
[2]Department of Applied Mathematics, SINTEF ICT
Postboks 4760 Sluppen, 7465 Trondheim, Norway
E-mail: {knut.nordanger, trond.kvamsdal}@math.ntnu.no,
runar.holdahl@sintef.no

Keywords: fluid-structure interaction, isogeometric analysis

ABSTRACT

Coupled fluid-structure simulations of wind turbines have traditionally been considered computatinally too expensive to carry out. However, with more powerful computers and better solution techniques based on isogeometric analysis, such simulations can become a far more attractive alternative.

An important goal in isogeometric analysis has been to represent the geometry exactly on the coarsest grid. Development has firstly been motivated by the need for simplifying building detailed analysis models from CAD representations [3]. Secondly, once an initial mesh has been constructed it is advantageous to avoid further communication with the CAD geometry system. A key feature of the isogeometric or isoparametric approach is therefore to use the same set of basis functions for both the geometry and the analysis [2].

An attractive feature of isogeometric analysis is the possibilty to use non-uniform rational B-splines (NURBS) for representing complex, smooth geometrical shapes. Furthermore, NURBS possesses the ability of representing circular geometries exactly. This is particularly useful for applications involving flows around or induced by rotating components [1]. By employing this approach, no geometric incompatibilities will be introduced as opposed to a traditional finite element discretization. In traditional finite element analysis the inherent mesh geometric approximation can lead to accuracy problems [3]. The solution per-degree-of-freedom accuracy is usually better for isogeometric analysis than for low-order finite elements.

Accurate modelling of wind turbines requires coupled fluid-structure interaction (FSI) simulations. Wind speed and air flow influence the motion and deformation of the wind turbine blades. At the same time, the motion and deformation of the blades influence the air flow. For fluid-structure interaction the structural elasticity problem will be coupled with the incompressible Navier-Stokes equations.

As a first step for coupled fluid-structure simulation of wind turbines, we present the results from the implementation of two-dimensional fluid-structure interaction in a isogeometric framework. Investigations are carried out to determine the interaction between air flow and a 2D structure similar to a cross-section of a relevant rotor blade which is allowed to move in the plane and to rotate. Particular focus is placed on the coupling algorithm which transfers loads from the fluid formulation to the structural formulation and displacements and velocities from the structural formulation to the fluid formulation. The problem is illustrated in Figure 1.

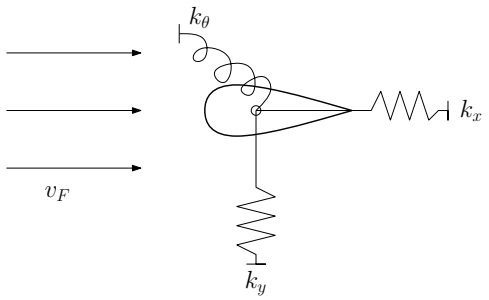

$$\underline{\mathrm{M}}\ddot{\mathbf{x}} + \underline{\mathrm{C}}_d\dot{\mathbf{x}} + \underline{\mathrm{K}}\mathbf{x} = \mathbf{F}(\mathbf{v_F})$$

Figure 1: Two-dimensional fluid-structure interaction problem

REFERENCES

[1] Y. Bazilevs and T.J.R. Hughes. NURBS-based isogeometric analysis for the computation of flows about rotating components. *Comput. Mech.*, 43(1):143–150, 2008.

[2] Thomas J. R. Hughes and John A. Evans. Isogeometric Analysis. ICES REPORT 10-18, The Institute for Computational Engineering and Sciences, The University of Texas at Austin, May 2010.

[3] T.J.R. Hughes, J.A. Cottrell, and Y. Bazilevs. Isogeometric analysis: CAD, finite elements, NURBS, exact geometry and mesh refinement. *Comput. Methods Appl. Mech. Eng.*, 194(39-41):4135–4195, 2005.

Uniaxial loading on in-plane hexagonal chiral structure with negative Poisson's ratio: adaptive structures for rotor blades

Oscar Castro, Fernando Casanova, Yesid Aguilar
Grupo de Investigación en Mejoramiento Industrial GIMI, Universidad del Valle
Calle 13 No 100-00, Cali-Colombia
E-mail: {oscar.gerardo.castro, gonzalo.casanova, yesid.aguilar}@correounivalle.edu.co

Keywords: Hexagonal chiral structure, Young modulus, negative Poisson's ratio, camber control

INTRODUCTION

The hexagonal chiral structure is a configuration whose negative in-plane Poisson's ratio leads to high shear modulus, while featuring some degree of in-plane bending compliance [1]. This structure was analyzed by different researches for helicopter rotor blades or airplane wings with chiral truss core [2-3]. These studies demonstrated that the hexagonal chiral honeycomb inside of the airfoil are a potentially superior alternative to conventional control surfaces because can provide continuous deflections in the airfoil resulting from flow conditions. In this document, a first analysis of the hexagonal chiral honeycomb applied to rotor blades of medium and small wind turbines is presented.

METHODS

Numerical analysis using element finite method was performed to predict the effect of the number of unit cells *N*, the ratio between the thickness of the nodes and the thickness of ligaments t_n/t and the aspect ratio between them *L/R*, on the in-plane mechanical behavior of hexagonal chiral structures, Fig. 1. The analysis was developed using ABAQUS 6.9 (Simulia Corp, Providence RI, USA) and was modeled by 8-nodes continuum shell elements. The structure material was Aluminum 6061 with E_s of 68,9 GPa.

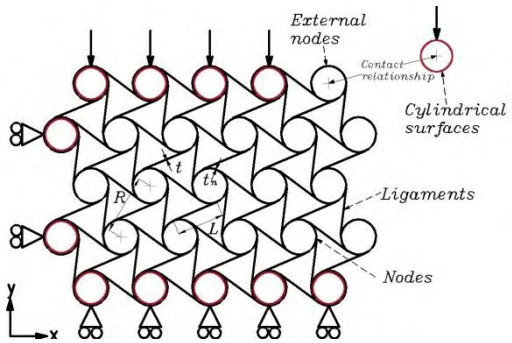

Figure 1: Hexagonal chiral structure with 2x5 unit cells. Load state and border conditions of numerical model.

RESULTS

The finite element models showed that the structure Young's modules *E* tend to be the same in both directions (consistent with the theoretical predictions [1]) when *N* is large, but are different in both directions when *N* is small. We also found that the structures with *L/R* ratio of 0,7 and 0,8 were more flexible than structures with ratio of 0,6, and that structures with *L/R* of 0,9 were the stiffest. On the other hand, this analysis confirmed that increasing the t_n/t ratio the structures were stiffer [1], E/E_s increase and tend to be constant as t_n/t is greater than 1,6.

The numerical models confirmed that hexagonal quiral structures have a negative Poisson's ratio υ, according with the theoretical predictions [1]. However, Poisson's ratio behavior was in-plane anisotropic. The υ_{yx} tend to -1 when the t_n/t ratio is greater that 1,33, and when the *L/R* ratio and *N* are increased. The υ_{xy} tend to stabilize too, but theirs values are around to -0,9 and depend of *L/R* ratio.

CONCLUSIONS

It was found that E/E_s and υ of the structures were affected by *N*, t_n/t and *L/R*. It was also found that the analyzed hexagonal chiral structures have an in-plane quasi-isotropic behavior caused by the number of nodes that satisfies the hexagonal chiral condition in the structure and the number of ligaments joined to the external nodes where the load is applied.

REFERENCES

[1] D. Prall and R.S. Lakes. Properties of a chiral honeycomb with a Poisson's ratio -1. In Journal of Mechanical Sciences, 39: 305-314, 1996.

[2] D. Bornengo, F. Scarpa, and C. Remilla. Evaluation of hexagonal chiral structure for morphing airfoil concept. In J. Aerospace Engineering, 219: 185-192, 2005.

[3] A. Spadoni and M. Ruzzene. Static aeroelastic response of chiral-core airfoils. In Journal of Intelligent Material Systems and Structures, 18: 1067-1075, 2007.

Poster Session 3

Control Systems

Increasing Energy Capture of Wind Turbines by Improved Yaw Control
R Young, W. Leithead, H. Yue

Improvement on Controller Design for a Small Scale VAWT Model
Claire Morris, David Infield

H∞ Control of a Wind Turbine
Mahmood Mirzaei, Niels Kjølstad Pouslen, Hans Henrik Niehmann

Electrical Production and Grid Integration

Performance Investigation of a 10MW AFPMSG
Zhaoqiang Zhang, Robert Nilssen, Arne Nysveen

Assessing Large-Scale, Economic Wind Energy Potential
Antriksh Singh, Ndaona Chokani, Reza S. Abhari

Offshore Technology & Innovative concepts

Floating offshore wind turbines – Concept screening and design sizing
Roberts Proskovics, Prof Shan Huang, Dr Julian Feuchtwang

Offshore Wind Capacity of the North Sea and the Promising Floating Wind Turbines
Onur Tunccan

Operation, Condition Monitoring and Maintenance

Automation of Wind Turbine Condition Monitoring
Donatella Zappalà, Peter J Tavner

Electrothermal Modelling for Wind Generator Reliability
Peter Wyllie, Li Ran, Peter J Tavner

Rotor and Wakes Aerodynamics

Analysis of aero-elastic simulations in wind farms with measurements at the offshore test field alpha ventus
B. Kuhnle, J.J. Trujillo, M. Kühn

Derive the relationship between in plane and out of plane bending moments for a HAWT
I.F.Dallas, W.E.Leithead, D.Infield

Navier-Stokes simulation of flow past pitched-regulated wind turbines using technique of sliding meshes
Dmitry Kolmogorov, Wen Zhong Shen, Jens Nørkær Sørensen

Instrumented UAV for Full-Scale Wind Turbine Measurements
G.Kocer, N.Chokani, R.S.Abhari

Wind Modelling, Forecasting and Resource Assessment

High resolved measurements performed with the 2d Laser-Cantilever-Anemometer
J. Puczylowski, M. Holling, J. Peinke

Pressure Measurements of the Detachment Bubble on the Bolund Island
Tee Seong Yeow, Alvaro Cuerva, Javier Perez

Wind Flow Simulations Using an Immersed Boundary Method
Samira Jafari, Ndaona Chokani, Reza S. Abhari

Windscanner: Preparation for the testing at Høvsøre
Nikola Vasiljević, Michael Courtney

Evaluation of turbulence scheme of the mesoscale model RAMS for high resolution wind ressource assessment
Barranger N., Kallos G.

Probabilistic forecasting of extreme wind speeds
Andrew K. Fish, Francisco Valero, Daniel Santos Muñoz

The representation of the marine atmospheric boundary layer in a mesoscale model
Erika Dautz

Wind Turbine Structural Design and Materials

Design and Finite Element Analysis of Mixed Aerofoil Wind Turbine Blades
Xinzi Tang, Ruitao Peng, Xiongwei Liu, Anthony Ian Broad

Structural design and analysis of a 10 MW wind turbine blade
Kevin Cox

Increasing Energy Capture of Wind Turbines by Improved Yaw Control

R Young, W. Leithead, H. Yue
Wind Energy Systems Doctoral Training Centre, University of Strathclyde
Royal College Building, George Street, Glasgow, United Kingdom
E-mail: {robert.young.100, w.leithead, hong.yue}@strath.ac.uk

Keywords: yaw control, energy capture, wind turbine,lidar

INTRODUCTION

Wind turbines operate in a dynamic, stochastic environment where instantaneous wind speeds and directions impinging on the rotor are difficult to predict, and affect power capture on a continuous basis. Generally, control of the wind turbine utilises feedback from disturbances already acting on the system.

With the continued development of cheaper, more accurate, distance wind measuring systems such as LIDAR (LIght Detection And Ranging), the possibility of including these instruments to improve wind turbine control has arisen. Harris, Hand and Wright [1] looked particularly at control of generator torque and blade pitch using this additional information, whilst project UpWind looked primarily at collective pitch control [2].

Conversely, yaw control can be used to achieve greater energy capture below rated speed by reducing the effective angle between the turbine rotor normal and the incoming wind.

It is proposed that using more accurate directional information e.g. from LIDAR, more active yaw control could result in higher energy capture.

ENERGY LOST UNDER CONVENTIONAL CONTROL SCHEMES

Due to their long averaging times the poor accuracy of wind vanes, conventional wind turbines do not accurately track wind direction. Figure1 shows the measured yaw error at a site in Denmark using a hub-mounted LIDAR, after [3]. It is the cosine of this yaw error that reveals the velocity component passing through the rotor, which, cubed, estimates the proportion of power which is extractable.

Even assuming no steady-state error, there is considerable fluctuation about the mean over various time-scales. It is these transverse gusts that a more active control scheme would try to capture.

MODELLING

GL GH Bladed was used to generate runs of 3 dimensional turbulent wind. As a first approximation, these wind runs

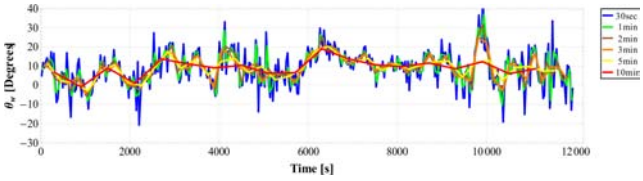

Figure 1: Yaw error from a hub-mounted LIDAR [3]

are assumed to be static (i.e. unaffected by the action of the wind turbine), and the comparison of the power passing through a rotor placed statically in this wind field, versus one moving to achieve the highest power extraction at each time step, provides the total envelope for improvement.

Constraints upon how much of an improvement can be achieved include the ability of the actuators to turn the nacelle and rotor to face the wind in the desired time, and the accuracy of information about the incoming wind field received by the controller. For a gross estimate, information is assumed to be perfect, and reasonable assumptions about the efficiency of the yaw motors, nacelle inertia, and rotor gyroscopic forces are made.

IMPROVED YAW CONTROL

Utilising this model, a control strategy is proposed that optimises the relationship between increased energy capture and loss to yaw actuator activation. An estimate of the increased energy output is provided.

CONCLUSIONS

Additional energy capture can be achieved by utilising a faster yaw controller in turbines with improved wind directional information. However, this must be weighed against the parasitic loss of driving the yaw motors.

REFERENCES

[1] M. Harris, M.Hand and A.Wright. Lidar for Turbine Control. Technical Report NREL/TP-500-39154, 2006.

[2] D. Schlipf. LIDAR assisted collective pitch control. Deliverable D5.1.3, 2006.

[3] T. Mikkelsen, K. Hansen, et al. Lidar wind speed measurements from a rotating spinner. EWEC, Warsaw, 2010.

Improvement on Controller Design for a Small Scale VAWT Model

Claire Morris, *student*, David Infield, *supervisor*
DTC Wind Energy Systems, Strathclyde University
Royal College Building, Room 3.36, 204 George Street, Glasgow, G1 1XW, UK
E-mail: claire.morris@strath.ac.uk , david.infield@eee.strath.ac.uk

Keywords: controller design, VAWT, small scale, variable speed, stall regulated

Introduction

A model is developed in Simulink for a small, variable speed, stall regulated vertical axis wind turbine (VAWT) and controller, based on an initial design from a paper published in 2010 [1]. The effectiveness of the controller is explored by analysing the impact of various wind models, adjusting the level and structure of turbulence. The controller design is adapted and improved to incorporate the turbine's dynamic behaviour, with particular attention to drive train loading.

1. Analysing the Existing Controller

The below-rated performance of the controller is evaluated for the Maximum Power Point Tracking regime, as outlined in the original work by Ahmed & Ran [1]. The behaviour is also investigated in the above rated, constant power stalling regime, considering the impact on the drive train of mechanical torque transients due to turbulent winds. Closed-loop stability analysis is carried out, and implications of the adaptive control method are discussed.

In this initial analysis, turbine dynamics used in the model are simplified to ignore rotor modes. The controller design is adjusted to take into consideration drive train modes and minimise the extent of structural stresses on the modelled wind turbine system.

2. Improving the Design

Extending the VAWT model

The aerodynamic model previously used, based on a second order polynomial Cp-λ curve fit up to Cp_{max}, is not considered accurate for a vertical axis turbine. Alternative system models are investigated and discussed, although it is recognised that an accurate description of any specific vertical axis machine would merit extensive further work.

Implementing an Improved Controller

The Soft Stall Controller proposed is tested and improved, by the incorporating the modelled system dynamics. Another (feed-forward) controller is then implemented, and comparisons drawn. This work highlights some of the technical issues presented by variable speed stall regulated wind turbines, and strategies to overcome these.

Conclusion

For reasons presented, variable speed stall regulated wind turbines have not been developed commercially. However if they do emerge, machines will be small scale (a few kW) to minimise financial risk. Controller designs investigated here are likely to be relevant to future small wind systems.

References

[1] A Ahmed & Li Ran; New Constant Electrical Power Soft-Stalling Control for Small-Scale VAWTs; IEEE Trans on Energy Conversion, Vol 25, No. 4, Dec 2010

H_∞ Control of a Wind Turbine

Mahmood Mirzaei, Niels Kjølstad Pouslen, Hans Henrik Niehmann
Technical University of Denmark
2800 Kgs. Lyngby, Denmark
E-mail: {mmir, nkp}@imm.dtu.dk, hhn@elektro.dtu.dk

Keywords: wind turbine control, robust control

Introduction

The problem of robust control of a wind turbine is considered in this work. A set of H_∞ controllers are designed based on a 2 degrees of freedom linearized model of a wind turbine. An extended Kalman filter is used to estimate effective wind speed and the estimated wind speed is used to find the operating point of the wind turbine. The resulting controller is applied on a full complexity simulation model and simulations are performed for stochastic wind speed according to relevant IEC standard.

Modeling

In this work we have set up two models. A simulation model and a set of control design models. FAST [**?**] is used as our simulation model and a set of linearized models of the nonlinear dynamical system equations of a wind turbine with two degrees of freedom is used as the design models.

Control

The most basic control objective of a wind turbine is to maximize captured power and prolong life time of the wind turbine. The second objective is achieved by minimizing the fatigue loads. Generally maximizing power capture is considered in the partial load and minimizing fatigue loads is mainly considered above rated. As we are operating in the full load region in this work, we have considered the second objective. In order to avoid high frequency activity of the actuators, we have put high pass filter on control signals to punish high frequency actions. Also we have setup low pass filters to punish low frequency of some of the system outputs.

Simulations

In this section simulation results for the obtained controllers are presented. The controllers are implemented in MATLAB and are tested on the full complexity FAST model of the reference wind turbine [**?**]. Kaimal model is used as the turbulence model and in order to stay in the above rated region, category C of the IEC turbulence categories with $18m/s$ mean wind speed is used.

Conclusions

The final controller is implemented on a FAST simulation model with 10 degrees of freedom and simulation with stochastic wind speed based on IEC standard is done. The results show good regulation of generated power and rotational speed for a big range of wind speed changes.

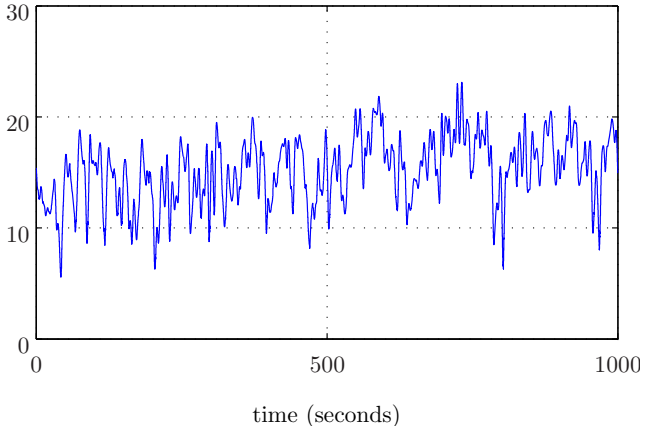

Figure 1: Blade-pitch reference

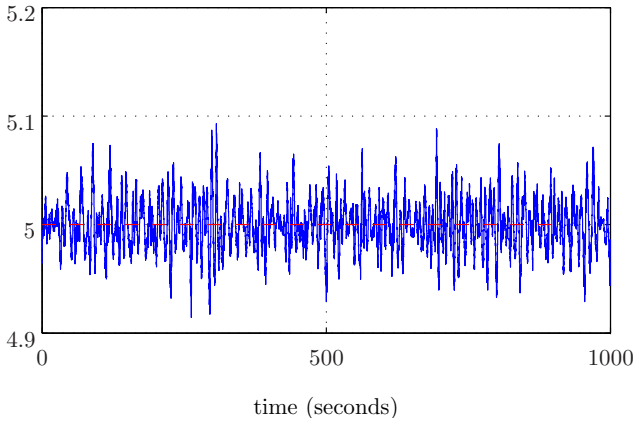

Figure 2: Electrical power (solid), reference (dashed)

References

[1] Jason M. Jonkman and Marshall L. Buhl Jr. Fast users guide. Technical Report NREL/EL-500-38230, National Renewable Energy Laboratory, August 2005.

[2] J. Jonkman, S. Butterfield, W. Musial, and G. Scott. Definition of a 5MW reference wind turbine for offshore system development. Technical report, National Renewable Energy Laboratory, 2009.

Performance Investigation of a 10MW AFPMSG

Zhaoqiang Zhang, Robert Nilssen, Arne Nysveen
Department of Electrical Power Engineering, Norwegian University of Science and Technology
O. S. Bragstads plass 2E, N-7034 Trondheim, Norway
zhaoqiang.zhang@elkraft.ntnu.no

Keywords: axial flux, concentrate winding, ironless, offshore, permanent magnet synchronous generator.

INTRODUCTION

Offshore wind application demands lightweight, highly efficient and reliable generators. Ironless AFPMSG has the advantages of low iron loss, and possibility of being integrated into turbine for a low top head mass.

This research investigates the performance of the ironless AFPMSG featuring with

- Double side rotor inner stator topology
- Multi-phase Overlapping concentrate winding
- Multi-section stator
- Halbach PM array rotor
- Multi-stage machine

SPECIFICATION AND SIZING

TABLE I: Machine specification

Rated power	P_{out}	10 MW
Rated speed	n	10 rpm
Phase voltage	U_{ph}	1.91 kV
Magnet load	B_{p1}	0.5 T
Electric load	A_i	50 kA/m
Power factor	$cos\phi$	1
Rated efficiency	η	95%
Filling factor	k_f	0.5
Current density	J	3 A/mm^2

This machine is sized with

$$P = \frac{\pi}{160\epsilon} K_d \sin\left(\frac{k_d}{1+k_d}\frac{\pi}{m}\right) n n_d B_{p1} A_i \eta cos\phi D_o^3$$

Active mass and copper loss are used as comparison criteria.

COMPARATIVE STUDY

One of the results is found bellow, and more will be given in the final paper.

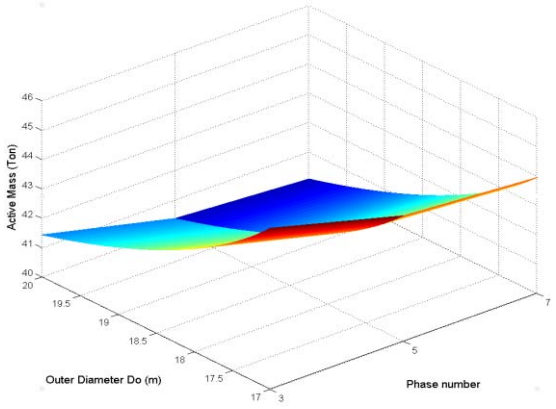

Figure 1: Active mass vs. phase number and external diameter.

VALIDATION OF THE METHOD

Finite element analysis is used to validate the method used.

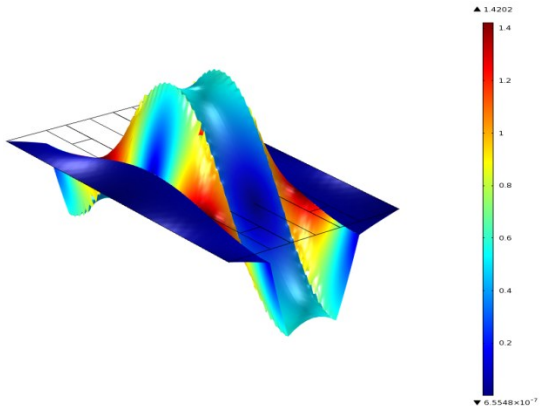

Figure 2: Axial flux distribution along one pole pair

CONCLUSIONS

Some of the conclusions:

- The favorable machine is with single stage, larger diameter,higher pole numbers and 4 section stator
- The analytical method developed can be used for performance investigation

REFERENCES

[1] J.F.Gieras, RJ. Wang, M.J. Kamper: Axial Flux Permanent Magnet Brushless Machines. 2nd. Springer. pp:107-110

Assessing Large-Scale, Economic Wind Energy Potential

Antriksh Singh, Ndaona Chokani, Reza S. Abhari
Laboratory for Energy Conversion, ETH Zürich
ML J 33, Sonneggstrasse 3, Zürich CH8092, Switzerland
E-mail: singh@lec.mavt.ethz.ch

Keywords: GIS, Econometrics, Performance Risk, Wind Energy Potential

INTRODUCTION

An integrated approach to identify, over large areas (that is land areas of order of 100'000km^2), sites that are suitable for the development of wind farms has been developed at ETH Zurich. Geo-spatially referenced data, within the framework of a Geographic Information System, are used to identify sites that are suitable, based on geographical, technical, anthropological and regulatory constraints. For the identified sites, the best-suited wind turbine technology is determined, and the wind farms' annual energy yield is then predicted; thus the economic benefits and risks of developing the wind farms can be assessed. Iowa, the second largest wind energy market in the United States, is used as a test case to demonstrate this integrated approach.

APPROACH

The rapid paradigm shift in energy policies of countries has resulted in a rapid growth (22% in 2010) of the wind industry. Policy makers and investors are thus focused on accurately estimating the economic wind energy potential across a portfolio of wind projects, in order to maximize generation and delivery wind-generated electricity to consumers at competitive prices.

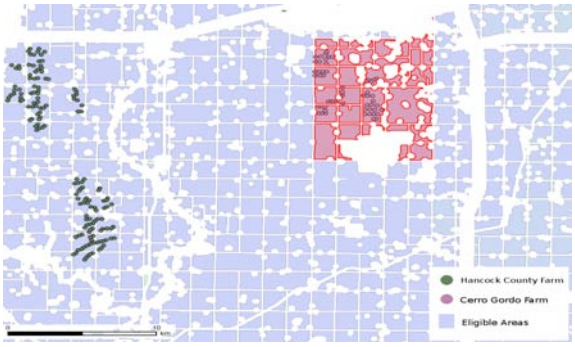

Figure 1: Comparison of Eligible Area and Reference Project.

The task of identifying economically viable wind farms is both challenging and time consuming. This task is further complicated by the involvement of several parties, whose goals and interests are usually not aligned. Thus, it is of interest to have an integrated approach, within which the geographical suitability of land (for example, avoiding water bodies, steep lands, urban areas etc.), the environmental impact (related to aviation, noise, visibility etc.), the availability of grid interconnection, the cost of wind-generated electricity, amongst a number of inputs can be simultaneously assessed [1]. Furthermore, as there are uncertainties in the wind resource and the turbines' response, an assessment of the performance risk is of particular interest to investors. In the present work, error propagation method, using parameterized Monte Carlo simulations, is used to assess the performance risk [2].

RESULTS

The integrated approach is applied to Iowa. Analysis shows that 41% of Iowa's land area is eligible for the siting of wind farms; the remaining land area is either protected, inaccessible or restricted land. Iowa is found to have an average capacity factor of 34%. Areas with high capacity factors are found in northern and western Iowa, but development of these areas is constrained by limited grid interconnection. Overall, Iowa has an estimated annual energy yield of 914TWh, to which the uncertainty in the wind speed is largest source of performance risk.

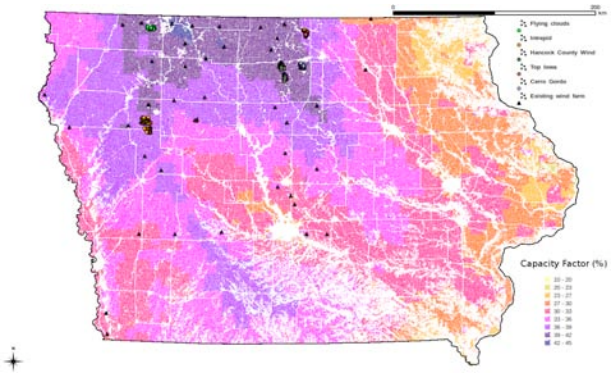

Figure 2: Predicted Capacity Factor, Iowa (Area 145'743km^2)

CONCLUSIONS

An integrated approach to identify, over large areas, sites that are suitable for the development of wind farms, has been developed. This approach is demonstrated using Iowa as a test case. It is shown that with this approach, the task of identifying economically viable wind farms

REFERENCES

[1] Grassi S., Chokani N., Abhari R. S., "Large-Scale Technical and Economical Assessment of Wind Energy Potential with GIS: Case Study Iowa," *In review.*

[2] Kochmann, E., "Estimating Uncertainty in Expected Return-on-Investment of Wind Energy Projects," *Internal Report*, Laboratory for Energy Conversion, ETH Zurich, 2011.

Floating offshore wind turbines – Concept screening and design sizing

Roberts Proskovics, Prof Shan Huang, Dr Julian Feuchtwang
Wind Energy Systems Doctoral Training Centre, University of Strathclyde
Royal College Building, George Street, Glasgow, United Kingdom
E-mail: roberts.proskovics@strath.ac.uk

Keywords: Wind turbines, floating, offshore, wind farms, shallow and deep waters, floater, static stability.

INTRODUCTION

Wind energy extraction is the most mature technique amongst the three offshore renewable energy options of wave, wind, and tidal current. In the offshore context, the majority of projects in the last few years, including all the UK Crown Estate Rounds 1 and 2 wind farm sites [1], were in shallow waters (up to 35m) and utilized structures fixed to the seabed. Whilst the UK has many more potential sites in shallow waters, some other countries only have much deeper water available for development. Currently, increasing efforts are being made to develop technologies for deeper waters, exceeding 40-50 meters depth, using floating wind turbines, as initially proposed by Heronemus [2] in the 1970s. Ultimately, floating wind turbines could be deployed further offshore in deep water where wind speeds are higher, hence increasing the power output. The oil and gas industry has proven that the technical challenges can be overcome, meaning that the challenge will primarily be economic one.

CONCEPT SCREENING

A wide variety of floating wind turbine concepts were assessed in terms of relevant criteria.

These included motion (static heel angle, heave etc), costs of the wind turbine, floater and mooring system and anchors. Costs were divided into contributions from material, fabrication, installation, maintenance and decommissioning.

Different concepts were then compared by giving appropriately weighted scores to each of the assessment criteria.

DESIGN SIZING

As a result of design screening, one particular concept was selected. A sizing or scaling study was then carried out to investigate how design parameters change as the concept increases in size. This was primarily based on the functional requirements and static loading conditions (wind loading, weight, buoyancy & mooring tension). The main criteria of the sizing are hydro-static stability and natural frequencies.

REFERENCES

[1] http://www.thecrownestate.co.uk/rounds-one-two

[2] Heronemus, W. E. “Pollution-Free Energy From Offshore Winds”, 8th Annual Conference and Exposition Marine Technology Society, Washington D.C., 1972.

Offshore Wind Capacity of the North Sea and the Promising Floating Wind Turbines

Onur Tunccan
Industrial Ph.D. Student
Hauschildt Marine A/S in cooperation with Aalborg University
Department of Civil Engineering
Sohngårdsholmsvej 57, Room: C-113
9000 Aalborg, Denmark
E-mail: ot@civil.aau.dk

ABSTRACT

The last two decades have witnessed innovative development and advancements in the offshore wind turbine technology, commencing with shallow water bottom fixed structures to floating wind turbine concepts in deep waters where there is vast amounts of wind to be harvested. Today, there are constant research and development activities worldwide, applying new designs and technologies for floating wind turbines in different stages of progress. The feasibility to deploy a floating wind turbine shall be based on the wind energy potential of the area of deployment and economical competitiveness. This paper, engaged in reviewing practice, presents research study for assessment of the offshore wind energy potential in the North Sea and a comprehensive review of the latest floating wind turbine concepts and designs developed in the industry. Availability of the highest amount of offshore wind energy to be absorbed by floating wind turbines with limitations are conducted throughout the North Sea region in order to identify importance of investment and progress. These findings are based on relevant literature, assessment data and up to date research. Besides, the major trends and developments of floating wind turbine technology in Europe are given, describing the state of the art in the field. A detailed assessment of existing prototypes and projects under development are reviewed including size and location. A preliminary overview of environmental considerations related to floating wind turbines is also provided.

Automation of Wind Turbine Condition Monitoring

Donatella Zappalà, Peter J Tavner
Energy Group, School of Engineering and Computing Science, Durham University
Durham DH1 3LE, UK
E-mail: donatella.zappala@durham.ac.uk, peter.tavner@durham.ac.uk

Keywords: Condition monitoring, Offshore wind, O&M.

INTRODUCTION

According to the European Wind Energy Association (EWEA) the wind resource around Europe's coasts is enough to supply Europe's electrical demand seven times over. The UK has potentially the largest offshore wind resource in Europe, with relatively shallow waters and strong winds extending far into the North Sea. The current trend in wind turbine (WT) development is for larger, more complex machines located in increasingly remote and hostile offshore locations. In these environments not only is the installation more difficult and expensive but access to the wind farms for maintenance purposes is also limited. The aim of this research is to develop automatic on-line WT monitoring and fault diagnostic procedures to improve offshore wind farm maintainability and availability, key features for their successful operation. Ultimately, results from this research should improve the cost-effectiveness of offshore wind farms.

OFFSHORE WIND O&M CHALLENGES

Offshore wind energy is expected to be a major contributor towards the UK Government's 2020 renewable generation target, aimed to improve energy security and reduce carbon emissions. The harsh offshore operating environment presents WT operation and maintenance challenges, whose costs are estimated to account for up to 30% of the total cost of energy, of which around 70% is due to unplanned maintenance [1]. These costs are too high for economically viable offshore projects. Significant savings can be made by moving to cost-effective, predictive, and proactive maintenance through use of reliable condition monitoring (CMS) and supervisory control and data acquisition (SCADA) systems. Increasingly installed in WTs, CMSs provide diagnostic information on the component health and alert the operator to trends that may be developing into failures. This helps to schedule maintenance tasks prior to complete component failure, which causes unplanned outages, downtime and lost revenue. Commercially available CMSs mainly use technologies initially developed for other industries, which can give frequent false alarms and require time consuming and costly manual data interpretation by expert engineers.

CONDITION MONITORING TEST RIG

Reliability surveys show that the lack of availability in WTs is concentrated in the drive train, with gearboxes and generators causing large downtimes and high costs [2]. A test rig, with features similar to operational WT drive trains, is used for the experimental investigation of electrical and mechanical faults. The rig consists of a 4-pole, 30 kW wound rotor induction generator driven through a 5:1 gearbox by a 54 kW DC motor. It is equipped with a torque transducer, two proximeters, two accelerometers and two tachometers. SKF WindCon, a commercial CMS, has been configured to record and process the sensor signals. This research aims to incorporate into WindCon an iterative localised discrete Fourier transform ($IDFT_{local}$) algorithm for fault-related frequency detection [3], focusing on three fault conditions applied to the test rig: rotor electrical asymmetry, high speed shaft mass unbalance, and gear tooth failure.

CONCLUSIONS

The incorporation of the $IDFT_{local}$ algorithm into a commercial CMS would result in an increasing degree of automation in the analysis of non-stationary, variable speed and load signals generated by WTs, reducing the man-power costs and eliminating the need for post-processing of WT CM signals.

REFERENCES

[1] G. J. W. Van Bussel and C. Schöntag. Operation and maintenance aspects of large offshore wind farms. Proc. Eur. Wind Energy Conf., Oct. 6–9, 1997, p. 272–275, Dublin, Ireland.

[2] P. J. Tavner, et al. Reliability & Availability of Wind Turbine Electrical & Electronic Components. EPE Journal, 20(4):45-50, 2010.

[3] C. J. Crabtree. Condition Monitoring Techniques for Wind Turbines, PhD Thesis, Durham University, November 2010.

Electrothermal Modelling for Wind Generator Reliability

Peter Wyllie, Li Ran, Peter J Tavner
Energy Group, Durham University
School of Engineering and Computing Sciences, Durham University, South Road, UK
E-mail: p.b.wyllie@durham.ac.uk, li.ran@durham.ac.uk, peter.tavner@durham.ac.uk

Keywords: power electronics, reliability

INTRODUCTION

Fluctuating power in a wind turbine (WT) results in cyclic thermal loading on the generator and converter. The semiconductor components (diodes and Insulated Gate Bipolar Transistors (IGBTs)) used in the back-to-back converter will suffer accelerated aging effects. These effects will have consequences for both reliability and lifetime of the converter. An accurate thermal model is required in order to improve reliability prediction and allow insight into likely failure modes. Methods for mitigating the effects of thermal cycling, such as advanced cooling techniques or by control of losses during operation will be investigated.

BACKGROUND

Wind power is set to play a crucial role in allowing government targets on reduction of carbon emissions to be met. The result will be an increased number of installed turbines both onshore and offshore. The remoteness of these wind farms, particularly those at offshore locations at which maintenance is costly, places an increased significance on reliability. Conventional steam turbogenerator units can outlast WTs by as much as 20 years: given the considerable research effort in the area of wind generation over the past 20 years this is a significant concern. A key distinguishing feature between the two operating environments is the fluctuating load developed by the stochastic nature of the wind. An understanding of the reliability implications of this stochastic mode of operation is crucial to allowing accurate prediction of turbine availability and lifetime energy yield. These turbine characteristics, of course, contribute to the cost of energy to the end user and thus the viability of wind generation of electricity.

The electrical subsystems (generator, converter and grid connection) have been identified as significant contributors to turbine failure rates and whilst reliability is improving failure rates for large WT generators especially in early life are still high [1]. It is hoped that a control strategy or design adaptation may be developed that will improve resistance to failure mechanisms of thermal origin within these systems.

METHOD

An electrothermal model of a large wind turbine is needed to allow us to understand the effect the varying wind has on the key electrical systems in the turbine. Reliability of converter and generator will, in part, be determined by the cycling of heat that arises due to varying electrical losses. In the case of a Doubly Fed Induction Generator (DFIG) the magnitude of this thermal cycling has been shown to be greater in the IGBTs that comprise the machine side converter than in those within the grid side converter. This problem may be used as a vessel to carry out research and to develop knowledge that may be applied to other topologies.

An electrothermal model of a 2.3 MW DFIG turbine has beed developed using MATLAB-SIMULINK to model the control of the WT and PLECS to model the electrical system. Loss data is extracted with a view to understanding the effects of thermal cycling on semiconductor aging in the converter.

REFERENCES

[1] F. Spinato, P.J Tavner, G.J.W. van Bussel and E. Koutoulakos Reliability of Wind Turbine Subassemblies. IET Renewable Power Generation. 3(4):1-15, 2009.

Analysis of aero-elastic simulations in wind farms with measurements at the offshore test field alpha ventus

B. Kuhnle, J.J. Trujillo, M. Kühn
Forwind - University of Oldenburg
Ammerländer Heerstraße 136, 26129 Oldenburg, Germany
E-mail: {bernd.kuhnle,trujillo,martin.kuehn}@forwind.de

Keywords: Turbine loading, wake dynamics, lidar measurements

1 Introduction

Due to economic and organizational aspects, the majority of turbines, such as offshore projects like Baltic I, are organized in parks. Thus, the mutual interaction resulting from the wake is omnipresent. The estimation of this interaction and the consequences for the wind turbines performance is very complex. Therefore simplified engineering models are being developed according to Thomsen, [1], and Frandsen, [2]. Here we test two engineering approaches for estimating the loading and eventually the loads of an offshore multi-MW wind turbine.

2 Methods

Two approaches are used for aero-elastic simulations of the inflow wind conditions according to the measurements at the offshore test field alpha ventus. Namely the effective turbulence, which is recommended in the standard for wind turbine design IEC61400-1, [3], and the dynamic wake meandering model (DWM from Risø), according to Larsen [4]. In the IEC approach the inflow environment of a wind turbine is divided into different wind direction sectors with corresponding effective turbulences according to the probability and the thrust of the upwind turbine.

For the DWM the large scale dynamics of the wake are prescribed based on measurements. These data come from the nacelle based lidars in alpha ventus where the inflow and wake conditions are monitored in the region near the rotor, mainly from -2 rotor diameters (D) until +2D.

By use of numerical modal analysis tools, the inflow conditions and the resulting loads will be reproduced and compared to adjusted generic 5MW turbine models.

3 Expected Results

Detailed measurement data of flow conditions in front and behind the turbine is expected in a resolution, which never existed in this form before. Further improvements of the knowledge of wakes in wind farms, their evolution and the resulting loads for wind turbines are expected. The comparison with engineering models will lead to their additional validation and improvement and further load mitigation strategies.

4 Conclusions

Mutual interaction is a significant contribution to wind turbines control and load characteristic. The new measurement campaign in alpha ventus will offer the possibility to an inter-connection of detailed flow and operational data and the resulting turbine load characteristic. An improvement in the accuracy of the simulation tools is expected. An influence on wind farm layout and wind turbine and substructure design may be the consequent result.

5 Acknowledgements

This research is funded by the German Federal Ministry for the Environment in the framework of the German joint project RAVE-OWEA (0327696).

References

[1] K. Thomsen et al., *Comparison of methods for load simulation for wind turbines operating in wake,* J. of Physics, Conf. Series, 75, 2007, 10.1088/1742-6596/75/1/012072.

[2] S. Fransen et al., *Turbulence and turbulence-generated structural loading in wind turbine clusters,* 2007, ISBN 87-550-3458-6

[3] International Electrotechnical Commission, *Wind turbines – Part 1: Design Requirements,* IEC 64100-1, 2005

[4] G.C. Larsen et al., *Dynamic wake meandering modeling,* 2007, ISBN 978-87-550-3602-4

Derive the relationship between in plane and out of plane bending moments for a HAWT

I.F.Dallas, W.E.Leithead, D.Infield
Wind Energy Doctoral Training Centre
16 Richmond Street, Glasgow G1 1XQ, United Kingdom
E-mail: {iain.dallas@strath.ac.uk}

Keywords: Bending Moments, Blade Geometry, Aerodynamic performance

INTRODUCTION

Background:

When analyzing and designing controllers, suitable simple models are required. In this context, the aerodynamic forces and moments are usually represented using aerodynamic coefficients. For individual blade control, both the in-plane root bending moment coefficient and the out-of-plane root bending moment coefficient are required but only the former is automatically provided by BLADED. It is possible to extract from BLADED the information from which the latter can be calculated but it is an extensive and time consuming process. It may be possible to determine the out-of- plane root bending moment coefficient from the in-plane root bending moment coefficient, the thrust coefficient and the blade geometry.

Objectives:

The objective is to determine a means of estimating the blade out-of-plane root bending moment coefficient from the in-plane root bending moment coefficient, the thrust coefficient and blade geometry information.

Tasks:

The program of work is the following.

1. Using simplified models of the blade and rotor determine an approximate relationship between the blade out-of-plane root bending moment coefficient, the in-plane root bending moment coefficient and the thrust coefficient.
2. From Bladed extract blade bending moment coefficients and the thrust coefficient.
3. Validate the relationship determined in the task 1 using the data from task 2.

Navier-Stokes simulation of flow past pitched-regulated wind turbines using technique of sliding meshes

Dmitry Kolmogorov, Wen Zhong Shen, Jens Nørkær Sørensen
Department of Mechanical Engineering, Technical University of Denmark
Nils Koppels Allé, Bygning 403, room 229, 2800 Kgs. Lyngby, Denmark
E-mail: {dkol, wzs, jns}@mek.dtu.dk

Keywords: wind turbines, sliding mesh technique, sliding interfaces, computational fluid dynamics.

INTRODUCTION

In the work the technique of sliding meshes is applied for simulation of flow past wind turbines with pitched-regulated blades. In the technique a structural and moving mesh is associated with the moving blades and a stationary mesh is associated with the ground, tower and nacelle. Between the two meshes, communications are achieved through the interfaces where one side is moving in relation to another side. The technique permits to treat the problem of bodies in relative motion in a simple way with a low computational cost.

SLIDING MESH ALGORITHM

The incompressible Navier-Stokes equations adapted for rotating frame of reference are used for computations in rotating domains of computational area. The exchange of data between relatively moving parts of a mesh is performed at interfaces, as shown at Figure 1. Here rotational velocity speed and magnitude of the domains may vary from one part to another part of the area.

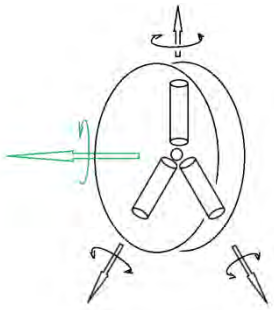

Figure 1: Sliding mesh interfaces around rotating parts of a wind turbine: rotor and each blade.

Interpolation and identification procedure

In general case as some parts of the domain may move, the grids at the block boundaries may not match. Here the exchange of data at block boundaries is performed with use of virtual cells. Data in centers of the virtual cells must be interpolated with data in cells, belonging to adjacent block. In current work the overlapping cell face technique with identification approach described at Ref.1 is used.

Future work

In a future a detail analysis of the aerodynamic behavior of the blades, the nacelle and the tower as well as unsteady rotor aerodynamics including wake interaction will be performed. Parametrical study will be carried out to simulate and analyze various operating conditions of a wind turbine, such as yaw, pitch regulation and turbulent inflow. Furthermore, the use of various pitching controllers for power control will be investigated. The developed technique will provide the basis for evaluating a wind turbine design.

CONCLUSIONS

The sliding mesh technique has been formulated in a form adapted for current block structured flow solver ELLYPSIS3D. Governing equations in rotating frame of reference have been shown. The main steps of the sliding mesh algorithm have been described. 2D simple structure cases such as a rotating cylinder and pitching airfoil is considered as a preliminary step for simulation of a full wind turbine and is the subject of current research work. Generalized formulation of the sliding mesh technique allows applying it for 3D wind turbine shape identically to 2D simple case. Parallelization algorithm, described in details in Ref. 1, will be adapted and implemented into the code enabling it to perform 3D computations.

REFERENCES

[1] Steijl, R., Barakos, 2008, «Sliding mesh algorithm for CFD analysis of helicopter rotor-fuselage aerodynamics», *Int. J. Numer. Meth. Fluids*; 58:527-549

[2] Michelsen, J. A., 1992, «Basis3D—A Platform for Development of Multiblock PDE Solvers,» Technical University of Denmark, Technical Report No. AFM 92-05.

[3] Gomez-Iradi, S., Steijl, R., and Barakos, G.N. (2009) Development and Validation of a CFD Technique for the Aerodynamic Analysis of HAWT. *ASME Journal of Solar Energy*, 131(8), pp.031009-1-13

Instrumented UAV for Full-Scale Wind Turbine Measurements

G.Kocer, N.Chokani, R.S.Abhari
Laboratory for Energy Conversion, ETH Zurich
Zurich, Switzerland
E-mail: gkocer@lec.mavt.ethz.ch

Keywords: UAV, wind turbine, near wake

INTRODUCTION

A novel measurement approach [Kocer et al, 2011] has been developed to measure the flow field around full-scale wind turbines. The key enabler for this novel approach is the integration of fast response aerodynamic probe technology with miniaturized hardware & software for uninhabited aerial vehicles (UAV) that enable autonomous UAV operation. The measurements of the near wake of a 2 MW wind turbine that is located in a topography of complex terrain and varied vegetation are reported here. The measurements are conducted to support the development of ETH Zurich's advanced wind simulation tool [Jafari et al, 2011].

MEASUREMENT SYSTEM

The unsteady, three-dimensional flowfield around the wind turbine is measured using the instrumented UAV shown in Fig. 3. This electric-powered, pusher-propeller-driven UAV has a wingspan of 800 mm, an overall length of 750 mm and a take-off mass of 900 g.

Figure 1: Instrumented UAV (wingspan, 800 mm) equipped with a seven-sensor fast response aerodynamic probe (diameter, 20 mm).

The UAV is instrumented with a seven-sensor fast response probe (7S-FRAP) for measurements of the wind flow [Mansour et al, 2011]. The sensing elements of the 7S-FRAP are miniature silicon piezo-resistive chips. These differential pressure sensors are embedded within a 20 mm hemispherical probe head; thus the 7S-FRAP yields measurements of the wind speed relative to the UAV. A GPS onboard the UAV yields the ground speed; therefore, the wind speed relative to the ground can be determined.

RESULTS

Vertical profiles of wind speed measured downstream of the wind turbine are shown in Fig. 2 [Kocer et al, 2011]. The profiles are at streamwise locations of x/D = 1, 1.5, 2, 2.5, and 3 and extend vertically from 60% to 180% of the hub height (z_{hub}). The horizontal error bars indicate the measurement uncertainty [Kocer et al, 2011]. The profiles show that after a 60% reduction in wind speed at x/D=1, the flow recovers to a deficit of 30% further downstream.

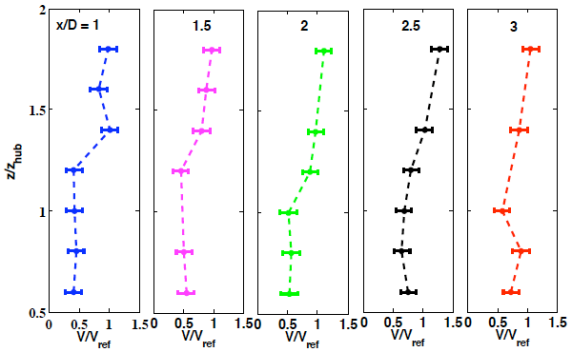

Figure 2 Profiles of wind speed measured in the near wake of a full-scale wind turbine.

CONCLUSIONS

Detailed measurements in the near-wake of a full-scale wind turbine are made using an instrumented UAV. These data are used to support the development of ETH Zurich's advanced wind simulation tool.

REFERENCES

[1] G. Kocer, M. Mansour, N. Chokani, R. S. Abhari, M. Mueller, "Full-Scale Wind Turbine Wake Measurements Using an Instrumented UAV," Proceedings of European Wind Energy Conference 2011.

[2] S. Jafari, N. Chokani, R. S. Abhari, "An Immersed Boundary Terrain Model for Efficient Simulation of Wind Flow over Complex Terrain," Proceedings of European Wind Energy Conference 2011.

[3] M. Mansour, G. Kocer, C. Lenherr, N. Chokani, R. S. Abhari, 2011, "Seven-Sensor Fast-Response Probe for Full-Scale Wind Turbine Flowfield Measurements," J. Eng. Gas Turbines Power, , 133, pp.081601-1 – 081601-8.

High resolved measurements performed with the 2d Laser-Cantilever-Anemometer

J. Puczylowski, M. Hölling, J. Peinke
ForWind - Center for Wind Energy Research, University of Oldenburg
Ammerländer Heerstr. 136 - 26129 Oldenburg, Germany
E-mail: {jaroslaw.puczylowski, michael.hoelling, joachim.peinke}@forwind.de

Keywords: turbulence, wind field analysis, 2d Laser-Cantilever-Anemometer

INTRODUCTION

Wind energy plays an important role for industry and the research sector. Although a lot of effort was undertaken during the last few years to characterize wind fields, there is still more demand on understanding atmospheric flows and turbulence. One focus in this area of research is clarity about small-scale properties of atmospheric turbulence. More knowledge about small-scale turbulence could be beneficial for many applications - for instance, the optimization of turbulence models for CFD [3]. In order to study the nature of turbulence, more measurements with highly-resolving anemometers are needed. The 2d Laser-Cantilever-Anemometer (2d-LCA) was developed at the University of Oldenburg in cooperation of the Fachhochschule Kiel with the intention to investigate turbulent structures on a millimeter scale at very high temporal resolutions. It was designed in such a way that it can operate in rough offshore environments for a long period of time. It therefore shows considerable advantages to other highly-resolving anemometers. Currently the 2d-LCA is undergoing the last testing phase before it will be installed at a met mast in the north sea (FINO3). First measurement results can be expected in a few weeks.

MEASURING PRINCIPLE

The sensing element of the 2d-LCA is a tiny cantilever measuring only 1.5mm in length and 0.4mm in width. It is attached to the tip of the sensor (see figure 1) and is facing the main flow direction. The acting drag force due to the moving medium changes its shape by linear elastic deformation. For a straight-line inflow the cantilever simply bends like a free-hanging and loaded beam structure, whereas oblique flow causes additional twisting [1],[2]. This mechanism is used to gain information about the flow. The deflection of the cantilever is measured by use of the laser pointer principle. This principle is also used in atomic force microscopes. Due to its two deflection modes, i.e. bending and twisting, it is capable of measuring 2 velocity components simultaneously. The resonance frequency, which is the limit for the temporal resolution is estimated to be above 30kHz. This measuring principle was already successfully applied for a laboratory version of the 2d-LCA, which is closely related to the current offshore version.

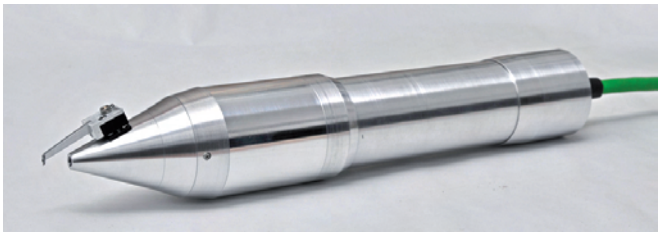

Figure 1: 2D Laser-Cantilever-Anemometer for offshore use.

CHALLENGES

Current work is mainly focussed on further development of the cantilever. Although the sensor works fine with the present setup, its performance can be improved by optimizing the surface and the shape of the cantilever. The main challenges in doing so is to refine the manufacturing steps. The shape of the cantilever plays a key role for the sensitivity of the sensor whereas a smooth surface is essential for the usage of the laser pointer principle.

REFERENCES

[1] M. Hölling, Sensorentwicklung für Turbulenzmessungen (Diss.), University of Oldenburg, Germany (2008).

[2] J. Puczylowski, Weiterentwicklung des 2D Laser-Cantilever-Anemometers (Master Thesis), University of Oldenburg, Germany (2009)

[3] K. R. Sreenivasan and R. A. Antonia, The phenomenology of small-scale turbulence, Annual Rev. Fluid Mech. 29:435-72 (1997)

Pressure Measurements of the Detachment Bubble on the Bolund Island

Tee Seong Yeow, Alvaro Cuerva, Javier Perez
Instituto Ignacio Da Riva, Universidad Politécnica de Madrid
Plaza de Cardenal Cisneros 3, 28040, Madrid, Spain
E-mail: teeseong.yeow@upm.es

Keywords: Bolund, wind tunnel, pressure measurements, detachment bubble

ABSTRACT

Pressure measurements on the surface of a 1:230 scale model of Bolund Island are presented. The model is smooth and no boundary layer generation has been considered since the experiment is designed as the simplest possible reference case. Measurement have been taken for a range of Reynolds numbers based on the average undisturbed wind speed U_∞ [5-25 m/s] and the maximum height of the island, h_{max} [$Re_{min} \approx 16500$, $Re_{max} \approx 260000$], as well as for a range of wind directions.

The scaled model has been obtained by numerical tooling from the same CAD file used by numerical modellers.

Three minutes time series of pressure in more than 400 points have been acquired and analysed to obtain the spatial distribution of both the time average and the variance of the pressure signal. The horizontal extension of the detachment bubble for the different Reynolds numbers and wind directions is identified by isobars and curves of constant value of pressure variance.

The applicability of this technique for evaluating the horizontal topology of high turbulence regions associated to detachment bubbles after escarpments in potential wind farm sites is analysed.

This experiment is part of the set of different analysis on the Bolund test case that is being undertaken within WAUDIT project by the different scientific groups. The main objective is to validate the capability of computational techniques to predict the flow topology on the island, using wind tunnel results and real field measurements and also to explore the validity of wind tunnels to predict certain characteristics of the real flow topology.

Figure 1: Model of the Bolund Island for wind tunnel testing

Wind Flow Simulations Using an Immersed Boundary Method

Samira Jafari, Ndaona Chokani, Reza S. Abhari
Laboratory for Energy Conversion, ETH Zürich
Zürich, Switzerland
E-mail: jafari@lec.mavt.ethz.ch

Keywords: micrositing, Reynolds-Averaged Navier Stokes, immersed boundary method

INTRODUCTION

The accurate modeling of the wind resource over complex terrain is required to optimize the micrositing of wind turbines. In this paper, an immersed boundary method that is used in connection with a Reynolds-Averaged Navier-Stokes solver with k-ω turbulence model is presented.

IMMERSED BOUNDARY METHOD

In this study, an immersed boundary method is used in connection with a RANS solver in order to simulate the different directions of a wind rose over any arbitrary topography using a single Cartesian grid. The method does not incur significant additional costs and changes in surface geometry, only require modification of the orientation of the topography. The method is described in more detail in [1].

RESULTS

To assess the performance, the method was applied to the moderate terrain test case, Askervein Hill and the complex terrain test case Bolund Hill. Figure 1 shows the results along line AA-AA over the Askervein Hill compared to the experiment [2].

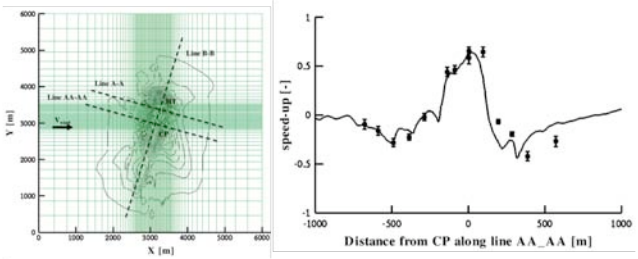

Figure 1: Speed-up along AA-AA over Askervein Hill

One Cartesian grid is used to simulate the flow over Bolund Hill for three different wind directions. Figure 2 shows the predicted normalized wind speed at 5 m above ground compared to experiment [3]. The results show that on the single Cartesian grid, variations in wind speed are captured for all the three directions with acceptable accuracy.

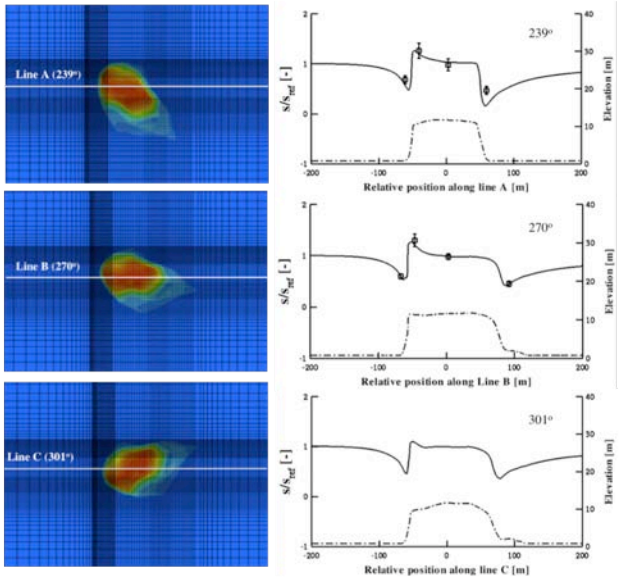

Figure 2: Wind speed over Bolund Hill for three different wind directions

CONCLUSIONS

The developed immersed boundary method is used to simulate the flow over Askervein Hill and Bolund Hill. The general good agreement observed between the predicted speed-up over the hill and experiments. Furthermore, results obtained with single grid for various wind direction demonstrates the relevance of the method to wind energy applications, since the same Cartesian grid, which is easily generated, can be used to produce results for different wind directions of a wind rose.

REFERENCES

[1] Jafari, S., Chokani N., and Abhari, R.S., "An Immersed Boundary Method for Efficient Simulation of Wind Flow over Complex Terrain," EWEC, 2011, Brussels, Belgium.

[2] Taylor, P.A., Mason, P.J., and Bradley, E.F., "Boundary Layer Flow over Low Hills," Boundary-Layer Meteorol., Vol. 39, 1987, 107-132.

[3] Bechmann, A., "Presentations from The Bolund Experiment: Workshop 3-4th December 2009," Riso-R-1745(EN), Riso DTU, 2010.

Windscanner: Preparation for the testing at Høvsøre

Nikola Vasiljević, Michael Courtney
Risø DTU
Frederiksborgvej 399 Building VEA-118, 4000 Roskilde, Denmark
E-mail: niva@risoe.dtu.dk

Keywords: Lidar, Remote Sensing, Resource Assessment

ABSTRACT

A windscanner is a system comprising three spatially separated wind lidar systems each with a fully-steerable scanner head (Figure 1). By steering the three beams to meet at a point, the 3D flow vector can be measured by combining these three independent radial wind speeds.

Figure 1: The long-range windscanner – the single device.

Since measurements are performed within a volume and not just at a point it is essential to identify and characterize all the central effects arising from the volumetric sampling. The investigation of these effects will be carried out by comparing the windscanner and sonic anemometer measurements at Risø's test site Høvsøre (Figure 2).

Figure 2: The row of wind turbines at the Høvsøre test site with the tall met. mast in the front.

Prior the testing, a preparation for this campaign will be performed using the windscanner simulator [1]. Since the simulator has a model of the lidar weighting function it is possible to simulate the measurement process. In relation to it positioning of the windscanner (Figure 3) will be studied using a detailed sketch of the test site (location of the masts and instruments).

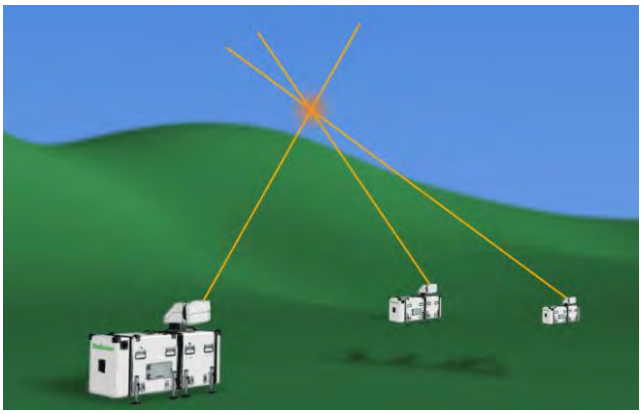

Figure 3: The windscanner – the complete system.

Based on the optimized positions of the windscanner angles for the scanner heads will be exported, therefore the testing prepared. After the testing, the measurements will be compared with the simulated results. This will give an insight how the modeled windscanner measurement process agrees with reality.

REFERENCES

[1] Vasiljevic N. et all. A Windscanner Simulator. EWEA Annual Event 2011. 2011. Brussels (BE).

Evaluation of turbulence closure scheme of the mesoscale model RAMS for high resolution wind resource assessment.

Barranger N., Kallos G.
Atmospheric Modeling and Weather Forecasting group, University of Athens
University Campus, Building Physics-5,15784 Athens, Greece
E-mail: {nbarranger,kallos}@mg.uoa.gr

Keywords: Mesoscale modelling, complex terrain, wind resource assessment.

INTRODUCTION

The regional atmospheric model RAMS has been developed for meteorological purpose. It solves the unsteady dynamical equations governing the atmospheric physics from the synoptic scale down to mesoscale and microscales. Its last evolution includes particle and pollutant dispersion as far as an elaborate parameterization of cloud physics.

The aim of this study is to use it as a tool for wind farm sitting and focus on the microscale physics of the so called atmospheric boundary layer. A special attention will be devoted to the interaction between the topography and the induced turbulence. A clear assessment of the turbulent scheme will be detailed and its limitations and improvement will be discussed.

TURBULENCE CLOSURE IN RAMS

The usual low resolution turbulence models (Mellor-Yamada) is often applied blindly at higher resolution that does not fit to microscale turbulence characteristics [2]. Two equation turbulence model E-epsilon and one equation E-l has been implemented this last decade [3]. This last development enables the use of very high grid resolution (order of meters) and models very precisely flow dispersion in complex area such as urban canopy [4]. In the continuity of this work, an E-ω scheme has been implemented and evaluated.

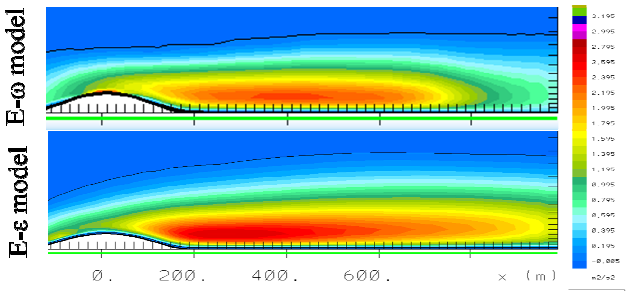

Figure 1: 2D hill turbulent kinetic energy production.

HIGH RESOLUTION CONFIGURATION

A simplification of the model has been processed to evaluate the new turbulent implementation. A neutral stratified flow has been initialized, the time scale is less than 1 second with a grid scale of few meters. A comparison with wind tunnel experiments is intended.

CONCLUSIONS

The effort that have been deployed to “tune” this mesocale model in order to solve turbulence on smaller scale is an asset in modeling wind speed and turbulent kinetic energy for wind sitting purpose.

The advantages of using this model are a complete description of the thermodynamic equations and the study of interaction between mechanically forced winds over stable, unstable or neutral conditions.

REFERENCES

[1] P. van Stangroom. CFD modeling of wind flow over complex terrain, PhD thesis, University of Nothingham, 2004.

[2] T. Hara, S. Trini-Castelli, R. Obha and C. Tremback. Validation of turbulence closure schemes for high resolution in mesoscale models – A case of gas dispersion at the local scale. Atmospheric Environments, 43: 3745-3753, 2009.

[3] S. Trini-Castelli, E. Ferrero and D. Anfossi. Turbulence closure in neutral boundary layer over complex terrain. Boundary Layer Meteorology, 100: 405-419, 2001.

[4] S. Trini-Castelli and T. G. Reisin, Application of a modified version of RAMS model to simulate the flow and turbulence in presence of buildings: the must COST 732 exercise, International Journal of Environment and Pollution. 44:394-402, 2011.

Probabilistic forecasting of extreme wind speeds

Andrew K. Fish (Present at EAWE), Francisco Valero, Daniel Santos Muñoz
Facultad de Fisícas, Universidad Complutense de Madrid
Madrid, Spain
E-mail: {akfish,valero,dsantos}@fis.ucm.es

Keywords: Ensemble forecasting, Numerical Weather Prediction, Ensemble Prediction System.

INTRODUCTION

The rapid increase in installed capacity of wind power has led to the need for more advanced methods for wind speed prediction. When trying to predict the state of the atmosphere in the future there are two main problems; the first is that there is uncertainty in the initial conditions, and the second is that the equations that govern the flow of the atmosphere cannot be fully solved. Traditional deterministic forecasting methods are unable to account for these uncertainties. Ensemble forecasting techniques provide a means for estimating these uncertainties, by perturbing the initial conditions and altering the physics used in the numerical weather prediction models it is possible to understand the influence of the initial conditions and physics on the predicted state of the atmosphere.

DEVELOPMENT OF AN ENSEMBLE PREDICTION SYSTEM

An ensemble prediction system (EPS) has been developed for the prediction of wind speeds over the Iberian peninsula. The model has a coarse outer domain with a resolution of 30km which covers the North Atlantic Region with a 2 way nested inner domain with 10km resolution centred over the Iberian Peninsula (Fig. 1). The EPS is composed of 10 members, which have been generated using 2 different initial conditions, and 5 different physics configurations of the WRF model. The design of the EPS has been based on a previous EPS by Santos [1] using the MM5 model, a predecessor of the WRF model.

Case Study: September 2006.

The EPS has been run for a period of one month, and the output from the model has been validated against the MM5 based EPS. The model output has also been validated against 6h mean wind speed observations at 10m height, collected at 72 sites across the Iberian Peninsula.

Over this one month period it can be seen that the WRF based EPS outperforms the MM5 based EPS. It can also be seen that there are clear benefits to using a probabilistic approach to wind speed forecasting. The ensemble mean has substantially smaller errors than the individual ensemble members, and the growth of model error with time is significantly slower. In addition to this it is possible for the EPS to provide further information about uncertainty in the weather forecast which is crucial when attempting to predict power output.

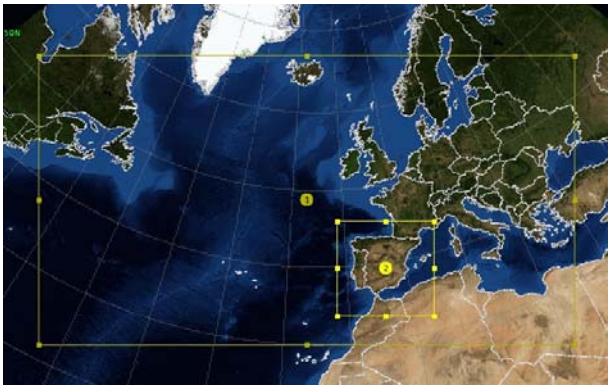

Figure 1: WRF model domains

CONCLUSIONS

The case study shows that the WRF based EPS has a greater degree of skill in predicting wind speeds compared to the MM5 based EPS. This higher level of skill can be attributed to the improved dynamics and physics of the WRF model. The study demonstrates the possibility for EPS to make a significant contribution in predicting wind power outputs.

REFERENCES

[1] Santos, D., Martin, M.L., Morata, A. Valero, F. And Pascual, C. Verification of a short-range ensemble precipitation prediction system over Iberia. Advances in Geosciences. 25:55-63, 2010.

The representation of the marine atmospheric boundary layer in a mesoscale model

Erika Dautz
ForWind, University of Oldenburg
Ammerländer Heerstraße 136, 26129 Oldenburg, Germany
E-mail: erika.dautz@forwind.de

Keywords: marine boundary layer, mesoscale model, observations, HELIPOD, LES

INTRODUCTION

The limited knowledge about the marine atmospheric boundary layer is still a difficulty for the efficient use of offshore wind power. The wind conditions in the marine boundary layer strongly deviate from onshore conditions due to a different thermal stratification, turbulence intensity and surface roughness, whereby the latter two are strongly affected by the wave field. In general, a stable stratification with weak turbulence, but usually large vertical wind shear, occurs more often in the marine boundary layer in the North Sea region, which has to be considered in the design of offshore wind farms.

MODEL SET-UP

The goal of this work is the evaluation and improvement of the planetary boundary layer (PBL) parameterizations in a mesoscale model. The Weather Research and Forecasting (WRF) model has been designed for operational and research use covering a broad range of scales. Its dynamical solver integrates the fully compressible, nonhydrostatic Euler equations in flux-form [1].

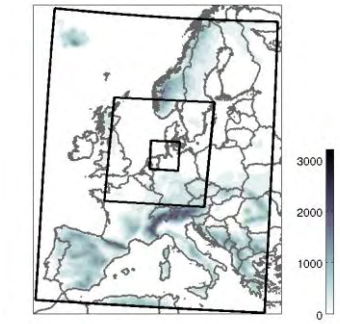

Figure 1: Grid configuration of the WRF simulations.

The input and boundary conditions for the runs are provided by the ECMWF. For the reference simulations three two-way nested domains are used (see Fig.1). Their horizontal mesh size is taken to be 27, 9 and 3 km, respectively. The innermost domain covers the German North Sea coast with the offshore met tower FINO-1 near the German test site Alpha Ventus.

RESULTS AND FUTURE PLANS

First sensitivity tests with varying planetary boundary layer schemes and different input data sets have been conducted for the period 6 to 11 May 2008. The results from these simulations are compared against data from soundings and weather stations. Statistical error measures reveal that the choice of the PBL scheme has a high impact on the quality of the simulations.

Later, the model simulations will be validated with observations from the offshore met-mast FINO-1 and measurements from a campaign with a helicopter-borne probe, called HELIPOD, in the North Sea Region (including measurements over land, coast and the open sea). The structure of the boundary layer will be investigated for different cases of thermal stratification over a longer time period. Beside the offshore boundary layer a main focus will be on the atmospheric conditions at land-sea discontinuities. Large-eddy simulations, which are able to resolve turbulent processes explicitly, are expected to provide a deep insight into the turbulent structure of the marine boundary layer and are another tool for the evaluation of the quality of parameterizations of turbulent processes in a mesoscale model, thus.

CONCLUSIONS

The results of this work will help to improve the representation of the offshore boundary layer in a mesoscale model. To enhance the knowledge of the structure of the boundary layer over sea data from various observations and simulations will be combined and analyzed.

REFERENCES

[1] Skamarock, W., et al., A Description of the Advanced Research WRF Version 3. NCAR Tech. Note NCAR/TN-475+STR, National Center for Atmospheric Research, USA.
[http://www.mmm.ucar.edu/wrf/users/docs/arwv3.pdf].

Design and Finite Element Analysis of Mixed Aerofoil Wind Turbine Blades

Xinzi Tang, Ruitao Peng, Xiongwei Liu, Anthony Ian Broad
School of Computing, Engineering and Physical Sciences, University of Central Lancashire
Preston, UK
E-mail: {xtang4,rtpeng,xliu9}@uclan.ac.uk

Keywords: wind turbine blade, finite element analysis.

1 INTRODUCTION

The performance of a wind turbine is highly dependent on the design of the rotor. Both aerodynamic and structural performances of wind blades show great influence on wind turbine system service life. Based on the Blade Element Momentum (BEM) theory and Finite Element Method (FEM), a 10KW fixed-pitch variable-speed wind turbine blade with five different thicknesses of aerofoil shapes along the span of the blade is designed, and deflections and strain distributions of the blade under extreme wind conditions are numerically predicted. The results indicate that the tip clearance is sufficient to avoid collision with the tower, and the behavior of the blade material is linear and safe.

2 BLADE DESIGN

2.1 Rotor Diameter and Material

Assuming a rotor efficiency of 40% and a total efficiency of 33.8%, a diameter of 5m is selected for the 10KW wind turbine. And the material of the blade is resin-reinforced fiber glass due to easy local availability.

2.2 Blade Aerofoil Shape

The basic aerofoil (from 30% to 90% radius sections) selected in this wind turbine blade is DU93-W-210. The aerofoil shapes at other stations are also derived from the DU series by changing the thickness. The transition between sections is obtained by linear interpolation.

2.3 Blade Chord and Twist

The optimal chords and twists are designed to a specific condition. The design tip speed of this 10KW wind turbine is set to 68m/s. The rated wind speed is 8.5m/s and the design tip speed ratio is 8.

2.4 Power, torque and thrust coefficients

Following an optimal blade geometry design at the specific tip speed ratio, the power, torque, and thrust coefficients for the whole range of tip speed ratios are analysed and predicted based on the BEM theory.

3 FINITE ELEMENT MODELING

A finite element blade shell model was developed based on CATIA and ABAQUS, and a composite material laminate schedule was presented. The blade was designed to survive an extreme wind speed of 60 m/s with the wind turbine was not in operation. The results indicate that the tip clearance is sufficient to avoid collision with the tower, and the blade material is still linear and safe.

4 CONCLUSIONS

A 5m composite blade of mixed aerofoil for a 10KW horizontal fixed-pitch variable-speed turbine was designed based on the BEM theory, and it is numerically validated that the design is positive and effective based on FEM.

Structural design and analysis of a 10 MW wind turbine blade

Kevin Cox
NOWITECH, Norwegian University of Science and Technology
Richard Birkelandsvei 2, 7034, Trondheim, Norway
E-mail: kevin.cox@ntnu.no

Keywords: Wind turbine blade, Finite element analysis, Hybrid composite materials

INTRODUCTION

This paper presents the design and analysis of the structural components of a 10 MW wind turbine blade. The process for designing a blade of this size requires the use of glass and carbon fiber composite materials to achieve a structurally stiff blade while maintaining a low weight.

STRUCTURAL DESIGN

The structure of the blade is shown in Figure 1 and consists of 3 main components: airfoil skin, spar cap, and shear web. As described in [1], components typically consist of a combination of glass fiber composite and foam core materials, with carbon fiber in the spar cap region in some cases. Ply thicknesses and properties were taken and oriented with 0^o and $\pm 45^o$ angles (where 0^o points along the pitching axis) to be consistent with [2]. Optimization of number of composite layers and location was performed to minimize total blade weight for the *50 year wind gust*, the assumed worst-case load scenario.

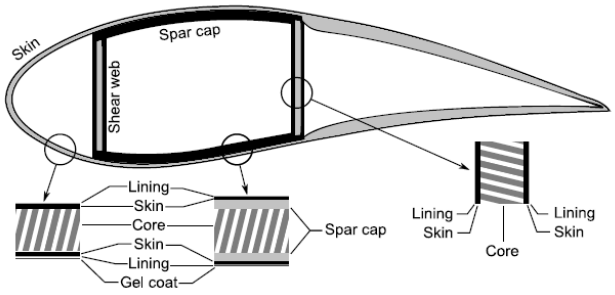

Figure 1: Structural components of turbine blade

SIMULATION

A 3D model of the 68m blade described in [2] was created with IEC load cases applied and submitted for finite element analysis using ABAQUS software to validate the results presented in the same paper. Blade weight and flapwise tip deflection were compared with [2]. Furthermore, buckling and dynamic load cases were studied to provide additional insight of the structural capability of the blade.

The aerodynamic forces subject to the blade from the various IEC load conditions were determined by BEM theory and applied as point forces on the nodes of the shell elements in the ABAQUS model. A total of 5 simulations were performed with nonlinear geometry effects included.

1. Extreme operating gust at cut-out wind speed: Quasi-static load.
2. Extreme operating gust at cut-out wind speed: Dynamic (gust) load as defined in [3].
3. Extreme wind speed in parked conditions: Quasi-static load.
4. Extreme wind speed in parked conditions: Dynamic (gust) load as defined in [3].
5. Buckling analysis.

Large wind turbine blades are subject to many possible failure modes though the two of focus in this study were (1) that all resulting nodal strains stay below their respective material failure strains, and (2) the maximum blade tip deflection must not violate the required minimum distance from the blade tip to the tower. A violation of either of these conditions was considered a failure, upon which material was added to the blade and the study was rerun until the failure criterion failed to occur.

CONCLUSIONS

Simulations are currently ongoing. Final conclusions for this study are therefore not yet available.

REFERENCES

[1] Griffin, D.A. Blade System Design Studies Volume II: Preliminary Blade Designs and Recommended Test Matrix. Sandia National Laboratories, 2004.

[2] L. Frøyd and O.G. Dahlhaug. Rotor Design for a 10MW Offshore Wind Turbine. ISOPE; Maui, USA, 2011.

[3] Wind turbines Part 1: Design requirements. NEK IEC 61400-1. Issue 3.0, 2007.

Index of Presenters